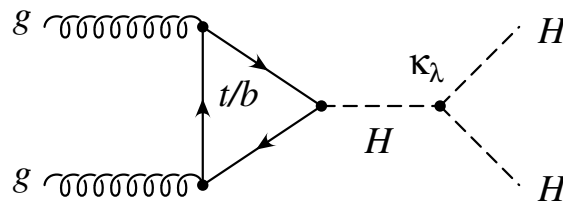# Higgs boson pair production at colliders:
status and perspectives

Editors:

Biagio Di Micco, Maxime Gouzevitch,

Javier Mazzitelli and Caterina Vernieri

arXiv:1910.00012v1 [hep-ph] 30 Sep 2019

Authors

B. Di Micco[1,2], M. Gouzevitch[3], J. Mazzitelli[4], C. Vernieri[5] (editors), J. Alison[6], K. Androsov[7], J. Baglio[8], E. Bagnaschi[9], S. Banerjee[10], P. Basler[11], A. Bethani[12], A. Betti[13], M. Blanke[11,14], L. Borgonovi[15], E. Brost[16], P. Bryant[17], G. Buchalla[18], T. J. Burch[16], V. M. M. Cairo[5], F. Campanario[11,19], M. Carena[17,20,21], A. Carvalho[22], N. Chernyavskaya[23], V. D'Amico[1,2], S. Dawson[24], N. De Filippis[25], L. Di Luzio[7,26], S. Di Vita[27], B. Dillon[28], C. Englert[29], A. Ferrari[30], E. Fontanesi[15], H. Fox[31], M. Gallinaro[32], P. P. Giardino[33], S. Glaus[14,34], F. Goertz[35], S. Gori[36], R. Gröber[37], C. Grojean[37,38], R. Gupta[10], U. Haisch[39], G. Heinrich[39], P. Huang[40], S. P. Jones[41], M. A. Kagan[42], S. Kast[11,43], M. Kerner[4], J. H. Kim[15], K. Kong[15], J. Kozaczuk[44,45], F. Krauss[10], S. Kuttimalai[5], H. M. Lee[46], K. Leney[13], I. M. Lewis[47], S. Liebler[34], Z. Liu[48], H. E. Logan[49], A. Long[50], F. Maltoni[51,52], S. Manzoni[53], L. Mastrolorenzo[54], K. Matchev[55], F. Micheli[23], M. Mühlleitner[34], M. S. Neubauer[44], G. Ortona[56], M. Osherson[57], D. Pagani[58], G. Panico[59], A. Papaefstathiou[60,61], M. Park[62], M. E. Peskin[5], J. Quevillon[63], M. Riembau[64], T. Robens[65], P. Roloff[66], H. Rzehak[67], J. Schaarschmidt[68], U. Schnoor[66], L. Scyboz[39], M. Selvaggi[66], N. R. Shah[69], A. Shivaji[51,70], S. Shrestha[42], K. Sinha[50], M. Spannowsky[10], M. Spira[9], T. Stefaniak[38], J. Streicher[8], M. Sullivan[47], M. Swiatlowski[17], R. Teixeira de Lima[5], J. Thomson[43], J. Tian[71], T. Vantalon[38,72], C. Veelken[22], T. Vickey[73], E. Vryonidou[41], J. Wells[74], S. Westhoff[43], X. Zhao[51], J. Zurita[11,14]

1 INFN, Sezione di Roma, Italy
2 Università degli Studi di Roma Tre, Rome, Italy
3 Institut de Physique Nucléaire de Lyon, France
4 Physik Institut, Universität Zürich, CH-8057 Zürich, Switzerland
5 SLAC, Stanford University, Menlo Park, California 94025 USA
6 Carnegie Mellon Univerisity, Pittsburgh, USA
7 INFN, Sezione di Pisa, Italy
8 Institute for Theoretical Physics, Eberhard Karls Universität Tübingen, Tübingen D-72076, Germany
9 Paul Scherrer Institut, Villigen PSI CH-5232, Switzerland
10 Institute for Particle Physics Phenomenology, Department of Physics, Durham University, Durham DH1 3LE, UK
11 Institute for Theoretical Particle Physics (TTP), Karlsruhe Institute of Technology, Karlsruhe D-76128, Germany
12 School of Physics and Astronomy, University of Manchester, Manchester, United Kingdom
13 Physics Department, Southern Methodist University, Dallas TX, USA
14 Institute for Nuclear Physics (IKP), Karlsruhe Institute of Technology, Eggenstein-Leopoldshafen D-76344, Germany
15 University of Kansas, Lawrence, USA
16 Department of Physics, Northern Illinois University, DeKalb IL, USA
17 Enrico Fermi Institute, University of Chicago, Chicago IL, USA
18 Ludwig-Maximilians-Universität München, Fakultät für Physik, Arnold Sommerfeld Center for Theoretical Physics, D–80333 München, Germany
19 Theory Division, IFIC, University of Valencia-CSIC, E-46980 Paterna, Valencia, Spain
20 Kavli Institute for Cosmological Physics, University of Chicago, Chicago, Illinois, 60637, USA
21 Theoretical Physics Department, Fermilab, P.O. Box 500, Batavia, IL 60510, USA
22 National Institute of Chemical Physics and Biophysics, Tallinn, Estonia
23 ETH Zurich - Institute for Particle Physics and Astrophysics (IPA), Zurich, Switzerland
24 Department of Physics, Brookhaven National Laboratory, Upton, N.Y., 11973, U.S.A.
25 INFN, Sezione di Bari and Politecnico di Bari, Italy

26 Dipartimento di Fisica dell'Università di Pisa

27 INFN, Sezione di Milano, Via Celoria 16, 20133 Milano, Italy

28 Department of Theoretical Physics, Jozef Stefan Institute, 1000 Ljubljana, Slovenia

29 SUPA, School of Physics and Astronomy, University of Glasgow, Glasgow G12 8QQ, U.K

30 Department of Physics and Astronomy, Uppsala University, Uppsala, Sweden

31 Lancaster University, Department of Physics, Lancaster, United Kingdom

32 Laboratório de Instrumentação e Física Experimental de Partículas, LIP Lisbon, Portugal

33 Instituto de Física Teórica UAM/CSIC, Universidad Autónoma de Madrid, 28049, Madrid, Spain

34 Institute for Theoretical Physics (ITP), Karlsruhe Institute of Technology, D-76131 Karlsruhe, Germany

35 Max-Planck-Institut für Kernphysik Saupfercheckweg 1, 69117 Heidelberg, Germany

36 Santa Cruz Institute for Particle Physics, University of California, Santa Cruz, CA 95064, USA

37 Institut für Physik, Humboldt-Universität zu Berlin, Berlin D-12489, Germany

38 DESY, Hamburg D-22607, Germany

39 Max Planck Institute for Physics, München 80805, Germany

40 Department of Physics and Astronomy University of Nebraska-Lincoln, Lincoln, NE, 68588

41 Theoretical Physics Department, CERN, Geneva, Switzerland

42 Ohio State University, Columbus OH, USA

43 Institute for Theoretical Physics (ITP), Heidelberg University, Heidelberg D-69120, Germany

44 Department of Physics, University of Illinois, Urbana IL, USA

45 Amherst Center for Fundamental Interactions, Department of Physics, University of Massachusetts, Amherst, MA 01003

46 Department of Physics, Chung-Ang University, Seoul 06974, Korea

47 Department of Physics and Astronomy, University of Kansas, Lawrence, Kansas 66045, USA

48 Maryland Center for Fundamental Physics, Department of Physics, University of Maryland

49 Ottawa-Carleton Institute for Physics, Carleton University, Ottawa, Ontario K1S 5B6, Canada

50 Department of Physics and Astronomy, University of Oklahoma, Norman, OK, 73019, USA

51 Centre for Cosmology, Particle Physics and Phenomenology (CP3), Université Catholique de Louvain, B-1348 Louvain-la-Neuve, Belgium

52 Dipartimento di Fisica e Astronomia, Università di Bologna and INFN, Sezione di Bologna, via Irnerio 46, 40126 Bologna, Italy

53 Nikhef National Institute for Subatomic Physics and University of Amsterdam, Amsterdam, Netherlands

54 RWTH Aachen University, III. Physikalisches Institut A, Aachen, Germany

55 Institute for Fundamental Theory, Physics Department, University of Florida, Gainesville, FL 32611, USA

56 INFN, Sezione di Torino, Italy

57 Rutgers, The State University of New Jersey, Piscataway, USA

58 Technische Universität München, Garching D-85748 , Germany

59 Università degli Studi di Firenze and INFN Firenze, Sesto Fiorentino (FI), Italy

60 Institute for Theoretical Physics Amsterdam and Delta Institute for Theoretical Physics, University of Amsterdam, Amsterdam 1098 XH, The Netherlands

61 Nikhef, Theory Group, Amsterdam 1098 XG, The Netherlands

62 Institute of Convergence Fundamental Studies and School of Liberal Arts, Seoultech, Seoul 01811, Korea

63 Laboratoire de Physique Subatomique et de Cosmologie, Université Grenoble-Alpes,

CNRS/IN2P3, 53 Avenue des Martyrs, Grenoble 38026, France

[64] Départment de Physique Théorique, Université de Genève, Genève 1211, Switzerland

[65] Theoretical Physics Division, Rudjer Boskovic Institute, Zagreb 10002, Croatia

[66] CERN, Geneva, Switzerland

[67] CP3-Origins, University of Southern Denmark, Denmark

[68] Department of Physics, University of Washington, Seattle WA, USA

[69] Department of Physics and Astronomy, Wayne State University, Detroit, MI 48201, USA

[70] Indian Institute of Science Education and Research, Knowledge City, Manauli 140306, Punjab, India

[71] University of Tokyo, Japan

[72] IFAE and BIST, Universitat Autónoma de Barcelona, Barcelona, Spain

[73] Department of Physics and Astronomy, University of Sheffield, United Kingdom

[74] Leinweber Center for Theoretical Physics, Department of Physics, University of Michigan Ann Arbor, MI 48109 USA

Preface

With the discovery of the Higgs boson [1–6] at the Large Hadron Collider (LHC) [7,8], all the particles predicted by the Standard Model (SM) of particle physics have now been observed. While for the moment the SM has been able to successfully describe the experimental measurements obtained in particle colliders, many predictions of the model still remain to be tested. Furthermore, the quest for a more fundamental description of nature is still ongoing.

The LHC, running between Switzerland and France from the year 2009 to 2018, has provided measurements of the Higgs boson couplings to the vector bosons W and Z, and to the heaviest generation of quarks and charged leptons. The more elusive couplings to the first two generations and to neutrinos are, however, still completely untested. Moreover, the energy potential of the Higgs boson field, responsible for the electroweak symmetry breaking (EWSB) mechanism, has not yet been measured by any experiment.

After EWSB the Higgs boson potential gives rise to cubic and quartic terms in the Higgs boson field, inducing a self-coupling λ which, within the SM, is fully predicted in terms of the Higgs boson mass and the Fermi coupling constant. A measurement of this coupling would therefore start shedding light into the actual structure of the potential, whose exact shape can have deep theoretical consequences.

Within the current uncertainty in the mass of the top quark, the self-coupling λ — whose value runs with the energy due to quantum corrections — could tend to zero at the Planck scale. In this case, it has been advocated [9] that a theory of quantum gravity can be built starting from the present formulation of general relativity and the SM, that is fully renormalisable in a non-perturbative manner. In addition, in this scenario of vanishing λ and in the presence of a non-minimal coupling between the Higgs field and gravity [10], or in the presence of new physics contributions [11], the Higgs boson field could be responsible for cosmological inflation. Finally, using the current central values of the measurements of the Higgs boson and the top quark mass, the Higgs potential energy function would have a new minimum at Higgs field values above 10^{11} GeV. This would imply that the vacuum state of the SM, as we see it today, is unstable, and that 10^{600} years in the future [12–14] our universe would be swallowed up in the transition to a new vacuum state with different laws of physics. These disturbing or enticing possibilities could be tested with a sufficiently accurate measurement of the Higgs self-coupling.

Despite the importance of a precise determination of λ, the SM prediction for this coupling is still far from being tested, since all precision observables show a very mild dependence on it. Constraints can be derived from perturbative unitarity arguments, but also in these cases they are quite weak, spanning up to five times the SM predicted value. For a direct determination of this coupling, the challenging measurement of di-Higgs boson production at colliders is needed.

The target of the present work is to summarise the present theoretical and experimental status of the di-Higgs boson production searches, and of the direct and indirect constraints on the self-coupling λ, with the wish to serve as a useful guide for the next years. The work has started as the

proceedings of the Di-Higgs workshop at Colliders, that was held at Fermilab from the 4th to the 9th of September 2018, but it went beyond the topics discussed at that workshop and included further developments. The editors would like to thank all contributors, the ATLAS and CMS collaborations and the Higgs cross section working group for supporting the editing of this white paper and for providing many useful inputs and advises, and in particular Michael Peskin for his careful review of the manuscript and his substantial contribution to the overall shaping of this work.

The editors
B. Di Micco
M. Gouzevitch
J. Mazzitelli
C. Vernieri

Contents

Part I

Theoretical status

In this Part we aim to provide an overview of the latest theory developments that are relevant to the measurement of the Higgs boson self-coupling and, more in general, to the study of the HH production process in the context of the SM and beyond. The theory efforts that are summarised here are vital in order to extract the maximum possible information from the experimental measurements.

In Chapter 1 we present the latest theoretical predictions for the production cross section of SM Higgs boson pairs in the different production modes, including fixed order results and Monte Carlo generators. We put special focus on the main production mode at the LHC, gluon fusion. We describe in Chapter 2 the developments on the effective field theory approach, crucial for the interpretation of non-resonant deviations from the SM expectations. We study the impact that a fit of the effective field theory coefficients would have on the Higgs self-coupling determination, both in double and single Higgs final states. Finally, in Chapter 3, we present specific beyond the SM scenarios that can have sizeable effects in the di-Higgs final state. We mostly focus on signatures coming from new resonant states decaying into Higgs boson pairs, though we also study the impact that new physics contributions might have via loop effects.

Chapter 1

HH cross section predictions

Editors: M. Spira, E. Vryonidou

While the quartic Higgs coupling λ_{H^4} cannot be probed directly at the LHC due to the small size of the triple-Higgs production cross section [15–18], the trilinear Higgs coupling can be accessed directly in Higgs pair production. At hadron colliders, Higgs boson pairs are dominantly produced in the loop-induced gluon-fusion mechanism $gg \to HH$, mainly mediated by top quark loops, similarly to how a single Higgs boson is produced. An estimate of the dependence of the cross section on the size of the trilinear coupling is given by the relation $\Delta\sigma/\sigma \sim -\Delta\lambda/\lambda$ in the vicinity of the SM value of λ. This fact clearly illustrates that, in order to determine the trilinear coupling, the theoretical uncertainties of the corresponding cross section need to be under control, hence the inclusion of higher-order corrections in the QCD perturbative expansion becomes indispensable.

In this chapter we will summarize the state of the art of the theoretical predictions concerning the production of SM Higgs boson pairs at hadron colliders. We start by describing in Sec. 1.1 all the different production modes, then in Sec. 1.2 we focus on the QCD corrections for the main production mode, gluon fusion, and in Sec. 1.3 we describe its dependence on the Higgs self-coupling. Finally, in Sec. 1.4 we review the available Monte Carlo generators.

1.1 Overview of production modes

We individually discuss below the main production modes of Higgs boson pairs at hadron colliders, briefly summarizing the status of the corresponding theoretical predictions. Examples of the leading-order (LO) Feynman diagrams are illustrated in Fig. 1.1, a summary plot of the total cross sections – to the highest available accuracy – as a function of the collider center-of-mass energy is shown in Fig. 1.2, and the predictions are also presented in Table 1.1.

Gluon fusion. Higgs-boson pairs are dominantly produced in the loop-induced gluon-fusion (ggF) mechanism that is mediated by top quark loops, supplemented by a smaller contribution of bottom quark loops. There are destructively interfering box (Fig. 1.1a left) and triangle (Fig. 1.1a right) diagrams, with the latter involving the trilinear Higgs coupling [20, 21]. The relative contribution of these two different pieces, as well as their interference, can be observed in the Higgs pair invariant mass distribution shown in Fig. 1.3. The effect of the trilinear Higgs self-coupling in the LO total cross section amounts to a reduction of about 50% with respect to the box-only contribution, due to the large destructive interference. The QCD corrections are known up to next-to-leading order (NLO) [22–24] and at next-to-next-to-leading order (NNLO) in the limit of heavy top quarks [25–28],
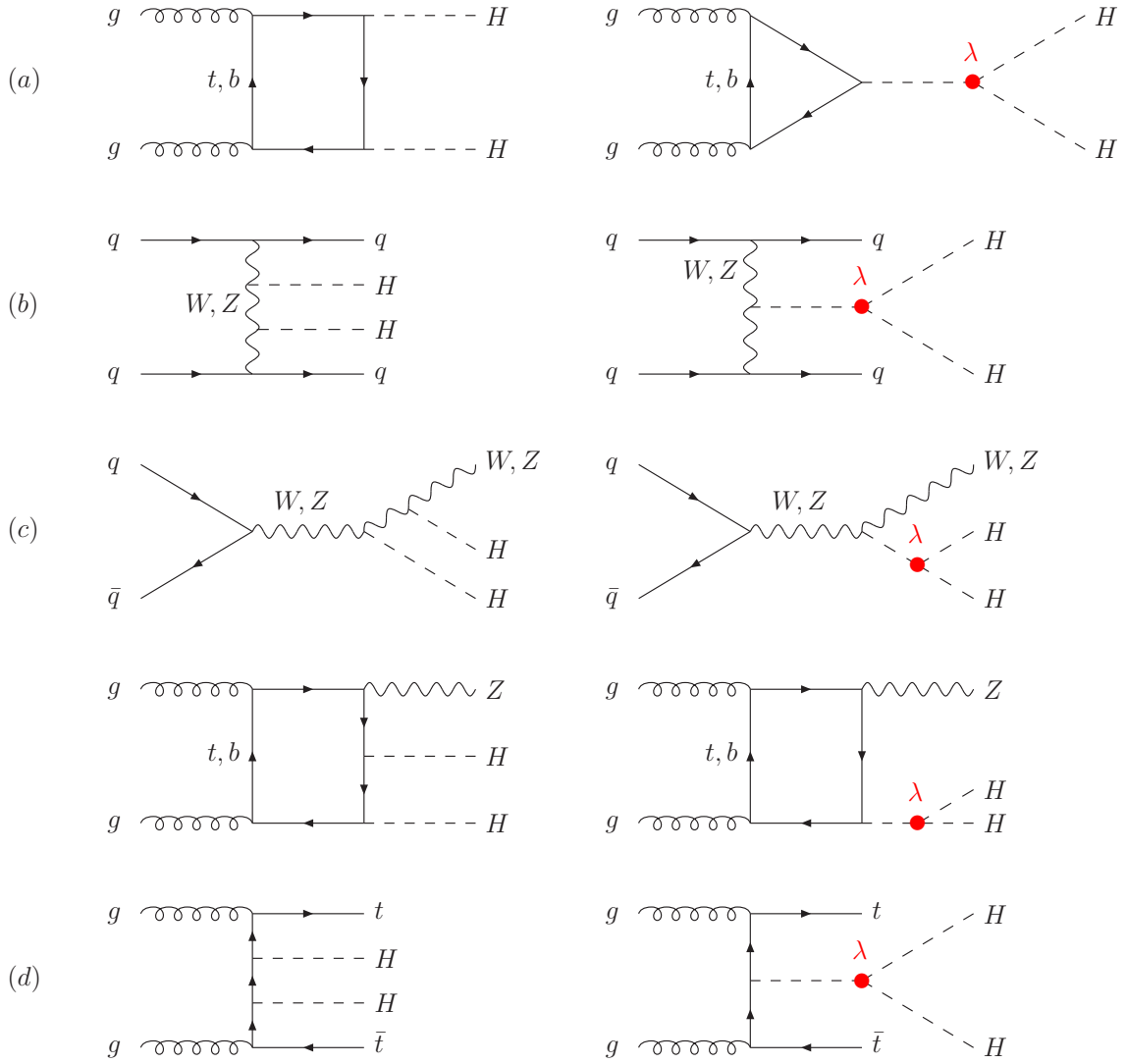
Figure 1.1: Diagrams contributing to Higgs pair production: (a) gluon fusion, (b) vector-boson fusion, (c) double Higgs-strahlung and (d) double Higgs bremsstrahlung off top quarks. The trilinear Higgs coupling contribution is marked in red.

including partial finite top quark mass effects [29]. They increase the total cross section by about a factor of two. The QCD corrections will be discussed in more detail in the following section.

Vector-boson fusion.   The vector-boson fusion (VBF) $qq \rightarrow HHqq$ is the second-largest production mechanism, and it is dominated by t-channel W and Z exchange in analogy to single Higgs production. It involves continuum diagrams originating from two Higgs radiations off the virtual W or Z bosons, and diagrams in which a single Higgs boson (off-shell) splits into a Higgs pair (Fig. 1.1b). The QCD corrections are only known in the structure-function approach, i.e. where only the t-channel W and Z exchange is taken into account and interference effects for external quarks of the same flavor are neglected. This approximation is valid at the level of a percent similar to the single Higgs case. Within this approach the QCD corrections to the total cross section are known up to N^{3}LO [30–32], while the exclusive calculation is available at NNLO [33]. The perturbative corrections alter the total cross section at the level of about 10%, while they can be larger for distributions. The moderate size of the QCD corrections can be traced back to the t-channel-
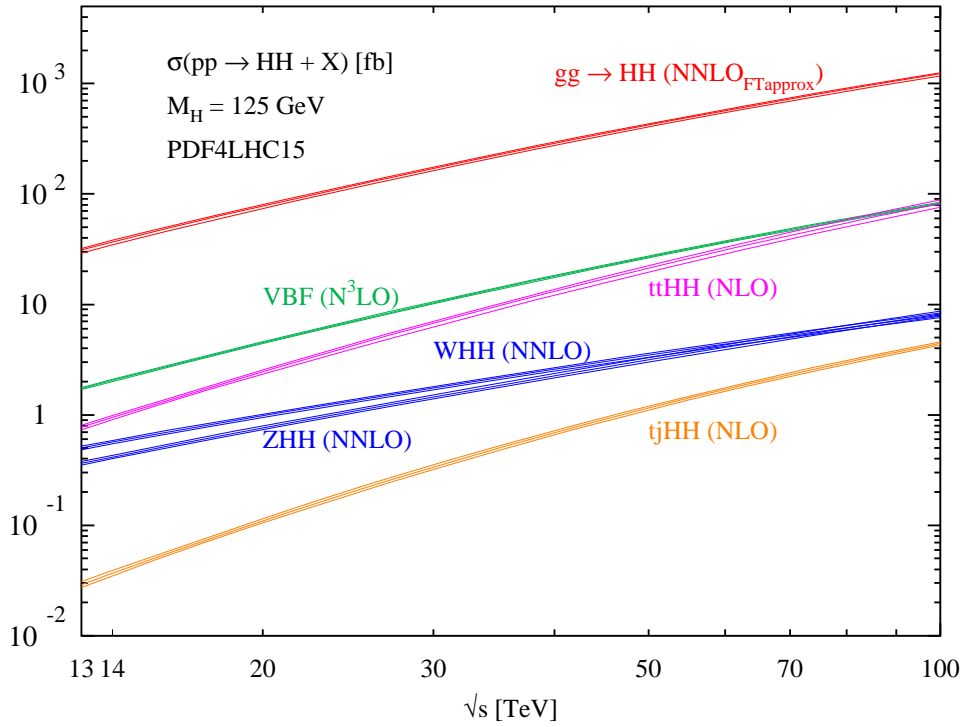
Figure 1.2: Total production cross sections for Higgs pairs within the SM via gluon fusion, vector-boson fusion, double Higgs-strahlung and double Higgs bremsstrahlung off top quarks. PDF4LHC15 parton densities have been used with the scale choices according to Table 1.1. The size of the bands shows the total uncertainties originating from the scale dependence and the PDF+α_s uncertainties.
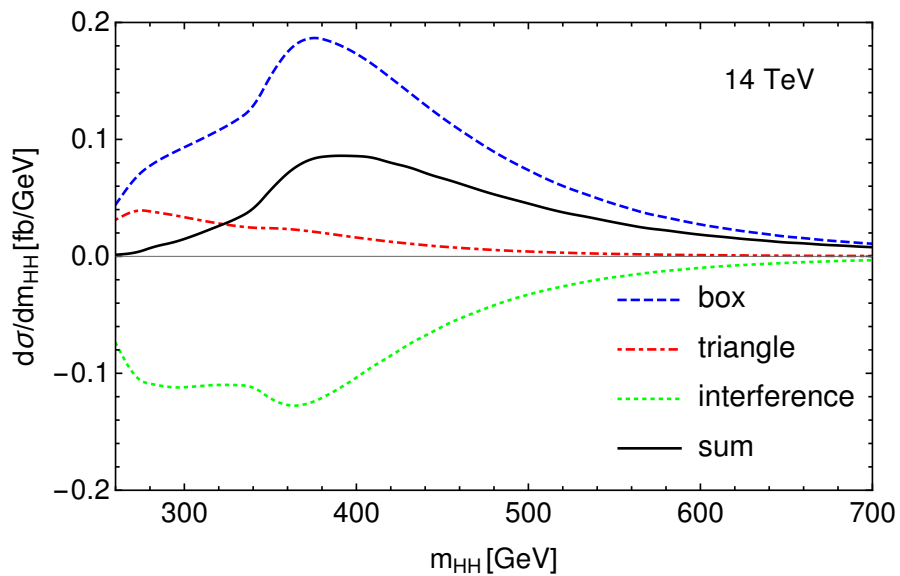
Figure 1.3: Higgs pair invariant mass distribution at leading order for the different contributions to the gluon fusion production mechanism and their interference.

$\sqrt{s}$	13 TeV	14 TeV	27 TeV	100 TeV
ggF HH	$31.05^{+2.2\%}_{-5.0\%} \pm 3.0\%$	$36.69^{+2.1\%}_{-4.9\%} \pm 3.0\%$	$139.9^{+1.3\%}_{-3.9\%} \pm 2.5\%$	$1224^{+0.9\%}_{-3.2\%} \pm 2.4\%$
VBF HH	$1.73^{+0.03\%}_{-0.04\%} \pm 2.1\%$	$2.05^{+0.03\%}_{-0.04\%} \pm 2.1\%$	$8.40^{+0.11\%}_{-0.04\%} \pm 2.1\%$	$82.8^{+0.13\%}_{-0.04\%} \pm 2.1\%$
ZHH	$0.363^{+3.4\%}_{-2.7\%} \pm 1.9\%$	$0.415^{+3.5\%}_{-2.7\%} \pm 1.8\%$	$1.23^{+4.1\%}_{-3.3\%} \pm 1.5\%$	$8.23^{+5.9\%}_{-4.6\%} \pm 1.7\%$
W^+HH	$0.329^{+0.32\%}_{-0.41\%} \pm 2.2\%$	$0.369^{+0.33\%}_{-0.39\%} \pm 2.1\%$	$0.941^{+0.52\%}_{-0.53\%} \pm 1.8\%$	$4.70^{+0.90\%}_{-0.96\%} \pm 1.8\%$
W^-HH	$0.173^{+1.2\%}_{-1.3\%} \pm 2.8\%$	$0.198^{+1.2\%}_{-1.3\%} \pm 2.7\%$	$0.568^{+1.9\%}_{-2.0\%} \pm 2.1\%$	$3.30^{+3.5\%}_{-4.3\%} \pm 1.9\%$
$t\bar{t}HH$	$0.775^{+1.5\%}_{-4.3\%} \pm 3.2\%$	$0.949^{+1.7\%}_{-3.1\%} \pm 3.1\%$	$5.24^{+2.9\%}_{-6.4\%} \pm 2.5\%$	$82.1^{+7.9\%}_{-7.4\%} \pm 1.6\%$
$tjHH$	$0.0289^{+5.5\%}_{-3.6\%} \pm 4.7\%$	$0.0367^{+4.2\%}_{-1.8\%} \pm 4.6\%$	$0.254^{+3.8\%}_{-2.8\%} \pm 3.6\%$	$4.44^{+2.2\%}_{-2.8\%} \pm 2.4\%$

Table 1.1: Signal cross sections (in fb) for HH production including the available QCD corrections according to the recommendations of the LHC Higgs Cross Section Working Group [19]. The renormalisation and factorisation scales have been set to $m_{HH}/2$ for gluon fusion, to the individual virtualities $Q_{1,2} = \sqrt{-q_{1,2}^2}$ of the t-channel vector-bosons for VBF (with a lower cut of 1 GeV), to m_{HHV} $(V = W, Z)$ for HHV production, to $m_{t\bar{t}}/2$ for $t\bar{t}HH$ and to $m_{HH}/2$ for $tjHH$ production. They have been varied up and down by a factor of two to obtain the scale uncertainties, indicated as superscript/subscript. PDF4LHC15 parton distributions have been used to obtain the results, and the corresponding α_s+PDF uncertainties. The cross sections for $tjHH$ involve both top and anti-top production.

diagram dominance, that implies that the QCD corrections are driven by vertex corrections which can be obtained from deep inelastic lepton-nucleon scattering (DIS). In turn, for DIS the residual radiative corrections beyond the proper implementation of the PDFs at higher orders are moderate; this happens by construction within the DIS factorization scheme, but holds as well in the $\overline{\text{MS}}$ scheme. The NNLO and N^{3}LO corrections range at the per-cent and sub-per-cent level [31, 32].

Double Higgs-strahlung. The double Higgs-strahlung's production rate, i.e. the associated production of Higgs pairs with a W or Z boson (Fig. 1.1c), is significantly lower than vector-boson fusion's one. The NLO and NNLO QCD corrections to this process are known [30, 34, 35], and their main component can be translated from the corresponding calculation of the Drell–Yan process. These corrections increase the total cross sections by about 30%. In the ZHH production channel there is a relevant contamination from the loop-induced process $gg \rightarrow ZHH$ adding another $20 - 30\%$ to ZHH production. The LO contribution of this gluon-induced subprocess is part of the full NNLO QCD corrections [30].

Double Higgs bremsstrahlung off top quarks. The associated production of Higgs pairs with top quark pairs (Fig. 1.1d) reaches a cross section value close to the vector-boson fusion cross section at a 100 TeV hadron collider. This is not the case for single Higgs boson production. The NLO QCD corrections are negative and modify the total cross section at the level of 20%, and reduce the residual scale dependence significantly [36]. In the case of single-top associated production, $tjHH$, the NLO QCD corrections are of a similar size but positive, and scale uncertainties are actually in-

creased with respect to the ones of the LO prediction, the latter not being a reliable estimate of the true perturbative uncertainties [36].

1.2 QCD corrections for gluon fusion

J. Baglio, F. Campanario, P. Giardino, S. Glaus, M. Mühlleitner, M. Spira, J. Streicher

The NLO QCD corrections to the gluon-fusion cross section $\sigma(gg \to HH)$ have first been obtained in the heavy top quark limit (HTL) [37] that simplifies the calculation since the top quark loop contributions reduce to effective couplings between the Higgs boson and gluons, described by the effective Lagrangian [38–42]

$$\mathcal{L}_{\text{eff}} = \frac{\alpha_s}{12\pi} G^{a\mu\nu} G^a_{\mu\nu} \left(C_1 \frac{H}{v} - C_2 \frac{H^2}{2v^2} \right), \tag{1.1}$$

with the Wilson coefficients ($L_t = \log \mu_R^2/m_t^2$) [27, 37, 43–48]

$$
\begin{aligned}
C_1 &= 1 + \frac{11}{4}\frac{\alpha_s}{\pi} + \left\{ \frac{2777}{288} + \frac{19}{16}L_t + N_F\left(\frac{L_t}{3} - \frac{67}{69}\right) \right\}\left(\frac{\alpha_s}{\pi}\right)^2 + \mathcal{O}(\alpha_s^3), \\
C_2 &= C_1 + \left(\frac{35}{24} + \frac{2}{3}N_F\right)\left(\frac{\alpha_s}{\pi}\right)^2 + \mathcal{O}(\alpha_s^3),
\end{aligned}
\tag{1.2}
$$

that are presented up to NNLO, but are known up to N^{4}LO [45–47]. Since the top quark is integrated out, the number of active flavors has to be taken as $N_F = 5$. Using these effective Higgs couplings to gluons, the calculation of the NLO QCD corrections is reduced to a one-loop calculation for the virtual corrections and a tree-level calculation for the matrix elements of the real corrections. The NLO final result for the total gluon-fusion cross section can be decomposed as [37]

$$\sigma_{\text{NLO}}(pp \to HH + X) = \sigma_{\text{LO}} + \Delta\sigma_{\text{virt}} + \Delta\sigma_{gg} + \Delta\sigma_{gq} + \Delta\sigma_{q\bar{q}},$$

where the different contributions take the following form:

$$
\begin{aligned}
\sigma_{\text{LO}} &= \int_{\tau_0}^1 d\tau \frac{d\mathcal{L}^{gg}}{d\tau} \hat{\sigma}_{\text{LO}}(Q^2 = \tau s), \\
\Delta\sigma_{\text{virt}} &= \frac{\alpha_s(\mu_R)}{\pi} \int_{\tau_0}^1 d\tau \frac{d\mathcal{L}^{gg}}{d\tau} \hat{\sigma}_{\text{LO}}(Q^2 = \tau s)\, C_{\text{virt}}, \\
\Delta\sigma_{gg} &= \frac{\alpha_s(\mu_R)}{\pi} \int_{\tau_0}^1 d\tau \frac{d\mathcal{L}^{gg}}{d\tau} \int_{\tau_0/\tau}^1 \frac{dz}{z} \hat{\sigma}_{\text{LO}}(Q^2 = z\tau s) \left\{ -z P_{gg}(z)\log\frac{\mu_F^2}{\tau s} \right. \\
&\qquad\qquad \left. + d_{gg}(z) + 6[1 + z^4 + (1-z)^4]\left(\frac{\log(1-z)}{1-z}\right)_+ \right\}, \\
\Delta\sigma_{gq} &= \frac{\alpha_s(\mu_R)}{\pi} \int_{\tau_0}^1 d\tau \sum_{q,\bar{q}} \frac{d\mathcal{L}^{gq}}{d\tau} \int_{\tau_0/\tau}^1 \frac{dz}{z} \hat{\sigma}_{\text{LO}}(Q^2 = z\tau s) \\
&\qquad\qquad \left\{ -\frac{z}{2}P_{gq}(z)\log\frac{\mu_F^2}{\tau s(1-z)^2} + d_{gq}(z) \right\}, \\
\Delta\sigma_{q\bar{q}} &= \frac{\alpha_s(\mu_R)}{\pi} \int_{\tau_0}^1 d\tau \sum_q \frac{d\mathcal{L}^{q\bar{q}}}{d\tau} \int_{\tau_0/\tau}^1 \frac{dz}{z} \hat{\sigma}_{\text{LO}}(Q^2 = z\tau s)\, d_{q\bar{q}}(z).
\end{aligned}
\tag{1.3}
$$

Here $\hat{\sigma}_{\text{LO}}(Q^2)$ denotes the leading-order partonic cross section involving the squared invariant mass Q^2 of the Higgs boson pair, $\alpha_s(\mu_R)$ the strong coupling constant at the renormalization scale μ_R, $d\mathcal{L}^{ij}/d\tau$ ($i, j = g, q, \bar{q}$) the corresponding parton-parton luminosities at the factorization scale μ_F, and $P_{ij}(z)$ ($i, j = g, q, \bar{q}$) the individual Altarelli–Parisi splitting functions [49]. The integration regions are bound by $\tau_0 = 4m_H^2/s$, with m_H being the Higgs boson mass and s the square of the hadronic center-of-mass energy.

The quark-mass dependence is in general encoded in the green factors $\hat{\sigma}_{\text{LO}}(Q^2)$ for the LO cross section and the red factors C_{virt}, $d_{ij}(z)$ for the virtual and real corrections, respectively. In the HTL, the latter simplify to

$$
\begin{aligned}
C_{\text{virt}} &\rightarrow \frac{11}{2} + \pi^2 + C_{\triangle\triangle}^{\infty} + \frac{33 - 2N_F}{6} \log \frac{\mu_R^2}{Q^2}, \\[2mm]
C_{\triangle\triangle} &= \text{Re} \frac{\int_{\hat{t}_-}^{\hat{t}_+} d\hat{t} \left\{ c_1 \left[(C_\triangle F_\triangle + F_\square) + \frac{p_T^2}{\hat{t}} G_\square \right] + (\hat{t} \leftrightarrow \hat{u}) \right\}}{\int_{\hat{t}_-}^{\hat{t}_+} d\hat{t} \left\{ |C_\triangle F_\triangle + F_\square|^2 + |G_\square|^2 \right\}}, \\[2mm]
C_{\triangle\triangle}^{\infty} &= C_{\triangle\triangle}\big|_{c_1 = 2/9}, \\[2mm]
d_{gg}(z) &\rightarrow -\frac{11}{2}(1-z)^3 \\[2mm]
d_{gq}(z) &\rightarrow \frac{2}{3}z^2 - (1-z)^2, \\[2mm]
d_{q\bar{q}}(z) &\rightarrow \frac{32}{27}(1-z)^3,
\end{aligned}
\tag{1.4}
$$

where p_T denotes the Higgs transverse momentum, $\hat{s}, \hat{t}$ the partonic Mandelstam variables and $C_{\triangle\triangle}$ is the contribution of the one-particle reducible diagrams, see Fig. 1.4. The integration bounds are given by

$$
\hat{t}_\pm = -\frac{1}{2} \left[Q^2 - 2m_H^2 \mp Q^2 \sqrt{1 - \frac{4m_H^2}{Q^2}} \right].
\tag{1.5}
$$

The couplings $C_\triangle$ and $C_\square$ and the form factors $F_\triangle$, $F_\square$ and $G_\square$ in the HTL take the form

$$
\begin{aligned}
C_\triangle &= \lambda_{H^3} \frac{6v}{\hat{s} - m_H^2 + i m_H \Gamma_H}, \qquad C_\square = 1, \\[2mm]
F_\triangle &\rightarrow \frac{2}{3}, \qquad F_\square \rightarrow -\frac{2}{3}, \\[2mm]
G_\square &\rightarrow 0,
\end{aligned}
\tag{1.6}
$$

with the trilinear coupling $\lambda_{H^3} = m_H^2/(2v^2)$.

For the NLO QCD corrections, the full mass dependence of the LO partonic cross section has been taken into account first, while treating the virtual corrections C_{virt} and the real corrections d_{ij} in the HTL. This approach is now called "Born-improved". This leads to a reasonable approximation for invariant Higgs pair masses in the lower range and approximates the full NLO result for the total cross section within about 15% [22–24]. The NLO corrections in the HTL increase the cross section by $80 - 90\%$ [37]. The NNLO QCD corrections have been calculated within the same approximation [25–28]. The main part of these corrections can be translated from the single Higgs case, since the effective Lagrangian of Eq. (1.1) does not induce a change of kinematics between single Higgs production and the differential Higgs pair production with respect to the invariant Higgs pair mass. The new ingredient of the NNLO calculation is the proper treatment of the one-particle-reducible
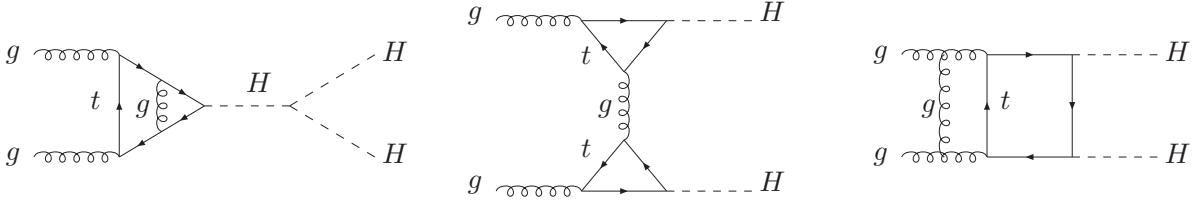
Figure 1.4: Examples of two-loop triangle (left), one-particle reducible (middle) and box (right) diagrams contributing to Higgs pair production via gluon fusion.

contributions $C_{\triangle\triangle}$ of the NLO corrections. These lead to additional contributions to the NNLO virtual corrections and the interference of the NLO-real and NLO-virtual corrections that contributes to the NNLO result, too. Including the full mass dependence of the LO cross section, the NNLO QCD corrections increase the total cross section by a more moderate amount of $20 - 30\%$ [26]. On top of these NNLO QCD corrections, the soft-gluon resummation (threshold resummation) has been performed at next-to-next-to-leading logarithmic accuracy (NNLL) for the total cross section and invariant mass distribution, resulting in a $\mathcal{O}(10\%)$ modification of the total cross section on top of the NNLO result for a central scale $\mu_R = \mu_F = m_{HH}$, while the effects are much smaller if the scale $\mu_R = \mu_F = m_{HH}/2$ is used [50, 51].

The calculations in the HTL have been refined by several steps including mass effects partially at NLO. The inclusion of the full mass effects in the real correction terms d_{ij} by means of incorporating the full one-loop real matrix elements for $gg \to HHg$, $gq \to HHq$, $q\bar{q} \to HHg$ reduces the Born-improved HTL prediction by about 10% [18, 36]. This improvement is denoted as "FTapprox" (for full-theory approximation). This step has been performed by using the MG5_aMC@NLO framework [52] for the automatic generation of the matrix elements. Another improvement has been accomplished by a systematic asymptotic large-top-mass expansion of the full NLO corrections at the integral [53] and at the integrand level [54]. This established sizeable mass effects emerging from the virtual two-loop corrections. In addition, the large-top-mass expansion has been extended to NNLO resulting in expected 5% mass effects of the NNLO corrections on top of the NLO result [54]. This situation necessitated the full calculation of the mass effects at NLO.

The full NLO QCD corrections have been derived by two quite different methods, both, however, building on a numerical integration of the two-loop contributions that cannot be integrated analytically with present state-of-the-art methods. Examples of diagrams of the NLO virtual corrections are depicted in Fig. 1.4. It can be decomposed into triangle, one-particle-reducible and box diagrams. The triangle diagrams can be obtained from the analogous calculation for $gg \to H$ with the Higgs mass replaced by the invariant Higgs pair mass $Q = m_{HH}$. The result of the one-particle-reducible diagrams is known analytically, i.e. in the notation of Eq. (1.4), [24, 55]

$$
\begin{aligned}
c_1 &= 2\left[I_1(\tau, \lambda_{\hat{t}}) - I_2(\tau, \lambda_{\hat{t}})\right]^2, \\
I_1(\tau, \lambda) &= \frac{\tau\lambda}{2(\tau - \lambda)} + \frac{\tau^2\lambda^2}{2(\tau - \lambda)^2}\left[f(\tau) - f(\lambda)\right] + \frac{\tau^2\lambda}{(\tau - \lambda)^2}\left[g(\tau) - g(\lambda)\right], \\
I_2(\tau, \lambda) &= -\frac{\tau\lambda}{2(\tau - \lambda)}\left[f(\tau) - f(\lambda)\right],
\end{aligned}
\tag{1.7}
$$

with $\tau = 4m_t^2/m_H^2$, $\lambda_{\hat{t}} = 4m_t^2/\hat{t}$ and the functions

$$
\begin{aligned}
f(\tau) &= \begin{cases} \arcsin^2 \dfrac{1}{\sqrt{\tau}} & \tau \geq 1 \\[2ex] -\dfrac{1}{4}\left[\log\dfrac{1+\sqrt{1-\tau}}{1-\sqrt{1-\tau}} - i\pi\right]^2 & \tau < 1 \end{cases}, \\[4ex]
g(\tau) &= \begin{cases} \sqrt{\tau-1}\,\arcsin\dfrac{1}{\sqrt{\tau}} & \tau \geq 1 \\[2ex] \dfrac{\sqrt{1-\tau}}{2}\left[\log\dfrac{1+\sqrt{1-\tau}}{1-\sqrt{1-\tau}} - i\pi\right] & \tau < 1 \end{cases}.
\end{aligned} \tag{1.8}
$$

This expression has to be inserted in the $C_{\triangle\triangle}$ coefficient of Eq. (1.4). The new and cumbersome part of the full virtual corrections is the calculation of the two-loop box diagrams that has only been obtained numerically by two different methods. The full virtual amplitude can be decomposed into two scalar form factors, one describing the spin-0 component of the full partonic process and the second the spin-2 one [20, 21].

The first method [22, 23] relies on the reduction of the two-loop form factors to master integrals, Feynman parametrization of these master integrals and a sector decomposition to isolate the ultraviolet and infrared singularities from the two-loop box integrals. This yields the numerical coefficients of the divergences that can be checked to cancel against the corresponding ultraviolet divergences of the counterterms and the infrared and collinear singularities of the real corrections numerically. For large invariant Higgs pair masses, however, the virtual top-antitop pair can become on-shell so that there are additional threshold singularities inside the integration region. This has been treated numerically by contour deformations that exploit the analyticity of the master integrals in the complex plane and by trading the physical integrals along the real axis for integrals off the real axis. This procedure leads to numerically stable results after suitable deformation choices and spending a sizeable amount of CPU time. The top mass has been renormalized on-shell and the strong coupling constant α_s in the $\overline{\text{MS}}$-scheme with five active flavors. By means of the first method a grid has been generated for the exclusive calculation of the virtual corrections to the Higgs pair cross section so that the invariant Higgs pair mass distribution and the transverse-momentum distribution of the Higgs bosons in the final state can be obtained. Typical results after adding the full top-mass corrections are shown in Fig. 1.5. The mass effects induce a reduction of the total cross section by about 15% at NLO but turn out to be more sizeable for large di-Higgs invariant masses in the differential cross section [22, 23]. The two-dimensional grids in the Higgs pair invariant mass and the transverse Higgs momentum are available and have been included in NLO event generators thus providing the proper matching to parton showers [56, 57].

The second method [24] does not perform any tensor reduction to master integrals, but introduces a Feynman parametrization of the full individual two-loop box diagrams. For the isolation of the ultraviolet divergences end-point subtractions have been made for most of the diagrams. However, the diagrams with an external gluon exchange between the gluons require special subtraction terms for the infrared singular part. This is also related to the property that these diagrams develop a second threshold at vanishing Higgs pair invariant mass in addition to the threshold at $m_{HH} = 2m_t$. This method uses special subtraction terms for these diagrams that cover all singularities and can be easily integrated analytically over one Feynman parameter. Using the transformation properties of hypergeometric functions, the infrared and collinear singularities can be isolated. The numerical stabilization of the integrations across the thresholds has been achieved by means of integration by parts to reduce the power of the singular denominators and introducing a small imaginary part for the virtual squared top masses. Since the dependence on this small imaginary part is regular,
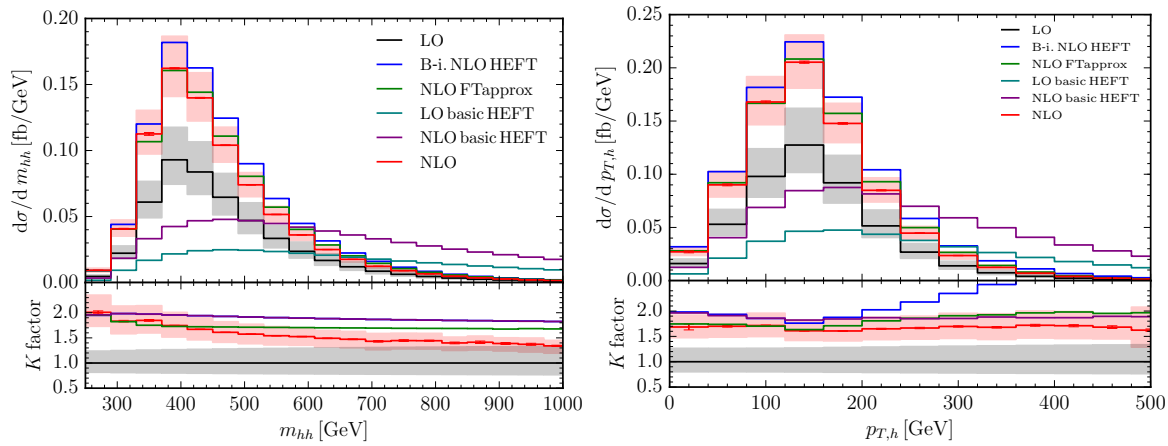
Figure 1.5: Higgs pair invariant mass and transverse-momentum distributions for a center-of-mass energy of 14 TeV in various approximations. The full NLO results are shown in red. The red bands show the renormalization and factorization scale dependence obtained from a 7-point scale variation around the central scales $\mu_R = \mu_F = m_{HH}/2$ [23].

i.e. polynomial, for small values a Richardson extrapolation [58] has been used to obtain the narrow-width approximation from results at finite values of this imaginary part. The observed convergence is good and can also be used for a quantitative estimate of the extrapolation error in addition to the numerical integration error. In addition to the six-dimensional integration over the Feynman parameters, the integration over the transverse momentum of the Higgs bosons in terms of the Mandelstam variable $\hat{t}$ has been included in the numerical integration so that the differential cross section in the invariant Higgs pair mass is obtained directly. Since the $\hat{t}$-integration is not finite for individual diagrams, the cancellation of the divergences in $\hat{t}$ in the sum of all of them serves as an additional consistency check of the final result. The numerical integration together with the Richardson extrapolation requires a huge amount of CPU time, similar to the other approach. The real corrections have been calculated by subtracting the corresponding matrix elements in the HTL for a suitably transformed LO kernel including the full LO mass dependence from the full real matrix elements. The subtracted pieces lead to the "Born-improved" real corrections in the HTL when added back. Typical final results of this method are displayed in Fig. 1.6, which includes a comparison to the HTL and real and virtual mass effects individually.

Both methods lead to final results in mutual agreement within their respective integration errors. The residual small differences are due to the different top masses chosen in the numerical analysis, $m_t = 173$ GeV for the first method and $m_t = 172.5$ GeV (as recommended by the LHC Higgs Cross Section Working Group) for the second method. The explicit NLO numbers are collected in Table 1.2 for several collider energies.

The virtual corrections have also been obtained by expansion methods. A first approach is based on the large top-mass expansion that is transformed into a complex polynomial by a suitable conformal mapping and using Padé approximants above the virtual $t\bar{t}$-threshold [59, 60]. The results are in mutual agreement with the full numerical integration up to Higgs pair invariant masses of about $700 - 800$ GeV [60], see Fig. 1.7. A promising method is provided by a different expansion in a Lorentz-invariant variable that mainly corresponds to the transverse momentum of the Higgs bosons. The first three terms of this expansion result in an excellent agreement with the full numerical integration for di-Higgs invariant masses up to $800 - 900$ GeV [61], see Fig. 1.7. Last but not least, the approximate result of the large-m_{HH} expansion has been obtained analytically, including subleading terms [62, 63]. The latter result exhibits the detailed logarithmic structure of the
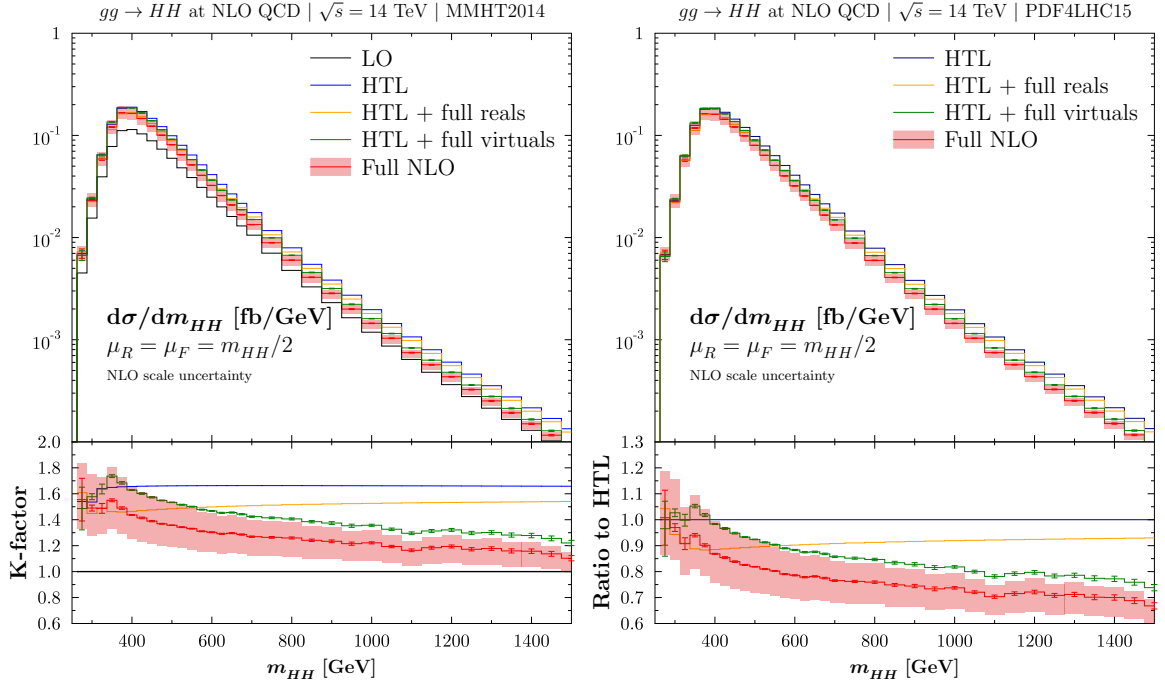
Figure 1.6: Higgs pair invariant mass distribution for a collider energy of 14 TeV in various approximations using MMHT2014 (left) and PDF4LHC15 (right) parton densities. The full NLO results are shown in red. The red bands show the renormalization and factorization scale dependence obtained from a 7-point scale variation around the central scales $\mu_R = \mu_F = m_{HH}/2$. From Ref. [24].

full NLO virtual corrections that may be useful for further improvements. In addition, it provides a first approach to the contribution of the bottom loops at NLO. Another proposal for a valuable approximation is provided by a strict expansion in the Higgs mass while keeping all other kinematical invariants arbitrary [64]. However, this last option has not been worked out completely for $gg \to HH$ yet.

These expansions considerably simplify the problem and allow for an analytical solution to be found in certain limits. Of course, an immediate drawback with respect to the numerical calculation is that the analytical result obtained in this way does not retain the full dependence on the parameters over which the expansion is performed. On the other hand, analytical calculations are usually faster and less computationally intensive than numerical calculations, and can reach high

Energy	$m_t = 173$ GeV	$m_t = 172.5$ GeV
13 TeV	$27.80(9)^{+13.8\%}_{-12.8\%}$ fb	$27.73(7)^{+13.8\%}_{-12.8\%}$ fb
14 TeV	$32.91(10)^{+13.6\%}_{-12.6\%}$ fb	$32.78(7)^{+13.5\%}_{-12.5\%}$ fb
27 TeV	$127.7(2)^{+11.5\%}_{-10.4\%}$ fb	$127.0(2)^{+11.7\%}_{-10.7\%}$ fb
100 TeV	$1149(2)^{+10.8\%}_{-10.0\%}$ fb	$1140(2)^{+10.7\%}_{-10.0\%}$ fb

Table 1.2: NLO cross sections for proton colliders at 13, 14, 27 and 100 TeV center-of-mass energy using PDF4LHC15 parton densities. The errors in brackets are the numerical integration/extrapolation errors, while the explicit percentage numbers present the renormalization and factorization scale dependences. The central scale choice is $\mu_R = \mu_F = m_{HH}/2$ [22–24].

Figure 1.7: Partonic virtual corrections to the Higgs pair invariant mass distribution for Padé approximants (left) and the p_T^2 expansion (right), for a Higgs transverse momentum $p_T = 100$ GeV. The full NLO results are shown as red points. The other curves represent different orders included in the corresponding expansions [60, 61].

precision, thus providing a sound alternative in specific instances and a valid check of the numerical result in the corresponding limits.

Apart from the renormalization and factorization scale dependence, the additional uncertainty due to the scale and scheme dependence related to the top mass has to be taken into account. This has been analyzed in the framework of the second numerical approach by deriving the full NLO result not only for the top pole mass, but also for the $\overline{\text{MS}}$ mass at the scales of the top mass itself and in the range of $m_{HH}/4$ to m_{HH} for the scale of the running top mass. The maximum and minimum of these results have been taken differentially in m_{HH}. This leads to sizeable additional uncertainties [24],

$$\frac{d\sigma(gg \to HH)}{dQ}\bigg|_{Q=300 \text{ GeV}} = 0.02978(7)^{+6\%}_{-34\%} \text{fb/GeV},$$

$$\frac{d\sigma(gg \to HH)}{dQ}\bigg|_{Q=400 \text{ GeV}} = 0.1609(4)^{+0\%}_{-13\%} \text{fb/GeV},$$

$$\frac{d\sigma(gg \to HH)}{dQ}\bigg|_{Q=600 \text{ GeV}} = 0.03204(9)^{+0\%}_{-30\%} \text{fb/GeV},$$

$$\frac{d\sigma(gg \to HH)}{dQ}\bigg|_{Q=1200 \text{ GeV}} = 0.000435(4)^{+0\%}_{-35\%} \text{fb/GeV} \tag{1.9}$$

for the differential cross section at $\sqrt{s} = 14$ TeV using PDF4LHC15 parton densities.

The full NLO corrections have been combined recently with the NNLO QCD corrections in the HTL, to construct a full NNLO Monte Carlo program for exclusive Higgs pair production via gluon fusion [29]. In this implementation, the second-order corrections have been improved via a reweighting technique to account for partial finite top quark mass effects, in what represents a NNLO extension of the "FTapprox". Within this approach, the NNLO parts of the virtual and real corrections that are obtained in the HTL at NNLO are rescaled by the ratio between the corresponding full one-loop (i.e. LO) amplitudes and the ones obtained in the HTL for each partonic subprocess individually. The double-real corrections are added including the full mass dependence, since the related one-loop amplitudes can be obtained by presently available automatic tools. This approximation is an improvement of the previous "Born-improved" and "FTapprox" approaches used at NLO, and is expected to deliver more reliable results at NNLO [29]. Final predictions at NLO and NNLO are presented in Table 1.3 for different center-of-mass energies with $m_t = 173$ GeV. From

Energy	13 TeV	14 TeV	27 TeV	100 TeV
NLO	$27.78^{+13.8\%}_{-12.8\%}$ fb	$32.88^{+13.5\%}_{-12.5\%}$ fb	$127.7^{+11.5\%}_{-10.4\%}$ fb	$1147^{+10.7\%}_{-9.9\%}$ fb
NLO$_{\text{FTapprox}}$	$28.91^{+15.0\%}_{-13.4\%}$ fb	$34.25^{+14.7\%}_{-13.2\%}$ fb	$134.1^{+12.7\%}_{-11.1\%}$ fb	$1220^{+11.9\%}_{-10.6\%}$ fb
NNLO$_{\text{FTapprox}}$	$31.05^{+2.2\%}_{-5.0\%}$ fb	$36.69^{+2.1\%}_{-4.9\%}$ fb	$139.9^{+1.3\%}_{-3.9\%}$ fb	$1224^{+0.9\%}_{-3.2\%}$ fb

Table 1.3: NLO and NNLO cross sections for proton colliders at 13, 14, 27 and 100 TeV center-of-mass energy using PDF4LHC15 parton densities. The explicit percentage numbers present the renormalization and factorization scale dependences. The central scale choice is $\mu_R = \mu_F = m_{HH}/2$ [29].
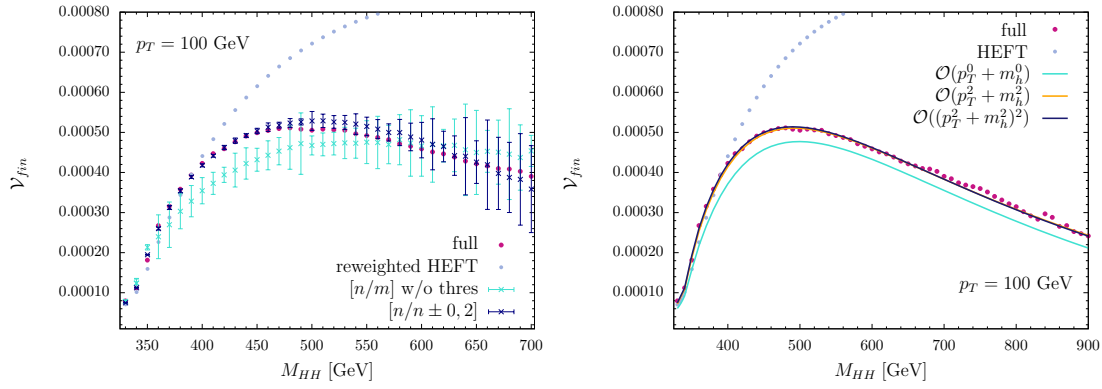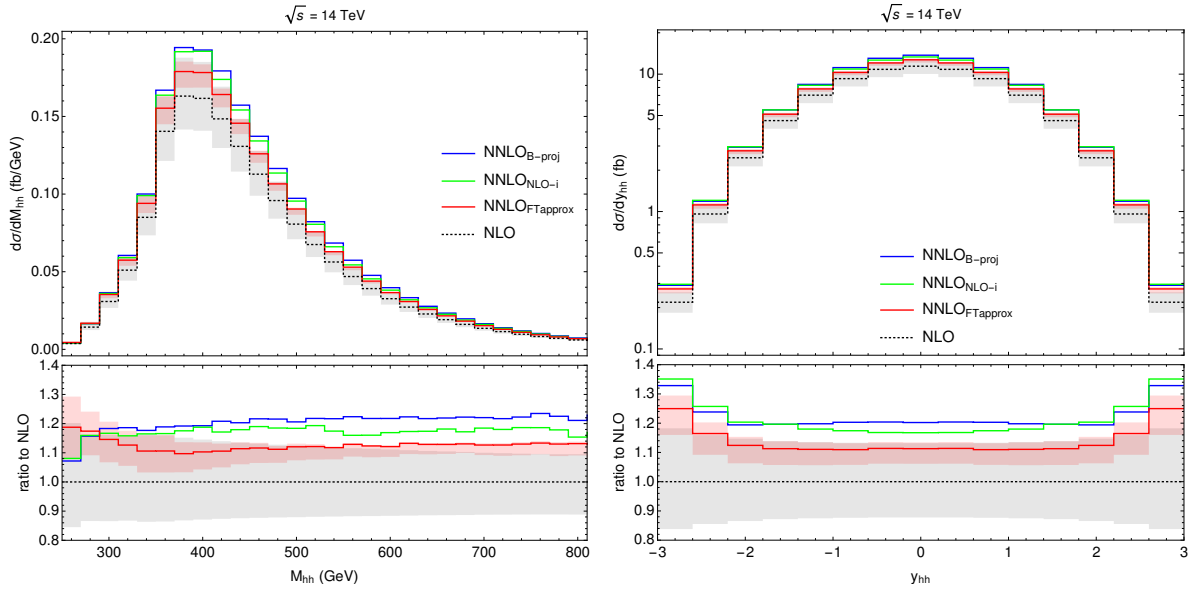

Figure 1.8: Higgs pair invariant mass and rapidity distributions for a collider energy of 14 TeV in various approximations using PDF4LHC15 parton densities. The NNLO$_{\text{FTapprox}}$ results are shown in red. The grey and red bands show the scale dependence at NLO and NNLO [29].

these values it is visible that the "FTapprox" method works with an accuracy of better than 10% at NLO, so that the NNLO$_{\text{FTapprox}}$ results are expected to be more reliable than the left-over uncertainties. The corresponding NNLO Monte Carlo program can be used to provide NNLO predictions for exclusive quantities, i.e. for distributions. Typical numerical results are shown in Fig. 1.8. In addition, the all-orders resummation of soft-gluon contributions has been performed at NNLL within this approximation, finding – as it happens in the HTL – that the effects are very small if the central scale $\mu_R = \mu_F = m_{HH}/2$ is used, indicating the stability of the perturbative expansion at this order [65].

1.3   Cross section as a function of κ_λ

G. Heinrich, S.P. Jones, M. Kerner, L. Scyboz

Non-resonant Higgs boson pair production in gluon fusion is the most promising process to test the trilinear Higgs boson self-coupling at hadron colliders. The current constraints at 95% confidence level from ATLAS and CMS searches, combining various decay channels, are $-5 \le \kappa_\lambda \le 12.1$ [66] and

κ_λ	σ_{NLO}, 13 TeV [fb]	σ_{NLO}, 14 TeV [fb]	σ_{NLO}, 27 TeV [fb]	K-factor, 14 TeV
-1	$116.71^{+16.4\%}_{-14.3\%}$	$136.91^{+16.4\%}_{-13.9\%}$	$504.9^{+14.1\%}_{-11.8\%}$	1.86
0	$62.51^{+15.8\%}_{-13.7\%}$	$73.64^{+15.4\%}_{-13.4\%}$	$275.29^{+13.2\%}_{-11.3\%}$	1.79
1	$27.84^{+11.6\%}_{-12.9\%}$	$32.88^{+13.5\%}_{-12.5\%}$	$127.7^{+11.5\%}_{-10.4\%}$	1.66
2	$12.42^{+13.1\%}_{-12.0\%}$	$14.75^{+12.0\%}_{-11.8\%}$	$59.10^{+10.2\%}_{-9.7\%}$	1.56
2.4	$11.65^{+13.9\%}_{-12.7\%}$	$13.79^{+13.5\%}_{-12.5\%}$	$53.67^{+11.4\%}_{-10.3\%}$	1.65
3	$16.28^{+16.2\%}_{-15.3\%}$	$19.07^{+17.1\%}_{-14.1\%}$	$69.84^{+14.6\%}_{-12.1\%}$	1.90
5	$81.74^{+20.0\%}_{-15.6\%}$	$95.22^{+19.7\%}_{-11.5\%}$	$330.61^{+17.4\%}_{-13.6\%}$	2.14

Table 1.4: Total cross section for Higgs boson pair production at full NLO for different values of κ_λ. The given uncertainties are scale uncertainties, and we use the central value $\mu_R = \mu_F = m_{HH}/2$ [68]. The K-factors reported for the 14 TeV results are also valid at 13 TeV, with the exception of the $\kappa_\lambda = 2$ K-factor which takes the value 1.57.

$-11.8 \leq \kappa_\lambda \leq 18.8$ [67], respectively, where $\kappa_\lambda = \lambda_{H^3}/\lambda_{H^3}^{\text{SM}}$ (see Sec. 7.2). In order to derive reliable limits on κ_λ from these searches, it is crucial to have accurate predictions for the cross sections corresponding to non-SM λ_{H^3} values. The results presented in this section for a generic κ_λ are NLO-accurate, including the full top quark mass dependence [68]. They are based on the original calculation of Refs. [22,23] for the SM cross section, which has been extended to include effects from anomalous couplings in the Higgs sector within a non-linear Effective Field Theory framework in Ref. [69].

To obtain a full-fledged NLO generator which also offers the possibility of parton showering, we implemented the calculation in the POWHEG-BOX [70–72], building on top of the code presented in Ref. [56] for the NLO+PS predictions within the SM; the code is publicly available in the POWHEG-BOX-V2 package.[1]

The results were obtained using the PDF4LHC15_nlo_30_pdfas [73–76] parton distribution functions interfaced to the code via LHAPDF [77], along with the corresponding value for α_s. The masses of the Higgs boson and the top quark have been fixed to $m_H = 125$ GeV, $m_t = 173$ GeV, respectively, where the pole mass scheme has been employed for the top quark mass. The widths Γ_H and Γ_t have been set to zero. Jets are clustered with the anti-k_T algorithm [78] as implemented in the fastjet package [79,80], with jet radius $R = 0.4$ and a minimum transverse momentum $p_{T,\text{min}}^{\text{jet}} = 20$ GeV. The scale uncertainties are estimated by varying the factorisation and renormalisation scales μ_F and μ_R. The scale variation bands result from varying $\mu = \mu_F = \mu_R$ by a factor of two around the central scale $\mu_0 = m_{HH}/2$. For $\lambda_{H^3} = \lambda_{H^3}^{\text{SM}}$, the envelope of the scale variations coincides with the 7-point scale variation band.

In Table 1.4 we list total cross sections at 13, 14 and 27 TeV for various values of the trilinear Higgs coupling. We observe that $\kappa_\lambda = -1$ leads to the largest total cross section of all the considered κ_λ values. Table 1.4 also shows that the K-factors vary substantially as functions of the trilinear coupling, which is different from the findings in the $m_t \to \infty$ limit [81, 82]. This fact is illustrated in Fig. 1.9, which shows that the K-factor takes values between 1.57 and 2.16 if the trilinear coupling is varied between $-5 \leq \kappa_\lambda \leq 12$.

---

[1] The code can be found at the website http://powhegbox.mib.infn.it in the User-Processes-V2/ggHH/ directory.
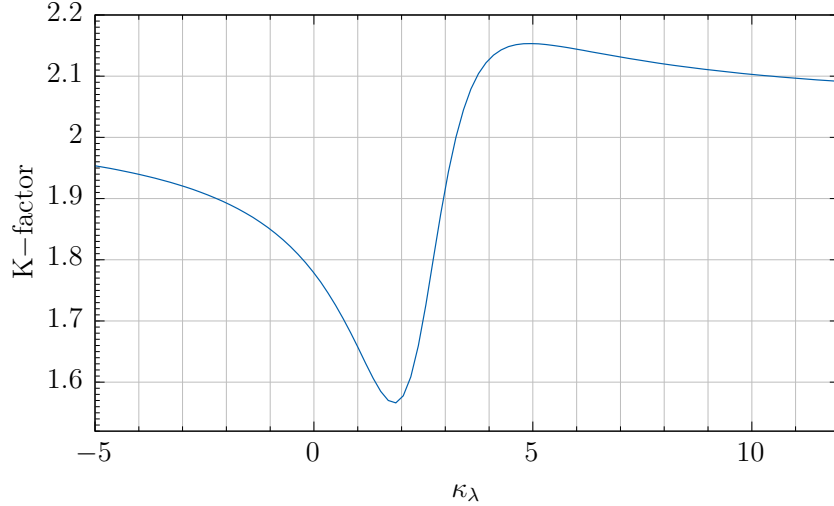
Figure 1.9: Variation of the NLO K-factor with the trilinear coupling for $\sqrt{s} = 14$ TeV [68].
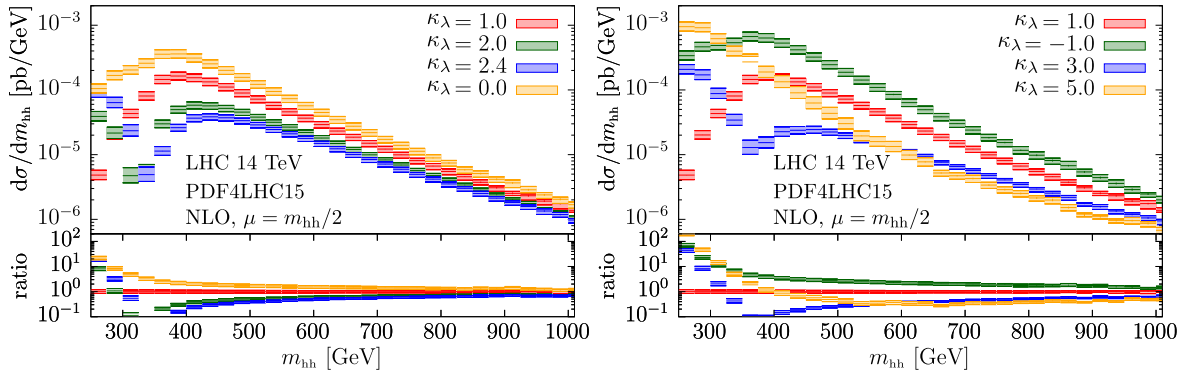
Figure 1.10: Higgs boson pair invariant mass distributions at 14 TeV for (left) positive small values of κ_λ and (right) larger or negative values of κ_λ [68].

In Figs. 1.10 and 1.11 we show the m_{HH} distribution for various values of κ_λ. The results in Fig. 1.11 are distributions normalised to the total cross section for the corresponding value of κ_λ. The ratio plots show the ratio to the Standard Model result. A characteristic dip develops in the m_{HH} distribution around $\kappa_\lambda = 2.4$, which is the value of maximal destructive interference between diagrams containing the trilinear coupling (triangle-type contributions) and "background" diagrams (box-type contributions). We provide results for a denser spacing of κ_λ values around this point. For $\kappa_\lambda < -1$ and $\kappa_\lambda > 5$ the triangle-type contributions dominate increasingly, leading to a shape where the low-m_{HH} region is more and more enhanced. In the transverse momentum distribution of one (any) of the Higgs bosons, shown in Fig. 1.12, effects of the destructive interference around $\kappa_\lambda = 2.4$ are also visible, however they are less pronounced.

Fig. 1.13 shows the Higgs boson pair invariant mass distribution at NLO as a function of κ_λ as a 3-dimensional heat map, where the dip in the m_{HH} distribution for κ_λ values close to 2.4 is again visible.

To summarise, we have presented in this section full NLO QCD results for Higgs boson pair production for various values of the trilinear Higgs boson coupling. We have provided total cross sections for 13, 14 and 27 TeV, and differential results at 14 TeV, including scale uncertainties. The matrix elements have been implemented in the POWHEG-BOX-V2 Monte Carlo framework and the corresponding generator is publicly available.

A combination of the NLO result with full top quark mass dependence presented in this section
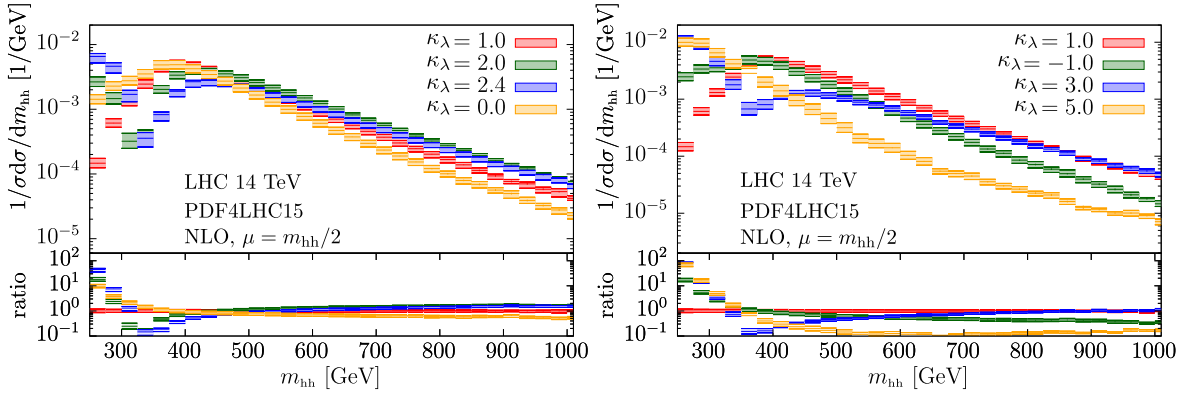
Figure 1.11: Normalised Higgs boson pair invariant mass distributions at 14 TeV for (left) positive small values of κ_λ and (right) larger or negative values of κ_λ [68].
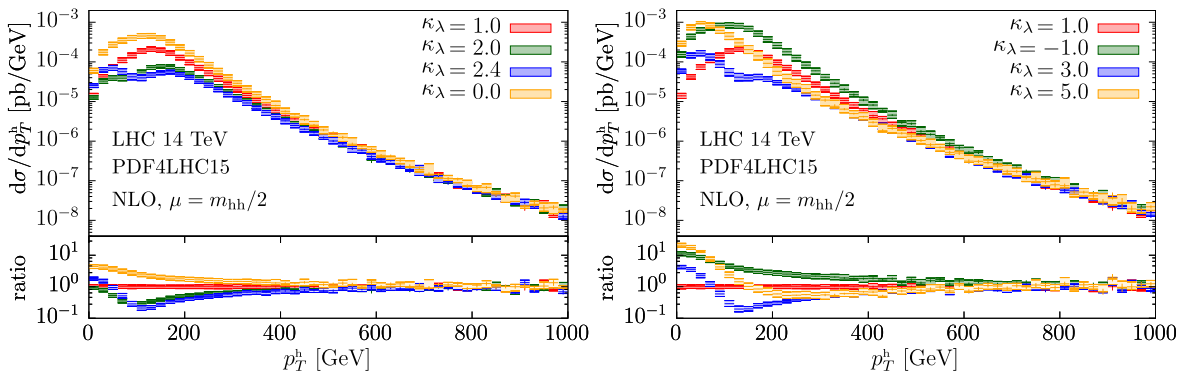
Figure 1.12: Higgs boson transverse momentum distributions at 14 TeV for the considered κ_λ values [68].

and the NNLO computed in the (improved) HTL has not yet been done for the case of non-SM κ_λ values, though work in this direction is in progress [83]. Such a combination would be desirable in order to match the level of accuracy obtained for the SM prediction. For the time being, the simplest approach to account for the higher order corrections consists in multiplying the results in Table 1.4 by the SM K-factor, i.e. the ratio of the NNLO$_{\text{FTapprox}}$ and NLO results in Table 1.3.

1.4 Differential predictions and MC generators

G. Heinrich, S.P. Jones, M. Kerner, S. Kuttimalai, E. Vryonidou

The non-resonant production of a pair of Higgs bosons in gluon fusion is available within several public Monte Carlo programs. Currently, the most sophisticated predictions which include a parton shower are based on the NLO matrix-element including a finite top quark mass [22, 23]. The fixed-order result was recently re-calculated and extended to allow also for a running top quark mass [24]. The NLO calculation was first interfaced to the POWHEG-BOX [71, 72] and MG5_aMC@NLO [52, 84] in Ref. [56], and to SHERPA [85] in Ref. [57].

The matching and parton shower uncertainties have been extensively studied in the literature [56, 57, 86], and were found to be large for certain observables. Similar effects have been observed in other processes including the production of a Higgs boson in gluon fusion [87, 88] and Z-boson pair production in gluon fusion [89].

Here, we briefly review the current status of these uncertainties focusing on one of the most sen-
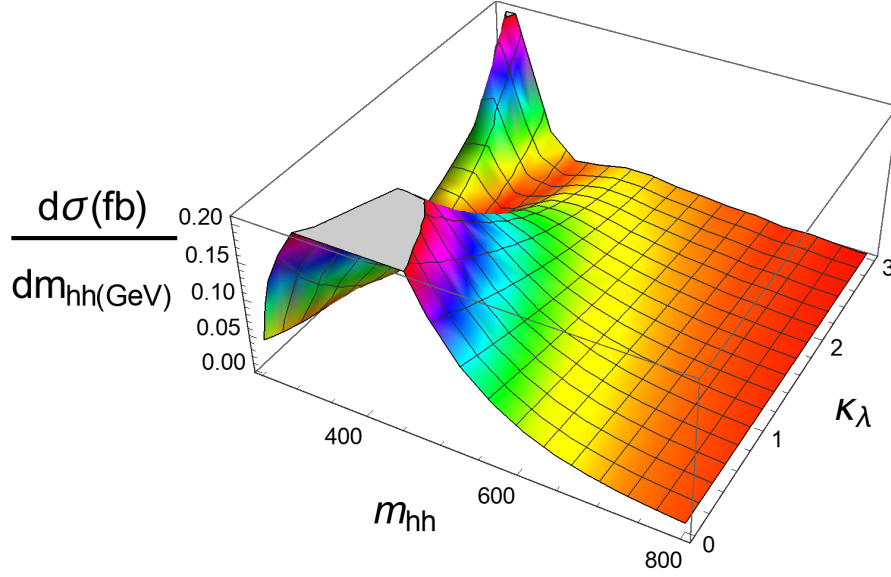
Figure 1.13: 3-dimensional visualisation of the m_{HH} distribution at 14 TeV, as a function of κ_λ and m_{HH} [68].

sitive distributions (the p_T of the di-Higgs boson system). We will summarise the MC@NLO [90] and POWHEG [70] matching schemes used in the literature. Results obtained from the POWHEG-BOX, MG5_aMC@NLO and SHERPA implementations and via analytic resummation [91] are compared. The shower uncertainty observed for the POWHEG-BOX implementation will also be discussed.

Parton Shower Matching

Already in a pure fixed-order NLO calculation there are contributions in both the Born phase space ϕ_B and in the real emission phase space $\phi_R = \phi_B \times \phi_1$. In a parton shower matched calculation, we denote them by $\bar{B}(\phi_B)$ and $H(\phi_R)$, respectively:

$$\bar{B}(\phi_B) = B(\phi_B) + V(\phi_B) + \int D(\phi_R)\Theta(\mu_{\mathrm{PS}}^2 - t(\phi_R))\, d\phi_1, \tag{1.10}$$

$$H(\phi_R) = R(\phi_R) - D(\phi_R)\Theta(\mu_{\mathrm{PS}}^2 - t(\phi_R)). \tag{1.11}$$

In Eqs. (1.10) and (1.11), B denotes the leading-order contributions, V the UV-subtracted virtual corrections, R the real-emission corrections, and D the differential infrared subtraction terms. The scale μ_{PS} is the parton shower starting scale and $t(\phi_R)$ is the evolution variable of the parton shower. Through variations of μ_{PS}, contributions can be shuffled around between $\bar{B}$ and H while leaving their sum constant.

When considering Eqs. (1.10) and (1.11) by themselves, real emission configurations are generated only in H events. Furthermore, the emissions are suppressed in the phase space region $t(\phi_R) < \mu_{\mathrm{PS}}$ due to the subtraction terms $D(\phi_R)$. For $t \ll \mu_{\mathrm{PS}}$, emissions are completely suppressed since there we have $R \sim D$, and thus $H \sim 0$. These missing real-emission terms are generated through the first parton shower emissions off the $\bar{B}$ events. Taking into account the first emission,

the sum of Eqs. (1.10) and (1.11) can be written as

$$\sigma_{\text{NLO+PS}} = \int \bar{B}(\phi_B) \left[\Delta(t_0, \mu_{\text{PS}}^2) + \int \Delta(t, \mu_{\text{PS}}^2) \frac{D(\phi_B, \phi_1)}{B(\phi_B)} \Theta(\mu_{\text{PS}}^2 - t) \Theta(t - t_0) \, d\phi_1 \right] d\phi_B$$

$$+ \int H(\phi_R) \, d\phi_R. \tag{1.12}$$

Here and in what follows we will assume that the parton shower splitting kernels are given by $\frac{D}{B}$, i.e. by the kernels that are also used in the infrared subtraction scheme. The Sudakov form factor is then given by $\Delta(t_0, t_1) = \exp\left[-\int_{t_0}^{t_1} \frac{D(\phi_R)}{B(\phi_B)} \, d\phi_1 \right]$ and the infrared cutoff scale of the parton shower is t_0. The first term in the square bracket of Eq. (1.12) corresponds to the probability of generating no emission above the parton shower cutoff scale for a $\bar{B}$ event. The second term represents the probability of generating an emission somewhere between the starting scale μ_{PS} and t_0. These terms therefore fill the remaining real-emission phase space region of soft emissions that are subtracted in H and would otherwise be missing. The scale μ_{PS} therefore separates the real emission phase space in a resummation region that is populated by the parton shower through the $\bar{B}$ events and a region that is populated mostly by the fixed-order real-emission contributions in H. Variations of this scale can be used in order to assess uncertainties associated with this separation.

The POWHEG method can be understood, in the formulation presented above, as the limit in which the parton shower starting scale is set equal to the collider energy $\mu_{\text{PS}} = \sqrt{s}$ and $D = R$. This choice leads to $H = 0$ and all real emission contributions are therefore generated by parton shower emission off $\bar{B}$ events. The choice $\mu_{\text{PS}} = \sqrt{s}$ ensures that the full real-emission phase space is covered. Setting $D = R$ in the first emission ensures that the fixed-order radiation pattern is recovered in the hard region where the Sudakov form factor is approximately one. However, setting $D = R$ also results in the full real-emission corrections being exponentiated in the Sudakov form factor. This is in general not justified since R contains hard, non-factorizing contributions. In Ref. [87] it was instead suggested to use

$$D = \frac{h_{\text{damp}}^2}{p_T^2 + h_{\text{damp}}^2} R, \tag{1.13}$$

where p_T is the transverse momentum of the Born final state ($p_T = p_T^{HH}$ in the case under consideration). This choice limits the amount of hard radiation that gets exponentiated.

Parton Shower Results

In the literature, the full NLO di-Higgs boson production calculation has been combined with a parton shower within the POWHEG-BOX, MG5_aMC@NLO and SHERPA frameworks. The POWHEG-BOX framework relies on the POWHEG scheme to match the fixed-order calculation with the parton shower, while MG5_aMC@NLO and SHERPA use the MC@NLO matching scheme. The POWHEG and MG5_aMC@NLO implementations generate showered events using a PYTHIA 8.2 [92, 93] shower whilst showered events are generated within SHERPA using the built-in Catani-Seymour (CS) [94] or Dire [95] showers.

In general, most distributions were found to be only moderately sensitive to the matching scheme. In particular, matching scheme uncertainties for NLO accurate observables were all found to be within the scale uncertainties [56]. However, the impact of the parton shower on the p_T^{HH} (transverse momentum of the di-Higgs boson system), $\Delta\Phi^{HH}$ (difference in azimuthal angle of the Higgs bosons) and ΔR^{HH} (radial separation of the Higgs bosons) was found to be fairly large. The sizeable
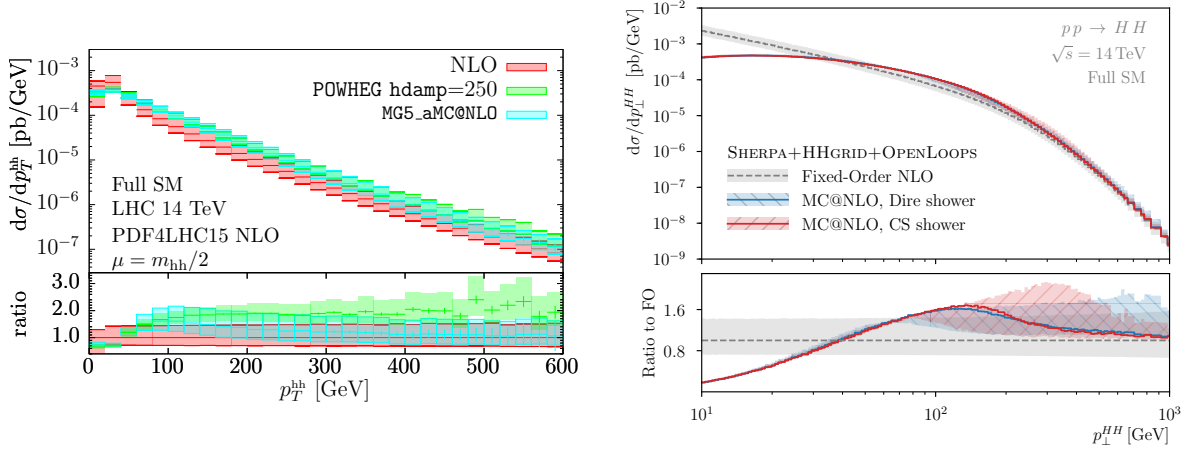
Figure 1.14: Left: Comparison between the POWHEG-BOX, MG5_aMC@NLO and NLO fixed-order results for the Higgs boson pair transverse momentum. The uncertainty bands were obtained through a 7-point scale variation of the factorization and renormalization scales [56]. Right: A comparison of the SHERPA and NLO fixed-order results. The SHERPA uncertainty bands indicate the shower scale uncertainty obtained by varying μ_{PS}. The bands on the fixed-order prediction were obtained by varying μ_F and μ_R [57].

impact of the parton shower is to be expected as the tails of these distributions are predicted only at the first non-trivial order in the fixed-order calculation. The matching scheme uncertainties for these distributions were also found to be significant and could even become larger than the scale uncertainties.

In Fig. 1.14 the NLO fixed-order result for the p_T of the di-Higgs boson system is compared to the showered predictions. The bands displayed on the left plot indicate the scale uncertainty, which is obtained via a 7-point scale variation of the factorization scale μ_F and renormalization scale μ_R around the central scale choice $\mu_0 = m_{HH}/2$, where m_{HH} is the invariant mass of the Higgs boson pair. In the right plot the grey band indicates the scale uncertainty while the coloured bands display the shower starting scale uncertainty. The MG5_aMC@NLO prediction is produced using a shower starting scale of $\mu_{\mathrm{PS}} = H_T/2$, where H_T is the sum of the transverse energies of the Higgs bosons. The POWHEG-BOX prediction is produced using $h_{\mathrm{damp}} = 250$ GeV. For the SHERPA predictions, the central parton shower starting scale choice in the case of the Dire shower is $\mu_{\mathrm{PS}} = m_{HH}/4$, whereas $\mu_{\mathrm{PS}} = m_{HH}/2$ is used for the CS shower. The shower scale uncertainty is obtained by varying the parton shower starting scale up and down by a factor of 2. It can be seen that for the central shower starting scale choice the MG5_aMC@NLO and SHERPA predictions reproduce the fixed-order result for sufficiently large p_T^{HH}, where the fixed-order result can be expected to be reliable to leading order accuracy. On the other hand, the POWHEG-BOX result overshoots the fixed-order result by about a factor of 2 for large p_T^{HH}. The Dire shower prediction can also significantly overshoot the fixed-order result, but only if the largest shower starting scale is chosen.

In Fig. 1.15 we display a comparison between the NLO parton shower matched results of POWHEG, MG5_aMC@NLO and SHERPA as well as the NLO+NLL result obtained using analytic resummation [91]. The bands displayed for the MG5_aMC@NLO and SHERPA predictions are produced by varying the shower starting scale μ_{PS} by a factor of 2 around their central values. Lacking a natural equivalent to μ_{PS} in the POWHEG framework, we display POWHEG-BOX predictions produced with various values of the h_{damp} parameter. The nominal (central) POWHEG-BOX prediction is produced with $h_{\mathrm{damp}} = 250$ GeV and the band is produced by varying the h_{damp} parameter between 150 GeV and infinity. We note that although the parton shower predictions differ from each other signifi-
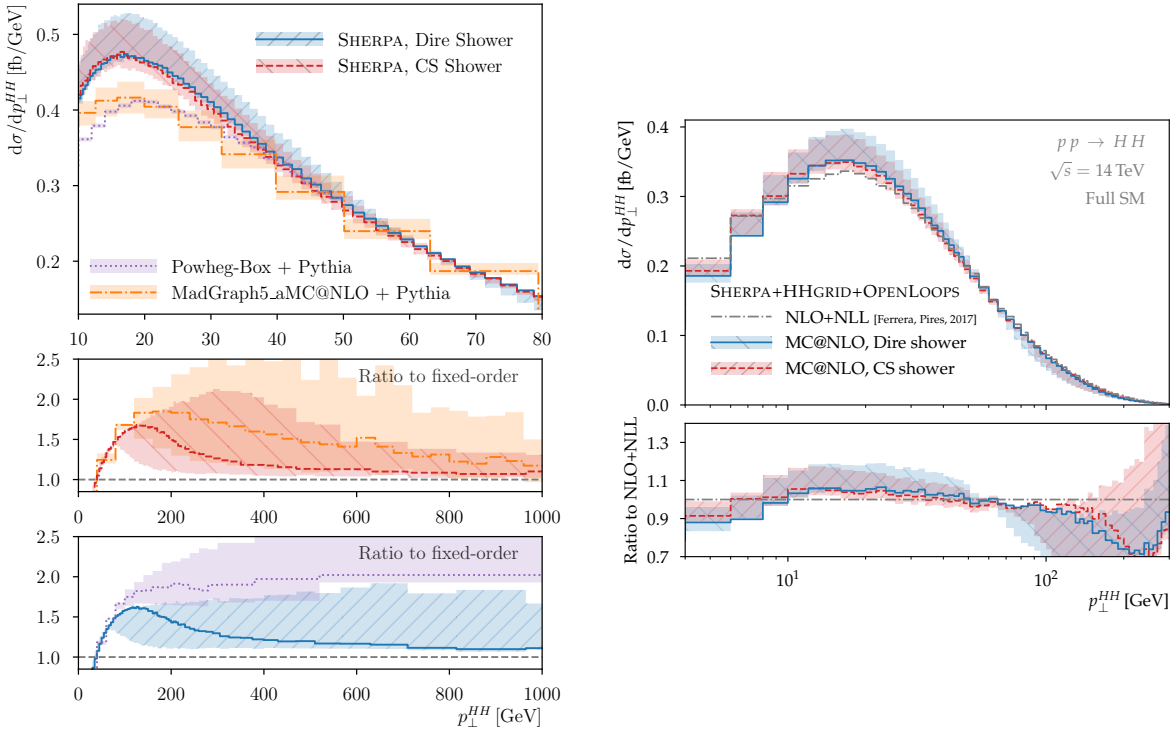
Figure 1.15: Left: Comparison of NLO parton shower matched predictions for the p_T^{HH} spectrum. The lower panels show ratios to the fixed-order prediction and cover a wider range of p_T^{HH} than the upper panel. The uncertainty bands on the parton shower matched predictions were obtained by varying μ_{PS} or h_{damp} as described in the text. Right: Comparison with the NLO+NLL analytic resummation results of Ref. [91]. The uncertainty bands on the SHERPA predictions were obtained by varying μ_{PS} [57].

cantly less in the low p_T^{HH} region, the shower starting scale uncertainty bands do not overlap. For low p_T^{HH}, where the analytic resummation can be trusted, it is found to be marginally compatible with the SHERPA result and lies between the SHERPA result and that of the other implementations.

Somewhat surprisingly, the matching uncertainties are very large also at high p_T^{HH}. They were investigated in detail in Refs. [57, 86]. It was shown that the large uncertainties are due to the formally sub-leading terms generated by parton shower emissions off the $\bar{B}$ terms. Such contributions are generally restricted to the phase space regions of soft emissions where $t < \mu_{PS}$, as shown in Eq. (1.12). For hard emissions where $t > \mu_{PS}$, only H event contributions remain, which should reproduce the fixed-order result. If μ_{PS} is sufficiently large, however, the parton shower emissions in Eq. (1.12) start contributing to the hard tail of the transverse momentum distribution. These parton shower emissions do not capture the correct, rapidly falling, fixed-order spectrum that one observes when the finite top quark mass is accounted for. They therefore produce the overshoot compared to fixed-order that we observe in the tails of Fig. 1.14. Varying μ_{PS} effectively switches this overshoot on and off, thus generating large uncertainty bands. It is worth noting, however, that for more moderate choices of the shower starting scale the fixed-order result is reproduced at large transverse momenta.

Within the POWHEG matching scheme the h_{damp} parameter can be reduced in order to suppress the overestimated real emission at large transverse momenta. In Ref. [56] it was shown that the choice $h_{damp} = 250\,\mathrm{GeV}$ is sufficient to reproduce the fixed-order result at large p_T^{HH} at the Les Houches event Level, i.e. after the first hard emission is generated according to the POWHEG method. Nevertheless, as can be seen in both Fig. 1.14 and Fig. 1.15, the POWHEG-BOX result when
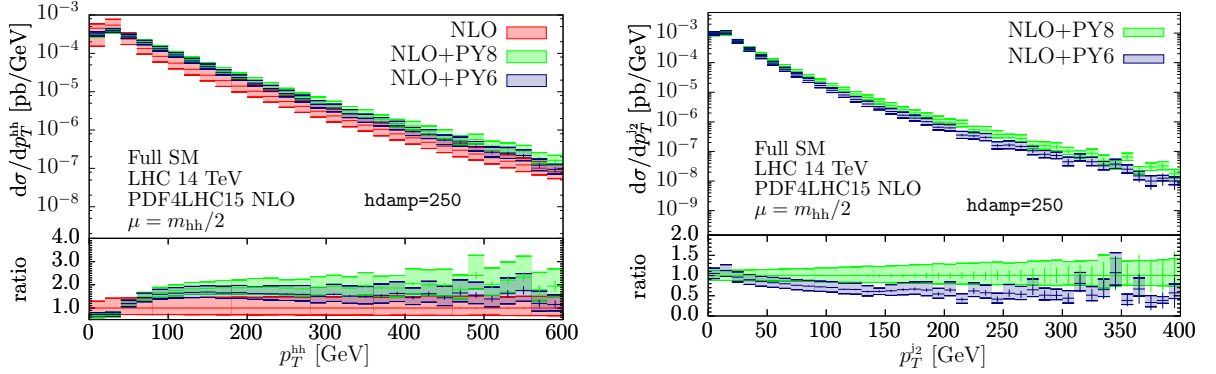
Figure 1.16: Left: The transverse momentum spectrum of the Higgs boson pair obtained using POWHEG-BOX in combination with a PYTHIA 8.2 and PYTHIA 6 shower. The scale uncertainty bands represent the variation of μ_F and μ_R. Right: Comparison of the sub-leading jet transverse momentum spectrum generated with POWHEG-BOX using a PYTHIA 8.2 and PYTHIA 6 shower [56].

showered with PYTHIA 8.2 was still found to be above the fixed-order result even at $p_T^{HH} \sim 600$ GeV. In Ref. [86], one explanation for this behaviour was found to be due to the emission of a relatively hard sub-leading jet, which at this order in perturbation theory is generated entirely by the parton shower. In Fig. 1.16 POWHEG-BOX predictions are shown with a PYTHIA 8.2 and PYTHIA 6 shower applied. The p_T^{HH} spectrum is considerably softer when the PYTHIA 6 shower is applied and tends towards the fixed-order prediction at large p_T^{HH}. In the right panel, the transverse momentum of the sub-leading jet, $p_T^{j_2}$, is shown, and we can observe that PYTHIA 8.2 predicts a significantly harder jet than PYTHIA 6. This behaviour is documented elsewhere in the literature [96, 97], and recent developments in PYTHIA 8.2 are likely to soften the observed behaviour in the tail of the p_T^{HH} distribution [98].

In summary, we have reviewed in this section the studies on the large matching scheme uncertainties present in Higgs boson pair production [56, 57, 86]. The origin of the uncertainty was found to partly be due to sub-leading terms present in the matching procedure, which can lead to a large overshoot of the parton shower relative to the fixed order prediction. There are three factors which play a role: the large K-factor ($\bar{B} - B$), large splitting kernel, and the shower starting scale. In particular, in the MC@NLO matching scheme the shower starting scale must be chosen small enough to prevent the parton shower from populating the full phase space, where it will overestimate the number of hard real emissions. Within the POWHEG matching scheme, a sufficiently low damping factor ($h_{\text{damp}} \lesssim 250$ GeV) or even a hard cut off on the hardness of shower emissions (SCALUP) must be used to suppress this behaviour.

In the POWHEG-BOX implementation it was found that the predictions for the transverse momentum of the Higgs boson pair differed significantly depending on whether a PYTHIA 8.2 or PYTHIA 6 parton shower is applied. This was found to be due to the fact that the PYTHIA 8.2 shower generates significantly harder sub-leading jets, which recoil against the di-Higgs boson system.

Chapter 2

Effective Field Theory

Editors: F. Goertz, D. Pagani, G. Panico

2.1 Introduction to the EFT formalism

G. Buchalla, C. Grojean, G. Heinrich, F. Maltoni, M. E. Peskin, E. Vryonidou

The goal of the study of Higgs pair production, and, more generally, multiple Higgs boson production, is to understand the form of the potential energy function of the Higgs field, and, through this, to understand why the Higgs field acquires a vacuum expectation value, fills the universe, and gives mass to all elementary particles. The simplest theory incorporating these phenomena is the Standard Model (SM). The SM in fact does not give any insight into these questions. It is simply a phenomenological model in which all properties of the Higgs field are input parameters and cannot be explained within the model. However, the SM is a tightly constrained structure. In particular, now that the Higgs boson mass has been measured and the other couplings of the theory are fixed by measurements of particle masses and electroweak boson couplings, the SM gives precise predictions for the Higgs field potential and other observables. Experiments, then, can test whether the SM accurately describes the phenomenon of electroweak symmetry breaking, or whether the SM must be replaced by a different, possibly more fundamental or predictive, underlying theory.

To test the SM through Higgs pair production, it is sufficient to work out the cross sections using the SM prediction for the potential and compare these results to experiment. However, to gain insight into the possibility of alternative theories of electroweak symmetry breaking, it is necessary to understand how these cross sections vary when we go outside the context of the SM. One way to do this is to compute the relevant pair production cross sections in specific alternative models. However, it would be good to have a formalism that is not so specific but rather summarizes the deviations that might appear in a very wide class of models beyond the SM.

This is the role of Effective Field Theory (EFT). It is one of the profound ideas of quantum field theory that interactions of arbitrary complexity that act at short distances can be approximated systematically by a Lagrangian with an enumerable set of parameters. This Lagrangian provides an "effective" description of any underlying model in this class. The EFT Lagrangian might not be renormalizable in the strictest sense, but it is nevertheless possible to carry out precise calculations that relate the parameters of this Lagrangian to observables [99]. For our purposes, the EFT Lagrangian will be the SM Lagrangian with corrections described by addition of local operators.

The EFT formalism addresses the problem of calculating corrections to the predictions of the SM in a systematic way. For example, it might seem that the most straightforward way to describe

the effects of new physics on the triple-Higgs coupling is simply to add to the SM Lagrangian a term

$$\Delta \mathscr{L} = -ch^3 \ . \tag{2.1}$$

This is equivalent to changing the Feynman rules of the SM by multiplying the triple Higgs boson vertex by κ_λ, with

$$\kappa_\lambda = 1 + 2\, c\, v / m_H^2 \ , \tag{2.2}$$

where m_H is the Higgs boson mass and $v \simeq 246$ GeV is the Higgs field vacuum expectation value. We have already seen calculations in this context in Sec. 1.3. However, the Lagrangian term in Eq. (2.1) is consistent with the $SU(2) \times U(1)$ gauge symmetry only if the field $h(x)$ is treated as a gauge singlet. This requires modifications elsewhere in the Lagrangian. Alternatively, we can keep $h(x)$ as a component of a complex scalar doublet, as in the SM. In that case, to have a gauge-invariant Lagrangian, we should recast Eq. (2.1) as

$$\Delta \mathscr{L} = -(c/v^2)|\Phi^\dagger \Phi|^3 \ , \tag{2.3}$$

where Φ is the SM Higgs doublet field. In both cases, the calculations done in Sec. 1.3 remain valid to the order at which they were presented. However, in both cases, the new terms added to $\mathscr{L}$ contain additional multi-Higgs vertices. These terms give new contributions to higher-order electroweak corrections. It turns out that these terms are needed to cancel potentially troublesome ultraviolet divergences. More generally, they allow us to treat these models with $\kappa_\lambda \neq 1$ in a well-defined way to arbitrary precision.

The second problem is that a modification of the Higgs self-coupling takes us outside of the SM. In this context, we might wish to consider the most general set of perturbations due to possible new physics. Those perturbations will affect the Higgs potential, but they will also modify other interactions that contribute to the Higgs pair production cross sections. How can we have control over these effects? The answer is that the possible gauge-invariant terms that we could add to the EFT Lagrangian can be classified according to a systematic expansion parameter, with only a finite number of new terms appearing at each order. Then we can, order by order, describe the possible ways in which new physics can affect the Higgs pair production cross sections with a finite number of parameters, and constrain them by measuring Higgs pair production. But the EFT Lagrangian is *the* Lagrangian, also describing single Higgs boson processes, reactions of the W and Z bosons that do not involve the Higgs boson, and precision electroweak observables. This allows us to use data from these other processes to constrain the new physics parameters and limit their influence on the Higgs pair production cross sections.

There is not a unique way to formulate an EFT description of new physics modifying the SM. In fact, two different formalisms are used in the literature and, within these, many different approximations are used to simplify the Lagrangians for practical purposes. In this chapter, we will describe these various approaches and their relation to specific underlying new physics models.

2.1.1   Two EFT extensions of the SM

In the literature, EFT descriptions of new physics beyond the SM are described within two different formalisms, called the HEFT (Higgs Effective Field Theory) and the SMEFT (Standard Model Effective Field Theory). The HEFT is also referred to as the Electroweak Chiral Lagrangian (EWChL). In relation to the discussion above, the HEFT follows the path of treating the Higgs field $h(x)$ as an $SU(2) \times U(1)$ singlet, while the SMEFT treats $h(x)$ as a component of an $SU(2) \times U(1)$ doublet field $\Phi(x)$. Both paths lead to self-consistent, gauge-invariant Lagrangians. The HEFT is the older of the two formalisms. The SMEFT has come to the fore more recently, specifically motivated by the dis-

covery that the mass of the Higgs boson is not large but, rather, close to the W and Z boson masses. In the discussion to follow, we will explain these approaches and some simplifying assumptions used with them in practical calculations.

It is important to emphasise at the start that the HEFT and the SMEFT are different ways to enumerate the same set of operators that can be added to the SM Lagrangian. In each case, operators are added systematically according to a given scheme of power-counting. However, the schemes are different in the two cases, so that the same operator might appear at the leading order in one scheme but at a higher order in the other scheme. In general, the SMEFT is more restrictive and therefore more predictive at a given order in its expansions.

2.1.2 SMEFT

The key idea of the SMEFT is to view a model of new physics that extends the SM as being built from the usual SM fields plus additional fields that act only at short distances or at high energy scales. We will refer to the mass scale of the new interactions as M in the following discussion. The fact that the LHC experiments have not yet discovered particles associated with new physics strongly suggests that there is a hierarchy between the mass scale m_Z at which SM interactions act and the scale M characteristic of new particle interactions, $M \gg m_Z$. In this picture, the Higgs field lives at the scale m_Z and is described as a full complex doublet of scalar fields Φ, as in the SM. The SMEFT Lagrangian is taken to be invariant under $SU(2) \times U(1)$. All of the fields in the Lagrangian transform *linearly* under gauge transformations. For example, the Higgs field with $I = \frac{1}{2}$, $Y = \frac{1}{2}$ transforms as

$$\Phi(x) \to \exp\left[-i\alpha^a(x)\frac{\sigma^a}{2} - i\beta(x)\frac{1}{2}\right]\Phi(x), \tag{2.4}$$

where $\alpha^a(x)$ and $\beta(x)$ are the $SU(2)$ and $U(1)$ gauge parameters, σ^a are the Pauli sigma matrices, and $\frac{1}{2}$ is the hypercharge Y of the field Φ. The gauge symmetry $SU(2) \times U(1)$ is spontaneously broken when the Higgs field acquires a vacuum expectation value

$$\langle\Phi(x)\rangle = \frac{1}{\sqrt{2}}\begin{pmatrix} 0 \\ v \end{pmatrix}. \tag{2.5}$$

The models considered today as the best candidates for a predictive theory of the Higgs potential follow this description. For example, in the supersymmetric extension of the SM, the Higgs doublet field is light, with a mass of the order of m_Z, while superpartner fields are heavy, with masses $M = M_{\text{SUSY}} \gg m_Z$ [100]. An alternative class of models assumes that the Higgs field is a multiplet of Goldstone bosons generated by symmetry breaking at a high mass scale M, with M at multi-TeV energies. The potential for the Higgs field is generated at the much lower scale $v \ll M$ by radiative corrections [101, 102].

To describe physics at energy scales below the scale M, we may integrate out the fields interacting only at high energy. Then we obtain a Lagrangian that contains only the SM fields, but possibly including operators of higher dimension built from these fields. In a renormalizable Lagrangian, all terms are operators of dimension 4 or less. If we add an operator of dimension $d > 4$, then, by dimensional analysis, that operator must have a coefficient proportional to $(\text{mass})^{4-d}$. When such operators appear after integrating out heavy fields, their coefficients will be proportional to M^{4-d}. The integration-out preserves the $SU(2) \times U(1)$ gauge symmetry. Then this procedure will give a Lagrangian of the most general form that can be built from gauge-invariant operators constructed from the SM fields.

However, it is a property of the SM that the SM Lagrangian is already the most general renormalizable $SU(2) \times U(1)$-invariant Lagrangian (with no strong-CP violation) that can be built from the SM fields. The EFT Lagrangian describing the most general types of new physics at the mass scale M then takes the form

$$\mathscr{L} = \mathscr{L}_{SM} + \sum_i \frac{\hat{c}_i}{M^2} \mathscr{O}_i + \sum_j \frac{\hat{d}_j}{M^4} \mathscr{O}_j + \cdots , \tag{2.6}$$

where the index i runs over dimension-6 operators, the index j runs over dimension-8 operators, and so on. There do exist operators of dimension $5, 7, \ldots$, but these involve lepton number violation. For example, the dimension 5 operators are neutrino mass terms. We may ignore them in discussing LHC processes.

Notice that, even though integrating out the new interactions can lead to order-1 modifications in the parameters of $\mathscr{L}_{SM}$, those changes are not observable, since in any event the parameters of $\mathscr{L}_{SM}$ are determined from experiment. This means that the observable effects of new physics at the scale M on cross sections at the much lower energy E are at most of size E^2/M^2. We can use this ratio of energies as an expansion parameter to control the number of new operators that we take under consideration. In particular, if E is of order m_H, M is of order 1 TeV, and we assume that the coefficients $\hat{c}_i$, etc., are of order 1, then the effects of dimension-6 operators are at the level of a few percent while the effects of dimension-8 operators are at the level of 10^{-4}. Then it can make sense to drop the terms with operators of dimension-8 and higher and consider only the effects of the dimension-6 operators. This gives a finite set of parameters describing the most general modification of the SM at short distances.

If we are considering the experimental implications of one dimension-6 operator, it is very physical to write the coefficient of this operator in terms of the parameter M, which then represents the scale of the new physics that gives rise to this operator. However, in analyses that involve a large number of dimension-6 operators (for example, 6 such operators appear in Eq. (2.10) below), it becomes awkward to define M in a consistent way. For the rest of this report, then, we will rewrite Eq. (2.6) using the Higgs field vacuum expectation value as the dimensionful parameter. This gives a definite, though arbitrary, choice for the dimensionful parameter in the EFT coefficients. Then the EFT Lagrangian will be expanded as

$$\mathscr{L} = \mathscr{L}_{SM} + \sum_i \frac{\overline{c}_i}{v^2} \mathscr{O}_i + \sum_j \frac{\overline{d}_j}{v^4} \mathscr{O}_j + \cdots . \tag{2.7}$$

The statement that $M \gg v$ appears here at the statement that the dimensionless coefficients $\overline{c}_i$ are much less than 1. Using the simple estimation scheme in the previous paragraph, in which we assume that the M is of order 1 TeV and the $\hat{c}_i$, $\hat{d}_j$ are of order 1, we would estimate that the $\overline{c}_i$ are generally of the order of a few percent, the $\overline{d}_j$ are generally of the order of 10^{-4}, etc. However, this argument is naive and there are important cases in which the $\overline{c}_i$ and $\overline{d}_j$ can be larger. Some of these are relevant to the Higgs self-coupling, as we will see in the next section.

How large are the SMEFT parameters?

Though the number of operators that appear in the SMEFT at dimension 6 is finite, it is very large. Naive enumeration gives more than 80 operators. However, linear combinations of operators that vanish by the SM equations of motion do not contribute to S-matrix elements, so we may drop some operators that appear in these linear combinations in favour of others. In the literature, there

are different choices of which operators to retain and which to drop. Two commonly used choices are the "Warsaw basis" [103] and the "SILH basis" [104, 105]. Comparing these schemes, different operators appear in the descriptions, but the final physics conclusions must be identical. Still, even after eliminating as many operators as possible, we are left with an unwieldy number of parameters to work with. For one generation of fermions (or assuming the strongest form of flavor universality), there are 59 independent baryon-number-conserving dimension-6 operators that one can build out of SM fields [103, 106].

One of these parameters—called $\overline{c}_6$—multiplies the dimension-6 operator in Eq. (2.3) and thus directly induces an h^3 vertex that shifts the Higgs self-coupling. However, other parameters can contribute in the calculation of Higgs pair-production cross sections. There is another parameter—called $\overline{c}_H$—that leads to an overall rescaling of all Higgs boson couplings. Other parameters not obviously related to the Higgs self-coupling can also have an influence. At the LHC, the Higgs pair production process $gg \rightarrow HH$ receives contribution from triangle and box top quark loop diagrams, with destructive interference. A change in the value of the top quark Yukawa coupling by 10%, which can be induced by another dimension-6 operator, then turns out to change the extracted value of the Higgs self-coupling by 50%. To control effects such as this, we must either argue that the relevant coefficients $\overline{c}_i$ are small *a priori* or that their values are restricted by other SM measurements. In this case, for example, precision measurement of the top quark Yukawa coupling could restrict this source of uncertainty. It is also possible to use measurements in different regions of phase space to distinguish the effects of different operators. This strategy has been studied for $gg \rightarrow HH$ in Refs. [107–109] and for $e^+e^- \rightarrow \nu\bar{\nu}HH$ in Ref. [110]. More generally, it is possible to combine data from Higgs pair production with that from other processes affected by dimension-6 perturbations, including precision electroweak observables, to extract the shift of the Higgs self-coupling through a global fit [111, 112].

It might also be possible to give *a priori* arguments allowing us to ignore some of the coefficients $\overline{c}_i$. In the previous section, we have argued that the $\overline{c}_i$ might be expected to be only a few percent in size. There are some examples in which $\overline{c}_i$ are known to be smaller. The S and T parameters of precision electroweak analysis [113] are induced by dimension-6 operator perturbations, and the corresponding $\overline{c}_i$ coefficients are then bounded by precision electroweak measurements to be less than 10^{-3} [114]. Constraints from the LHC on the Higgs couplings to W, Z, and heavy fermions are still at the 10–20% level [115, 116], but the estimate that the corresponding $\overline{c}_i$ are at the few-percent level neatly explains why no deviations from the SM have yet been observed. In this report, we will discuss experiments that constrain the Higgs self-coupling at the level of tens of percent. So perhaps we might even have the opposite problem, that, within the SMEFT, we predict that no deviations of the Higgs self-coupling from the SM will be observable.

Fortunately, there are models in which the deviations of the Higgs self-coupling can be of order 1 while the deviations in other parameters remain small. A variety of such models are studied in Chapter 3. We have the possibility for such large deviations when the Higgs field mixes with a SM singlet field that does not directly communicate with the W and Z bosons, or with a new fermion or boson sector that is relatively light compared with the 1 TeV mass scale. It is typical in these models that the same effects that give order-1 shifts of the Higgs potential also give few-percent shifts of the HWW and HZZ couplings that can be observed in measurements on single Higgs processes. These couplings, which are measured in single Higgs processes, are already constrained by LHC data, as noted above, and are expected to be measured with much higher accuracy. So it is possible to bring these pieces of information together to test proposed models.

The largest effects occur in models in which a new boson provides an s-channel resonance that can decay to HH. In such models, the di-Higgs mass spectrum in HH production can have two

distinct peaks, one at high mass corresponding to the resonance and one at 400-500 GeV containing the bulk of the HH production. The di-Higgs mass spectrum for a model in this class is shown in Fig. 3.4. It should be noted that the EFT description applies only to the lower-energy part of this spectrum, while the resonance at high mass must be described by a Lagrangian that contains the new particle explicitly.

A specific motivation for large modifications of the Higgs potential comes from the idea of electroweak baryogensis [117, 118]. The cosmic excess of baryons over anti-baryons must have been generated in the early universe during a time when the universe was out of equilibrium. This could have been possible at the electroweak phase transition, but only if this phase transition was strongly first-order. In the SM, for $m_H = 125$ GeV, this is not the case. Altering the Higgs potential to produce a strongly first-order phase transition requires a significant change, with a h^3 coefficient about a factor 2 larger than that in the SM [119–123]. Such a large effect could potentially be observed with high significance in the measurements we will describe. More information on this point is given in Sec. 3.6.

Finally, it is also reasonable to take a completely agnostic point of view and ask what is the maximal allowed value of the Higgs self-coupling. One possible limit comes from perturbative unitarity, that is, the constraint that tree-level diagrams involving this coupling not violate unitarity bounds. This gives [111, 124]

$$|\kappa_\lambda| < \text{Min}\left(600\xi, 4\pi\right),\tag{2.8}$$

where ξ is the typical size of the deviation of the Higgs couplings to other SM particles [104]. From the LHC measurements quoted above, ξ could be as large as 0.1-0.2. The stability of the Higgs potential places a stronger bound on κ_λ [124],

$$|\kappa_\lambda| < 70\xi.\tag{2.9}$$

This limit still gives considerable leeway in the search for modifications of the Higgs self-coupling.

Further discussion about the theoretical constraints that can be imposed on κ_λ from vacuum stability, perturbativity, and by considering specific UV-complete models can be found in Sec. 2.2.

$gg \rightarrow HH$ in the SMEFT

None of the analyses described in this report confronts the full problem of controlling the dependence of Higgs pair production cross sections on 59 (or more) dimension-6 operators available in the SMEFT. Most studies restrict themselves either to modification of the h^3 coupling only or modifications from a small set of especially relevant operators. As we discuss the current analyses, we will clarify for each of them precisely which set of operator contributions is being considered.

If our goal is to extract the Higgs self-coupling at the level of tens of percent, it can make good sense to consider only the subset of operators contributing at the leading order to the process under consideration. In this section, we describe a sensible reduction of the operator set for the process $gg \rightarrow HH$.

For this process, choosing the "Warsaw basis" of dimension-6 operators defined in Ref. [103], the most important contributions come from the 6 operators

$$\Delta\mathcal{L}_6 = \frac{\overline{c}_H}{v^2}\partial_\mu(\Phi^\dagger\Phi)\partial^\mu(\Phi^\dagger\Phi) + \frac{\overline{c}_u}{v^2}(\Phi^\dagger\Phi)\,\bar{Q}_L\widetilde{\Phi}\,t_R + \frac{\overline{c}_6}{v^2}\left(\Phi^\dagger\Phi\right)^3$$
$$+ \frac{\overline{c}_{tG}}{v^2}\bar{Q}_L\sigma^{\mu\nu}G_{\mu\nu}\widetilde{\Phi}\,t_R + \frac{\overline{c}_{\Phi G}}{v^2}(\Phi^\dagger\Phi)\,G^a_{\mu\nu}G^{a\mu\nu} + \frac{\overline{c}_{\Phi\widetilde{G}}}{v^2}(\Phi^\dagger\Phi)\,G^a_{\mu\nu}\widetilde{G}^{a\mu\nu}\,.\tag{2.10}$$
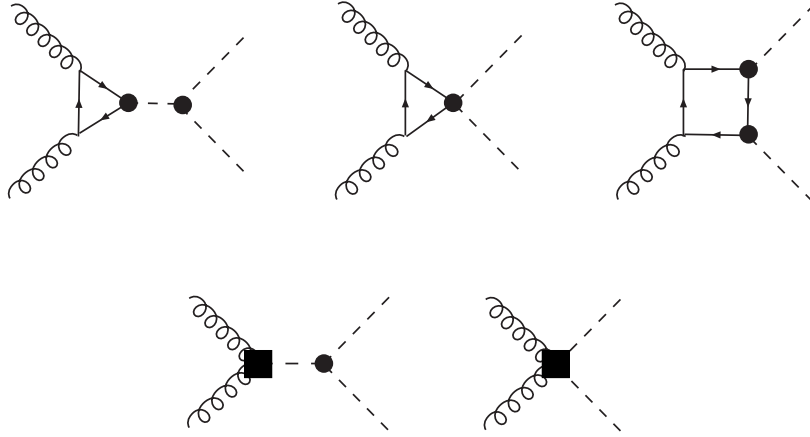
Figure 2.1: Feynman diagrams contributing to $gg \to HH$, including SM EFT effects of $D = 6$ operators, whose potential insertions are indicated by black squares and blobs (for simplicity we are neglecting additional diagrams that come from the top dipole operator). See text for details. These diagrams also correspond to the lowest non-vanishing order (one-loop order in this case) in the non-linear EFT.

In this formula, Q_L is the $(t, b)_L$ doublet, $\widetilde{\Phi} \equiv i\sigma_2\Phi$ denotes the charge conjugate Higgs doublet, and $\widetilde{G}^a_{\mu\nu} \equiv 1/2\epsilon_{\mu\nu\rho\sigma}G^{a\rho\sigma}$. If we assume CP conservation, the coefficients of the dimension-6 operators $\mathscr{O}_u$ and $\mathscr{O}_{tG}$ will be real and the CP-violating operator $\mathscr{O}_{\Phi\widetilde{G}}$ can be ignored.

The operators $\mathscr{O}_H$ and $\mathscr{O}_6$ modify the Higgs self interactions. The modifications as a function of the $\overline{c}_H$ and $\overline{c}_6$ coefficients are given by

$$\lambda_{H^3}/\lambda^{\mathrm{SM}}_{H^3} \equiv \kappa_\lambda = 1 - \frac{3}{2}c_H + c_6\,, \qquad \lambda_{H^4}/\lambda^{\mathrm{SM}}_{H^4} = 1 - \frac{25}{3}c_H + 6\,c_6\,, \qquad (2.11)$$

where $c_H \equiv 2\overline{c}_H$ and $c_6 \equiv (2v^2/m^2_H)\overline{c}_6$. The parameter c_6 only affects Higgs pair production, but the parameter c_H also induces a universal rescaling of single Higgs production cross sections.

The operators $\mathscr{O}_u$ and $\mathscr{O}_{tG}$ modify the Higgs coupling to the top quark. The operator $\mathscr{O}_u$ shifts the top quark Yukawa coupling (relative to the SM relation $m_t = y_t v/\sqrt{2}$). The operator $\mathscr{O}_{tG}$ induces an anomalous color magnetic dipole for the top quark and a contact interaction including the Higgs, the gluon and the top quark. These two operators enter the amplitude for $gg \to HH$ at the one-loop level. The remaining two interactions $\mathscr{O}_{\Phi G}$ and $\mathscr{O}_{\Phi\widetilde{G}}$ give contact interactions involving two Higgs bosons and two gluons. These operators contribute to Higgs pair production already at tree-level. The relevant diagrams for double Higgs production are shown in Fig. 2.1.

Additional SMEFT operators modifying the coupling of the Higgs to the gauge bosons and b quarks become relevant once the decays of the Higgs bosons are taken into account. Similarly, additional operators will enter once QCD and EW corrections are considered. The consideration of these operators is beyond the scope of this discussion.

In many SMEFT analyses of Higgs pair production [107, 108] a restricted set of dimension-6 operators is used, namely O_H, O_u, O_6 and $O_{\Phi G}$. This choice is motivated by theoretical considerations on the possible origin and size of the effective operators. In a large class of UV theories (including renormalizable, weakly coupled theories) the dipole operator O_{tG} and the $O_{\Phi G}$ and $O_{\Phi\widetilde{G}}$ operators are only induced at loop level, so that their coefficients are expected to be suppressed with respect to the other dimension-6 operators that can instead be induced at tree level. When this happens, the contributions of the dipole operator to double Higgs production can be formally considered as
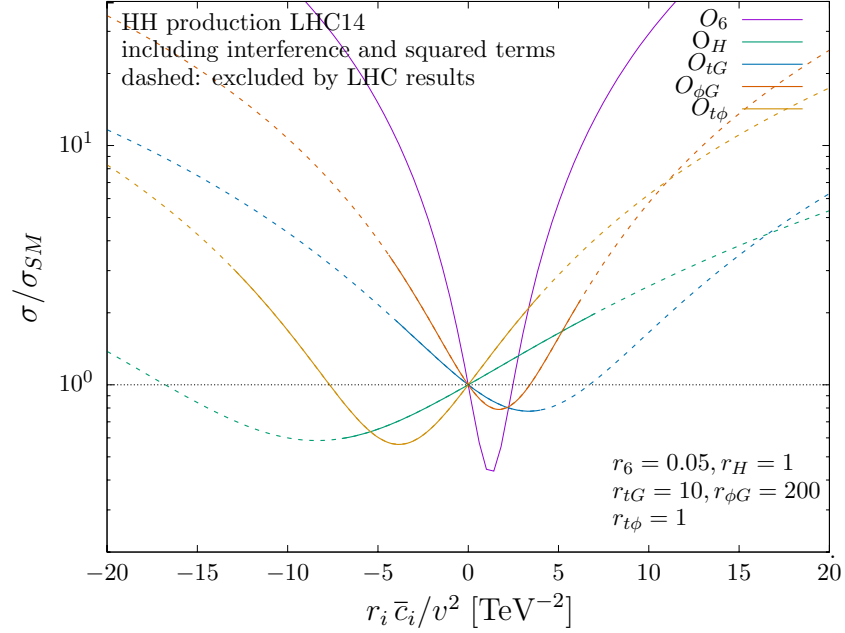
Figure 2.2: Dependence of double Higgs production cross-section on the Wilson coefficients of the relevant dimension-6 operators. The dashed part of the contours are excluded by LHC Run 1 Higgs and top quark measurements.

two-loop effects, and can be neglected with respect to the other corrections that arise at one-loop order. Notice that the $O_{\Phi G}$ operator, although suppressed by a loop factor, contributes at tree-level to double Higgs production. Therefore it is expected to give corrections comparable to the O_H, O_u and O_6 operators. On the other hand, if no theory bias is assumed on the origin of the effective operators, a full fit including the dipole operator O_{tG} should be performed. The contribution of O_{tG} in double Higgs production has been computed in Ref. [125], where its impact on the differential distributions was also studied.

In the context of the SMEFT, extracting the triple Higgs coupling from the measurement of the Higgs pair production cross section is more difficult, since all five operators listed above enter the process. The dependence of the total HH cross-section on the EFT coefficients of the operators of Eq. (2.10) is shown in Fig. 2.2. We see that the total cross section depends rather strongly on all of these coefficients.

A compensating factor is that the coefficients of the operators $\mathscr{O}_H$, $\mathscr{O}_u$, $\mathscr{O}_{tG}$ and $\mathscr{O}_{\Phi G}$ can be constrained by measurements of other processes at the LHC. In particular, top quark measurements will constrain the dipole operator $\bar{c}_{tG}$, while the top Yukawa operator $\bar{c}_u$ will be constrained by measurements of $t\bar{t}H$ production and other single Higgs processes. Similarly, $\bar{c}_{\Phi G}$ is constrained by measurements of the Higgs production cross section from gluon fusion, and $\bar{c}_H$ can be extracted as a uniform rescaling of all Higgs couplings. The current constraints obtained from Run 1 Higgs and top quark measurements are shown in Fig. 2.2 as the points where the various lines become dashed. Given these bounds, only the effect of $\bar{c}_6$ can lead to deviations of order 10 in the HH cross section from the SM predictions. However, to constrain $\bar{c}_6$ at levels of order 1, we will need precise constraints on all of other coefficients that enter the analysis. This demands a global SMEFT interpretation. We will discuss the impact of a such global fit in Sec. 2.3.1.

Another aspect to be stressed is the fact that the various effective operators induce different distortions in the double Higgs invariant mass distribution. A shape analysis can thus help in disentangling the various operators in a global fit. We will discuss this point in Sec. 2.4.

Single Higgs production in the SMEFT

As we already discussed, another process that is sensitive to modifications of the Higgs trilinear self-coupling is single Higgs production. Accessing the self coupling in this way has been entertained in Refs. [111, 112, 126–132] and is discussed in detail in Sec. 2.3.2. First experimental results employing this method can be found in Refs. [133, 134], and are discussed in Sec. 7.6 (see also Sec. 8.3). Differently from double Higgs production, in which the Higgs trilinear interaction enters in LO diagrams, in single Higgs processes such coupling contributes only through NLO corrections and its effects are thus suppressed by a loop factor. In such situation, model-independent bounds can only be obtained by performing a fit that simultaneously takes into account all the possible deformations of single Higgs interactions that contribute at LO. As discussed in the literature [111, 127–129] and reviewed in Sec. 2.3.2, the sensitivity on κ_λ obtained from single Higgs processes in an exclusive fit (i.e. allowing only κ_λ to vary and setting all the other couplings to their SM values) is comparable to the one from double Higgs production. However, once a global fit including deformations in single Higgs couplings is performed, the sensitivity is reduced, especially if no differential information is taken into account (see Fig. 2.10).

The question of identifying a minimal set of effective operators is more complex than what we discussed in the case of $gg \to HH$. The difficulty mostly comes from the fact that even small contributions from operators that enter at LO can easily overshadow the effects due to a modified Higgs trilinear coupling. Here we discuss the minimal set proposed in Ref. [111] for an analysis at the high-luminosity LHC. We however stress the fact that a suitable set of operators can crucially depend not only on the actual collider but also on the sensitivity reached in precision EW measurements (see for instance Ref. [112] in the context of future lepton colliders).

Before quoting the operators that we will include, we first discuss our simplifying assumptions. In fact, we will not consider dipole operators (analogous to the one we mentioned in the basis for double Higgs production) and operators that correct the W and Z interactions with the SM fermions. Moreover, we omit four-fermion contact operators (where in particular the ones involving the top quark could be relevant in principle). In all these cases the experimental constraints are weak enough to allow for non-negligible corrections to single Higgs processes. So, to remove these operators from a global fit, some theoretical assumptions might be needed, which we will rely on in the following. For instance, as we discussed for $gg \to HH$, the assumption that dipole operators only arise at loop level makes their contributions negligible. Moreover, under the assumption of flavor-universality for the new-physics contributions, the corrections of the W and Z couplings to the SM fermions are constrained at the $10^{-2} - 10^{-3}$ level and can be safely neglected.

A minimal set of operators, following this reasoning, was proposed in Ref [111] and includes 9 effective operators in addition to the deformation of the Higgs trilinear coupling. These operators can be expressed within the SMEFT framework in the "Higgs basis" [135] and correspond to

- 3 for the Yukawa interactions ($\delta y_t, \delta y_b, \delta y_\tau$),

- 2 for the contact interactions involving gluons and photons ($c_{gg}, c_{\gamma\gamma}$),

- 1 for the rescalings of the HZZ and HWW interactions (δc_z), assuming custodial symmetry is unbroken,

- 3 for the parameterisation of Higgs interactions with electroweak bosons featuring non-SM tensor structures ($c_{zz}, c_{z\square}, c_{z\gamma}$).[1]

---

[1] Since two combinations of these coefficients can also be constrained by di-boson data, the interplay between the gauge and the Higgs sectors cannot be neglected.

The resulting corrections to the Higgs interactions in the unitary gauge are given by

$$
\mathscr{L} \supset \frac{h}{v}\left[\delta c_w \frac{g^2 v^2}{2} W_\mu^+ W^{-\mu} + \delta c_z \frac{(g^2 + g'^2)v^2}{4} Z_\mu Z^\mu \right. \tag{2.12}
$$

$$
+ c_{ww} \frac{g^2}{2} W_{\mu\nu}^+ W^{-\mu\nu} + c_{w\Box} g^2 \left(W_\mu^- \partial_\nu W^{+\mu\nu} + \text{h.c.} \right) + \hat{c}_{\gamma\gamma} \frac{e^2}{4\pi^2} A_{\mu\nu} A^{\mu\nu}
$$

$$
\left. + c_{zz} \frac{g^2 + g'^2}{4} Z_{\mu\nu} Z^{\mu\nu} + \hat{c}_{z\gamma} \frac{e\sqrt{g^2 + g'^2}}{2\pi^2} Z_{\mu\nu} A^{\mu\nu} + c_{z\Box} g^2 Z_\mu \partial_\nu Z^{\mu\nu} + c_{\gamma\Box} g g' Z_\mu \partial_\nu A^{\mu\nu} \right]
$$

$$
+ \frac{g_s^2}{48\pi^2}\left(\hat{c}_{gg} \frac{h}{v} + \hat{c}_{gg}^{(2)} \frac{h^2}{2v^2} \right) G_{\mu\nu} G^{\mu\nu} - \sum_f \left[m_f \left(\delta y_f \frac{h}{v} + \delta y_f^{(2)} \frac{h^2}{2v^2} \right) \bar{f}_R f_L + \text{h.c.} \right],
$$

where the parameters δc_w, c_{ww}, $c_{w\Box}$, $c_{\gamma\Box}$, $\hat{c}_{gg}^{(2)}$ and $\delta y_f^{(2)}$ are dependent quantities defined as

$$
\delta c_w = \delta c_z,
$$

$$
c_{ww} = c_{zz} + 2\frac{g'^2}{\pi^2(g^2 + g'^2)}\hat{c}_{z\gamma} + \frac{g'^4}{\pi^2(g^2 + g'^2)^2}\hat{c}_{\gamma\gamma},
$$

$$
c_{w\Box} = \frac{1}{g^2 - g'^2}\left[g^2 c_{z\Box} + g'^2 c_{zz} - e^2 \frac{g'^2}{\pi^2(g^2 + g'^2)}\hat{c}_{\gamma\gamma} - (g^2 - g'^2)\frac{g'^2}{\pi^2(g^2 + g'^2)}\hat{c}_{z\gamma} \right],
$$

$$
c_{\gamma\Box} = \frac{1}{g^2 - g'^2}\left[2g^2 c_{z\Box} + \left(g^2 + g'^2 \right) c_{zz} - \frac{e^2}{\pi^2}\hat{c}_{\gamma\gamma} - \frac{g^2 - g'^2}{\pi^2}\hat{c}_{z\gamma} \right],
$$

$$
\hat{c}_{gg}^{(2)} = \hat{c}_{gg},
$$

$$
\delta y_f^{(2)} = 3\delta y_f - \delta c_z, \tag{2.13}
$$

and the relations between the independent couplings and the operator coefficients in the Warsaw basis, as appearing in Eq. (2.10), have been worked out in Ref. [135]. Finally, in the above expressions g, g', g_s denote the $SU(2)_L$, $U(1)_Y$ and $SU(3)_c$ gauge couplings respectively, and e is the electric charge.

2.1.3 HEFT

The HEFT gives a different way of organizing possible operator modifications of the SM Lagrangian. The idea of the HEFT is to describe the low-energy dynamics of electroweak symmetry breaking using a nonlinear realization of $SU(2) \times U(1)$. The SM naturally includes an unbroken global $SU(2)$ symmetry, called "custodial symmetry", that protects against radiative corrections to the relation $m_W = m_Z \cos\theta_w$ [136]. It is compelling to assume that this custodial symmetry is also present at least approximately in more general models of electroweak symmetry breaking. Then the pattern of symmetry breaking is $SU(2) \times SU(2)$ broken to $SU(2)$, the same as the pattern seen in chiral symmetry breaking in the QCD strong interactions. This suggests taking over the formalism of chiral perturbation theory used there to successfully describe low energy pion interactions [137, 138].

In this approach, we take the symmetry-breaking field to be a unitary matrix of $SU(2)$,

$$
U(x) = \exp[i\pi^a(x)\sigma^a / v], \tag{2.14}
$$

where π^a are the Goldston boson fields of the SM and v is the SM Higgs vacuum expectation value. Global $SU(2) \times SU(2)$ transformations act on $U(x)$ by $U \to V_L U(x) V_R^\dagger$. This is a *nonlinear* action

on the π^a fields. The $SU(2)$ gauge symmetry is identified with the left $SU(2)$, and the $U(1)$ gauge symmetry is identified with the rotations about the $\hat{3}$ axis in the right $SU(2)$, so that an $SU(2) \times U(1)$ gauge transformation is given by

$$U(x) \rightarrow \exp\left[-i\alpha^a(x)\frac{\sigma^a}{2}\right] U(x) \exp\left[i\beta(x)\frac{\sigma^3}{2}\right].$$ (2.15)

This transformation law should be contrasted with Eq. (2.4). The state of spontaneously broken gauge symmetry is described by

$$\langle U(x) \rangle = \mathbf{1}.$$ (2.16)

The expectation value leaves invariant the diagonal subgroup of the two original $SU(2)$ symmetries, and this subgroup can be identified with the custodial symmetry. The subgroup within this $SU(2)$ of rotations about the $\hat{3}$ axis is an unbroken gauge symmetry that can be identified with electromagnetism.

A problem with Eq. (2.15) is that it has no place for the Higgs boson field $h(x)$. In this formalism, $h(x)$ must be introduced as an $SU(2) \times U(1)$ singlet. Couplings of the Higgs boson will be introduced into the HEFT Lagrangian as polynomials in the dimensionless ratio $h(x)/v$.

As in the case of the SMEFT, the HEFT Lagrangian is organised according to power-counting rules. Following the guidance of chiral perturbation theory, the Lagrangian can be built up as terms with increasing *chiral dimension* χ [139,140]. In this scheme, boson fields are assigned $\chi = 0$, derivatives $\chi = 1$, and fermion bilinears $\chi = 1$. The zeroth order Lagrangian has chiral dimension $\chi = 2$,

$$\mathcal{L} = \frac{1}{2}(D_\mu \pi^a)^2 + \frac{1}{2}(\partial_\mu h)^2 + \bar{\psi}_f(i\slashed{D})\psi_f,$$ (2.17)

where D_μ is an appropriate covariant derivative. It is useful to think of the effective Lagrangian as being generated perturbatively in successive loop orders L, with $\chi = 2L + 2$. In this case, a weak coupling constant should also be assigned $\chi = 1$. This counting assigns to $h(x)/v$ the dimension $\chi = 0$ and so arbitrary powers of this quantity can appear at each order. To control this, the HEFT Lagrangian should be thought of as a double expansion in L and $h(x)/v$. A systematic expansion of the HEFT Lagrangian and evaluation of constraints on its parameters can be found in Ref. [141].

The HEFT approach is well adapted to models of electroweak symmetry breaking in which the symmetry breaking has two distinct sources, one from the Higgs field vacuum expectation value, one from strong interaction dynamics at a higher energy. Some models in this class are the low-scale technicolor [142], Higgs-dilaton [143], composite Higgs [101, 102, 144], conformal Higgs [145], and induced EWSB [146, 147] models. These models are not yet excluded, but they may be strongly challenged by future more precise measurements of Higgs couplings to fermions.

In the HEFT, the leading terms in the Lagrangian contributing to a quark mass and fermion-Higgs interactions are

$$\Delta\mathcal{L} = -m_f \bar{Q}_L U q_R \left(1 + c_f \frac{h}{v} + c_{ff} \frac{h^2}{v^2}\right) - \text{h.c.}.$$ (2.18)

In the SM, $c_f = 1$ and $c_{ff} = 0$. In the HEFT power-counting, the coefficient c_f is not fixed and can deviate from 1 by any amount, and the coefficient c_{ff} also is an independent parameter. This contrasts strongly with the situation in the SMEFT, in which $c_f = 1 + av^2/M^2$, where a is a parameter of order 1, and c_{ff} is predicted to be $c_{ff} = \frac{3}{2}av^2/M^2$ with the same value a (ignoring the contribution from c_H), up to corrections of order $1/M^4$. At the LHC, the Higgs boson couplings are found to be equal to their SM values in terms of the particle masses, to an accuracy of 10-20%. This is natural in the SMEFT, but it is a strong constraint on the parameters of the HEFT.
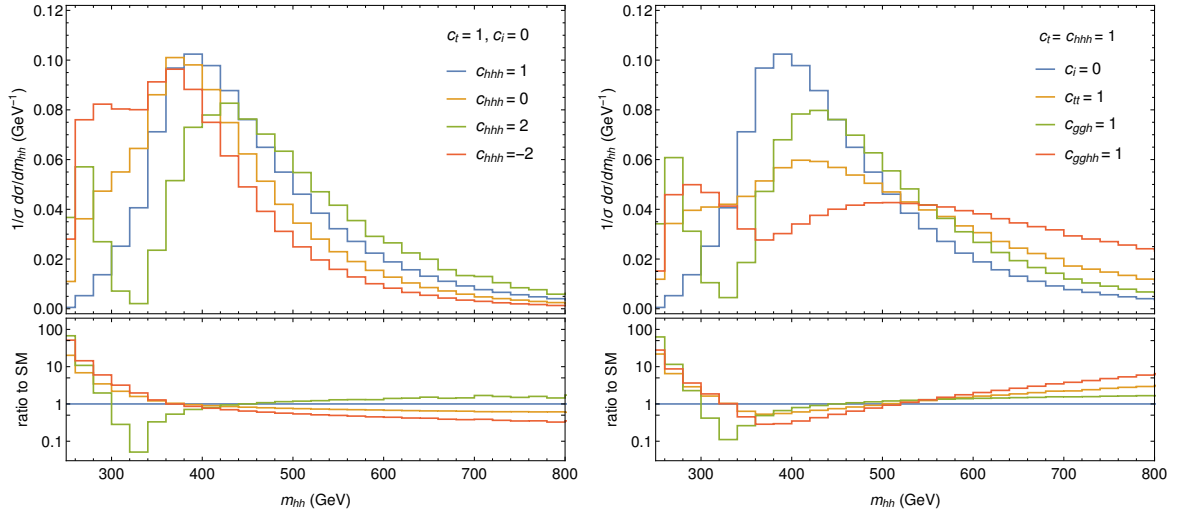
Figure 2.3: Normalized Higgs pair invariant mass distribution at 14 TeV for different combinations of the HEFT couplings in Eq. (2.19), and the ratio to the SM prediction. Here $c_i = 0$ means $i \in \{tt, ggh, gghh\}$, i.e. the blue curve denotes the SM case. The coefficient c_{hhh} is also known as κ_λ in experimental papers. All curves are computed at NLO with full top-quark mass dependence [69].

With this introduction, we can present the terms in the HEFT Lagrangian most relevant to the prediction of the cross section for $gg \to HH$. These are

$$\Delta \mathscr{L}_\chi = - m_t \left(c_t \frac{h}{v} + c_{tt} \frac{h^2}{v^2} \right) \bar{t}\, t - c_{hhh} \frac{m_H^2}{2v} h^3$$
$$+ \frac{\alpha_s}{8\pi} \left(c_{ggh} \frac{h}{v} + c_{gghh} \frac{h^2}{v^2} \right) G_{\mu\nu}^a G^{a,\mu\nu} . \tag{2.19}$$

The couplings c_t and c_{tt} are the top quark couplings from Eq. (2.18). To lowest order in the SM, $c_t = c_{hhh} = 1$ and $c_{tt} = c_{ggh} = c_{gghh} = 0$. In the HEFT framework, the deviations of the various couplings from their SM values are not expected to be small. The relation found in the SMEFT between c_t and c_{tt} and the similar SMEFT relation $c_{gghh} = \frac{1}{2} c_{ggh}$ are not present here. However, there is one simplification: the chromomagnetic operator does not appear in Eq. (2.19) because it contributes to $gg \to HH$ only at 2-loop order in the chiral power counting.

The contributing diagrams to lowest order are shown in Fig. 2.1. All diagrams are at the same order in the chiral power counting (chiral dimension 4, equivalent to one-loop order). The diagrams illustrate the interplay between leading-order anomalous couplings (black dots) within loops, and next-to-leading order terms (black squares) at tree level. In Fig. 2.3 we show, as an illustrative example, the effect that the different operators in Eq. (2.19) can have on the di-Higgs invariant mass distribution, for several points in the HEFT parameter space. These distributions are computed at NLO in QCD including the full top quark mass dependence, based on the results presented in Ref. [69].

As in the case of the SMEFT analysis described earlier, the prediction for the Higgs pair production cross section depends strongly on all of the parameters in Eq. (2.19). Thus, to extract the coupling c_{hhh} that determines the shape of the Higgs potential, we need to constrain the other couplings in Eq. (2.19) through a global analysis. This is more difficult in the HEFT formalism compared to the SMEFT because two of the relevant parameters—c_{tt} and c_{gghh} in Eq. (2.19)—appear only in processes with two Higgs bosons. Thus it is not possible to use single Higgs data to fix these parameters. A full analysis in the HEFT thus needs a strategy for constraining the auxiliary HEFT

parameters. For example, analyzing $t\bar{t}HH$ production separately from other HH production processes may allow a determination of c_{tt} independently from c_{hhh}.

In conclusion, the HEFT Lagrangian yields a consistent parametrization of anomalous Higgs boson properties. Its power-counting encodes the assumption that anomalous Higgs couplings are the dominant effects of new physics in the electroweak sector. In essence, the HEFT formalism gives a field-theory basis for the empirical κ-framework of modified Higgs couplings.

2.2 EFT vs. complete models: theoretical constraints on κ_λ

L. Di Luzio, R. Gröber, S. Gupta, F. Maltoni, D. Pagani, H. Rzehak, A. Shivaji, M. Spannowsky,

J. Wells, X. Zhao

The current bounds on the trilinear Higgs self-coupling λ_{H^3} are much weaker than those for other Higgs couplings. At the moment, the strongest experimental constraint from double Higgs production has been obtained by the ATLAS collaboration combining three different analyses [66,148–150], setting a bound $-5.0 < \kappa_\lambda < 12.1$, where $\kappa_\lambda \equiv \lambda_{H^3}/\lambda_{H^3}^{\text{SM}}$. An indirect measurement $\kappa_\lambda = 4.0^{+4.3}_{-4.1}$ has also been extracted by the ATLAS collaboration from single Higgs production measurements [134], following the strategy described in Sec. 7.6. No experimental constraints on the quartic Higgs self coupling are available at all. Given the current situation one can ask the following questions:

- is there any theoretical argument for constraining the Higgs self-couplings?

- how large can Higgs self-couplings be in UV-complete models?

In order to address the first question, we will consider both arguments based on vacuum stability and perturbativity. Then, we will consider specific UV-complete models for answering the second question.

Vacuum stability

If we consider the modifications induced to the SM potential by dimension-6 operators in Eq. (2.10), in particular the $(\Phi^\dagger\Phi)^3$ operator, one can distinguish 6 cases for the different sign possibilities for the parameters μ^2 (where $v^2 = -\mu^2/\lambda$), λ and c_6 [151]. Two different kinds of instabilities can arise, the most obvious one is at large field values for $\mu^2 > 0$, $\lambda > 0$, $c_6 < 0$. The other one has to do with the destabilization of the electroweak minimum against the minimum at zero field value, potentially occurring for $\mu^2 < 0$, $\lambda < 0$, $c_6 > 0$. In Ref. [152] it has been shown that both instabilities cannot be reliably assessed within the EFT, so that one cannot infer a model-independent bound on the trilinear Higgs self-coupling from stability arguments. The instability at large field configurations cannot be trusted due to the breakdown of the EFT expansion in the region close to the instability [153], while the occurrence of the low-scale instability requires a rather small value of the cutoff scale, making the use of the EFT language questionable.[2]

Also in UV-complete models with modifications of the scalar potential at tree level the vacuum instability and the modifications of the trilinear Higgs self-coupling are not directly connected, due to the presence of many couplings in the scalar potential that decorrelate the two effects. Instead, an almost one-to-one correspondence between the two is achieved in models where the Higgs self-couplings modifications are due to new fermions running in the loop, as in the case of right-handed

---

[2]However, in a recent study [124] it is argued that vacuum stability argument can still be relevant under some reasonable assumptions about the underlying EFT.
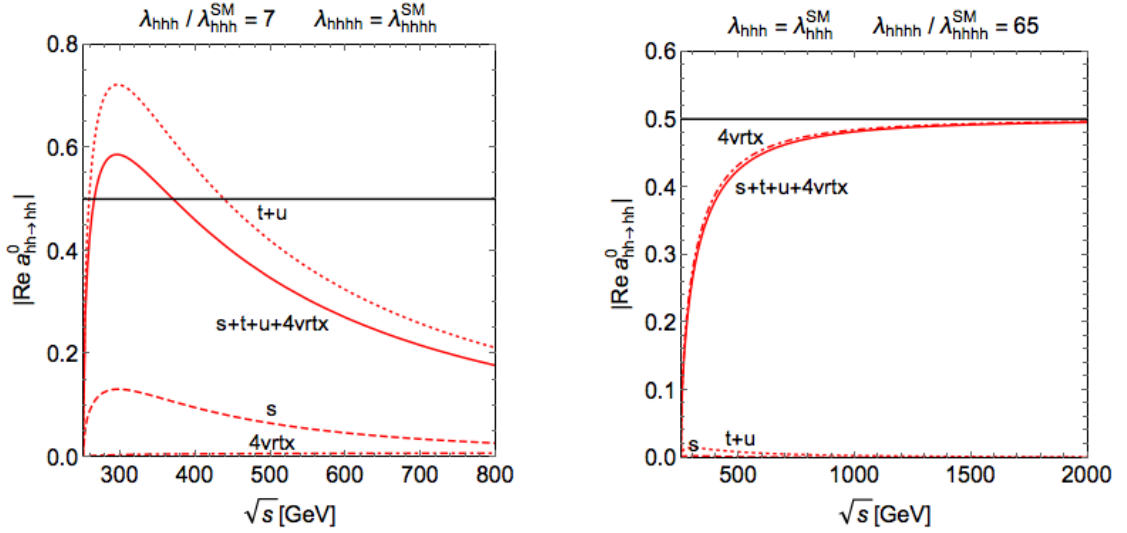
Figure 2.4: Dependence of the $J = 0$ partial wave a^0 on the center-of-mass energy $\sqrt{s}$ for modified trilinear Higgs self-coupling (left) and modified quartic Higgs-self-coupling (right). The plots are taken from Ref. [152].

neutrinos. While in low-scale inverse seesaw models one can find modifications in the trilinear Higgs self-coupling up to 30% [154], the scenarios providing such a large deviation of the trilinear Higgs self-coupling drive the Higgs potential into the unstable regime. Requesting that this does not occur within one order of magnitude from the mass scale of the right-handed neutrinos (hence not requiring any UV completion below that scale), one can bound the trilinear Higgs self-coupling modifications to be smaller than $\kappa_\lambda = 0.1\%$ [152] via metastability arguments (see e.g. Ref. [155]).

Perturbativity

On general grounds, one expects that too large values of the Higgs self-couplings will eventually enter the non-perturbative regime. A violation of perturbativity implies that new phenomena such as strong interactions may appear or new massive particles have to be present in the UV-finite model in order to restore perturbativity. On the other hand, non-perturbativity also indicates that LO predictions as well as higher-order corrections cannot be trusted. In view of the following discussion these two complementary aspects have to be kept in mind.

A possible tool to estimate the perturbativity range is based on partial wave unitarity. By looking at the $HH \to HH$ scattering amplitude in the SM broken phase and requiring that for the $J = 0$ partial wave $|\mathrm{Re}\, a^0| < \frac{1}{2}$, one finds $|\kappa_\lambda| \lesssim 6.5$ and $|\lambda_{H^4}/\lambda_{H^4}^{\mathrm{SM}}| \lesssim 65$. Note that the κ_λ bound is extracted at small $\sqrt{s}$, being the trilinear coupling associated to a super-renormalizable operator (cf. Fig. 2.4 – left panel), while the contribution of the quartic coupling to the partial wave becomes important only at large $\sqrt{s}$ (cf. Fig. 2.4 – right panel). Thanks to this very distinctive kinematical feature, one can separately set a model-independent bound on the trilinear and quadrilinear Higgs self-couplings.

An alternative perturbativity criterium is obtained by requiring that the loop-corrected trilinear vertex should be smaller than the tree-level vertex, or in the case of the quartic that the beta-function satisfies $|\beta_{\lambda_{H^4}}/\lambda_{H^4}| < 1$ [156, 157]. Such criteria lead to bounds very similar to the above

mentioned ones, leaving us with

$$|\kappa_\lambda| \lesssim 6, \tag{2.20}$$

$$|\lambda_{H^4}/\lambda_{H^4}^{SM}| \lesssim 65. \tag{2.21}$$

Following the same alternative perturbativity criterium, in Ref. [132] a bound equivalent to Eq. (2.20) has been set for $c_6 \equiv \kappa_\lambda - 1$. Parameterising any possible deviation to the SM potential as[3]

$$V^{NP}(\Phi) \equiv \sum_{n=3}^{\infty} \frac{c_{2n} m_H^2}{2 v^{2n-2}} \left(\Phi^\dagger \Phi - \frac{1}{2} v^2 \right)^n, \tag{2.22}$$

one finds that one-loop corrections to the HHH vertex are smaller than its tree-level value only for

$$|\kappa_\lambda - 1| \lesssim 5. \tag{2.23}$$

It is important to note that the bounds in Eqs. (2.20) and (2.23) originate from the requirement that the HHH vertex, setting two Higgs bosons on-shell, is perturbative for the full spectrum $\sqrt{\hat{s}} > 2m_H$. The strongest bound arises form the configuration $m_{HH} \simeq 2m_H$. In general, in other kinematic configurations, the bound is looser. For instance, the HHH vertex enters via one-loop electroweak corrections the predictions for single-Higgs production and decays modes, however, never with two Higgs bosons on-shell. Therefore, the bound in Eqs. (2.20) and (2.23), which indicates where it is sensible to perform a perturbative calculation, does not directly apply to the studies presented in Refs. [111, 112, 126–132] and discussed also in Sec. 2.3.2, where precise predictions for single Higgs production have been proposed as alternative method for the extraction of κ_λ. Trilinear coupling values corresponding to $|\kappa_\lambda| \sim 10$ still lead to reliable perturbative calculations *in single Higgs production*, though will lead also to large higher order corrections.[4]

On the other hand, the kinematic configuration corresponding to the most stringent perturbative bounds for κ_λ corresponds to the threshold region in double-Higgs production. This means that if $|\kappa_\lambda| \gtrsim 6$, perturbative predictions for total cross sections in double-Higgs production are meaningless.

In Fig. 2.5 we show a plot taken from Ref. [158] where the 2σ constraints that can be obtained at HL-LHC on c_6 as function of σ^{exp}/σ^{SM} are presented. The quantity σ^{exp} is the supposedly measured value for the double Higgs cross section, while σ^{SM} is the corresponding SM prediction. The constraints are derived using two different approximations: taking into account $\kappa_\lambda = 1 + c_6$ effects only at LO or including also loop-corrections induced by c_6 itself,[5] *i.e.*, at NLO. For $|c_6| \gtrsim 5$, where perturbativity is violated, NLO and LO constraints are not compatible. The bottom line is: when data are fitted via σ_{LO} predictions, κ_λ or equivalently c_6 is a parameter of ignorance; only for $|\kappa_\lambda - 1| = |c_6| \lesssim 5$ this parameter coincides to the quantity one is interested in. Moreover, NLO or any higher-order corrections would not improve this situation. Therefore, one can set bounds outside the range $|\kappa_\lambda - 1| = |c_6| \lesssim 5$, but only within this region they refer to the parameter in the Lagrangian.

Starting from the parameterisation of BSM effects in Eq. (2.22), one can derive from the one loop corrections to the HHH vertex perturbative bounds on the coefficient c_8, which is connected to the quantity $\lambda_{H^4}/\lambda_{H^4}^{SM}$ via the relation $\lambda_{H^4}/\lambda_{H^4}^{SM} = 1 + 6c_6 + c_8$. Following this strategy, in Ref. [158],

---

[3]Note that, at variance with Eq. (2.10), the dimension-6 operator is $(\Phi^\dagger \Phi - \frac{1}{2} v^2)^3$, so the coefficients c_6 and $\bar{c}_6$ are not simply related by a different normalisation. For more details see Ref. [132].

[4]More details can be found in Refs. [128, 157].

[5]For a precise definitions of the NLO predictions see Ref. [158]. Including NLO contributions, it is more convenient to organise the calculation according to c_6 than κ_λ.
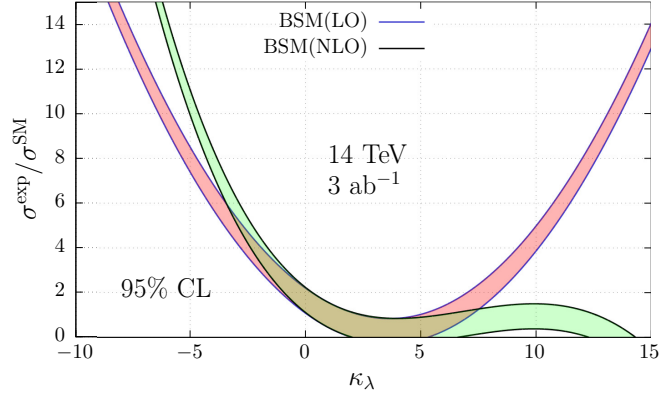
Figure 2.5: Bounds on κ_λ that can be set according to the supposedly double-Higgs measured cross section, normalised to the corresponding SM prediction. The red band is obtained considering the LO prediction, while the green taking into account one-loop corrections induced by κ_λ. This plot has been taken from Ref. [158] and adapted for this report.

a bound

$$|c_8| \lesssim 31 , \tag{2.24}$$

has been found and, taking into account the bound $|c_6| \lesssim 5$, it translates into

$$|\lambda_{H^4} / \lambda_{H^4}^{\mathrm{SM}}| \lesssim 61 , \tag{2.25}$$

which, although being κ_λ-dependent (*e.g.* $|\lambda_{H^4}/\lambda_{H^4}^{\mathrm{SM}}| \lesssim 31$ for $\kappa_\lambda \simeq 1$), is in good agreement with Eq. (2.21), obtained via a different approach.

Summarizing, we find that current limits on the trilinear Higgs self-couplings do not reach the interesting range yet; they are in fact still above the perturbative regime. Before concluding this subsection, however, we want to mention the results of recent studies [124, 159] that appeared during the writing of this report. In these works, a different approach to the investigation of the possible size of the trilinear has been pursued. In particular, a different question has been posed:

- if we measure a deviation on the value of the trilinear Higgs self coupling, at which energy scale at least we should expect new physics?

Parametrising the deviation via $\delta_\lambda = \kappa_\lambda - 1$ it has been found [159] that perturbation theory breaks down at the E_{max} scale

$$E_{\mathrm{max}} \lesssim \frac{13\,\mathrm{TeV}}{|\delta_\lambda|} , \tag{2.26}$$

regardless of the specific shape of the Higgs potential. Thus, if a deviation from $\lambda_{H^3}^{\mathrm{SM}}$ is observed, it would provide a target for the energy to explore at future colliders.

UV-complete models

We now turn to our second question, namely how large the trilinear Higgs self-coupling can be in renormalizable models. As a first step, we need to identify the class of models with potentially the largest trilinear Higgs self-coupling modifications. For simplicity, we restrict ourselves to one particle extensions of the SM and focus on the regime where the new states are heavier than the SM ones but not necessarily yet in the EFT regime. This is motivated by the fact that we want to

ϕ	$\mathcal{O}_\phi$
$(1,1,0)$	$\phi\Phi\Phi^\dagger$
$(1,2,\frac{1}{2})$	$\phi\Phi\Phi^\dagger\Phi^\dagger$
$(1,3,0)$	$\phi\Phi\Phi^\dagger$
$(1,3,1)$	$\phi\Phi^\dagger\Phi^\dagger$
$(1,4,\frac{1}{2})$	$\phi\Phi\Phi^\dagger\Phi^\dagger$
$(1,4,\frac{3}{2})$	$\phi\Phi^\dagger\Phi^\dagger\Phi^\dagger$

Table 2.1: List of new scalars ϕ inducing a tree-level modification of κ_λ via the tadpole operator $\mathcal{O}_\phi$. The $(SU(3), SU(2), U(1))$ representation is displayed in the left column.

concentrate on the case where the leading effects in di-Higgs production are due to the deviation in the Higgs trilinear.

The EFT regime can still be very useful in order to classify the SM extensions that can potentially yield the largest effects. In fact, we want to select those representations that can contribute to the operator $(\Phi^\dagger\Phi)^3$ once integrated out (see also Ref. [160]). In Table 2.1 we give the complete list of scalar representations ϕ that introduce a tree-level modification to the trilinear Higgs self-coupling in the EFT limit and that are characterized by the presence of a tadpole operator $\mathcal{O}_\phi$. The ϕ states $(1,3,0)$, $(1,3,1)$, $(1,4,\frac{1}{2})$ and $(1,4,\frac{3}{2})$ receive a vacuum expectation value that violates custodial symmetry and hence these cases are strongly constrained by electroweak precision measurements, while $(1,2,\frac{1}{2})$ with the operator $\phi\Phi\Phi^\dagger\Phi^\dagger$ corresponds to a general two-Higgs doublet model without Z_2 symmetry. Such a model leads in general to flavour-changing neutral currents and hence requires extra assumptions in the flavour structure. We will hence concentrate on the simplest case of a singlet extension $(1,1,0)$, with potential

$$V(\Phi,\phi) = \mu_1^2|\Phi|^2 + \lambda_\Phi|\Phi|^4 + \frac{\mu_2^2}{2}\phi^2 + \mu_4|\Phi|^2\phi + \frac{\lambda_3}{2}|\Phi|^2\phi^2 + \frac{\mu_3}{3}\phi^3 + \frac{\lambda_2}{4}\phi^4. \tag{2.27}$$

Some of the parameters above can be replaced by phenomenologically more accessible ones, like the mixing angle $\cos\theta$ between the singlet and the doublet fields, the vacuum expectation values and the masses of the Higgs bosons. Choosing as input parameters $m_1 = 125$ GeV, m_2, θ, $v_H = 246$ GeV, v_S, λ_2, λ_3, we scan them in the range 800 GeV $< m_2 < 2000$ GeV, $|v_S| < m_2$, $0.9 < \cos\theta < 1$, and in the perturbative regime $0 < \lambda_2 < \frac{8}{3}\pi$, $|\lambda_3| < 16\pi$. We further check the compatibility with electroweak precision observables, where the strongest bound comes from the measurement of the W-boson mass [161] and a combined fit to the Higgs signal (see also the discussion in Sec. 3.1). The perturbativity bound on $\lambda_{2,3}$ is set by perturbative unitarity, while for the dimensionful coupling μ_3 we require the loop-corrected vertex to be smaller than the tree-level one [157]. In addition, we required the potential to be bounded from below and checked for vacuum stability by means of the code VEVACIOUS [162], with the model file generated by SARAH [163, 164].

The results of the parameter scan can be found in Fig. 2.6. All points on the left of the light blue dashed line are excluded by Higgs coupling measurements, while everything on the left of the dark blue line is excluded by the measurement of m_W. The red, yellow, green points correspond respectively to an unstable, metastable, stable electroweak vacuum. As it can be inferred from the figure, the vacuum instability cannot constrain the modification of the trilinear Higgs self-coupling.
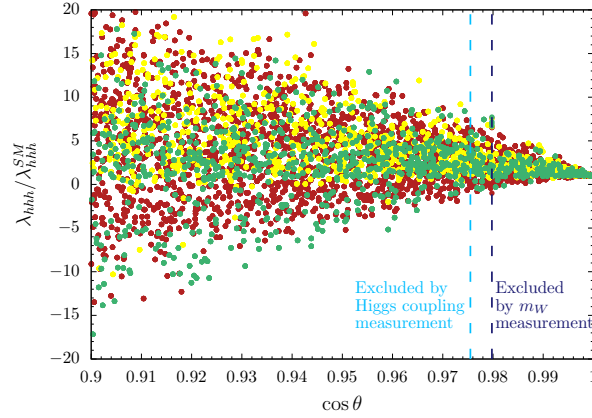
Figure 2.6: Modification of the trilinear Higgs self-coupling obtained from a scan over the singlet model parameters.

The maximal possible deviations allowed in the model are given by

$$-1.5 < \kappa_\lambda < 8.7 .\tag{2.28}$$

We now discuss the case of the MSSM as an example of a UV-complete model where BSM effects are more complex than in the scenario just considered. Assuming that at the LHC no further particle related to the electroweak symmetry breaking is discovered, in particular no further Higgs bosons, in Ref. [165] the maximal SM deviations of the triple Higgs coupling of the light CP-even Higgs boson was estimated. Constraints from the W-boson mass have a minimal influence, while viable deviations are mainly constrained by the shape of the discovery potential and the size of the Higgs boson mass.

For a correct determination of the maximal deviations of the triple Higgs coupling, in the MSSM it is crucial that the same approximation is used for the prediction of both the Higgs mass and the triple-Higgs coupling. Also, the input parameters must be the same in order to find the decoupling behaviour of the MSSM [166], $i.e.$, $\lambda \to \lambda^{\mathrm{SM}}$ for $M_A \to \infty$. Taking into account all the corrections given in Ref. [167], which especially includes the $\mathcal{O}(M_Z^2/v^2 y_t^2)$ terms, the largest deviations were found for $\tan\beta = 5$ and low M_A values, $M_A \sim 200$ GeV,[6] leading to about a 15% deviation of the SM Higgs triple coupling. Note that the approximation from Ref. [167] partly leads to smaller Higgs mass values and, hence, a wider exclusion of parts of the parameter points due to a too low Higgs-boson mass value w.r.t. other approximations including further higher-order corrections. In order to account for this effect, a relaxed Higgs-mass constraint was applied, see Ref. [165] for details. Instead, for $\tan\beta \gtrsim 10$, the estimated maximal deviation is about 2%. The latter limit does not change if one assumes that stop quarks are heavier than 2.5 TeV (one should note however that the approximations used to derive the MSSM Higgs mass value and the corresponding triple Higgs coupling have a much larger uncertainty for large stop masses, since large logarithms are not resummed in this approximation). On the other hand, the up-to-date results of the searches for heavy Higgs bosons and, in particular, the measurements of the properties of the discovered Higgs boson disfavour such a low value of M_A. For $M_A \gtrsim 350$ GeV, the maximal deviations found are $\lesssim 4\%$. Thus, it will be very difficult to discover the imprint of the MSSM on the trilinear Higgs self-coupling both

---

[6]It is important to note that in the region of $\tan\beta = 5$ a relatively light CP-odd Higgs boson of a mass of 200 GeV could be present and still be undiscovered according to the discovery potential assumed in Ref. [165].

at the HL-LHC and at a 100 TeV future collider.

2.3 Impact of EFT fit

2.3.1 EFT fit for HH production

F. Goertz, A. Papaefstathiou, J. Zurita

In terms of the EFT coefficients, as defined in Eq. (2.10), the relevant interaction terms entering HH production in gluon-gluon fusion read [107]

$$
\mathcal{L}_{HH} = -\frac{m_H^2}{2v}\left(1 + c_6 - \frac{3}{2}c_H\right)h^3 - \left[\frac{m_t}{v}\left(1 + c_t - \frac{c_H}{2}\right)\bar{t}_L t_R h \right.
$$
$$
\left. -\frac{m_t}{v^2}\left(\frac{3c_t}{2} - \frac{c_H}{2}\right)\bar{t}_L t_R h^2 + \text{h.c.}\right] + \frac{\alpha_s c_g}{4\pi}\left(\frac{h^2}{2v^2} + \frac{h}{v}\right)G_{\mu\nu}^a G_a^{\mu\nu},
$$

(2.29)

where we neglected light fermions, whose impact is in general expected to be small [116, 168], and also neglected effects from the chromomagnetic operator, $\mathcal{O}_{tG}$. Moreover, in order to canonically normalize the Higgs kinetic term (after EWSB) and to remove derivative interactions, we employed the field redefinition $h \rightarrow \left(1 - \frac{c_H}{2}\right)h - \frac{c_H}{2v}h^2 - \frac{c_H}{6v^2}h^3$.

Beyond modifying the trilinear self-coupling and the top-Yukawa coupling (first two terms in Eq. (2.29)), entering Higgs pair production via the SM-like triangle and box diagrams, as given in the upper panel of Fig. 2.1, the $D = 6$ operators induce new topologies, producing a Higgs pair via 4-point contact interactions with a scalar quark current or with the gluon field strength squared, or finally via a splitting from a contact-like single Higgs production, see the second row of Eq. (2.29). The corresponding Feynman diagrams are given in the lower panel of Fig. 2.1. The resulting differential cross section in the (linear) EFT becomes [107]

$$
\frac{d\hat{\sigma}(gg \rightarrow HH)}{d\hat{t}}\bigg|_{\text{EFT}} = \frac{G_F^2 \alpha_s^2}{256(2\pi)^3}\left\{\left|(1 - 2c_H + c_t + c_6)\frac{3m_H^2}{\hat{s} - m_H^2}F_\triangle + (1 - c_H + 2c_t)F_\square\right.\right.
$$
$$
\left.\left. + (3c_t - c_H)3F_\triangle + 2c_g\left(1 + \frac{3m_H^2}{\hat{s} - m_H^2}\right)\right|^2 + \left|G_\square\right|^2\right\},
$$

(2.30)

where we ordered the various contributions accordingly, and the form factors $F_{\triangle,\square}, G_\square$ take the same form as in the SM [107] (see Sec. 1.2) and can be obtained from Ref. [21]. Note that the spin-2 contribution to the box topology, $G_\square$, receives no $D = 6$ corrections.

For our phenomenological analysis we have implemented the Lagrangian in Eq. (2.29) into the HERWIG++ event generator, which allows to appropriately take into account changes in kinematic distributions that will substantially modify the efficiency of the experimental analysis. To treat higher order QCD corrections, we normalize our results to the NNLO QCD SM calculation of the cross section of ~ 40 fb [26] and include a conservative theory uncertainty of $f_{\text{th}} = 30\%$, comprising scale, PDF plus strong coupling, and K-factor uncertainties of $\mathcal{O}(10\%)$ each [82]. Regarding the decays of the Higgs pair, we consider the $HH \rightarrow b\bar{b}\tau^+\tau^-$ final state, where we also include the impact of the $D = 6$ operators on the partial widths, via modified Yukawa couplings, as well as the NP effects on the total width, and follow the analysis steps lined out in Ref. [169]. For more details, the reader is referred to Ref. [107].

In the following, we consider the six-dimensional parameter set $(c_6, c_H, c_g, c_t, c_b, c_\gamma)$, fixing in addition $c_\tau \equiv c_b$ for simplicity. As a first result we present, in the left panel of Fig. 2.7, the impact of
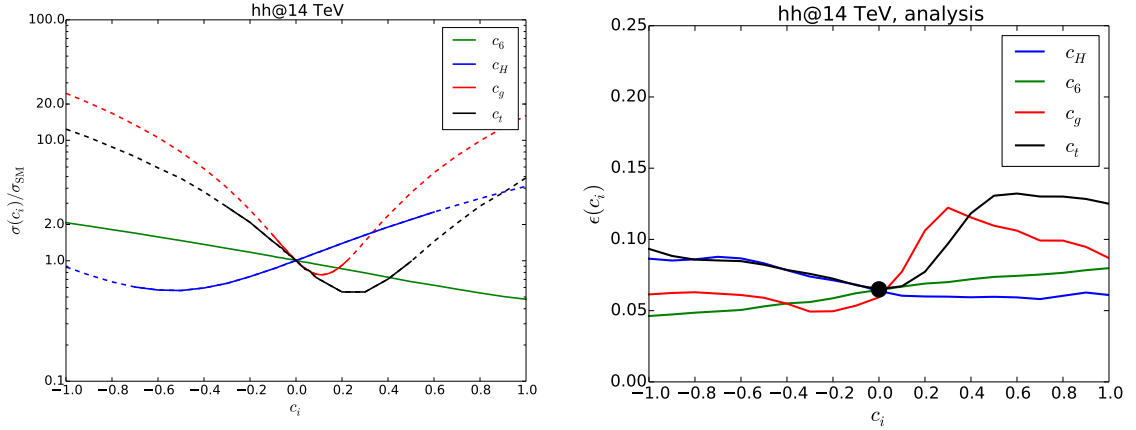
Figure 2.7: Left: Relative change in the HH cross section in dependence on individual operators. The dashed parts of the curves are excluded at 95% C.L. from Higgs boson data. Right: Corresponding efficiency of the analysis. See text for details.

varying individual coefficients out of this set on the HH production cross section relative to the SM value $\sigma(c_i)/\sigma_{\mathrm{SM}}$. The dashed parts of the curves represent regions which are excluded at the 95% C.L. by Higgs boson data[7], employing `HiggsBounds` and `HiggsSignals`. We can see a particularly pronounced dependence on the Yukawa-like and gluonic $D = 6$ operators, while the negative interference between the triangle and box diagrams leads to a decreased cross section for positive c_6. In the right panel of the same figure, we show the efficiency of our analysis, varying the same coefficients, where the non-trivial curves confirm the importance of using Monte Carlo event generation.

The resulting projected constraints on the EFT coefficients at the HL-LHC with an integrated luminosity of $3000\,\mathrm{fb}^{-1}$, assuming the SM to be true, are presented in Fig. 2.8. Here, we consider three different two-parameter planes, varying c_t, c_g, and c_b, each along with c_6. We marginalize over those parameters that are not shown, employing a Gaussian weight that corresponds to a projected measurement of the respective (single Higgs) observables at the HL-LHC at the 10% level [107]. The plots display the p-values obtained for a grid of points in the corresponding planes via a color code and the 1-sigma contours as black dashed lines.

Looking at the (c_t, c_6) plane, shown in the left plot, we see a strong dependence of the self-coupling constraint on c_t. In fact, for $c_t \sim 0.2$ the projected bound is significantly shifted compared to $c_t = 0$, since the effects of both coefficients on the production cross section can compensate each other. Beyond that, a similar sensitivity is found with respect to the gluonic contact interactions, entering the (c_g, c_6) plane presented in the middle plot, and on changes in the bottom Yukawa coupling, appearing in the rightmost (c_b, c_6) plane (with $c_b \equiv c_\tau$). In the latter case, a reduction in the production cross section via $c_6 > 0$ could for example be lifted by an enhanced branching ratio into bottom quarks and τ leptons.

Finally, we summarize our projected HL-LHC constraints on c_6, marginalizing over all other coefficients, in the following table:

full	full (**future**)	c_6-only
$c_6 \gtrsim -1.2$	$c_6 \in (-0.6, 0.6)$	$c_6 \in (-0.4, 0.4)$

.

The result given in the left column corresponds to a marginalization assuming *present* experimental uncertainties for the Higgs couplings, and delivers a very week projected constraint [107], leaving c_6

---

[7]The 95% C.L. limits obtained in Fig. 2.7 correspond to the bounds available at the time of the publication of Ref. [107]. Note the different sign convention in the top-Yukawa coupling c_t with respect to Fig. 2.2.
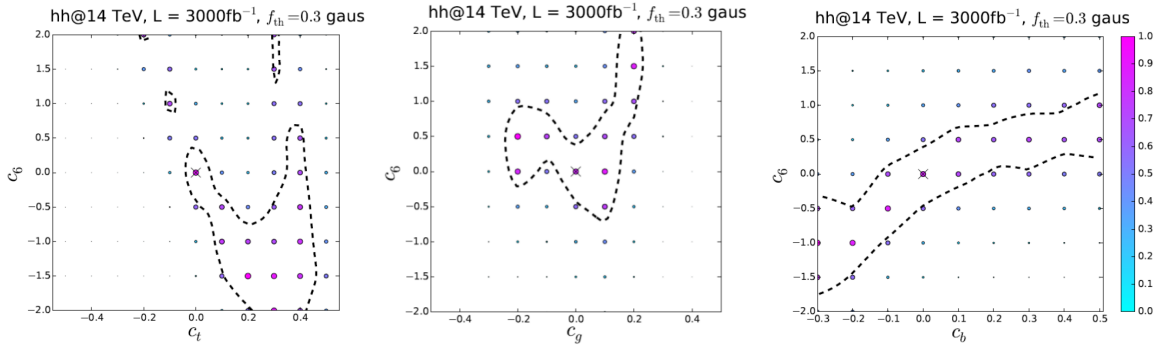
Figure 2.8: Projected exclusions in the (c_t, c_6), (c_g, c_6), and (c_b, c_6) planes at the HL-LHC, assuming a theoretical uncertainty of $f_{\text{th}} = 0.3$. The plots show the p-values obtained after marginalization over the directions orthogonal to the respective planes, including the 1-sigma contours as black dashed lines. See text for details.

unbounded from above, which highlights the importance of a combined analysis. Once we consider an improved determination of the Higgs properties via single Higgs production at the 10% level, as discussed above, the projected constraint on c_6 improves significantly, reaching the 60% level as presented in the middle column. This is rather close to, but still worse than, the naive bound where only variations in c_6 are allowed, leading to a projected 40% determination as given in the last column and agreeing with previous estimates [170].

We close noting that a constraint on the trilinear coupling at the $\lesssim 100\%$ level would in particular mean that one could probe the presence of the only relevant operator in the SMEFT, namely the μ^2 term, whose existence has so far not been established experimentally yet [160] and whose absence would lead to a strong decrease of the Higgs pair production cross section of $\sim 70\%$. It is clear that further studies of Higgs pair production, especially considering its kinematic distributions, would be interesting to still improve constraints and to disentangle different EFT effects, see e.g. Refs. [108, 158, 171].

2.3.2   Impact of single Higgs production

S. Di Vita, C. Grojean, U. Haisch, F. Maltoni, D. Pagani, G. Panico, M. Riembau, A. Shivaji, T. Vantalon, X. Zhao

In this section we discuss an alternative strategy for extracting the information on the trilinear Higgs self-coupling: the precise measurement of single Higgs production [111, 112, 126–132] at the LHC. Indeed, single Higgs production is sensitive to the trilinear Higgs self-coupling via electroweak one-loop corrections (two loops for gluon-gluon fusion production and $H \rightarrow \gamma\gamma$ decay). Thus, this strategy is based on indirect measurements and it is complementary to the direct measurements via double Higgs production. In single Higgs production, the effects of a modified Higgs self-coupling are much smaller, but the precision of the experimental measurements is and will be much better than in the case of double Higgs production. Moreover, many different final states (at the differential level) can be measured, leading to competitive bounds for the trilinear Higgs self-coupling. Even electroweak (EW) precision observables can be helpful for setting these bounds [172, 173].

In this section we recall the most important points of the calculation framework introduced in Refs. [127, 128]. Recently, updated numerical results for the effects induced by a modified trilinear Higgs coupling have been presented in Ref. [174] for inclusive and differential quantities; we do not report them here, but they have been exploited for the projections of the determination of the trilinear Higgs self-coupling that are discussed in this section.

Assuming on-shell single Higgs production, the signal strength for the process $i \to H \to f$, *i.e.* its rate normalised to the corresponding SM prediction, is $\mu_i^f = \mu_i \times \mu^f$, where μ_i and μ^f are the signal strengths for the production process $i \to H$ and the decay $H \to f$, respectively. Therefore, μ_i and μ^f can be expressed as

$$\mu_i = 1 + \delta\sigma_{\lambda_{H^3}}(i), \qquad \mu^f = 1 + \delta\mathrm{BR}_{\lambda_{H^3}}(f), \tag{2.31}$$

where $\delta\sigma_{\lambda_{H^3}}(i)$ and $\delta\mathrm{BR}_{\lambda_{H^3}}(f)$ are the deviations induced by an anomalous interaction, including the case of the trilinear Higgs self-coupling, to the production cross sections and branching ratios, respectively. This definition can be also extended to the differential level.

In the case of vector boson fusion, WH, ZH, $t\bar{t}$H and tHj production, the trilinear Higgs self interactions start to enter only at the one-loop level. On the contrary, gluon-gluon fusion production and the decays H$\to gg, \gamma\gamma$ depend on this coupling only via two-loop EW corrections. It is important to note that in all single Higgs processes the dependence on the quadrilinear Higgs self-coupling is further delayed by one loop order. On the other hand, it is possible in a similar way to probe quartic Higgs self-couplings via EW corrections to double Higgs production [132, 158, 175]. Results for future hadron colliders exploiting this strategy to set bounds on the quartic self-coupling are discussed in Sec. 10.8, and in Sec. 9.7 for the case of e^+e^- machines.

The anomalous trilinear Higgs self interactions can be parameterized via κ_λ (see (2.11)). Each single Higgs production or decay channel receives two different kinds of λ_{H^3}-dependent contributions [127, 128]. First, a process and kinematic dependent contribution, denoted in the literature as C_1, which parametrizes the linear dependence on κ_λ. Second, a universal contribution that is associated to the renormalization of the Higgs wave function and induces a quadratic dependence on κ_λ. On the contrary, in the case of the decays only a linear dependence on κ_λ is present, due to the cancellation of the effects associated to the Higgs wave function renormalization. Specifically, the signal strength μ_i for the production process $i \to H$ can be written in the following way,

$$\mu_i(\kappa_\lambda) = \frac{\sigma^{\mathrm{BSM}}(i)}{\sigma^{\mathrm{SM}}(i)} = 1 + \delta\mu_i(\kappa_\lambda) + Z_H^{\mathrm{BSM}}(\kappa_i^2 - 1), \tag{2.32}$$

where $Z_H^{\mathrm{BSM}}(\kappa_\lambda)$ is defined as:

$$Z_H^{\mathrm{BSM}}(\kappa_\lambda) = \frac{1}{1 - (\kappa_\lambda^2 - 1)\delta Z_H} \quad \text{with} \quad \delta Z_H = -1.536 \times 10^{-3}; \tag{2.33}$$

$\kappa_i^2 = \sigma_{\mathrm{LO}}^{\mathrm{BSM}}(i)/\sigma_{\mathrm{LO}}^{\mathrm{SM}}(i)$ takes into account additional variations of Higgs boson couplings to other particles (*e.g.* fermions, vector bosons) or it can be taken equal to one when variations of the trilinear-coupling only are considered. Assuming that (NLO) QCD corrections factorise anomalous κ_λ effects and taking into account also NLO EW corrections in the SM and on top of Z_H^{BSM}, the quantity $\delta\mu_i(\kappa_\lambda)$ is defined as

$$\delta\mu_i(\kappa_\lambda) = \frac{\sigma_{\mathrm{NLO}}^{\mathrm{BSM}}(i)}{\sigma_{\mathrm{NLO}}^{\mathrm{SM}}(i)} - 1 = Z_H^{\mathrm{BSM}}\left[1 + \frac{(\kappa_\lambda - 1)C_1^i}{K_{\mathrm{EW}}(i)}\right] - 1, \tag{2.34}$$

where $K_{\mathrm{EW}}(i) \equiv \sigma_{\mathrm{NLO_{EW}}}^{\mathrm{SM}}(i)/\sigma_{\mathrm{LO}}^{\mathrm{SM}}(i)$ is the NLO EW K-factor in the SM, which therefore includes also the Higgs self-coupling one-loop corrections in the SM. The values of $K_{\mathrm{EW}}(i)$ and C_1^i for the different production mechanisms can be found in Ref. [131] for the inclusive case, and also the differential values have been presented therein (see Figs. 2-10). It is worth to note that, although the size of
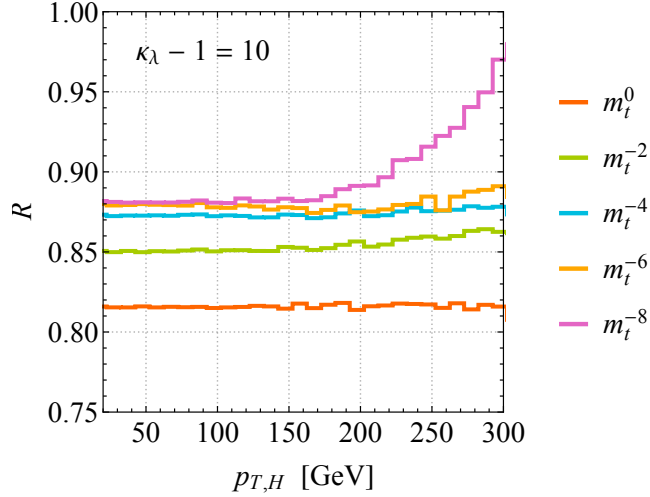
Figure 2.9: Effect of κ_λ corrections on the $p_{T,H}$ spectrum in $pp \to H + \text{jet}$ production. As indicated, the curves correspond to different orders in the asymptotic expansion in the top-quark mass m_t, and all show the ratio between the new-physics and the SM prediction for the choice $\kappa_\lambda - 1 = 10$.

$K_{\text{EW}}(i)$ is quite sizable and has a non-negligible impact on the prediction of the (differential) cross sections σ, in the case of $\delta\mu_i(\kappa_\lambda)$ its impact is very small [131]. Finally, each decay process $H \to f$ is scaled by the signal strength

$$\mu^f(\kappa_\lambda) \simeq \frac{\kappa_f^2 + (\kappa_\lambda - 1)C_1^f}{\sum_j \text{BR}^{\text{SM}}(j)[\kappa_j^2 + (\kappa_\lambda - 1)C_1^j]}, \tag{2.35}$$

where $\sum_j$ runs over all the Higgs boson decay channels and κ_j is the branching fraction modifier for the j final state, $\kappa_j^2 = \text{BR}_{\text{LO}}^{\text{BSM}}(j)/\text{BR}_{\text{LO}}^{\text{SM}}(j)$.

The processes WH, ZH, and especially $t\bar{t}H$, entail a larger linear dependence on λ_{H^3} with respect to the other processes. Moreover, also a stronger kinematic dependence is present, with larger values associated to the threshold region [128, 129, 131]. In the case of VBF, the kinematic dependence is instead rather flat [128, 129, 131]. Fully differential results for these production mechanisms can be obtained with the code presented in Ref. [131]. The calculation of differential effects for gluon-gluon fusion would be desirable, but it is not yet available due to its higher complexity, as it involves the evaluation of two-loop EW diagrams for the process $pp \to H + \text{jet}$. The calculation of the relevant amplitudes in an asymptotic expansion near the limit of infinitely heavy top quark has been performed for a generic κ_λ in Ref. [176]. The corresponding numerical results indicate that the effect of κ_λ variations in the $p_{T,H}$ spectrum are almost flat within the range of validity of the expansion (i.e. $p_{T,h} < m_t \simeq 173\,\text{GeV}$). This feature is illustrated in Fig. 2.9 for the choice $\kappa_\lambda - 1 = 10$. Above the top threshold, distortions of the $p_{T,H}$ distribution due to the κ_λ corrections are, however, expected.

Since single Higgs production processes have already been measured, constraints on λ_{H^3} can be set following this strategy. Especially, since C_1 is different for any production and decay channel, a fit involving different measurements can be very powerful for the determination of a single parameter. Based on the results presented in Ref. [177], which do not exploit differential information, assuming the only deviations from the SM are associated to λ_{H^3}, the following 2σ bounds can be set [128]:

$$-9.4 < \kappa_\lambda < 17.0 \qquad \text{at } 8\,\text{TeV} \tag{2.36}$$

and following the same approach, based on the results presented in Ref. [116],

$$-4.7 < \kappa_\lambda < 12.6 \qquad \text{at 13 TeV.} \tag{2.37}$$

Notably, bounds in Eq. (2.37) are competitive with the currently strongest bounds from double Higgs production measurements [66]. Very recently, the first experimental results obtained following this strategy have been presented by ATLAS [134]. This measurement is in good agreement with the estimate in Eq. (2.37) and is discussed in detail in Sec. 7.6.

The aforementioned limits, however, assume a very peculiar BSM scenario, in which the only relevant effects originate from the trilinear Higgs coupling, allowing for $\mathcal{O}(1)$ deviations without any effect on other Higgs couplings. In fact, these limits critically depend on other aspects [111, 131]. First, the number of additional parameters, which are related to other anomalous interactions, and the number of independent measurements that are taken into account in the fit. Second, the inclusion or not of the information from differential distributions. Third, the fit assumptions on the size of the theoretical and experimental uncertainties. Also for these reasons, ATLAS and CMS analyses with a full-fledged treatment of all the correlations and with different assumptions on the the number of BSM parameters are essential. The first of these kind of analyses, which has been presented in Ref. [134] and it is also discussed in Sec. 7.6, is supporting the validity of this strategy.

As shown in Ref. [131], assuming only deviations on the Yukawa coupling of the top quark (κ_t) and/or a common rescaling of the Higgs-gauge interactions (κ_V), limits are mildly affected. On the other hand, in general, a new dynamic affecting the Higgs self-coupling would leave a more complex imprint on the other Higgs interactions and can have a strong impact on the bound on λ_{H^3} [111]. Adopting the EFT framework described in Ref. [111], nine additional coefficients parameterise the possible deviations in single Higgs production (see Eq. (2.12) and related discussion):

$$\delta y_t, \delta y_b, \delta y_\tau, c_{gg}, c_{\gamma\gamma}, \delta c_z, c_{zz}, c_{z\square}, c_{z\gamma}. \tag{2.38}$$

For the determination of λ_{H^3}, a global fit is important not only because involves different processes that entail a different dependence on λ_{H^3}, but also because it allows to assess the robustness of bounds such as those in Eqs. (2.36) and (2.37), where only λ_{H^3} variations are considered. For example, a global fit using only inclusive single Higgs observables such as those presented in Ref. [111], which is based on only nine independent measurements, and taking into account the additional nine EFT deviations listed above, suffers from a flat direction. Therefore, λ_{H^3} remains unconstrained under these assumptions. On the other hand, its presence in the fit decreases the accuracy in the determination of some of the other nine coefficients. In order to lift this degeneracy, it is possible to include data from differential measurements. Indeed $\delta\kappa_\lambda \equiv \kappa_\lambda - 1$ has a non-flat effect on single Higgs distributions.

We summarise the global fit for the HL-LHC in Fig. 2.10. The width of the bands represent the results obtained assuming two different uncertainty scenarios, S1 and S2, which correspond to the projected uncertainties on the inclusive signal strengths recommended by the ATLAS and CMS collaborations for the different production and branching ratio. In the case of differential distributions, as a first step, the projections of the uncertainties are estimated by rescaling the statistical uncertainties bin by bin. However, this is a very conservative estimate, because it assumes the background to be flat, while this one is typically larger at lower energies. Therefore, following the CMS analysis on $t\bar{t}H$ production with $H \to \gamma\gamma$ [133] as a template, we have tilted the background accordingly[8]. In the left plot, we show the $\Delta\chi^2$ for single Higgs projections including differential informa-

---

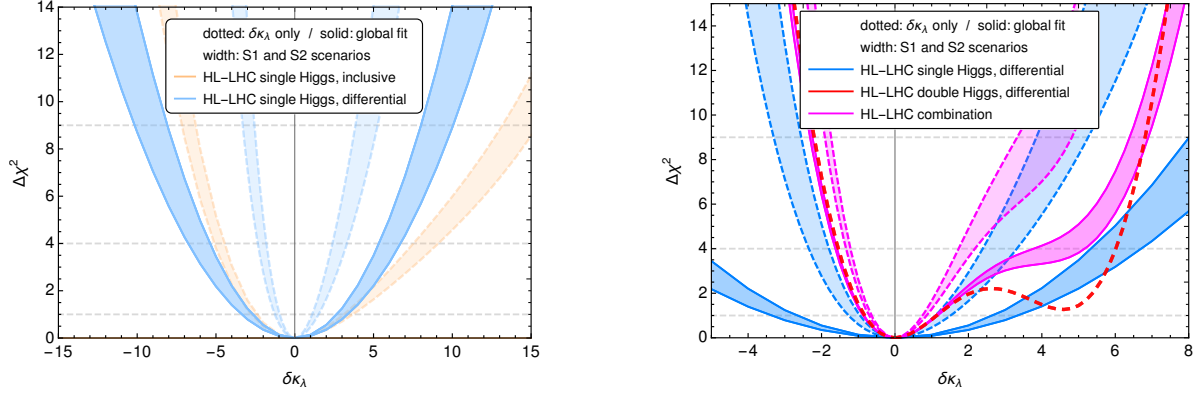[8]With this procedure a good agreement with the CMS analysis is found, for this channel only. As a simple guess, we

Figure 2.10: HL-LHC at 13 TeV and $3\,\text{ab}^{-1}$. Left: Single Higgs with only inclusive measurements (orange) and including differential information (blue) with only κ_λ (pale colour) or marginalising over the nine EFT coefficients (strong colour). Right: Constraints from differential single Higgs (blue), differential double Higgs (dashed red) and their combination (pink).

tion (blue), both assuming only $\delta\kappa$ effects (pale colour between dotted lines) and profiling over the other nine parameters (strong colour between solid lines). Since the lines are not very separated, we can understand that constraints are mostly dominated by statistics. In the case of orange bands, we do not include the differential information and we show only the case in which only $\delta\kappa_\lambda$ effects are present. As can we see form Fig. 2.10, including the nine EFT parameters, the constraints on the trilinear coupling are weaker due to correlations. The strongest effects are due to the correlations between δy_t and c_{gg}, and also between δy_b and δc_z. On the other hand, the differential information partially removes flat directions. In the right plot we compare and combine the constraints, including differential observables (blue), with those achievable via double Higgs production, according to Ref. [108] (red). Their combination is depicted in pink. Allowing non-negligible effects from all the nine EFT parameters, double Higgs is leading to much stronger constraints. Nevertheless, single Higgs data are expected to be relevant and help in lifting the degenerate minima around $\delta\kappa_\lambda \sim 5$.

In conclusion, the indirect bounds on the Higgs self-coupling arising from single Higgs production are competitive to those obtained from double Higgs measurements in the case of exclusive κ_λ variations, and while they become weaker in a fit that includes all the relevant EFT operators, they can still help to improve the bounds obtained from double Higgs production if differential information is included. At the LHC both direct and indirect constraints on κ_λ have been independently derived, mostly by considering only κ_λ variations. In some cases also a restricted set of additional operators was considered, though still not including potentially large effects from others (e.g. simultaneous κ_λ-δy_t fits without including c_{gg}, which can produce effects of a similar size as δy_t in gluon fusion). The natural step forward is the simultaneous fit of both direct and indirect constraints, and the gradual inclusion of the relevant EFT operators in the analysis, which becomes even more important as the experimental sensitivity increases.

2.4 EFT shape benchmarks

A. Carvalho, F. Goertz

The differential distributions for the non-resonant HH signal depend critically on the Higgs boson anomalous couplings to the SM particles. This happens in all the di-Higgs production modes, however due the quantity of possible free parameters and a cancellation between some of the diagrams

use it for the rest of the uncertainties

contributing to the process, the effect is stronger in the ggF production mode, the dominant production process of Higgs boson pairs in the most reasonable parts of the EFT parameter space. The dependence of the signal on m_{HH} can vary as much as being localized around m_{HH} = 250 GeV, to contain dips around m_{HH} = 400 GeV and/or to contain a non-negligible tail of events that could extend up to 800 GeV or even beyond 1 TeV, when Higgs anomalous couplings are allowed to vary on a theoretically reasonable range (see for instance Fig. 2.3).

In order to construct an analysis aiming to find new physics effects, it is very useful to have a finite set of benchmarks that cover the most typical kinematic scenarios for the signal, especially if we expect a small signal rate on top of a sizeable background. On the experimental side, benchmarks are used for very practical reasons: they define a finite number of simulations to be done with optimal coverage of signal possibilities; those simulations are primary used to check the sanity of the data analysis on different phase space regions, and eventually for specific selections, optimization and/or design of subcategories. In a scenario where small variations of continuous parameters lead to non-negligible changes on signal shapes, it is not obvious how to construct a finite set of benchmarks that would be comprehensive on most of the possible signal shapes based solely on theoretical principles. To maximize the potential of an early LHC discovery to anomalous di-Higgs production, it seems natural to define the benchmarks based on kinematic features. As by construction only kinematic features are used to define the benchmark points, those are referred as *shape benchmarks* [178].

To define the shape benchmarks, a Monte Carlo is used to simulate the possible signal shapes on a large portion of the theory parameter space. At LO in ggF, the di-Higgs system can be fully described with two kinematic variables: m_{HH} and the angle between one of the bosons and the beam pipe measured in the di-Higgs center of mass reference frame ($\cos\theta^*$). A large Monte Carlo sampling (1507 samples) populating the parameter space of Higgs anomalous couplings with a range of variations slightly larger than the reasonable theory and experimental limits, provided a rich sampling of possible distributions on the ($m_{HH}, \cos\theta^*$) plane. The parameters used for this scan are the ones described in Eq. (2.19). In the scan c_{hhh} is allowed to vary between -15 and 15, c_t between 0.5 and 2.5, while c_{ggh} and $2c_{gghh}$ range between -1 and 1 and c_{tt} between -3 and 3. A more detailed description of the input grid can be found in Ref. [178] (note the different normalization of the EFT parameters).

A statistical Two-Sample test (TS-test) based on binned distributions on the m_{HH} and $\cos\theta^*$ variables is then used as an order parameter to group the large input sample on a smaller set of clusters, such that on each of these clusters the members are the most similar between themselves. The shape benchmark is defined as the element most similar to all the other samples of the cluster (according to the TS-test). The final number of clusters, N_{clus}, and therefore the number of shape benchmarks, was chosen such that a reasonable trade-off between homogeneity and numerousness of the clusters is achieved. To this end, the value N_{clus} = 12 was found to be optimal: one cluster less would result on a too heterogeneous cluster, while one more would define a redundant subset of shape benchmarks. The values of the EFT coefficients for each of the benchmarks are listed in Table 2.2, and the m_{HH} distribution for each of the clusters (and benchmarks) is presented in Fig. 2.11.

A large variability in the kinematic topologies is related to the local minima of the total cross sections (where the largest cancellations among the different contributions occur). As a result of this connection, the points in a given cluster are usually distributed in a couple of simply connected regions of couplings (see Figs. 7-9 in Ref. [178]), demonstrating the robustness of the method on consistently separating regions of the theory parameter space. The same strategy can be applied to the other di-Higgs processes, as for example VBF, considering that more kinematic variables are

Benchmark	c_{hhh}	c_t	c_{tt}	c_{ggh}	c_{gghh}
1	7.5	1.0	-1.0	0.0	0.0
2	1.0	1.0	0.5	$-\frac{1.6}{3}$	-0.2
3	1.0	1.0	-1.5	0.0	$\frac{0.8}{3}$
4	-3.5	1.5	-3.0	0.0	0.0
5	1.0	1.0	0.0	$\frac{1.6}{3}$	$\frac{1.0}{3}$
6	2.4	1.0	0.0	$\frac{0.4}{3}$	$\frac{0.2}{3}$
7	5.0	1.0	0.0	$\frac{0.4}{3}$	$\frac{0.2}{3}$
8	15.0	1.0	0.0	$-\frac{2.0}{3}$	$-\frac{1.0}{3}$
9	1.0	1.0	1.0	-0.4	-0.2
10	10.0	1.5	-1.0	0.0	0.0
11	2.4	1.0	0.0	$\frac{2.0}{3}$	$\frac{1.0}{3}$
12	15.0	1.0	1.0	0.0	0.0
SM	1.0	1.0	0.0	0.0	0.0

Table 2.2: Parameter values of the twelve benchmarks [178]. The SM reference is also shown.

necessary to feed the TS-test, as more variables are necessary to describe the process.

The comparison of the constraints obtained by a given experimental analysis on each of these shape benchmarks can provide a useful insight, since they summarize the typical distortions on the signal distributions, therefore allowing to understand to which portion of the phase space each analysis is more/less sensitive. CMS results interpreted in terms of these shape benchmarks are presented in Sec. 7.1; the observed upper limits on the di-Higgs production cross section can vary up to two orders of magnitude across different shape benchmarks. It is important to highlight, however, that the usage of shape benchmarks and its presence on a set of final results does not substitute the need for other ways of producing and presenting results. If we want to have precise limits on Higgs anomalous couplings, a possible approach is to propose sets of 1D and 2D scans to be directly produced by the collaborations. However, it is not practical to generate large grids only for interpretation purposes. In this sense, to have the MC generated on terms of shape benchmarks can be useful as basis for MC reweighting, as they by construction contain events that populate all parts of the possible phase space [171].

Even with a reweighting method that allows to produce results in several kinds of parameter scans without large computing resources, it is not possible for the experiments to cover with a finite set of scans all the dimensionality of the EFT considering any possible correlation between anomalous couplings of all possible EFT UV completions . The design of a format for the results that allows an easy reinterpretation is imperative for the long-term usage of the huge experimental work that is invested on di-Higgs searches. Some ideas are discussed in Sec. 6. As long as such method is not defined and implemented, an alternative for a first coarse estimation of the effects of anomalous couplings in specific portions of the EFT is to use the TS-test to find which is the shape benchmark that these specific points are more similar to. The limit for this point can be estimated to be equal to the one of the most similar shape benchmark. An exercise of such procedure on the Run 2 $HH \rightarrow b\bar{b}\gamma\gamma$ ATLAS and CMS analyses can be found in Ref. [171]. As the mapping between a new investigated point and the most similar shape benchmark is based only on kinematic information, this technique also allows to estimate the limits beyond the EFT domain, as for example the case of interference with resonances when a localized peak is not obvious.
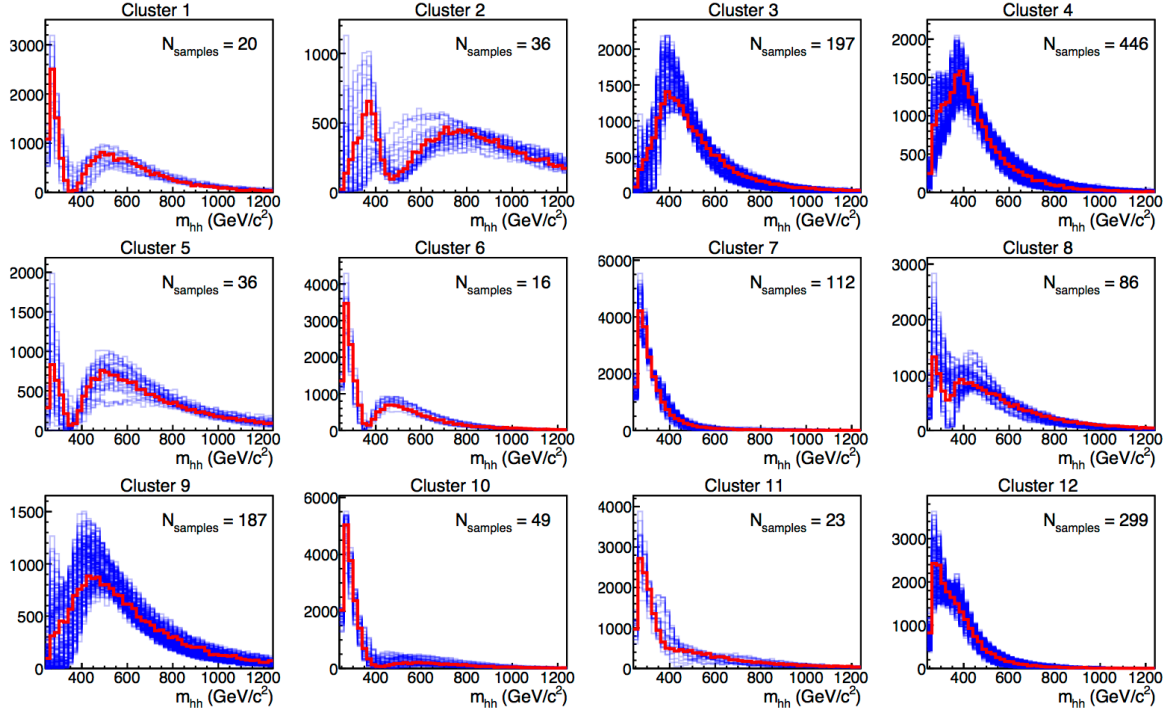
Figure 2.11: Generation-level distributions for the di-Higgs invariant mass m_{HH}. The red lines correspond to the benchmark of each cluster, while the blue lines describe the other members of each cluster [178].

The shape benchmarks were also used to study the typical shape modifications that can occur at NLO level, including the full top-quark mass dependence [69]. While the main qualitative features of the distributions (the position of peaks, dips, and the presence or not of sizeable high mass tails) are mostly unchanged from LO to NLO, it was found that the NLO corrections are important for a correct experimental assessment of the Higgs anomalous couplings, with K-factors that can present large variations across the m_{HH} range, and whose size also depends considerably on the value of the anomalous couplings (see e.g. Fig. 1.9 for the case of c_{hhh}). Based on these results, it is clear that an extension of the shape benchmarks to NLO is desirable. However, having in mind that the main goal of these benchmarks is to provide a first assessment of the sensitivity of a given analysis to shape modifications and their connection to the EFT parameter space, and not to provide a precise description that includes all the richness present in a full EFT scan, their present LO formulation might be sufficiently accurate for their purpose, though NLO studies (in the lines of Ref. [69]) to confirm this statement are in order.

Chapter 3

New Physics in Higgs pair production

Editors: R. Gröber, I. M. Lewis, Z. Liu

While model-independent approaches in effective field theory are usually applicable for heavy new physics, spectacular new physics signatures can show up in Higgs boson pair production in the presence of new degrees of freedom, with masses below the validity range of an effective field theory. Strongly enhanced cross sections for Higgs pair production are typical in the presence of a light new resonance decaying to a Higgs boson pair. This is a common feature of models with extended scalar sectors with sizeable couplings of the new resonance to a pair of Higgs bosons.

The simplest extension providing such a new scalar resonance is the SM augmented with a new scalar that is a singlet under the SM gauge groups, which we discuss in Sec. 3.1. We put a particular emphasis on the interference effects with the background of the box diagrams and the triangle diagram with SM Higgs boson exchange in Sec. 3.2. In Sec. 3.4, we turn to various other models with extended Higgs sectors, the complex two-Higgs doublet model (C2HDM), the singlet extension of the 2HDM, the next-to-minimal supersymmetric extension of the SM (NMSSM) and the Georgi-Machacek model. In the context of these models, we provide benchmarks for resonant production of a SM-like Higgs boson pair and final states with different Higgs bosons. We will shortly comment on spin-2 resonances decaying to a Higgs pair in Sec. 3.3.

The Higgs boson pair production cross section can also be modified by the presence of new colored particles in the gluon-induced loop. Prime examples are scalar particles, as for instance top squarks in supersymmetry [179–181], or new vector-like fermions, as they would appear for instance in Composite Higgs Models [182, 183]. Double Higgs production allows to break the degeneracy present in single Higgs production between a shift in the top Yukawa coupling and new physics in the gluon fusion loop [108, 182, 184]. We will discuss the impact of new particles in the loop in Sec. 3.5.

In Sec. 3.6, we address the impact of a measurement of the Higgs pair production cross section on cosmology. Since in successful models of electroweak baryogenesis a deformed potential with respect to the SM one is required, a measurement of the trilinear Higgs self-coupling has a direct impact on possible explanations of the matter-antimatter asymmetry of the universe. Finally, in Sec. 3.7, we will show that searches for final states with Higgs pairs and missing energy have the potential to uncover a dark sector that could provide a dark matter candidate.

3.1   Spin-0 models

S. Dawson, I. M. Lewis, T. Robens, T. Stefaniak, M. Sullivan

Resonant double Higgs production is one of the most spectacular signatures to look for in Higgs physics. The simplest extension of the SM, the addition of a real gauge singlet scalar [185–189], can result in resonant double Higgs production [189–209]. The most general renormalizable scalar potential can be expressed (using the parametrization of Ref. [194]) in the following way [188, 210]

$$
\begin{aligned}
V(\Phi, S) \quad = \quad & -\mu^2 \Phi^\dagger \Phi + \lambda \left(\Phi^\dagger \Phi\right)^2 + \frac{a_1}{2}\Phi^\dagger \Phi S + \frac{a_2}{2}\Phi^\dagger \Phi S^2 \\
& + b_1 S + \frac{b_2}{2}S^2 + \frac{b_3}{3}S^3 + \frac{b_4}{4}S^4,
\end{aligned}
\tag{3.1}
$$

where $S = (v_S + s)/\sqrt{2}$ is a gauge singlet scalar, $\Phi = \left(0, v + h\right)^{\mathrm{T}}/\sqrt{2}$ is the Higgs doublet, v_S is the S vacuum expectation value (vev), v is the Higgs vev, h is the SM Higgs boson, and s is a new scalar boson. At the renormalizable level, Eq. (3.1) contains all possible interactions between S and the SM particles.[1] After electroweak symmetry breaking, S and h mix, resulting in two mass eigenstates $h_{1,2}$ with masses $m_{1,2}$, where by definition $m_2 \geq m_1$. Here we concentrate on the case that $m_1 = 125\,\mathrm{GeV}$.[2] The $h - s$ mixing angle θ is defined as

$$
\begin{pmatrix} h_1 \\ h_2 \end{pmatrix} = \begin{pmatrix} \cos\theta & \sin\theta \\ -\sin\theta & \cos\theta \end{pmatrix} \begin{pmatrix} h \\ s \end{pmatrix}
\tag{3.2}
$$

Due to this mixing, the couplings of h_1 (h_2) to SM fermions and gauge bosons are universally suppressed by $\cos\theta$ ($\sin\theta$), relative to the SM Higgs couplings. Hence, the production cross section for h_2 is given by the SM Higgs production rate at a mass of m_2 suppressed by $\sin^2\theta$, and the observed Higgs boson h_1 rates are suppressed by $\cos^2\theta$ relative to the SM.

If $m_2 > 2\,m_1$, Eq. (3.1) allows for on-shell $h_2 \to h_1 h_1$ decays. The branching ratios of the decays of the heavy scalar h_2 to a Higgs boson pair, $h_1 h_1$, and to final states with SM particles (collectively denoted by 'SM') are given by

$$
\mathrm{BR}_{h_2 \to h_1 h_1} \quad = \quad \frac{\Gamma_{h_2 \to h_1 h_1}}{\sin^2\theta\,\Gamma_{\mathrm{SM,\,tot}} + \Gamma_{h_2 \to h_1 h_1}}, \ \mathrm{BR}_{h_2 \to \mathrm{SM}} = \frac{\sin^2\theta\,\Gamma_{\mathrm{SM},h_2 \to \mathrm{SM}}}{\sin^2\theta\,\Gamma_{\mathrm{SM,\,tot}} + \Gamma_{h_2 \to h_1 h_1}},
\tag{3.3}
$$

respectively, where $\Gamma_{h_2 \to h_1 h_1}$ is the partial width of the $h_2 \to h_1 h_1$ decay, $\Gamma_{\mathrm{SM},h_2 \to \mathrm{SM}}$ is the partial width of the SM Higgs boson at mass m_2 decaying to a SM particle final state, and $\Gamma_{\mathrm{SM,\,tot}}$ denotes the total width of the SM Higgs boson with mass m_2.[3]

Imposing further symmetries decreases the number of free parameters. For example, a Z_2 symmetry with the transformation properties $S \to -S$, $\Phi \to \Phi$, $\mathrm{SM} \to \mathrm{SM}$ requires that $a_1 = b_1 = b_3 = 0$. If S acquires a vev, $v_S \neq 0$, the Z_2 symmetry becomes softly broken. We will discuss both the non-Z_2 and softly broken Z_2 case below.

---

[1]At dimension-5 in an effective field theory, S can have additional couplings to SM particles [211–213] and has a qualitatively different phenomenology, which we neglect here.

[2]The case $m_2 = 125\,\mathrm{GeV}$ is also viable, see e.g. Refs. [199, 201, 214].

[3]Electroweak higher-order corrections to the $h_2 \to h_1 h_1$ decay width have e.g. been presented in Ref. [200] and can amount to up to 10%. We neglect these effects in the remainder of our discussion.

Constraints

Detailed discussions of experimental and theoretical constraints on the model can be found in Refs. [191, 199, 201, 214]. Here we briefly summarize these constraints, which are obeyed by the benchmark scenarios proposed here, and refer the reader to the literature for more details.

The theoretical constraints that we consider are vacuum stability (both at the low and high scale, $\mu \sim 10^{10}$ GeV), perturbative unitarity, as well as perturbativity of the couplings in the scalar potential (at the low and high scale, $\mu \sim 10^{10}$ GeV). The experimental constraints are the agreement with electroweak precision observables [215], with the observed W boson mass [216–219], $M_W = 80.379 \pm 0.012$ GeV following Ref. [161], with null-results from LHC Higgs searches (using `HiggsBounds`, version 5.4.0beta [220–224]), and with Run-1 and Run-2 Higgs boson rate measurements (using `HiggsSignals`, version 2.2.3beta [225]).[4]

Z_2

In the softly-broken Z_2-symmetric scenario, the scalar sector is described by five parameters after electroweak symmetry breaking, namely, m_1, m_2, v, $\sin\theta$, and $\tan\beta \equiv \frac{v}{v_s}$. Two of these parameters, $v \approx 246$ GeV and $m_1 \approx 125$ GeV, are fixed by experimental measurements, leaving only three free model parameters. The analytic expression for the partial decay width for $h_2 \to h_1 h_1$ at leading order can be found in Refs. [186, 189, 199, 201]. Note that the specific choice of $\tan\beta = \cot\theta$ leads to $\Gamma_{h_2 \to h_1 h_1} = 0$.

Given the constraints in Sec. 3.1, Table 3.1 lists the allowed values of $\sin\theta$ and $\mathrm{BR}_{h_2 \to h_1 h_1}$ for scenarios with $m_2 \geq 2m_1$. The maximal allowed signal rate (i.e. production cross section times branching ratio) for $pp \to h_2 \to h_1 h_1$ at the 13 TeV LHC is shown in Fig. 3.1, in direct comparison with the current strongest upper cross section limit from the CMS combination of $h_2 \to h_1 h_1$ searches [67].[5] Both Table 3.1 and Fig. 3.1 present maximal $\mathrm{BR}_{h_2 \to h_1 h_1}$ values after applying all constraints, as well as after applying EW-scale constraints only. The latter includes tests of vacuum stability and perturbativity at the EW-scale, but does not require perturbitivity and vacuum stability at a higher scale $\mu \sim 10^{10}$ GeV.

Non-Z_2

In the non-Z_2 limit, all parameters in Eq. (3.1) are allowed. Since there is no symmetry associated with the scalar S, its vev is non-physical and we are allowed to set it to zero: $v_S = 0$ [194, 205]. There are now five physical parameters: the Higgs doublet vev $v = 246$ GeV, the scalar singlet vev $v_S = 0$, the observed Higgs boson mass $m_1 = 125$ GeV, the heavy scalar mass m_2 assumed to be $m_2 > 2m_1$, and the $h - s$ mixing angle θ. Hence, 5 of the potential parameters $\mu^2, b_1, a_1, b_2, \lambda$ can be solved for [194, 205]:

$$\mu^2 = \lambda v^2, \quad b_1 = -\frac{v^2}{4} a_1, \quad a_1 = \sqrt{2} \frac{m_1^2 - m_2^2}{v} \sin 2\theta$$

$$b_2 = 2 m_1^2 \sin^2\theta + 2 m_2^2 \cos^2\theta - \frac{a_2}{2} v^2, \quad \lambda = \frac{m_1^2 \cos^2\theta + m_2^2 \sin^2\theta}{2 v^2}. \tag{3.4}$$

---

[4]With respect to the most recent literature [214], this work contains updated LHC Higgs search limits, in particular for $h_2 \to h_1 h_1$ signatures [67, 150, 226, 227], updated Higgs boson signal rate measurements from LHC Run 2, as well as an updated W boson mass value.

[5]We rescaled the NNLO+NNLL gluon fusion cross section of the SM Higgs boson [19] by $\sin^2\theta$.

m_2 [GeV]	$|\sin\theta|_{\max}$	$\mathrm{BR}_{\min}^{h_2 \to h_1 h_1}$	$\mathrm{BR}_{\max}^{h_2 \to h_1 h_1}$ (*all constraints*)	$\mathrm{BR}_{\max}^{h_2 \to h_1 h_1}$ (*EW-scale constraints*)
255	0.22	0.13	0.26	0.47
260	0.22	0.17	0.32	0.54
265	0.22	0.20	0.35	0.57
280	0.22	0.23	0.39	0.60
290	0.22	0.24	0.40	0.61
305	0.22	0.25	0.40	0.60
325	0.22	0.26	0.40	0.58
345	0.22	0.26	0.39	0.56
365	0.22	0.24	0.36	0.53
395	0.20	0.23	0.33	0.49
430	0.20	0.23	0.30	0.45
470	0.22	0.21	0.28	0.42
520	0.21	0.21	0.27	0.39
590	0.20	0.22	0.26	0.36
665	0.21	0.21	0.26	0.35
770	0.20	0.22	0.25	0.33
875	0.19	0.22	0.25	0.31
920	0.18	0.23	0.25	0.31
975	0.17	0.23	0.25	0.31
1000	0.16	0.23	0.25	0.31

Table 3.1: Maximal and minimal allowed branching ratios of the decay $h_2 \to h_1 h_1$, evaluated at the maximal allowed value of $|\sin\theta|$. Note that minimal values for the BR($h_2 \to h_1 h_1$) stem from $\sin\theta \geq 0$. For the maximal BR($h_2 \to h_1 h_1$) we give the values obtained after applying all constraints as well as after applying only EW-scale constraints, i.e. requiring perturbative couplings and vacuum stability at the EW scale but not up to a high scale $\mu \sim 10^{10}$ GeV. The numbers supersede those presented in Table V of Ref. [201].

This leaves the additional potential parameters a_2, b_3, b_4 free. The free parameters of the model are then:

$$m_1 = 125 \text{ GeV}, m_2, v = 246 \text{ GeV}, v_S = 0, \theta, a_2, b_3, b_4. \tag{3.5}$$

This situation differs from the Z_2 limit, where all potential parameters can be solved for in terms of masses, vevs, and the mixing angle. This additonal freedom leads to a more complex vacuum structure. Indeed, with the additional freedom in the non-Z_2 model, there are six potential extrema of the potential in Eq. (3.1) with Higgs vevs that are not 246 GeV. The new scalar is a gauge singlet and its vev cannot contribute to the W and Z masses. Hence, to get the observed electroweak symmetry breaking pattern, we demand that $(v, v_S) = (246 \text{ GeV}, 0)$ is the global minimum. This puts stringent constraints on the potential parameters a_2 and b_3 which contribute to the $h_2 - h_1 - h_1$ coupling relevant for $h_2 \to h_1 h_1$ decays:

$$\begin{aligned} V(h_1, h_2) &\supset \frac{\lambda_{211}}{2} h_2 h_1^2 \\ \lambda_{211} &= \frac{b_3}{\sqrt{2}} \sin^2\theta \cos\theta + \frac{a_1}{2\sqrt{2}} \cos\theta \left(\cos^2\theta - 2\sin^2\theta \right) \\ &\quad + \frac{a_2}{2} v \sin\theta \left(2\cos^2\theta - \sin^2\theta \right) - 6\lambda v \sin\theta \cos^2\theta. \end{aligned} \tag{3.6}$$
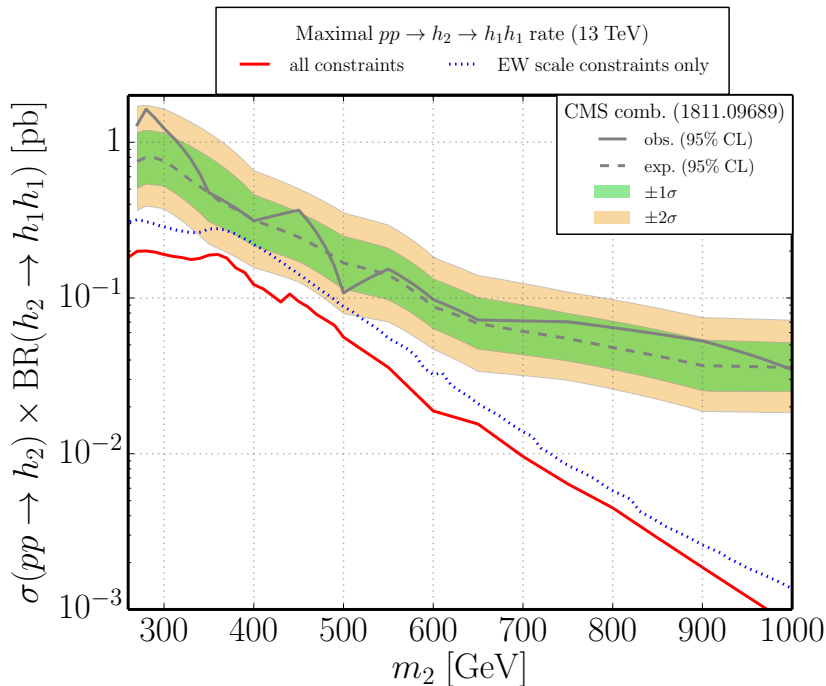
Figure 3.1: Maximal allowed $pp \to h_2 \to h_1 h_1$ signal rate at the 13 TeV LHC in the softly-broken Z_2-symmetric case. Shown are values after applying (red solid) all constraints and (blue dotted) only constraints at the EW scale. The corresponding $\mathrm{BR}_{\mathrm{max}}^{h_2 \to h_1 h_1}$ values are given in Table 3.1. For comparison we include the current strongest cross section limit (at 95% CL), obtained from the combination of various CMS $h_2 \to h_1 h_1$ searches at 13 TeV with up to 36 fb^{-1} of data [67].

This limits how large the $h_2 \to h_1 h_1$ branching ratios and $pp \to h_1 h_1$ production cross section can be [194, 205].

In Fig. 3.2 we show the largest $h_2 \to h_1 h_1$ branching ratios (left) and $pp \to h_1 h_1$ production cross sections (right) allowed under the constraint the the global minimum correctly breaks electroweak symmetry [205]. The S^4 potential parameter b_4 is set to the upper limit consistent with perturbative unitarity [194, 205]. The lines $\sin \theta_{\mathrm{max}}$ correspond to the maximal allowed mixing angle from Higgs precision measurements and W mass measurements: $|\sin \theta| \lesssim 0.22$ for $250 \text{ GeV} \lesssim m_2 \lesssim 622 \text{ GeV}$ and $|\sin \theta| \lesssim 0.21$ for $m_2 \gtrsim 622 \text{ GeV}$. We do not take into account perturbative limits from RGE running up to a scale of $\sim 4 \times 10^{10}$ GeV. The mixing angle, and hence h_2 production rate, for $\sin^2 \theta = 0.01$ is smaller than any mixing angle considered in Fig. 3.1. Hence, even though $\mathrm{BR}(h_2 \to h_1 h_1)$ is largest for $\sin^2 \theta = 0.01$, it is still allowed due to the suppressed production rates of h_2. Even with these constraints, the $h_2 \to h_1 h_1$ branching ratio can be above 80%, and the $pp \to h_1 h_1$ production rate can be one order of magnitude larger than the SM prediction.

3.2 Interference Effects

It has been noted recently that the gluon-induced production of Higgs boson pairs via a heavy scalar resonance often has large and non-trivial interference effects with the continuum SM Higgs pair production process, which can be considered in this case a background to the resonant BSM signal. Furthermore, in realistic models, the interfering non-resonant processes are often modified as well with respect to the SM amplitude due to modifications to the Higgs couplings. In this section, we examine these subtle interference effects. First, we discuss the interference effects of the
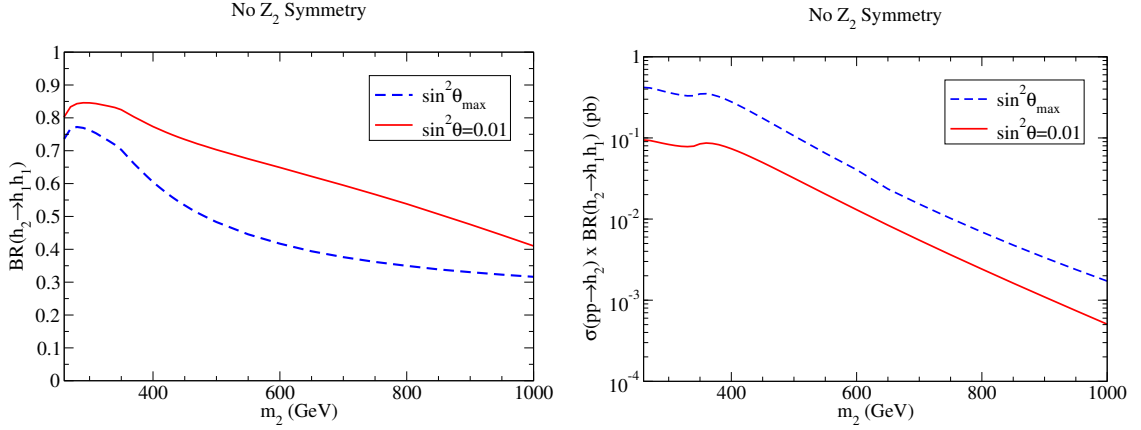
Figure 3.2: Maximum (left) branching ratios for $h_2 \rightarrow h_1 h_1$ and (right) resonant double Higgs production normalized to the SM rate in the non-Z_2 singlet model for various $h-s$ mixing angles [205].

underlying scalar resonance. Second, we show the importance of the on-shell interference effect driven by the dynamical phase generated by the loop diagrams. At the end of this section, a general parametrization of the effective interactions and a general picture of the overall interference effects are shown.

3.2.1 Off-shell Interference

I. M. Lewis

In the narrow-width approximation (NWA), it is usually assumed that the interference effects near a resonance scale as Γ/M, where Γ is the width of the resonance and M its mass. In the limit $\Gamma/M \ll 1$, these effects are negligible. Indeed, in the narrow width approximation only the resonance makes an important contribution to the process (see the next section for when these arguments fail). However, away from the resonance peak interference effects can be sizeable. This is especially true for the Higgs boson and other scalars, where there are non-decoupling effects due to couplings being proportional to masses. To illustrate this, we consider the Z_2 symmetric singlet model introduced in Sec. 3.1.

The di-Higgs invariant mass ($m_{h_1 h_1}$) distributions for $pp \rightarrow h_1 h_1$ and various heavy scalar masses are shown on the left of Fig. 3.3. We can observe that, if $m_{h_1 h_1} \ll m_2$, the invariant mass becomes independent of the resonance mass. There are three contributions to $gg \rightarrow h_1 h_1$: a top quark triangle with s-channel h_1, a top quark triangle with s-channel h_2, and a top quark box diagram. The box diagram is independent of h_2, although there is a uniform suppression from the scalar coupling, as discussed in Sec. 3.1. However, both s-channel diagrams depend on the trilinear scalar couplings which are altered from SM predictions.

The trilinear scalar couplings are defined in the scalar potential as

$$V(h_1, h_2) \supset \frac{\lambda_{111}}{3!} h_1^3 + \frac{\lambda_{112}}{2} h_1 h_2^2, \tag{3.7}$$

and in the Z_2 singlet extension of the SM they are

$$\lambda_{111} = \frac{3 m_1^2}{v} \left(\cos^3\theta + \tan\beta \sin^3\theta \right),$$

$$\lambda_{112} = -\frac{m_2^2}{2v} \sin 2\theta \left(\cos\theta - \tan\beta \sin\theta \right) \left(1 + \frac{2 m_1^2}{m_2^2} \right). \tag{3.8}$$
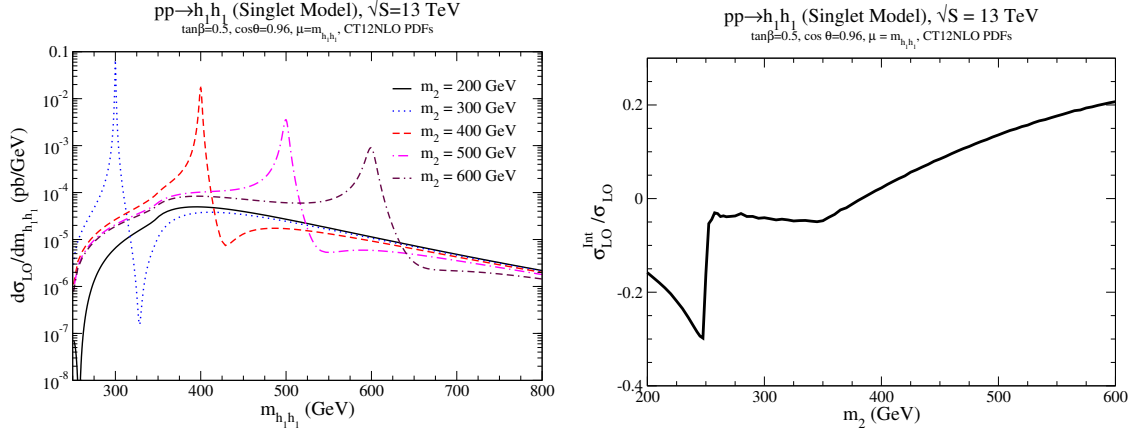
Figure 3.3: Left: Invariant mass distributions of di-Higgs final state in the Z_2 symmetric singlet model for various singlet masses. Right: Fractional contribution of the interference of h_2 s-channel contribution with h_1 s-channel and box diagram contributions Ref. [196].

The s-channel contribution to the leading order amplitude is then

$$F_1^{\text{tri}} = m_{h_1 h_1}^2 \left(\frac{\lambda_{111}\, v \cos\theta}{m_{h_1 h_1}^2 - m_1^2 + i\, m_1\, \Gamma_{h_1}} - \frac{\lambda_{112}\, v \sin\theta}{m_{h_1 h_1}^2 - m_2^2 + i\, m_2\, \Gamma_{h_2}} \right) F_\Delta, \qquad (3.9)$$

where Γ_{h_j} is the total width of h_j, s is the center or momentum energy squared, and F_Δ is a form factor for the triangle top loop [20, 21] normalized according to Ref. [196]. In the limit $m_1, m_{h_1 h_1} \ll m_2$, Eq. (3.9) becomes

$$F_1^{\text{tri}} \xrightarrow[m_1, m_{h_1 h_1} \ll m_2]{} \quad m_{h_1 h_1}^2 \left(\frac{3\, m_1^2 \left(\cos^3\theta + \tan\beta \sin^3\theta \right) \cos\theta}{m_{h_1 h_1}^2 - m_1^2 + i\, m_1\, \Gamma_{h_1}} \right.$$

$$\left. - \frac{1}{2} \sin 2\theta \sin\theta \left(\cos\theta - \tan\beta \sin\theta \right) \right) F_\Delta. \qquad (3.10)$$

Hence, the amplitude has no explicit dependence on m_2 and the distribution is independent of m_2 for $s \ll m_2^2$ as shown in the left of Fig. 3.3 [196].

Since the di-Higgs invariant mass distribution is independent of m_2, the interference between the s-channel h_2 resonance and other contributions are independent of h_2 for $m_1, m_{h_1 h_1} \ll m_2$. As m_2 increases, the area of of the distribution satisfying $m_{h_1 h_1} \ll m_2$ increases. Hence, the size of the interference between the h_2 resonance and other contributions becomes increasingly large [196]. To illustrate this effect, the fractional contribution of the interference of the h_2 s-channel with h_1 s-channel and box diagram contributions is shown on the right hand side of Fig. 3.3. The leading order interference cross section is labeled as $\sigma_{\text{LO}}^{\text{Int}}$ while the total cross section with all contributions is labeled as σ_{LO}. As can be seen, the interference can contribute upwards of 20% to the total cross section for $m_2 \sim 600$ GeV and the interference contribution increases as m_2 increases.

It should be noted this is effect is due to the $h_1 - h_2 - h_2$ couplings being proportional to the h_2 mass squared. The mass dependence of the coupling then cancels the mass dependence in the propagator. Since the Higgs is at the very least a major contributor to fundamental mass, this effect is relatively generic and interference effects are important in Higgs physics.[6]

---

[6]Interference effects between scalar contributions to $gg \to VV$, where $V = W^\pm, Z$, and continuum SM contributions can also be important [228–230].

3.2.2   On-shell Interference

M. Carena, Z. Liu, M. Riembau

In the case of a singlet resonance, constraints from SM precision measurements make these searches more challenging. From one side, precision measurements imply that the singlet-doublet mixing parameter is constrained to be small over a large region of parameter space. From the other side, the singlet only couples to SM particles through mixing with the SM Higgs doublet. This results in a reduced di-Higgs production via singlet resonance decays. In particular, the singlet resonance amplitude becomes of the same order as the SM triangle and box diagram amplitudes. Most important, in this work we show that a large relative phase between the SM box diagram and the singlet triangle diagram becomes important. This special on-shell interference effect has important phenomenological implications.

We will consider the simplest extension of the SM that can assist the scalar potential to induce a strongly first-order electroweak phase transition, consisting of an additional real scalar singlet with a Z_2 symmetry. Detailed relations between the bare parameters and physical parameters can be found in Ref. [209].

The on-shell interference effect may enhance or suppress the conventional Breit-Wigner resonance production. Examples in Higgs physics known in the literature, such as $gg \to h \to \gamma\gamma$ [231] and $gg \to H \to t\bar{t}$ [232], are both destructive. We discuss in detail in this section the on-shell interference effect between the resonant singlet amplitude and the SM di-Higgs box diagram. We show that in the singlet extension of the SM considered in this paper, the on-shell interference effect is generically constructive and could be large in magnitude, thus enhances the signal production rate.

The interference effect between two generic amplitudes can be denoted as nonresonant amplitude A_{nr} and resonant amplitude A_{res}. The resonant amplitude A_{res}, defined as

$$A_{res} = a_{res} \frac{\hat{s}}{\hat{s} - m^2 + i\Gamma m},$$

(3.11)

has a pole in the region of interest and we parametrize it as the product of a fast varying piece containing its propagator and a slowly varying piece a_{res} that generically is a product of couplings and loop-functions. The general interference effect can then be parametrized as [231, 232],

$$
\begin{aligned}
|\mathcal{M}|^2_{int} &= 2\mathrm{Re}(A_{res} \times A^*_{nr}) = 2\left(\mathcal{I}_{int} + \mathcal{R}_{int}\right), \\
\mathcal{R}_{int} &\equiv |A_{nr}||a_{res}| \frac{\hat{s}(\hat{s} - m^2)}{(\hat{s} - m^2)^2 + \Gamma^2 m^2} \cos(\delta_{res} - \delta_{nr}) \\
\mathcal{I}_{int} &\equiv |A_{nr}||a_{res}| \frac{\hat{s}\Gamma m}{(\hat{s} - m^2)^2 + \Gamma^2 m^2} \sin(\delta_{res} - \delta_{nr}),
\end{aligned}
$$

(3.12)

where δ_{res} and δ_{nr} denote the complex phases of a_{res} and A_{nr}, respectively.

The special interference effect $\mathcal{I}_{int}$ only appears between the singlet resonant diagram and the SM box diagram. This interference effect is proportional to the relative phase between the loop functions $\sin(\delta_{\triangleright} - \delta_{\square})$ and the imaginary part of the scalar propagator which is sizable near the scalar mass pole.

In Fig. 3.4 we display the differential cross section as a function of the Higgs pair invariant mass for a benchmark point with a heavy scalar mass of 900 GeV, mixing angle $\sin\theta = 0.3$ and $\tan\beta = 10$. The differential cross section is shown in linear scale for a broad range of di-Higgs invariant masses, including the low invariant mass regime favored by parton distribution functions at hadron colliders.
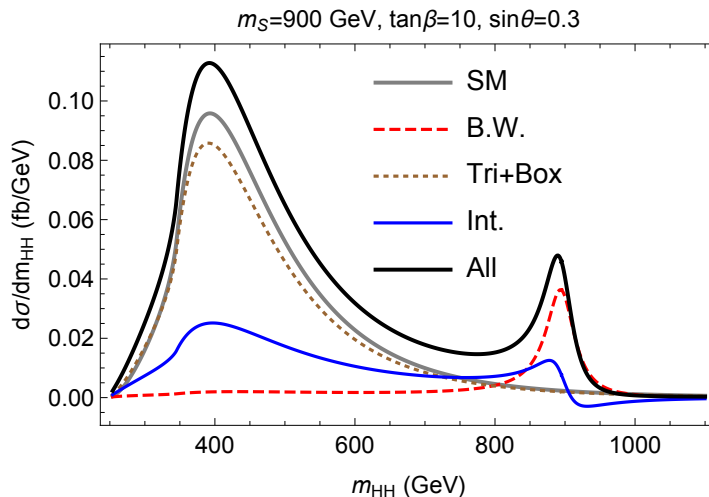
Figure 3.4: The differential di-Higgs distribution for a benchmark point of the singlet extension of the SM shown in linear scale and over a broad range of the di-Higgs invariant mass. The full results for the SM and the singlet SM extension are shown by the gray and black curves, respectively. In the singlet extension of the SM, the contributions from the resonant singlet diagram, the nonresonant diagram and the interference between them are shown in red (dashed), brown (dotted) and blue curves, respectively [209].

This particular choice for the benchmark shows well the separation of the scalar resonance peak and the threshold enhancement peak above the $t\bar{t}$-threshold. The SM Higgs pair invariant mass distribution is given by the gray curve while the black curve depicts the di-Higgs invariant mass distribution from the singlet extension of the SM. It is informative to present all three pieces that contribute to the full result of the di-Higgs production, namely (i) the resonance contribution (red, dashed curve), (ii) the SM nonresonance contribution (box and triangle diagrams given by the brown, dotted curve), and (iii) the interference between them (blue curve). Note that the small difference between the "Tri+Box" and the "SM" line shapes is caused by the doublet-singlet scalar mixing, which leads to a $\cos\theta$ suppression of the SM-like Higgs coupling to top quarks as well as a modified SM-like Higgs trilinear coupling λ_{HHH}. We observe that the full results show an important enhancement in the di-Higgs production across a large range of invariant masses. This behavior is anticipated from the decomposition analysis in the previous section. There is a clear net effect from the interference curve shown in blue. Close to the the scalar mass pole at 900 GeV, the on-shell interference effect enhances the Breit-Wigner resonances peak (red, dashed curve) by about 25%. Off-the resonance peak, and especially at the threshold peak, the interference term (blue curve) enhances the cross section quite sizably as well. Hence, a combined differential analysis in the Higgs pair invariant mass is crucial in probing the singlet extension of the SM.

The interference pattern between the resonant heavy scalar contribution and the SM nonresonant triangle and box contributions show interesting features. We highlight the constructive on-shell interference effect that uniquely arises between the heavy scalar resonance diagram and the SM box diagram, due to a large relative phase between the loop functions involved. We observe that the on-shell interference effect can be as large as 40% of the Breit-Wigner resonance contribution and enhances notably the total signal strength, making it necessary taking into account in heavy singlet searches. Detailed parametric dependence of the on-shell interference on the model parameters can be found in Ref. [209].

3.2.3   Overall Interference

E. Bagnaschi, A. Carvalho, R. Gröber, S. Liebler, J. Quevillon

The search for a heavy Higgs boson resonance in the di-Higgs final states is accompanied by interferences between the resonant signal and the di-Higgs continuum background, where the latter includes the SM-like Higgs boson s-channel contribution. In this section we summarize a model-independent study on such interference effects, see also Ref. [233].

We introduce an effective coupling of the heavy Higgs boson H to gluons,

$$\mathscr{L} \supset \frac{\alpha_s}{12\pi v}\, c_H\, H\, G^a_{\mu\nu} G^{a,\mu\nu}. \tag{3.13}$$

The Wilson coefficient c_H can in general be complex number, parameterized as

$$c_H = |c_H| e^{i\theta_H}. \tag{3.14}$$

This effective interaction accounts for particles P coupling the new Higgs boson H to gluons, for which the threshold $2m_P$ of the corresponding loop can be either lighter or heavier than the Higgs boson mass m_H; in the former case the effective loop-induced coupling becomes complex. Note that while formally the description through an effective operator is not valid for $2m_P \lesssim m_H$, we do not restrict ourselves to a specific model and can hence condense the amplitude to the given form. However, we assume the Wilson coefficient and its phase to be constant, whereas for a concrete model realization the loop-induced coupling can inherit a dependence on the final-state invariant mass m_{hh}, where h denotes the SM-like Higgs boson. This is particularly true for large width Γ_H and in the vicinity of the threshold region $m_{hh} \sim 2m_P$.

In addition to c_H, we also choose the mass of H, the width Γ_H and the trilinear Higgs-boson self-coupling of the SM-like Higgs boson λ_{hhh} (normalised to its SM value) as free input parameters. Any effect in the Higgs-boson self-coupling λ_{Hhh} can be absorbed into c_H, which is why we keep λ_{Hhh} fixed. In summary, we vary the following parameters freely

$$|c_H|,\ \theta_H,\ \Gamma_H,\ m_H,\ \lambda_{hhh}. \tag{3.15}$$

For our analysis we use the code HPAIR [234], which incorporates the s-channel resonance by a Breit-Wigner propagator of the heavy Higgs boson H

$$\frac{1}{m_{hh}^2 - m_H^2 + i m_H \Gamma_H}, \tag{3.16}$$

with m_{hh} again denoting the invariant mass of the Higgs-boson pair. In order to classify the interferences we split the differential cross section in three contributions

$$\frac{d\sigma}{dm_{hh}} = \frac{d\sigma_S}{dm_{hh}} + \frac{d\sigma_I}{dm_{hh}} + \frac{d\sigma_B}{dm_{hh}}. \tag{3.17}$$

The signal cross section σ_S contains the s-channel exchange of a heavy Higgs boson $gg \to H \to hh$ only, while the background cross section σ_B contains all non-resonant diagrams with final state hh, namely the triangle and box diagrams equivalent to the ones of the SM process. The interference cross section σ_I is proportional to $2\mathrm{Re}(A_S A_B^*)$, where A_S denotes the signal amplitude and A_B the background amplitude.
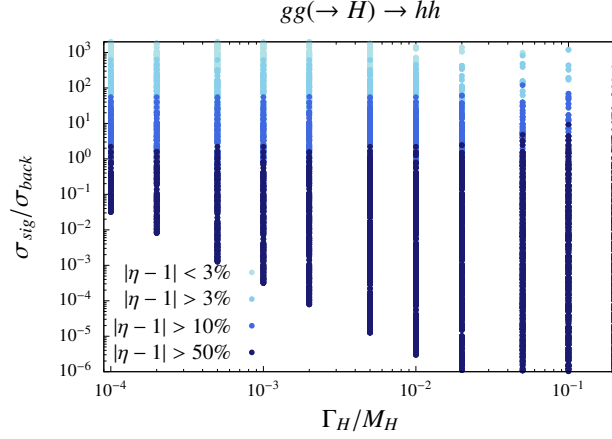
Figure 3.5: Relative difference (in percentage) of the interference factor η from 1 in the $(\Gamma_H/m_H, \sigma_{sig}/\sigma_{back})$ plane. The scan was performed as indicated in the main text [233].

As a measure of the interference effects we introduce the following parameters

$$
\eta = \int_{m_H-10\Gamma_H}^{m_H+10\Gamma_H} dm_{hh} \left(\frac{d\sigma_S}{dm_{hh}} + \frac{d\sigma_I}{dm_{hh}} \right) \Bigg/ \int_{m_H-10\Gamma_H}^{m_H+10\Gamma_H} dm_{hh} \left(\frac{d\sigma_S}{dm_{hh}} \right),
$$

$$
\eta_- = \int_{m_H-10\Gamma_H}^{m_{hh}^I} dm_{hh} \left(\frac{d\sigma_S}{dm_{hh}} + \frac{d\sigma_I}{dm_{hh}} \right) \Bigg/ \int_{m_H-10\Gamma_H}^{m_{hh}^I} dm_{hh} \left(\frac{d\sigma_S}{dm_{hh}} \right),
$$

$$
\eta_+ = \int_{m_{hh}^I}^{m_H+10\Gamma_H} dm_{hh} \left(\frac{d\sigma_S}{dm_{hh}} + \frac{d\sigma_I}{dm_{hh}} \right) \Bigg/ \int_{m_{hh}^I}^{m_H+10\Gamma_H} dm_{hh} \left(\frac{d\sigma_S}{dm_{hh}} \right). \tag{3.18}
$$

The first parameter η yields, if multiplied with the signal cross section, the overall change of the signal cross section due to the interference effects. Instead η_+ and η_- measure the interference effects if the peak structure is distorted. For instance, typically there could be a peak-dip structure. In this case the two curves $d\sigma_S/dm_{hh}$ and $d(\sigma_S+\sigma_I)/dm_{hh}$ intersect in m_{hh}^I and we can define η_+ and η_- as the measures of the peak distortion. The boundaries in the definition of the η's, $m_H \pm 10\Gamma_H$, capture the majority of the peak structure. We refrain from using very large widths or an even larger boundary of the integration, since (i) the crossing of the top threshold for the background diagrams at $m_{hh} \sim 2m_t$ would require a more thorough analysis of the background effects for this peculiar case, and (ii) we choose the Wilson coefficient to be constant.

For the scan over the parameter space we consider

$$
|c_H| \in [0.001, 5], \quad \theta_H \in \{0, \frac{\pi}{4}, \frac{\pi}{2}\}, \quad m_H \in [0.3, 1.4]\,\text{TeV}, \quad \Gamma_H/m_H \in [10^{-4}, 0.2]. \tag{3.19}
$$

For the trilinear Higgs-boson self-coupling we use the values $\lambda_{hhh} \in (0, 1, 2)\lambda_{hhh}^{SM}$ while keeping $\lambda_{Hhh} = \lambda_{hhh}^{SM}$. In Fig. 3.5 we show the dependence of our measure η on Γ_H/m_H and $\sigma_{sig}/\sigma_{back}$. The latter ratio is defined through

$$
\sigma_{sig} = \int_{m_H-10\Gamma_H}^{m_H+10\Gamma_H} dm_{hh} \frac{d\sigma_S}{dm_{hh}} \quad \text{and} \quad \sigma_{back} = \int_{m_H-10\Gamma_H}^{m_H+10\Gamma_H} dm_{hh} \frac{d\sigma_B}{dm_{hh}}. \tag{3.20}
$$

The different colors in the figure indicate if η differs from 1 by less than 3%, between 3–10%, between 10–50% or by more than 50%. It turns out that the interference effects mostly depend on the size of the ratio of the signal over background cross section. Instead the interference shows little
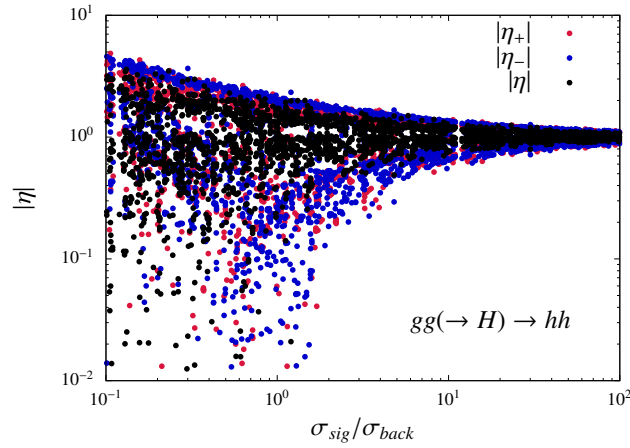
Figure 3.6: Interference factors η, η_+ and η_- as a function of $\sigma_{sig}/\sigma_{back}$ for $gg \to H \to hh$ [233].

dependence on the width of the heavy Higgs boson, Γ_H, as long as we consider masses $m_H > 2m_t$, i.e. the region in which the background process develops an imaginary part. Though, the largest values in η are obtained for large width only. In order to emphasize the dependence on $\sigma_{sig}/\sigma_{back}$ we show η (black points), η_+ (red points) and η_- (blue points) over $\sigma_{sig}/\sigma_{back}$ in Fig. 3.6. We see that for $\sigma_{sig}/\sigma_{back} \approx 10$ the interference effects can already increase the cross section by a factor of 1.5, and therefore should be definitely taken into account in order to obtain accurate predictions.

In conclusion, we find that interference effects should be taken into account once the LHC reaches sensitivity of 10 times the SM di-Higgs background process. We parameterised the increase in the signal cross section due to interference effects by a parameter η. To get a handle on the possible peak distortion we introduced the parameters $\eta_\pm$. Note that neither of the parameters accounts for a possible peak shift. Further work should assess whether a peak distortion can be resolved experimentally and how the proposed general parameterisation compares to concrete model realizations.

3.3 Spin-2 models

B. Dillon, H. M. Lee

Extra-dimensional models provide ideal benchmark scenarios for spin-2 resonances decaying to a pair of Higgs bosons. Warped extra dimensional models in particular are very well motivated extensions to the SM, providing a natural solution to the electroweak hierarchy problem and an explanation of the hierarchies in the flavour sector. In addition to this, they are intimately connected with strongly coupled extensions of the SM such as composite Higgs models through the AdS/CFT correspondence. Metric fluctuations in an extra dimension give rise to massive towers of spin-2 states, the Kaluza-Klein (KK) gravitons, and a light spin-0 state, the radion. The couplings of these states are determined by the wavefunction overlaps between the SM particles and the metric fluctuations. Most phenomenoligical studies of the KK gravitons and the radion assume a warped extra dimension described by the Randall-Sundrum (RS) metric [235]. The masses of the KK gravitons are typically above 1 TeV, while the radion may take a much lighter mass due to it being generated from backreaction on the metric [236]. In this RS scenario the electroweak hierarchy is solved by localising the wavefunction of the Higgs field near the IR brane, where the overlaps with the metric fluctuation wavefunctions are large. For this reason channels with a resonant di-Higgs production

are important to probe the KK graviton and radion.

We assume that only the lightest KK graviton, which we denote as $X_{\mu\nu}(x)$, is accessible in the experiment. This state couples to the SM particles through the energy-momentum tensor as $\mathcal{L}_X = -\frac{c_i}{\Lambda} X_{\mu\nu} T_i^{\mu\nu}$, and we can write the partial decay widths to SM particles as [237, 238]

$$\Gamma(X \to gg) = \frac{c_g^2 m_X^3}{10\pi\Lambda^2}, \quad \Gamma(X \to \gamma\gamma) = \frac{c_{\gamma\gamma}^2 m_X^3}{80\pi\Lambda^2},$$

$$\Gamma(X \to hh) = \frac{c_h^2 m_X^3}{960\pi\Lambda^2}(1 - 4r_h)^{5/2},$$

$$\Gamma(X \to rr) = \frac{c_r^2 m_X^3}{960\pi\Lambda^2}(1 - 4r_r)^{5/2},$$

$$\Gamma(X \to f\bar{f}) = \frac{N_c(c_{fl}^2 + c_{fr}^2) m_X^3}{320\pi\Lambda^2}(1 - 4r_f)^{3/2}(1 + 8r_f/3),$$

$$\Gamma(X \to ZZ) = \frac{m_X^3}{80\pi\Lambda^2}\sqrt{1 - 4r_Z}\left(c_{ZZ}^2 + \frac{c_h^2}{12} + \frac{r_Z}{3}\left(3c_h^2 - 20c_h c_{ZZ} - 9c_{ZZ}^2\right)\right.$$

$$\left. + 2\frac{r_Z^2}{3}\left(7c_h^2 + 10c_h c_{ZZ} + 9c_{ZZ}^2\right)\right),$$

$$\Gamma(X \to WW) = \frac{m_X^3}{40\pi\Lambda^2}\sqrt{1 - 4r_W}\left(c_W^2 + \frac{c_h^2}{12} + \frac{r_W}{3}\left(3c_h^2 - 20c_h c_W - 9c_W^2\right)\right.$$

$$\left. + 2\frac{r_W^2}{3}\left(7c_h^2 + 10c_h c_W + 9c_W^2\right)\right),$$

$$\Gamma(X \to Z\gamma) = \frac{c_{Z\gamma}^2 m_X^3}{40\pi\Lambda^2}(1 - r_Z)^3\left(1 + \frac{r_Z}{2} + \frac{r_Z^2}{6}\right), \tag{3.21}$$

where Λ is the IR scale determining the KK graviton interactions, the c_i coefficients are determined by integrals over the wavefunctions of the states, $r_i = (m_i/m_X)^2$, and m_X is the lightest KK graviton mass. The decay width to two radion states is also included here with the radion field denoted by $r(x)$, where we assume that the radion mass is lower than $m_X/2$. We also use the following relations: $c_{\gamma\gamma} = s_\theta^2 c_W + c_\theta^2 c_B$, $c_{ZZ} = c_\theta^2 c_W + s_\theta^2 c_B$, $c_{Z\gamma} = s_\theta c_\theta(c_W - c_B)$. The decay to $Z\gamma$ is only non-zero when brane-kinetic terms for the gauge fields are present, since it is only this that can break the degeneracy between c_W and c_B. Without fine-tuning we can assume that these brane-kinetic terms are negligible.

There are important differences that occur between different incarnations of RS models regarding the nature of the SM fields. In the most basic set-up, all SM fields are placed on the IR brane. This is problematic since large couplings between light fermions and the KK states are induced leading to unacceptable levels of flavour violating processes for KK masses in the TeV range. The solution is then to allow all SM fields to propagate in the bulk of the extra dimension, with the lighter fermions localised near the UV region such that the overlap of their wavefunctions and those of the KK gravitons is significantly reduced. This also leads to an elegant description of fermion mass generation, whereby the Yukawa couplings of light fermions receive natural exponential suppression due to wavefunction overlaps. With the Higgs field and the top quark being localised in the IR region and the lighter fermions towards the UV region, it has been shown that the flavour hierarchy structure of the SM can be achieved with $\mathcal{O}(1)$ 5D Yukawa couplings [239]. The gauge fields in the extra dimension are restricted to having flat profiles by gauge invariance. The same mechanism that gives rise to hierarchical Yukawa couplings also gives rise to hierarchical KK graviton couplings, since its
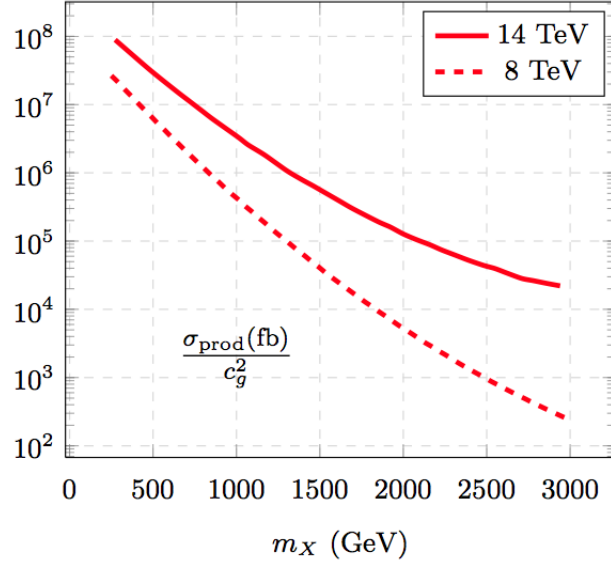
Figure 3.7: Production cross-section of the KK graviton via gluon fusion at centre of mass energies of 8 and 14 TeV, figure taken from Ref. [242]. The dependence of this quantity on the graviton coupling to gluons has been factored out.

wavefunction is localised in the IR region of the extra dimension. Therefore the most important decay modes of this state will be to the heavier particles of the SM: $t\bar{t}$, HH, W^+W^-, and ZZ. The dominant production mechanism for the lightest KK graviton is via gluon fusion, and in Fig. 3.7 the corresponding cross-section is shown as a function of the coupling c_g for both the 8 TeV and 14 TeV centre of mass energies. While VBF typically has a production cross-section an order of magnitude lower than gluon fusion, it has been shown that VBF searches can sometimes provide better sensitivity due to an enhanced background rejection [240, 241]. More work is required for a detailed study of the phenomenology of the KK graviton produced via VBF.

We consider a benchmark scenario for resonant di-Higgs production due to the decay of a KK graviton with the Higgs field localised on the IR brane, while the SM gauge fields and fermions propagate in bulk. In this case, we have $c_g = c_W = c_Z = [\log(M_P/\Lambda)]^{-1} \sim 0.03$ and $c_h = 1$. The localization of the top quark is controlled by the bulk mass parameter, $\mathcal{L}_{5D} \supset -\text{sgn}(y)\nu_{ti}k\,\bar{t}_i t_i$ with $i = l, r$ for the bulk fermions containing either left-handed or right-handed top quarks. For $\nu_{tl} = -\frac{1}{2}$ (that is, a flat left-handed top) and arbitrary ν_{tr}, we have the couplings of the KK graviton to the top quark [237, 243] as

$$c_{tl}^2 = 0, \qquad c_{tr}^2 = \frac{1 - 2\nu_{tr}}{1 - e^{-kL(1-2\nu_{tr})}} \int_0^1 dy\, y^{2-2\nu_{tr}} \frac{J_2(3.83y)}{J_2(3.83)}, \tag{3.22}$$

where J_2 represents the second order Bessel function. Finally, the radion coupling to KK graviton is determined geometrically [244] by

$$c_r = \frac{1}{3} \int_0^1 dy\, y^3 \frac{J_2(3.83y)}{J_2(3.83)} = 0.09. \tag{3.23}$$

In Fig. 3.8, we depict the branching ratios of the KK graviton as a function of the KK graviton mass for the bulk RS model with $\nu_{tr} = \frac{1}{3}$ on the left and $\nu_{tr} = -\frac{1}{2}$ on the right. We have chosen the radion mass to $m_r = 100\,\text{GeV}$ in both plots. The branching ratio to the di-Higgs channel is as large as 10% or so, while the $t\bar{t}$ channel can be comparable to WW and ZZ channels when the top quark is
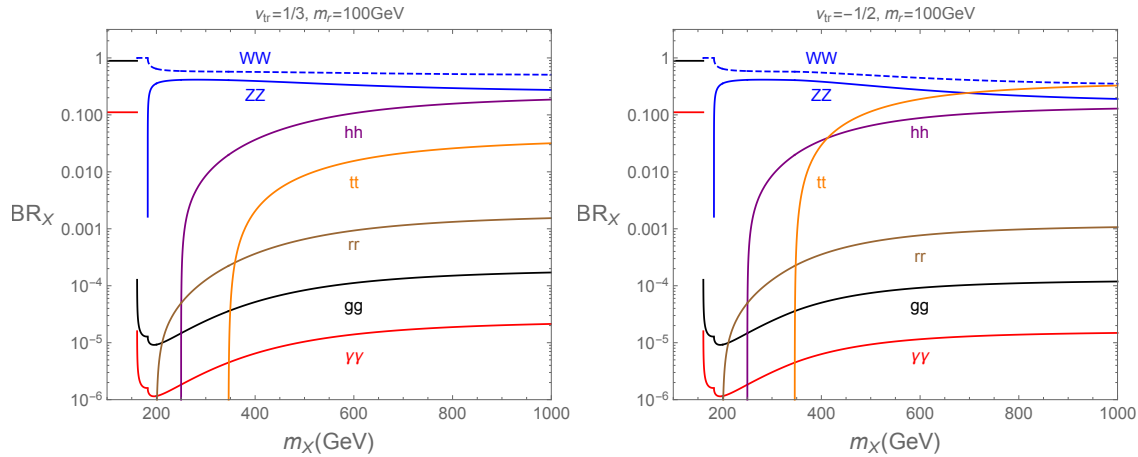
Figure 3.8: Branching ratios of KK graviton for the bulk RS benchmark model with $v_{tr} = -\frac{1}{3}$ (left) and $v_{tr} = -\frac{1}{2}$ (right).

localised near the IR brane. The branching ratio to the di-radion channel is at the level of 0.1% but it can be also interesting, depending on its decay modes.

We also remark on the case where the SM particles are localised away from the IR brane and dark matter is localised on the IR brane. This is the so-called the dark brane scenario considered in Ref. [237]. In this case, the KK graviton can be regarded as a mediator for dark matter [244–248], leading to a sizable invisible decay rate of the KK graviton into a dark matter pair. Furthermore, the KK graviton can decay sizably into a radion pair, which then decays into SM particles [244]. For a relatively heavy radion, the radion decays into massive particles such as top quarks, di-Higgs, etc., with comparable branching ratios as those for massive particles, even if there is a volume suppression for the SM particles delocalized from the IR brane. Therefore, in the dark brane scenario there are interesting signatures from multiple Higgs production due to the cascade decay of the KK graviton.

Recent results from the ATLAS collaboration place a lower bound of 3.4 TeV on the mass of a KK graviton resonance decaying to an all hadronic final state via $t\bar{t}$ [249]. Searches for a KK graviton decaying via $t\bar{t}$ to lepton-plus-jets final states can constrain the lightest state to lay above 3.8 TeV for a 15% width [250]. Weaker constraints have been obtained through consideration of the VBF production mode [241, 251], however these will be interesting for future study. Direct production of a radion can also give rise to di-Higgs signatures, however this is covered by the sections on scalar mediators, and for a recent in depth analysis of radion phenomenology we refer the reader to Ref. [252]. Interesting effects on both the radion and KK graviton phenomenology has been observed in the presence of brane-localised kinetic terms [242, 253–256], most notably resulting in a lowering of the KK graviton mass with respect to the scale of other resonances. Interesting and detailed studies of KK graviton effects in di-Higgs production have been studied in Refs. [257, 258]. In Ref. [257] the authors studied both the scenario with the SM on the IR brane and the SM in the bulk. They developed a strategy to search for resonant di-Higgs production via a KK graviton in the $b\bar{b}b\bar{b}$ final state and showed that a large range of the parameter space can be explored. Lastly, it is noteworthy that these techniques and results are equally applicable to the search for spin-2 composite resonances arising in composite Higgs models, thus expanding the theoretical motivation to search for spin-2 resonances in di-Higgs production.

	u-type	d-type	leptons
type I (T1)	Φ_2	Φ_2	Φ_2
type II (T2)	Φ_2	Φ_1	Φ_1
lepton-specific	Φ_2	Φ_2	Φ_1
flipped	Φ_2	Φ_1	Φ_2

Table 3.2: The four Yukawa types of the Z_2-symmetric 2HDM, defined by the Higgs doublet that couples to each kind of fermions.

3.4 BSM Models and Benchmarks

3.4.1 Complex 2-Higgs-Doublet Model

P. Basler, S. Dawson, C. Englert, M. Mühlleitner

The 2-Higgs-Doublet Model (2HDM) [259, 260] contains 2 $SU(2)_L$ doublets, Φ_1 and Φ_2. Assuming no flavor changing neutral currents and a softly broken Z_2 symmetry, there are four different types of 2HDMs, which are defined by the Higgs doublet that couples to each kind of fermions, and are summarized in Table 3.2. The complex or CP-violating 2HDM (C2HDM), described in Ref. [261], allows for two complex phases, and the C2HDM has nine independent parameters [262],

$$v , \quad t_\beta , \quad \alpha_{1,2,3} , \quad m_{H_i} , \quad m_{H_j} , \quad m_{H^\pm} , \quad \mathrm{Re}(m_{12}^2) , \tag{3.24}$$

where $t_\beta = \frac{v_2}{v_1}$, α_i are the angles that diagonalize the Higgs mass matrix, and m_{H_i} and m_{H_j} are any two of the three neutral Higgs boson mass eignestates. The third mass is calculated from the other parameters [262].

Within the C2HDM it is possible to produce final states with two different Higgs bosons. Compared to the SM di-Higgs production rate, in the C2HDM the cross sections can be enhanced in the case of resonant production of a heavy Higgs boson that decays into a pair of lighter Higgs bosons, or due to Higgs self-couplings that differ from the SM value.

CP-conserving 2HDM benchmarks for double Higgs production can be found in Refs. [263, 264]. Here we summarize the benchmark points for the C2HDM model presented in Ref. [265]. Table 3.3 gives the maximum cross section values for Higgs pair production that are compatible with all present experimental and theoretical constraints. The SM-like Higgs boson is h, the lighter of the non-SM-like neutral Higgs bosons is $H_\downarrow$, and the heavier one is $H_\uparrow$. Table 3.3 demonstrates that in both the T1 and T2 scenarios the maximum cross section for hh production can exceed the SM value: in T1 by a factor of about 40 and in T2 by a factor of about 3.2. The large enhancements are

$H_i H_j$/model	T1	T2
hh	794	63.2
$h H_\downarrow$	49.17	11.38
$h H_\uparrow$	17.65	13.50
$H_\downarrow H_\downarrow$	3196	0.31
$H_\downarrow H_\uparrow$	12.58	0.31
$H_\uparrow H_\uparrow$	7.10	0.23

Table 3.3: Maximum cross section values at $\sqrt{s} = 14$ TeV in fb for LO gluon fusion into Higgs pairs, $\sigma(gg \to H_i H_j)$, in the C2HDM T1 and T2 scenarios, with an exclusion luminosity ≥ 64 fb^{-1} that satisfy all theoretical and experimental constraints [265, 266].
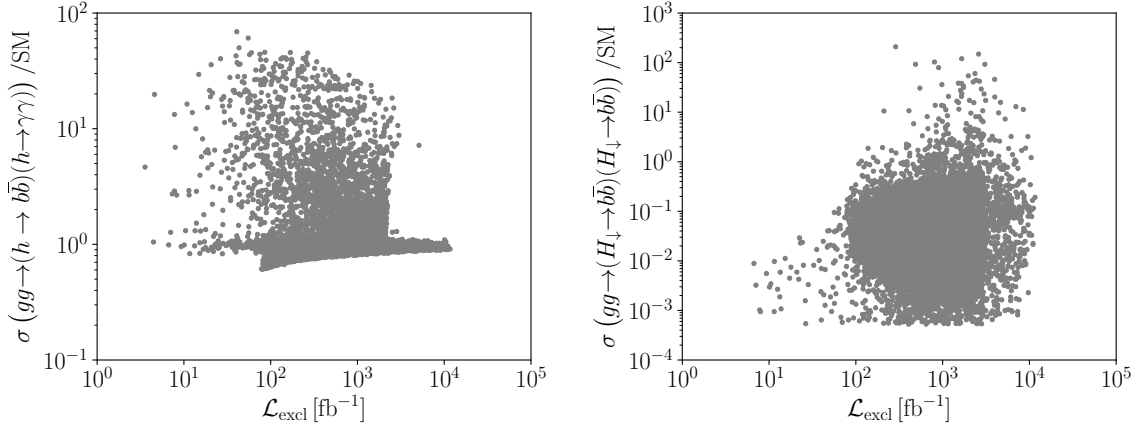
Figure 3.9: Higgs pair production cross sections normalized to the SM value for SM-like Higgs pairs decaying into $b\bar{b}\gamma\gamma$ (left) and light-non-SM-like Higgs pairs decaying into $b\bar{b}b\bar{b}$ (right) as a function of the exclusion luminosity, for the C2HDM T1 scenarios passing our applied constraints [265, 266].

due to the resonant production of an $H_\downarrow$ or $H_\uparrow$ that decays into a pair of SM-like Higgs bosons. The reason for the smaller enhancement in hh production in T2 compared to T1 is the overall heavier Higgs spectrum.

Based on extrapolations from current searches, we study the exclusion luminosity, i.e., the integrated luminosity at which a parameter point could be excluded experimentally. The most promising final states are $b\bar{b}\gamma\gamma$ [267], $b\bar{b}\tau^+\tau^-$ [169, 268, 269] and $b\bar{b}b\bar{b}$ [268, 270, 271]. In Fig. 3.9 we show (for all the parameter points that pass the theoretical and experimental constraints), the cross section values for hh production in the T1 scenario normalized to the SM Higgs pair production in the $b\bar{b}\gamma\gamma$ final state (left) and for $H_\downarrow H_\downarrow$ production in the $b\bar{b}b\bar{b}$ final state as a function of the exclusion luminosity. Fig. 3.9 shows that the production of a SM-like Higgs pair decaying to $b\bar{b}\gamma\gamma$ can exceed the SM rate by up to a factor of 68. This maximum enhancement factor is roughly the same for all final states.

In the $H_\downarrow H_\downarrow$ final state with both $H_\downarrow$'s decaying into bottom quarks or to $b\bar{b}\tau^+\tau^-$, the enhancement can be up to a factor of about 200. Due to a smaller branching ratio into photons, however, the maximum allowed enhancement in the $b\bar{b}\gamma\gamma$ final state is a factor of 40.

The remaining di-Higgs production processes are less promising. The enhancement factor for $hH_\downarrow$ production is less than 3 in the $b\bar{b}b\bar{b}$ and $b\bar{b}\tau^+\tau^-$ final states. The $h \to b\bar{b}, H_\downarrow \to \gamma\gamma$ rate is below the SM rate, while $h \to \gamma\gamma, H_\downarrow \to b\bar{b}$ has an enhancement factor around 3. Other final states have rates below the SM values.

The situation is less promising in the C2HDM T2. The maximum enhancement over the SM rate for hh production with the decay into the $b\bar{b}\tau^+\tau^-$, $b\bar{b}b\bar{b}$, or $b\bar{b}\gamma\gamma$ final states is around 4.5. All other final states lead to smaller rates than in the SM.

We conclude that there are promising di-Higgs signatures with large rates in the C2HDM T1 for SM-like Higgs pair production and also for final states with non-SM-like Higgs bosons. The new neutral Higgs bosons appear in SM-like final states, however, with different kinematic correlations due to different masses. The stringent constraints on the di-Higgs production rates present in the T2 scenario could exclude it if signatures much larger than in the SM were to be found.

3.4.2   Singlet extensions of 2HDM
N. R. Shah

The extension of a 2HM by a complex singlet S gives rise to the generic Higgs potential [272, 273]:

$$V = V_{\text{2HDM}} + V_S \,,\tag{3.25}$$

where

$$
\begin{aligned}
V_{\text{2HDM}} = {} & m_{11}^2 \Phi_1^\dagger \Phi_1 + m_{22}^2 \Phi_2^\dagger \Phi_2 - \left(m_{12}^2 \Phi_1^\dagger \Phi_2 + \text{h.c.} \right) \\
& + \frac{\lambda_1}{2} \left(\Phi_1^\dagger \Phi_1 \right)^2 + \frac{\lambda_2}{2} \left(\Phi_2^\dagger \Phi_2 \right)^2 + \lambda_3 \left(\Phi_1^\dagger \Phi_1 \right) \left(\Phi_2^\dagger \Phi_2 \right) + \lambda_4 \left(\Phi_1^\dagger \Phi_2 \right) \left(\Phi_2^\dagger \Phi_1 \right) \\
& + \left[\frac{\lambda_5}{2} \left(\Phi_1^\dagger \Phi_2 \right)^2 + \lambda_6 \left(\Phi_1^\dagger \Phi_1 \right) \left(\Phi_1^\dagger \Phi_2 \right) + \lambda_7 \left(\Phi_2^\dagger \Phi_2 \right) \left(\Phi_1^\dagger \Phi_2 \right) + \text{h.c.} \right],
\end{aligned}\tag{3.26}
$$

and

$$
\begin{aligned}
V_S = {} & \left(\xi S + \text{h.c.} \right) + m_S^2 S^\dagger S + \left(\frac{m_S'^2}{2} S^2 + \text{h.c.} \right) \\
& + \left(\frac{\mu_{S1}}{6} S^3 + \text{h.c.} \right) + \left(\frac{\mu_{S2}}{2} S S^\dagger S + \text{h.c.} \right) \\
& + \left(\frac{\lambda_1''}{24} S^4 + \text{h.c.} \right) + \left(\frac{\lambda_2''}{6} S^2 S^\dagger S + \text{h.c.} \right) + \frac{\lambda_3''}{4} \left(S^\dagger S \right)^2 \\
& + \left[S \left(\mu_{11} \Phi_1^\dagger \Phi_1 + \mu_{22} \Phi_2^\dagger \Phi_2 + \mu_{12} \Phi_1^\dagger \Phi_2 + \mu_{21} \Phi_2^\dagger \Phi_1 \right) + \text{h.c.} \right] \\
& + S^\dagger S \left[\lambda_1' \Phi_1^\dagger \Phi_1 + \lambda_2' \Phi_2^\dagger \Phi_2 + \left(\lambda_3' \Phi_1^\dagger \Phi_2 + \text{h.c.} \right) \right] \\
& + \left[S^2 \left(\lambda_4' \Phi_1^\dagger \Phi_1 + \lambda_5' \Phi_2^\dagger \Phi_2 + \lambda_6' \Phi_1^\dagger \Phi_2 + \lambda_7' \Phi_2^\dagger \Phi_1 \right) + \text{h.c.} \right].
\end{aligned}\tag{3.27}
$$

Φ_1, Φ_2 are $SU(2)$ doublets with hypercharge $Y = 1/2$. The m_{ij}^2 parameters have dimension mass squared, while the λ_i are dimensionless. The parameter ξ has dimensions mass cubed, the parameters $\{\mu_{Si}, \mu_{ij}\}$ have dimension mass, and the $\{\lambda_i', \lambda_i''\}$ are dimensionless. In the CP-conserving case, all parameters can be chosen manifestly real. As customary, after minimization, we define $v_1 \equiv \langle \Phi_1 \rangle$, $v_2 \equiv \langle \Phi_2 \rangle$, $v_S \equiv \langle S \rangle$, $v \equiv \sqrt{v_1^2 + v_2^2}$ and $\tan \beta \equiv v_1 / v_2$. The observed mass of the Z boson $m_Z = 91.2 \, \text{GeV}$ is obtained for $v = 174 \, \text{GeV}$. A similar structure for the Higgs potential is also obtained for the general NMSSM [274], and a mapping is provided to both the general and the Z_3 invariant NMSSM in Ref. [273].

The potential given above is described by 27 arbitrary parameters and at first glance appears difficult to analyze. However, the 125 GeV Higgs mass and its SM-like couplings enable us to constrain these significantly. In particular, most of the relevant phenomenology can be mostly parameterized in terms of physical parameters like masses and mixing angles.[7] To see this, it is useful to rotate the

---

[7] The mapping from the physical parameters to the parameters in the potential can be found in Ref. [273].

Higgs fields to the *extended Higgs basis* [259, 272, 275–280][8]

$$\begin{bmatrix} G^+ \\ \frac{1}{\sqrt{2}}\left(H^{\text{SM}} + iG^0\right) \end{bmatrix} = \sin\beta\,\Phi_1 + \cos\beta\,\Phi_2\,, \tag{3.28}$$

$$\begin{bmatrix} H^+ \\ \frac{1}{\sqrt{2}}\left(H^{\text{NSM}} + iA^{\text{NSM}}\right) \end{bmatrix} = \cos\beta\,\Phi_1 - \sin\beta\,\Phi_2\,, \tag{3.29}$$

$$\frac{1}{\sqrt{2}}\left(H^{\text{S}} + iA^{\text{S}}\right) = S\,, \tag{3.30}$$

where $\{H^{\text{SM}}, H^{\text{NSM}}, H^{\text{S}}\}$ and $\{A^{\text{NSM}}, A^{\text{S}}\}$ are the neutral CP-even and CP-odd real Higgs basis interaction states and G^0 ($G^\pm$) is the neutral (charged) Goldstone mode. In this basis, of the states coming from the doublets, only $\langle H^{\text{SM}} \rangle = \sqrt{2}v$ acquires a vev, and it is straightforward to work out the coupling of SM fermions to the Higgs basis states. For concreteness, in the following a Type II Yukawa structure is assumed. However, the results shown will in general hold for a different Yukawa structure. Some quantitative details may change due to the change in the Yukawa enhancement or suppression of the fermion couplings, but such modifications will be small since mostly the low $\tan\beta = \mathcal{O}(1)$ regime is considered.

The three CP-even mass eigenstates are denoted

$$h_i = \{h_{125}, H, h\}\,, \tag{3.31}$$

where h_{125} is identified with the $m_{h_{125}} \approx 125\,\text{GeV}$ SM-like state observed at the LHC, and H and h are ordered by masses, $m_H > m_h$. Each mass eigenstate is an admixture of the extended Higgs basis interaction states,

$$h_i = S^{\text{SM}}_{h_i} H^{\text{SM}} + S^{\text{NSM}}_{h_i} H^{\text{NSM}} + S^{\text{S}}_{h_i} H^{\text{S}}\,, \tag{3.32}$$

where $S^{j}_{h_i}$ with $j = \{\text{SM, NSM, S}\}$ denotes the components of the mass eigenstates in terms of the interaction basis. Likewise, the two CP-odd mass eigenstates are denoted

$$a_i = \{A, a\}\,, \tag{3.33}$$

where again $m_A > m_a$, and

$$a_i = P^{\text{NSM}}_{a_i} A^{\text{NSM}} + P^{\text{S}}_{a_i} A^{\text{S}}\,, \tag{3.34}$$

where the components are similarly denoted by $P^{j}_{a_i}$. The observed SM-like nature of h_{125} implies that

$$S^{\text{SM}}_{h_{125}} \approx 1\,, \qquad \{(S^{\text{NSM}}_{h_{125}})^2, (S^{\text{S}}_{h_{125}})^2\} \ll 1\,, \tag{3.35}$$

or, in other words, h_{125} mass eigenstate must approximately be *aligned* with the H^{SM} interaction state.

First a few conditions that alignment imposes on the phenomenology are highlighted. The most important point is that alignment forbids the coupling of the NSM or S like CP-even Higgs bosons from coupling to pairs of h_{125} or vector bosons (W or Z). Additionally the CP-odd state couplings to h_{125} and Z are also forbidden. Instead, there can be interesting *Higgs cascade decays* of the heavy Higgs bosons to final states involving only one h_{125} or a Z such as ($H^{\text{NSM}} \to H^{\text{S}} H^{\text{SM}}$) or ($A^{\text{NSM}} \to$

---

[8]Note that there are different conventions in the literature for the Higgs basis differing by an overall sign of H^{NSM} and A^{NSM}. Taking these into account, the potential in Eq. (3.25) and couplings for the 2HDM+S can be mapped directly to the potential and couplings given in the appendices of Ref. [272].
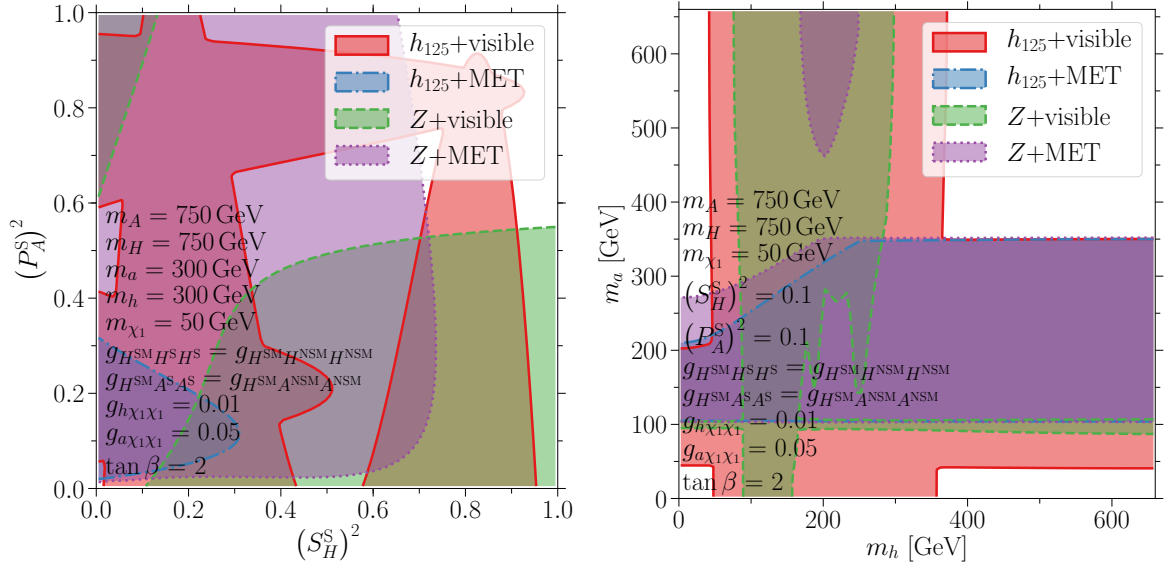
Figure 3.10: Regions of 2HDM+S parameter space within the future reach of the different Higgs cascade search modes as indicated in the legend at the LHC with $\mathscr{L} = 3000\,\text{fb}^{-1}$ of data. The left panel shows the accessible regions in the plane of the singlet fraction of the parent Higgs bosons $(S_H^S)^2$ vs $(P_A^S)^2$. The right panel shows the reach in the plane of the masses of the daughter Higgs bosons produced in the Higgs cascades, m_h vs m_a. The remaining parameters are fixed to the values indicated in the labels [273].

$H^S Z$). The singlets couple only to SM particles via their mixing with the other states, or to a possible Dark Matter (DM) state χ_1. Hence depending on the mixing angles and the arbitrary coupling to DM, such decays could result in h_{125} or Z plus visible or invisible signatures.

We collected all the current search results and projections available for the relevant decays, as well as performed detailed collider simulations where needed, to obtain the projection for the reach at the LHC with 3000 fb^{-1} of data [273]. Fig. 3.10 presents an example of the reach we obtain for benchmark scenarios. While the mass of the parent Higgs bosons is fixed at 750 GeV in Fig. 3.10, and perfect alignment is assumed, the effect of varying these quantities is easy to deduce. First, different masses for the parent Higgs bosons would primarily affect the gluon fusion production cross section, whose scaling with mass is well known. The affect of misalignment would be quantitatively negligible on the reach of the Higgs cascades discussed here. However, various decay chains not considered in the above analysis, such as $(H \to h_{125} h_{125})$ or $(A \to Z h_{125})$, would be present. Such decays are suppressed by either the NSM or S component of h_{125} compared to decays into h. The reach for such decays can be extrapolated from those presented by the convolution of the relevant decay widths with the misalignment of h_{125} and identifying $m_h = 125$ GeV in the right panel of Fig. 3.10. Observe that the results presented can also be mapped to the case of the decoupled singlet, i.e. an effective 2HDM, with non-degenerate CP-odd and CP-even NSM-like Higgs bosons, by appropriately choosing the NSM and S components for the parent and daughter Higgs bosons in the decay chain of interest.

Finally, note that Fig. 3.10 is meant to summarize only the prospects of exploring the 2HDM+S parameter space using Higgs cascades. The regions displayed do not take into account existing bounds from searches for additional Higgs boson beyond h_{125}. In particular, the charged Higgs does not play a role in any of the searches shown. Existing constraints on charged Higgs bosons, e.g. from flavor physics observables, can be satisfied by choosing a sufficiently large mass of the charged Higgs. Recall that the masses of the physical Higgs bosons are treated as free parameters.

Even without considering effects of mixing, mass splittings of order of a few 100 GeV between the mostly doublet-like pseudo-scalar and the charged Higgs are easily achievable. Furthermore, in more complete models with larger particle content than the 2HDM+S considered here, such as the NMSSM, indirect observables such as those from flavor physics receive additional contributions beyond those from the charged Higgs which may loosen the bounds on the mass of the charged Higgs, cf. Refs. [281, 282].

In summary, as evident from Fig. 3.10, there are large regions of parameter space in reach of the different Higgs cascade search modes. In particular, Higgs cascades enable the LHC to probe regions of parameter space challenging to access with traditional searches for the direct decays of additional Higgs states: singlet-like light states are difficult to directly produce due to the small couplings to pairs of SM particles. On the other hand, doublet-like states are readily produced, but if their mass is above the kinematic threshold allowing for decays into pairs of top quarks, for low $\tan\beta$, $\Phi \to t\bar{t}$ decays will dominate over the decays into other SM states. Pairs of top quarks produced from an s-channel resonance are very difficult to detect at the LHC due to interference effects with the QCD background, which makes the $m_\Phi \gtrsim 350$ GeV, low $\tan\beta$ region extremely challenging to probe at the LHC through direct Higgs decays with current search strategies [232, 283–289].

3.4.3 hMSSM

S. Liebler, M. Mühlleitner, M. Spira

An effective approximation of the MSSM for scenarios of large SUSY particle masses but small and moderate values of the Higgsino mass parameter μ relative to the stop masses is provided by the hMSSM [290–293]. This approach starts from the scalar Higgs mass matrix including radiative corrections,

$$\mathcal{M}^2 = M_Z^2 \begin{pmatrix} c_\beta^2 & -s_\beta c_\beta \\ -s_\beta c_\beta & s_\beta^2 \end{pmatrix} + M_A^2 \begin{pmatrix} s_\beta^2 & -s_\beta c_\beta \\ -s_\beta c_\beta & c_\beta^2 \end{pmatrix} + \begin{pmatrix} \Delta\mathcal{M}_{11}^2 & \Delta\mathcal{M}_{12}^2 \\ \Delta\mathcal{M}_{12}^2 & \Delta\mathcal{M}_{22}^2 \end{pmatrix}, \qquad (3.36)$$

where we use the short–hand notation $s_\beta \equiv \sin\beta$, etc., and introduce the radiative corrections through the general matrix elements $\Delta\mathcal{M}_{ij}^2$. The hMSSM approach starts by neglecting diagonal and off-diagonal entries of the radiative corrections,

$$\Delta\mathcal{M}_{11}^2 \sim \Delta\mathcal{M}_{12}^2 \sim 0, \qquad (3.37)$$

and just keeping $\Delta\mathcal{M}_{22}^2$. Since the off-diagonal entries are proportional to the μ parameter, this approximation restricts μ to small or moderate values in comparison with the other SUSY masses, thus excluding large μ parameters [293–295]. In this way, all radiative corrections can be described by the parameter ϵ,

$$\epsilon = \Delta\mathcal{M}_{22}^2 = \frac{M_h^2(M_A^2 + M_Z^2 - M_h^2) - M_A^2 M_Z^2 c_{2\beta}^2}{M_Z^2 c_\beta^2 + M_A^2 s_\beta^2 - M_h^2}, \qquad (3.38)$$

which is related to the pseudo-scalar mass M_A, the parameter $\tan\beta = v_2/v_1$ that is determined by the vevs of the two neutral CP-even Higgs fields, and the light scalar Higgs mass M_h. In this way the radiative corrections are traced back to the known light scalar Higgs mass that is identified with the mass of the discovered SM-like Higgs boson $M_h = 125$ GeV. The remaining parameters of the MSSM

Higgs sector are given by

$$
M_H^2 \;=\; \frac{(M_A^2 + M_Z^2 - M_h^2)(M_Z^2 c_\beta^2 + M_A^2 s_\beta^2) - M_A^2 M_Z^2 c_{2\beta}^2}{M_Z^2 c_\beta^2 + M_A^2 s_\beta^2 - M_h^2},
$$

$$
\alpha \;=\; -\arctan\left(\frac{(M_Z^2 + M_A^2) c_\beta s_\beta}{M_Z^2 c_\beta^2 + M_A^2 s_\beta^2 - M_h^2} \right),
$$

$$
M_{H^\pm}^2 \;=\; M_A^2 + M_W^2, \tag{3.39}
$$

where M_H denotes the heavy scalar Higgs mass, α the CP-even mixing angle, $M_{H^\pm}$ the charged Higgs mass and M_W the W mass. The upper bound on the light scalar Higgs mass is lifted to

$$
M_h^2 \leq M_Z^2 \cos^2 2\beta + \epsilon \sin^2 \beta. \tag{3.40}
$$

The hMSSM determines all Higgs masses and mixing angles by three input parameters, M_A, M_h and $\tan\beta$. The hMSSM approach, however, can be understood as an approximation to a low-energy 2HDM with heavy SUSY particles being integrated out [296,297]. The parameter ϵ then plays the role of the matching of the low-energy 2HDM to the full MSSM. This point of view allows to extend the simplified ϵ approximation to the Higgs self-couplings, too. However, an explicit analysis revealed additional contributions to the effective ϵ parameter for the Higgs self-couplings that are determined by the top mass alone [297],

$$
\bar{\epsilon} = \epsilon - \frac{24\sqrt{2} G_F m_t^4}{(4\pi)^2 s_\beta^2} \frac{2}{3}. \tag{3.41}
$$

The trilinear Higgs self-couplings induce Higgs pair production processes at the LHC and are given, in terms of this modified $\bar{\epsilon}$ parameter,

$$
\lambda_{hhh}^{\bar{\epsilon}} = \lambda_{hhh} + \frac{3 c_\alpha^3}{v s_\beta} \bar{\epsilon}, \qquad\qquad \lambda_{Hhh}^{\bar{\epsilon}} = \lambda_{Hhh} + \frac{3 s_\alpha c_\alpha^2}{v s_\beta} \bar{\epsilon},
$$

$$
\lambda_{HHh}^{\bar{\epsilon}} = \lambda_{HHh} + \frac{3 s_\alpha^2 c_\alpha}{v s_\beta} \bar{\epsilon}, \qquad\qquad \lambda_{HHH}^{\bar{\epsilon}} = \lambda_{HHH} + \frac{3 s_\alpha^3}{v s_\beta} \bar{\epsilon},
$$

$$
\lambda_{hAA}^{\bar{\epsilon}} = \lambda_{hAA} + \frac{c_\alpha c_\beta^2}{v s_\beta} \bar{\epsilon}, \qquad\qquad \lambda_{HAA}^{\bar{\epsilon}} = \lambda_{HAA} + \frac{s_\alpha c_\beta^2}{v s_\beta} \bar{\epsilon}, \tag{3.42}
$$

where the tree-level couplings are given (in terms of the radiatively corrected mixing angle α) by

$$
\lambda_{hhh} = 3 \frac{M_Z^2}{v} c_{2\alpha} s_{\alpha+\beta}, \qquad\qquad \lambda_{Hhh} = \frac{M_Z^2}{v} (2 s_{2\alpha} s_{\alpha+\beta} - c_{2\alpha} c_{\alpha+\beta}),
$$

$$
\lambda_{HHh} = \frac{M_Z^2}{v} (-2 s_{2\alpha} c_{\alpha+\beta} - c_{2\alpha} s_{\alpha+\beta}), \qquad\qquad \lambda_{HHH} = 3 \frac{M_Z^2}{v} c_{2\alpha} c_{\alpha+\beta},
$$

$$
\lambda_{hAA} = \frac{M_Z^2}{v} c_{2\beta} s_{\alpha+\beta}, \qquad\qquad \lambda_{HAA} = -\frac{M_Z^2}{v} c_{2\beta} c_{\alpha+\beta}. \tag{3.43}
$$

The vacuum expectation value v is related to the Fermi constant by $v = 1/\sqrt{\sqrt{2} G_F}$. Using these radiatively corrected Higgs masses, mixing angles and trilinear Higgs couplings, the corresponding Higgs pair production processes can be investigated involving the dominant radiative corrections within the hMSSM approximation.

3.4.4 NMSSM

P. Basler, S. Dawson, C. Englert, M. Mühlleitner

The NMSSM contains a complex gauge singlet superfield, $\hat{S}$, along with the $SU(2)_L$ doublet superfields $\hat{H}_u$ and $\hat{H}_d$ of the MSSM [274, 298]. The additional contribution to the superpotential due to $\hat{S}$ is,

$$\Delta \mathscr{W} \quad = \quad -\epsilon_{ij}\lambda \hat{S}\hat{H}_d^i\hat{H}_u^j + \frac{\kappa}{3}\,\hat{S}^3\,, \tag{3.44}$$

with the $SU(2)_L$ indices $i, j = 1, 2$ and the totally antisymmetric tensor ϵ_{ij} where $\epsilon_{12} = \epsilon^{12} = 1$. The scalar component of the singlet, S, contributes the trilinear soft SUSY breaking interactions,

$$-\mathscr{L}_{\rm tril} \quad = \quad -\epsilon_{ij}\lambda A_\lambda S H_d^i H_u^j + \frac{1}{3}\kappa A_\kappa S^3\,. \tag{3.45}$$

The set of six parameters describing the tree-level NMSSM Higgs sector is

$$\lambda\,,\,\kappa\,,\,A_\lambda\,,\,A_\kappa,\,\tan\beta = v_u/v_d\,,\,\mu_{\rm eff} = \lambda v_s/\sqrt{2}\,. \tag{3.46}$$

The sign conventions are such that λ and $\tan\beta$ are positive, while $\kappa, A_\lambda, A_\kappa$ and $\mu_{\rm eff}$ can take both signs. Diagonalizing the scalar mass matrix gives three CP-even mass eigenstates, h, $H_\downarrow$, and $H_\uparrow$, two CP-odd mass eigenstates $A_\downarrow$ and $A_\uparrow$, and two charged Higgs bosons. Here, h denotes the SM-like Higgs boson and $H_\downarrow$ ($H_\uparrow$) the lighter (heavier) non-SM-like CP-even Higgs boson, $A_\downarrow$ and $A_\uparrow$ denote the lighter and heavier pseudoscalar, respectively. Note that we restrict ourselves to the CP-conserving NMSSM. The Higgs boson masses are calculated from the input parameters.

We scan the NMSSM parameter space [265] [9] and require that all experimental constraints from Higgs production, LHC SUSY searches, and dark matter limits are satisfied. Within the allowed parameter space we are interested in double Higgs production with non-SM like signatures. After satisfying the constraints, we define an approximate "exclusion luminosity" at which single Higgs measurements would become sensitive to a particular scenario. This allows us to directly compare the discovery potential of double-Higgs production to single Higgs measurements and to identify interesting regions of the NMSSM parameter space.

The enlarged Higgs sector of the NMSSM leads to processes with two different Higgs bosons in the final state. Also the production of two pseudoscalars in the final state is possible. The cross sections can be enhanced relative to the SM HH rate in the case of the resonant production of a heavy Higgs boson that decays into a pair of lighter Higgs bosons. Note, however, that due to supersymmetry, the Higgs self-couplings are determined in terms of the gauge couplings, restricting large deviations from the SM Higgs self-couplings. The Higgs bosons can additionally decay into non-SM final states such as e.g. neutralinos, giving signatures with new and interesting features.

Scanning over NMSSM parameter points that meet all criteria and that have exclusion luminosities above 64 fb^{-1}, the maximum enhancement of the gluon fusion rate to hh pairs is found to be slightly less than a factor of two. The $H_\downarrow H_\downarrow$ cross section can become very large mainly because of the allowed smallness of the $H_\downarrow$ mass, $m_{H_\downarrow} \sim 38$ GeV. The maximum value [10] of 70 fb in $hA_\downarrow$ production is due to the rather small mass, $m_{A_\downarrow} = 69$ GeV, in combination with resonant $A_\uparrow$ production followed by the decay to $hA_\downarrow$. Finally, the enhancement in $A_\downarrow A_\downarrow$ production with a production cross

---

[9]In contrast to [265] HiggsSignals v.2.2.2 [220–223, 225] is used for the following part and the lower bound on the chargino mass has been relaxed to the LEP limit of 94 GeV.

[10]All values are for a center of mass energy of 14 TeV and at LO. The inclusion of NLO QCD corrections roughly adds a factor of 2.
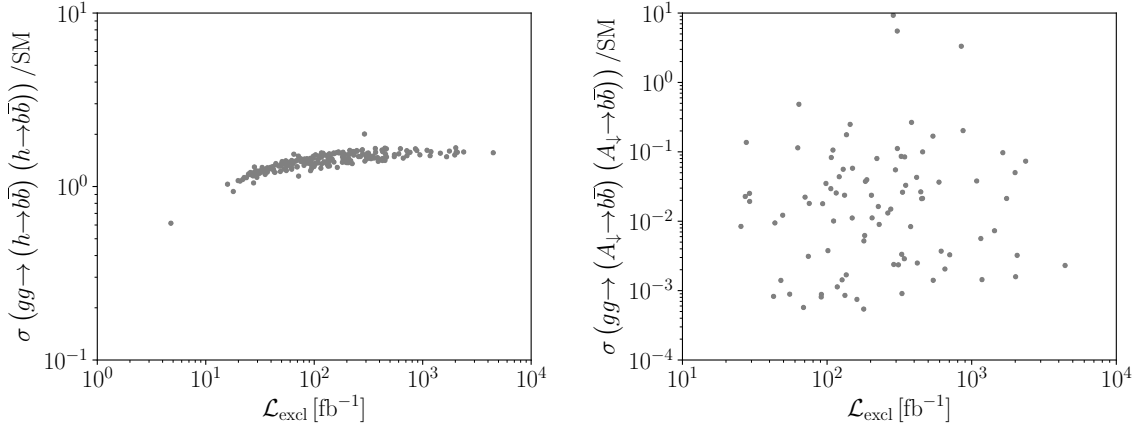
Figure 3.11: Scatter plots for NMSSM scenarios passing the applied experimental constraints: Higgs pair production cross sections normalized to the SM value for SM-like Higgs pairs decaying into $b\bar{b}b\bar{b}$ (left) and $A_\downarrow A_\downarrow$ Higgs pairs decaying into $b\bar{b}b\bar{b}$ (right) as a function of the exclusion luminosity [265].
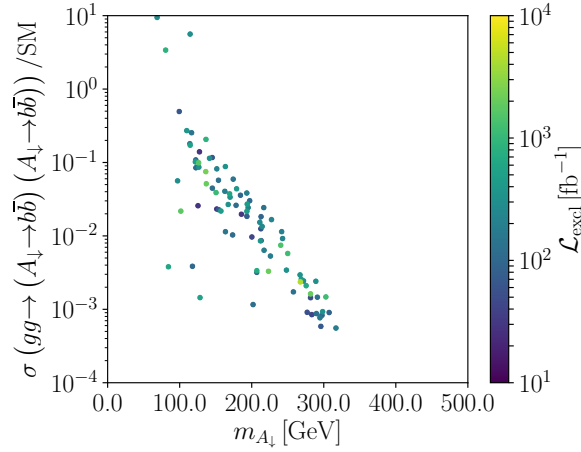

Figure 3.12: NMSSM: Scatter plots for $b\bar{b}b\bar{b}$ final state rates from $A_\downarrow A_\downarrow$ production normalized to the SM rate as a function of $m_{A_\downarrow}$. The colour code denotes the exclusion luminosity [265].

section of 70 fb is due to the smallness of the $A_\downarrow$ mass of $m_{A_\downarrow} = 69$ GeV combined with the resonant $H_\downarrow$ production decaying subsequently into $A_\downarrow A_\downarrow$. (The branching ratio of $H_\uparrow \to A_\downarrow A_\downarrow$ is very small for this parameter point.)

In Fig. 3.11 we show the NMSSM cross sections for hh pair production in the $b\bar{b}b\bar{b}$ final state (left) and for $A_\downarrow A_\downarrow$ production in the $b\bar{b}b\bar{b}$ final state (right) normalized to the corresponding SM values as a function of the exclusion luminosity and for all parameter points that pass the experimental restrictions. As seen in Fig. 3.11 (left), the $b\bar{b}b\bar{b}$ final state rates from SM-like Higgs pair production exceed the SM HH rate by at most a factor of 2 and only for higher exclusion luminosities. As can be inferred from Fig. 3.12 (right), the maximum value for $A_\downarrow A_\downarrow$ production with subsequent decay into $b\bar{b}b\bar{b}$ is 9.3 compared to the SM value, at an exclusion luminosity of 287 fb^{-1}. The maximum value found for the production of a SM like Higgs boson h together with $H_\downarrow$ and subsequent decay into $b\bar{b}b\bar{b}$ (not shown here), has an enhancement of ~ 4.6 at an exclusion luminosity of 449 fb^{-1}.

Because the light pseudoscalar, $A_\downarrow$, can be relatively light and decays dominantly into $b\bar{b}$, the enhancement factors can be up to $\sim 5\text{-}10$ in these processes. Fig. 3.12 shows the production of

$A_\downarrow A_\downarrow$ with decay into the $b\bar{b}b\bar{b}$ final state normalized to SM di-Higgs HH production decaying into the $b\bar{b}b\bar{b}$ final state, as a function of the mass of the light pseudoscalar. The color code denotes the exclusion luminosity. For masses below 125 GeV, the rates are enhanced because of the large di-Higgs production cross sections. Above the top-pair threshold, the exclusion luminosities are on average lower than below the threshold due to the exclusion limits in the top-pair final state. For masses below the SM-like Higgs mass, however, there are parameter points where the exclusion luminosities can exceed 100 fb^{-1} up to about 900 fb^{-1} while still featuring enhanced rates. The reason that these points are not excluded from single Higgs searches is that light Higgs states with dominant decays into $b\bar{b}$ final states are difficult to probe. On the other hand this enhancement combined with the large di-Higgs production cross section implies significant $b\bar{b}b\bar{b}$ final state rates that may be tested at the high luminosities. This is an example of the interplay between difficult single-Higgs searches and large exotic di-Higgs rates, where new physics may be found.

3.4.5 Georgi-Machacek Model

H. E. Logan

The Georgi-Machacek (GM) model [299, 300] is an extended Higgs model whose scalar sector consists of the usual complex isospin doublet (ϕ^+, ϕ^0) with hypercharge $Y = 1/2$, a real triplet (ξ^+, ξ^0, ξ^0) with $Y = 0$, and a complex triplet $(\chi^{++}, \chi^+, \chi^0)$ with $Y = 1$. The scalar potential is constructed to preserve a global SU(2)$_L \times$SU(2)$_R$ symmetry so that custodial symmetry is preserved after electroweak symmetry breaking, ensuring that the electroweak ρ parameter is equal to one at tree level. Additional details can be found in Sec. IV.4.4 of Ref. [19].

In addition to a light custodial-singlet scalar h, usually identified with the SM-like 125 GeV Higgs boson, the physical spectrum contains a custodial fiveplet $(H_5^{++}, H_5^+, H_5^0, H_5^-, H_5^{--})$ with common mass m_5, a custodial triplet (H_3^+, H_3^0, H_3^-) with common mass m_3, and a heavier custodial singlet H with mass m_H. Here we focus on the decay $H \to hh$. Custodial symmetry forbids H_3^0 and H_5^0 from decaying into hh.

H can be produced at the LHC via the same processes as a heavy SM Higgs boson. For H masses above $2m_h$, the only relevant production modes are gluon fusion and vector boson fusion. We compute the signal cross sections for the 13 TeV LHC as follows, focusing on the $HH \to b\bar{b}b\bar{b}$ final state:

$$
\begin{aligned}
\sigma(gg \to H \to hh \to b\bar{b}b\bar{b}) &= \sigma(gg \to H_{\text{SM}}) \times (\kappa_f^H)^2 \times \text{BR}(H \to hh) \\
&\quad \times [\text{BR}(h \to b\bar{b})]^2, \qquad (3.47) \\
\sigma(\text{VBF} \to H \to hh \to b\bar{b}b\bar{b}) &= \sigma(\text{VBF} \to H_{\text{SM}}) \times (\kappa_V^H)^2 \times \text{BR}(H \to hh) \\
&\quad \times [\text{BR}(h \to b\bar{b})]^2. \qquad (3.48)
\end{aligned}
$$

We take the SM cross sections $\sigma(gg \to H_{\text{SM}})$ and $\sigma(\text{VBF} \to H_{\text{SM}})$ from Ref. [19], where for the gluon fusion process we use the cross sections computed to NNLO+NNLL QCD accuracy. The remaining factors are computed using the public code GMCALC 1.4.1 [301]. κ_f^H and κ_V^H are the coupling modification factors for H couplings to fermion pairs and vector boson pairs, respectively. The branching ratio of $H \to hh$ depends on a combination of the parameters of the scalar potential. The branching ratio of $h \to b\bar{b}$ depends mainly on the custodial-singlet Higgs boson mixing angle and the triplet scalar vacuum expectation value, and is constrained by LHC Higgs signal strength measurements to be close to its SM value.

We scan over the full GM model parameter space, requiring that the scalar quartic couplings satisfy perturbative unitarity constraints [302, 303] and that the potential is bounded from below
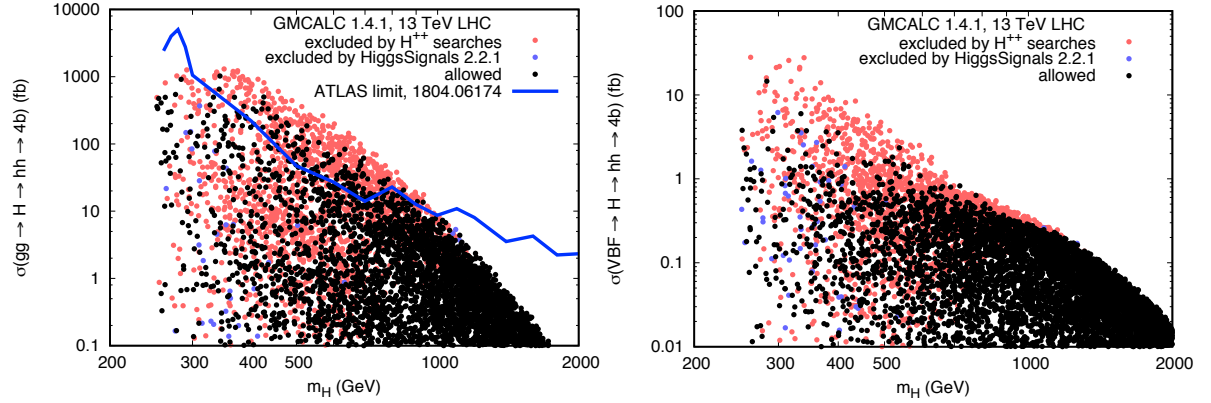
Figure 3.13: Cross sections for $H \to hh \to b\bar{b}b\bar{b}$ in 13 TeV pp collisions produced via gluon fusion (left) or vector boson fusion (right) as a function of the H mass in the Georgi-Machacek model. The points represent a scan over the full model parameter space imposing only theoretical constraints. Red and violet points are already excluded by other searches.

and has no deeper minima than the desired vacuum [303]. The resulting signal cross sections are shown in Fig. 3.13 as a function of the H mass. We include only the resonant processes of Eqs. (3.47) and (3.48), and do not consider interference with the nonresonant SM-like $pp \to h^* \to hh \to b\bar{b}b\bar{b}$ process (for comparison, the *total* SM cross sections times branching ratios for the nonresonant $gg \to hh \to b\bar{b}b\bar{b}$ and VBF$\to hh \to b\bar{b}b\bar{b}$ processes are 10 fb [29] and 0.55 fb [19], respectively).

In red we indicate the scan points that are excluded by existing LHC searches other than $H \to hh$. The most stringent of these is a CMS search for doubly-charged scalar production in VBF with decays to like-sign W bosons using 35.9 fb^{-1} of pp data at 13 TeV [304], which sets an upper bound on the production cross section of $H_5^{\pm\pm}$ as a function of its mass.

In violet we indicate the scan points that are allowed by direct searches but excluded by measurements of the 125 GeV Higgs boson properties. We apply the constraint by using HiggsSignals 2.2.1 [225] to compute a p-value, which we require to be larger than 0.05 for the point to be allowed at the 95% confidence level. Because we want to apply the constraint separately for each scan point, we take the number of free model parameters to be zero in the calculation of the p-value. This maximizes the p-value and (conservatively) excludes the smallest number of points. The black points in Fig. 3.13 are still allowed after applying these constraints.

The thick blue line in the left panel of Fig. 3.13 shows the current ATLAS limit on $\sigma(pp \to \text{Scalar} \to hh \to b\bar{b}b\bar{b})$ using 27.5–36.1 fb^{-1} of pp data at 13 TeV [148]. This search already excludes new parameter space in the GM model for m_H between about 300 GeV and 1 TeV that is not otherwise constrained by previous searches. The model therefore serves as a useful benchmark for interpreting $H \to hh$ searches that will be performed using the full LHC Run 2 dataset.

3.5   New Particles in the Loop

S. Dawson, I. M. Lewis

BSM physics can contribute to di-Higgs production through new colored scalars [179, 305–309] or fermonic [310–317] particles contributing to the loop amplitudes. If new particles get their masses from a different source than the Higgs, the contributions to single and double Higgs production can be different [312]. These new particles can then significantly change the rates as well the kinematic distributions in double production and keep single Higgs production close to the SM
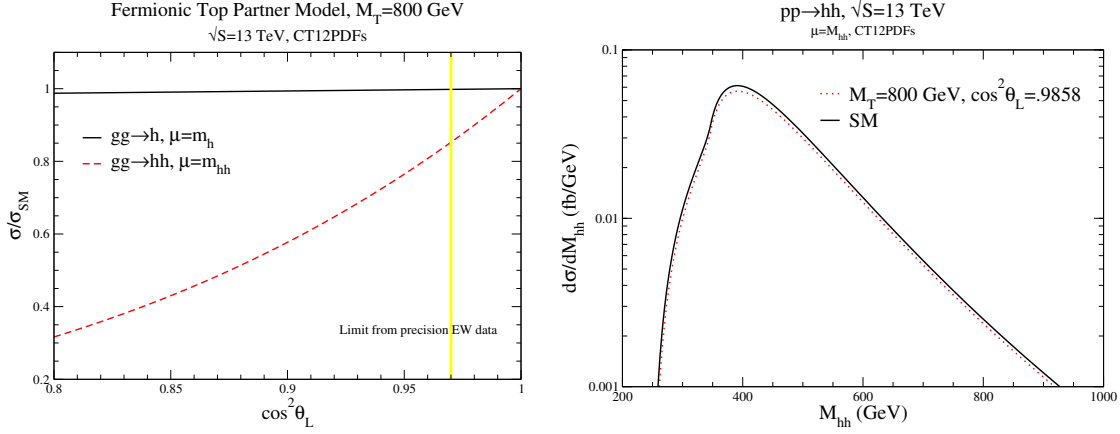
Figure 3.14: Left: Deviations in (solid black) single Higgs and (red dashed) double Higgs production away from SM predictions in the singlet VLQ model. Vertical yellow band indicates EW precision constraints on θ_L and allowed values are to the right. Right: Di-Higgs invariant mass distributions in (black) SM and (red dashed) singlet VLQ model in Eq. (3.51) [323].

prediction [180, 306, 318].

Heavy VLQs

To be consistent with single Higgs rates, new heavy quarks cannot get all their mass from the Higgs mechanism and must be vector-like [319]. We focus on two cases: $SU(2)_L$ singlet up-type vector-like quark (VLQ) U and a full generation of up- and down-type VLQs.

$$Q = \begin{pmatrix} T \\ B \end{pmatrix}, U, D, \tag{3.49}$$

where Q is a vector-like $SU(2)_L$ doublet, U is an up-type vector-like $SU(2)_L$ singlet, and D is a down-type vector-like $SU(2)_L$ singlet. For simplicity and to avoid low energy constraints, we only consider mixing with the third generation SM quarks:

$$q_L = \begin{pmatrix} t_L \\ b_L \end{pmatrix}, t_R, b_R. \tag{3.50}$$

Singlet VLQ

The singlet VLQ, third generation quarks, and Higgs boson couple via

$$\mathscr{L} = -\lambda_b \overline{q}_L \Phi b_R - \lambda_t \overline{q}_L \widetilde{\Phi} t_R - \lambda_1 \overline{q}_L \widetilde{\Phi} U_R + M_1 \overline{U}_L t_R + M_2 \overline{U}_L U_R + \text{h.c.} \tag{3.51}$$

Since U_R and t_R have the same quantum numbers, M_1 can be rotated via a field redefinition between U_R and t_R [315]. Hence, there are four physical free parameters: the bottom quark mass m_b, the observed top quark mass $m_t = 173$ GeV, the heavy top partner mass m_T, and the left-handed mixing angle between the top quark and top partner θ_L. The right-handed mixing angle θ_R can be determined by the Higgs vev, m_t, m_T, and θ_L [315]. Electroweak precision constraints constrain $\sin\theta_L \lesssim 0.16 - 0.12$ for $m_T \sim 1 - 2$ TeV [320–322].

In left hand side of Fig. 3.14 we show deviations away from SM predictions for single and double Higgs production in the singlet VLQ model as a function of the mixing angle with $M_T = 800$ GeV [317]. The single Higgs production is always nearly SM-like, while substantial deviations in double Higgs
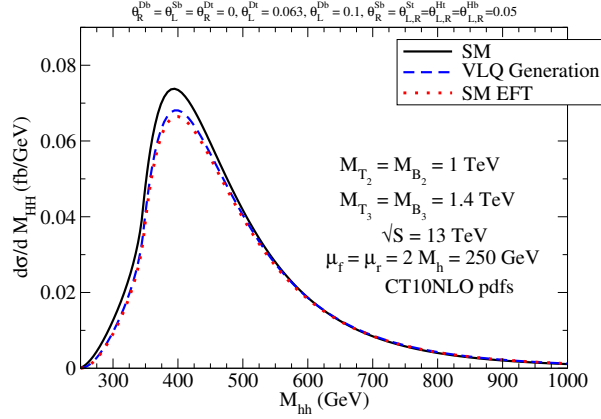
Figure 3.15: Double Higgs invariant mass distribution for the (solid) SM, (blue dashed) VLQ generation described in Eq. (3.52), and (red dotted) the VLQs integrated out and matched onto the SM EFT [317].

production are possible. These deviations are always a suppression [315, 317]. However, once (yellow solid) EW precision measurements are taken into account, double Higgs production is forced to be within $\sim 15\%$ the SM value. The kinematic distributions are nearly SM like, as shown in the right hand side of Fig. 3.14. For higher top partner masses, EW precision constraints on θ_L become more stringent [320–322], the effects of the top partner decouple more, and invariant mass distributions continue to be SM like [317].

Full VLQ Generation

A more complicated scenario is to assume a full generation of VLQs. The couplings with the third generation quarks and Higgs are [317]

$$
\begin{aligned}
\mathscr{L} \;=\; & -\lambda_b \overline{q}_L \Phi b_R - \lambda_t \overline{q}_L \widetilde{\Phi} t_R - M \overline{Q}_L Q_R - M_U \overline{U}_L U_R - M_D \overline{D}_L D_R \\
& -\lambda_1 \overline{Q}_L \widetilde{\Phi} U_R - \lambda_2 \overline{Q}_L \Phi D_R - \lambda_3 \overline{Q}_R \widetilde{\Phi} U_L - M_4 \overline{q}_L Q_R - M_5 \overline{U}_L t_R \\
& -M_6 \overline{D}_L b_R - \lambda_7 \overline{q}_L \widetilde{\Phi} U_R - \lambda_8 \overline{q}_L \Phi D_R - \lambda_9 \overline{Q}_L \widetilde{\Phi} t_R - \lambda_{10} \overline{Q}_L \Phi b_R \\
& -\lambda_{11} \overline{Q}_R \Phi D_L + \text{h.c.}
\end{aligned}
\tag{3.52}
$$

There are the top quark, the bottom quark, two top partners $T_{1,2}$, and two bottom quark partners $B_{1,2}$ mass eigenstates after electroweak symmetry breaking. The free parameters are the top quark mass, the bottom quark mass, the two top partner masses $M_{T_{1,2}}$, two bottom partner masses $M_{B_{1,2}}$, and twelve mixing angles.

The invariant mass distributions for this model are shown in Fig. 3.15. The pattern of the top and bottom partner masses and values of mixing angles are chosen to be consistent with electroweak precision data, single Higgs rates, and maximize deviations in double Higgs rates [317]. After all constraints are taken into account, the (black solid) SM and (blue dashed) VLQ distributions are very similar.

The red dotted line in Fig. 3.15 shows the distribution calculated by integrating out the heavy top and bottom partners and matching on the SM EFT. This introduces new point-like interactions between the gluons and Higgs boson and new four point interactions $t - t - h - h$ [317]. The EFT agrees very well with the VLQ model in the region of validity $M_{hh} < M_{T_{1,2}}, M_{B,1,2}$. In the EFT it is clear that the single and double Higgs rates depend on the same parameters. Hence, the two rates are tightly related, and indeed de-correlated [317]. That is, if the single Higgs rate increases the
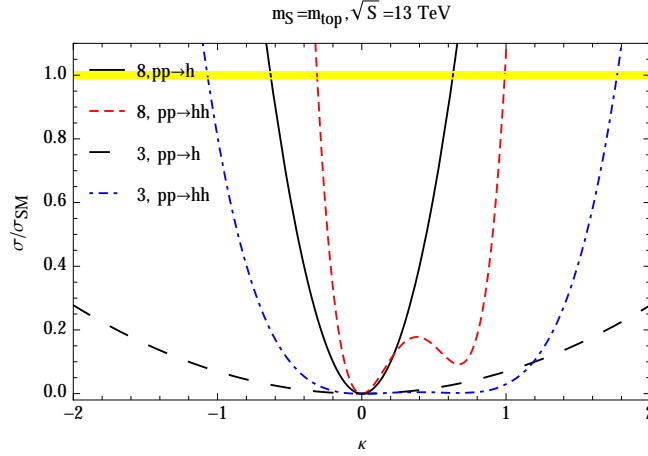
Figure 3.16: Comparison of $1h$ (dashed black) and $2h$ production (blue dot-dash) to the SM rate, when the SM top quark is replaced by a color triplet scalar with mass, $m_s = 173$ GeV. The solid black (red dashed) curves correspond to the ratios to the SM predictions for $1h$ and $2h$ with a color octet scalar replacing the top quark [323].

double Higgs rate is decrease. Since single and double Higgs rates are bound together, we must go to a region of parameters space where new particles are light and the EFT is not valid [180, 306, 318].

Colored scalars

We consider an $SU(2)_L$ singlet, $SU(3)_c$ complex scalar, s,

$$\mathcal{L}_{s,c} = (D_\mu s)^* (D^\mu s) - m_0^2 s^* s - \frac{\lambda_s}{2} (s^* s)^2 - \kappa s^* s \left| H^\dagger H \right| + \mathcal{L}_{SM}, \qquad (3.53)$$

where H is the SM $SU(2)_L$ doublet with $\langle H \rangle = (0, v/\sqrt{2})^T$. If the scalar, s, is real,

$$\mathcal{L}_{s,r} = \frac{1}{2} (D_\mu s)(D^\mu s) - \frac{m_0^2}{2} s^2 - \frac{\lambda_s}{4} s^4 - \frac{\kappa}{2} s^2 \left| H^\dagger H \right| + \mathcal{L}_{SM}. \qquad (3.54)$$

The physical mass for either a real or complex scalar is, $m_s^2 = m_0^2 + \frac{\kappa v^2}{2}$ and $m_0 = 0$ is the limit where the scalar gets all of its mass from electroweak symmetry breaking.

Scalar Top Partners

We compare the results for HH production when the loop particles are the SM top with those for a colored scalar with $m_s = m_t = 173$ GeV. Fig. 3.16 shows the ratio of the total cross sections for both $1h$ and $2h$ production, normalized to the lowest order SM predictions in this scenario. We note that in order to reproduce the SM rate for $1h$ production (the black dashed line), κ needs to be quite large, $\kappa \sim 2$. If κ is tuned to obtain $\sigma/\sigma_{SM} = 1$ for $gg \to h$, then a color octet intermediate particle replacing the top quark with positive κ (the solid black line) would predict a highly suppressed rate for $2h$ production (the red dashed line). Although the total rates are identical to the SM predictions, the kinematic distributions from color octet and triplet intermediate states are quite different than those from the SM top, as plotted in Fig. 3.17. The scalar needs to be quite light to reproduce the SM rates, and the distribution is peaked at much lower m_{hh} than the SM prediction.

Assuming the top Yukawa is SM-like, adding an additional scalar receiving all of its mass from electroweak symmetry breaking gives an unacceptably large contribution to the $1h$ production
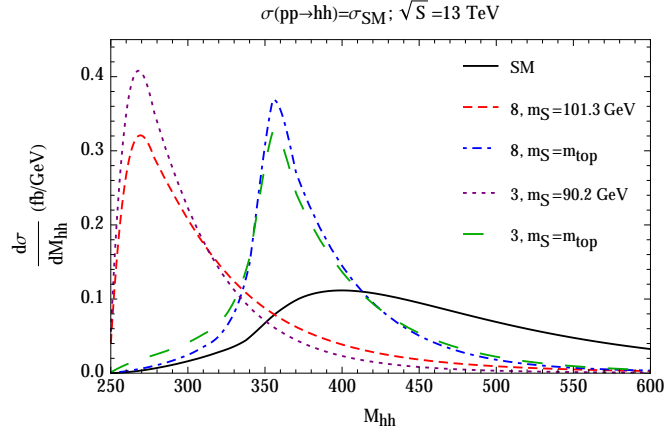
Figure 3.17: Distributions for $2h$ production when the parameters are tuned to give the SM total cross sections for $1h$ and $2h$ production [323].
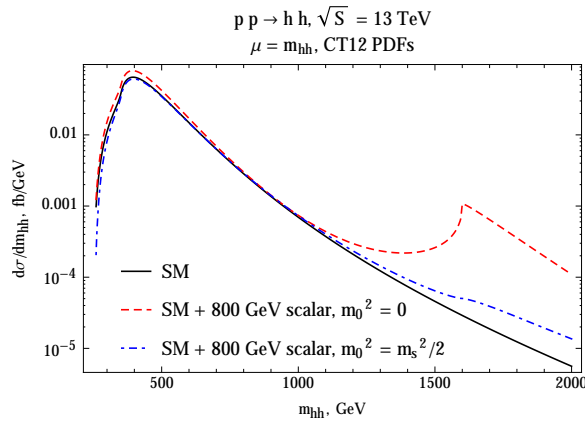

Figure 3.18: Invariant mass distribution in $2h$ production with the SM top quark in addition to an 800 GeV color triplet scalar that gets all (red dashed) or half (blue dot-dashed) of its mass from the Higgs. The SM (black solid) is shown for comparison [323].

cross section, regardless of the scalar mass and $SU(3)$ representation. A heavy color triplet scalar with $\kappa = 2m_s^2/v^2$, for example, changes the $1h$ production rate by 54%. Lighter scalars and scalars in other color representations result in even larger deviations. Heavy scalars receiving all their masses from the Higgs have $m_0 = 0$, and are not compatible with LHC limits on the $1h$ production rate from gluon fusion. Heavy scalars decouple quickly in the $1h$ rate and may show up in the high m_{hh} tail of the $2h$ distribution. The invariant mass distributions for $2h$ production are shown in Fig. 3.18 assuming a SM-like top quark and an additional 800 GeV color triplet scalar. If the scalar receives half of its mass squared from electroweak symmetry breaking, $m_0^2 = m_s^2/2$, the $1h$ rate is in roughly 2σ tension with the current measurement, and the $2h$ distribution deviates from the SM expectation starting at $2m_s$, roughly speaking.
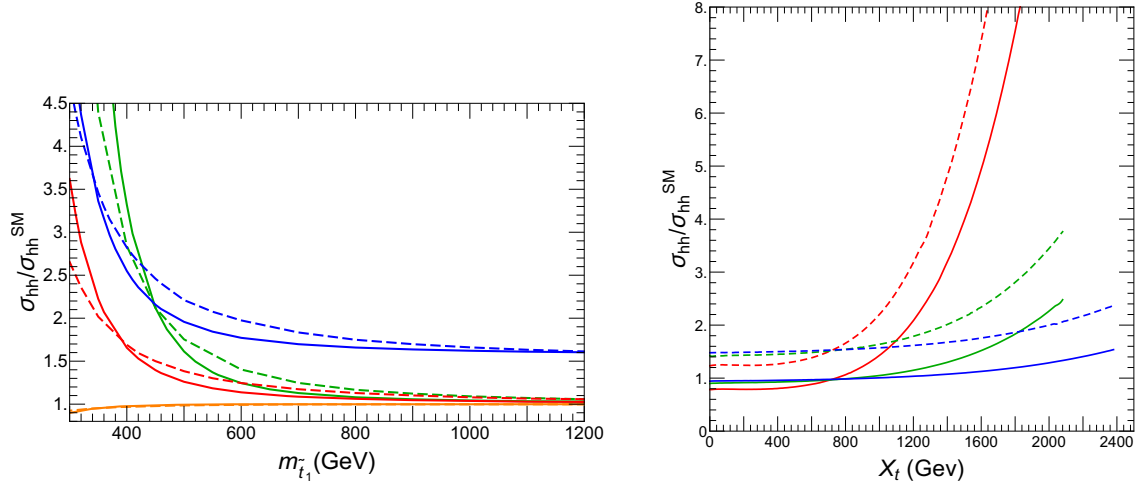
Figure 3.19: Double Higgs production cross section normalized to the SM values as a function of the lightest stop mass(left) and X_t(right) [318]. The color coding is explained in the main text.

MSSM

P. Huang

Now we discuss the modification to double Higgs production in the presence of light stops [180, 305, 318]. We first write down the stop mass matrix

$$\mathbf{M}_{\tilde{\mathbf{t}}}^{\mathbf{2}} = \begin{pmatrix} m_Q^2 + m_t^2 + D_Q & m_t X_t \\ m_t X_t & m_U^2 + m_t^2 + D_U \end{pmatrix}. \tag{3.55}$$

The parameters m_Q and m_U are soft SUSY breaking mass terms of the left-handed and right-handed stops respectively, X_t is the stop mixing parameter, D_U and D_Q are the D-term contributions. The dimensionful trilinear coupling of the Higgs to the stops has a strong dependence on the Higgs mixing parameter X_t, which can be larger than the stop masses. Given that the LHC has excluded stops that are not significantly heavier than the top quarks, a large X_t is preferred to generate relevant contributions to the double Higgs production cross section. However, a large X_t may affect the Higgs vacuum stability [324–329], which leads to constraints in the stop sector in addition to constraints from the direct stop searches. X_t also contributes to the gluon fusion of a single Higgs production. Including possible modifications in the Higgs coupling to tops, the modification in κ_g is given by [330–334]

$$\kappa_g = \kappa_t + \frac{\kappa_t}{4} m_t^2 \left[\frac{1}{m_{\tilde{t}_1}^2} + \frac{1}{m_{\tilde{t}_2}^2} - \frac{\tilde{X}_t^2}{m_{\tilde{t}_1}^2 m_{\tilde{t}_2}^2} \right], \tag{3.56}$$

with κ_i defined as g_{hii}/g_{hii}^{SM}.

The contribution of light stops to double Higgs production is summarized in Fig. 3.19 [318]. In the left panel of Fig. 3.19, we show the double Higgs production cross section normalized to the SM value as a function of the light stop mass using the full one loop calculation (solid lines), and the EFT calculation (dashed lines). κ_t is chosen to be 1 for the orange, red and green lines, and 1.1 for the blue lines. For the orange line, X_t^2 is chosen to be $m_{\tilde{t}_1}^2 + m_{\tilde{t}_2}^2$. This choice makes the effective Higgs gluon coupling SM like. In the red and blue lines, instead, X_t^2 is chosen to saturate

the vacuum stability condition,

$$A_t^2 \leq \left(3.4 + 0.5 \frac{|1-r|}{1+r} \right) (m_Q^2 + m_U^2) + 60 \left(\frac{m_z^2}{2} \cos(2\beta) + m_A^2 \cos^2 \beta \right) \tag{3.57}$$

in a conservative way by neglecting the m_A and m_Z terms, For the green lines, X_t^2 is chosen to saturate the vacuum stability condition with $m_A = 350$ GeV, $\mu = 400$ GeV, and $\tan\beta = 1$. In the right panel of Fig. 3.19, we show the effect of stop mixing parameter X_t on the double Higgs production cross section for a fixed value of the mass of the lighter stop. Red, green and blue lines represent fixed lighter stop mass of 300, 400 and 500 GeV respectively. Solid lines correspond to $\kappa_t = 1$, while dashed lines correspond to $\kappa_t = 1.1$.

The cross section for a given final state depends not only on the double Higgs production cross section, but also on the relevant Higgs decay branching ratios. In the MSSM, some small modifications to the Higgs decay branching ratios are expected. The largest modification is about $\pm 20\%$ for the $b\bar{b}\gamma\gamma$ channel [318]. Light stops also lead to modifications to the double Higgs invariant mass distribution. In the presence of a light stop, the amplitudes develop imaginary parts when the invariant mass m_{hh} crosses the $2m_{\tilde{t}}$ threshold, inducing a second peak in the m_{hh} distribution a little above $2m_{\tilde{t}}$ [318].

3.6   Connection to Cosmology

J. Kozaczuk, A. Long, K. Sinha

Measurements of di-Higgs production test the hypothesis that the Higgs boson couples to new physics with a mass scale $m \sim 100\,\text{GeV} - 1\,\text{TeV}$. In the hot conditions of the early universe, these particles would have been in thermal equilibrium with the SM plasma. As the universe expanded and cooled, the presence of this new physics could affect the nature of the electroweak phase transition (EWPT).

Electroweak phase transition and electroweak baryogenesis: The electroweak phase transition is the dynamical process by which the Higgs field acquired its nonzero vacuum expectation value in the early universe. The SM predicts that the phase transition is a smooth, continuous crossover with the Higgs field evolving almost homogeneously from 0 to $246\,\text{GeV}$ as the temperature is decreased through the weak scale. However, the presence of new physics can easily and dramatically change the predicted nature of the phase transition, even leading to a first order phase transition. Unlike the gentle continuous crossover, a first order phase transition is a violent event during which bubbles nucleate, expand, collide, and eventually merge to overtake the whole system. Today, our understanding of Higgs physics is too poor to discriminate between even these two qualitatively different scenarios.

If the cosmological electroweak phase transition was a first order one, it would have profound implications for cosmology. The out-of-equilibrium conditions of a first order phase transition provide the right environment for the generation of cosmological relics. In this way, a first order electroweak phase transition could explain why our universe has an excess of matter over antimatter on cosmological scales through the mechanism of electroweak baryogenesis [121, 335]. A strong first-order electroweak phase transition can have other interesting cosmological consequences, such as the dilution of pre-existing thermal relics through entropy injection [336] and the generation of a stochastic gravitational wave background (discussed below).

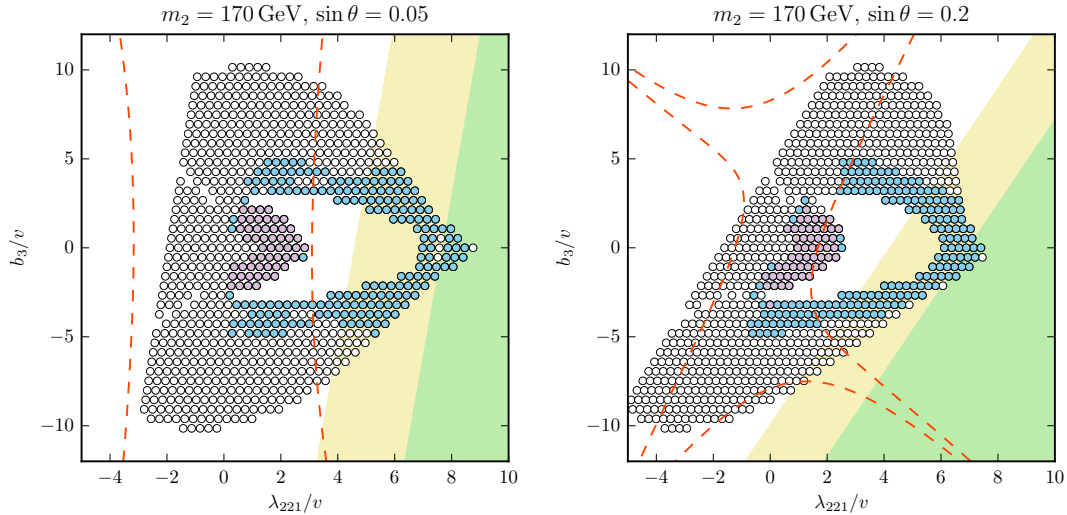Double Higgs production at colliders allows for a direct probe of the couplings in the Higgs po-

Figure 3.20: Figure adapted from Ref. [337] showing slices of the real singlet extension of the SM for a singlet-like scalar mass of 170 GeV and two different mixing angles with the Higgs. Blue and purple shaded points feature a strong first-order electroweak phase transition. Regions outside of the red dashed contours feature deviations in the 125 GeV Higgs self-coupling larger than 30%. The green (yellow) shaded regions show the discovery (exclusion) reach for pair production of the new scalar at the 14 TeV HL-LHC in a trilepton final state discussed further in Ref. [337].

tential responsible for strengthening the electroweak phase transition. A typical example of this in the real singlet extension of the SM is illustrated in Fig. 3.20 (adapted from Ref. [337]), which shows slices of the parameter space consistent with a strong first-order electroweak phase transition (blue and purple points). Outside of the red dashed contours the deviations in the Higgs self coupling are larger than 30%. Precise measurements of the double Higgs production rate can thus provide a powerful probe of the electroweak phase transition in this scenario (see also Ref. [338]). Similar conclusions hold in other extensions of the SM as well [120, 123]. For scenarios in which a new scalar heavier than 250 GeV coupled to the Higgs generates a strong first-order EWPT, resonant double Higgs production mediated by the new scalar provides a powerful handle on the nature of electroweak symmetry breaking [193]. The prospects for such a search at the high luminosity LHC are shown in Fig. 3.21 (adapted from Ref. [209]), again for slices of the singlet model parameter space. Strong first order phase transitions generated by new scalars with masses up to the TeV scale can be probed by resonant di-Higgs production (see also Refs. [190, 193, 203]). In models with additional scalars, pair production of the other scalar states can provide a complementary probe of the electroweak phase transition [337, 339]. The shaded regions of Fig. 3.20 correspond to the projected HL-LHC sensitivity to pair production of singlet-like scalars in a particular trilepton channel detailed in Ref. [337]. The sensitivity shown is likely conservative, and searches for double scalar pair production involving states other than the 125 GeV Higgs can be a promising avenue for probing electroweak symmetry breaking in the early Universe at the LHC and beyond.

Complementarity with gravitational wave observations: The inhomogeneous nature of a first order phase transition provides the requisite quadrupole moment to source gravitational waves [340]. Since gravitational waves are very weakly interacting, they propagate freely until reaching us at Earth today. If we can observe this primordial stochastic gravitational wave background, it could provide direct evidence for a first order electroweak phase transition and thereby indicate the presence of new physics coupled to the Higgs.

Our ability to measure gravitational waves (GWs) has recently been demonstrated in spectac-
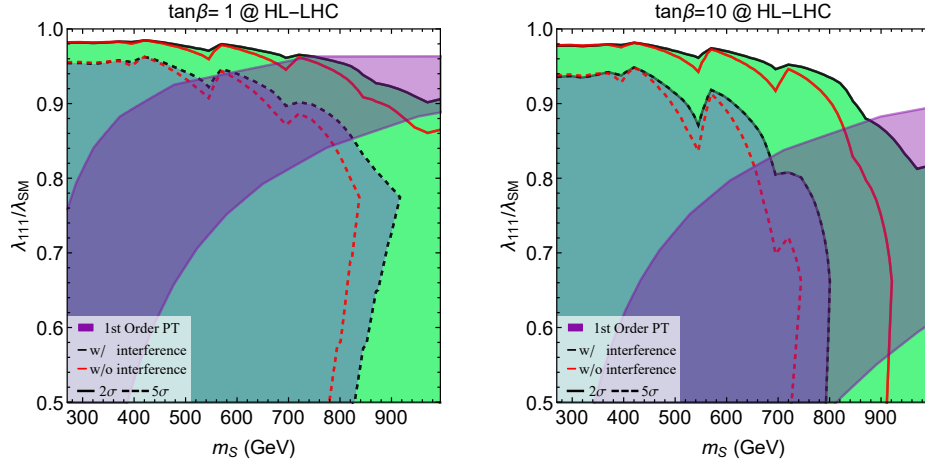
Figure 3.21: Sensitivity of resonant di-Higgs production (black and red contours) to regions of the singlet model parameter space with a strong first-order electroweak phase transition (purple). Details can be found in Ref. [209] from which this figure was adopted.

ular fashion by the LIGO and VIRGO collaborations [341]. Moreover, efforts are underway to build and launch a gravitational wave interferometer in space. The Laser Interferometer Space Antenna (LISA) [342] collaboration has recently celebrated a successful pathfinder mission and is expected to be launched in the early 2030s. With an interferometer that is no longer tethered to the Earth, the length of its arms can be increased to millions of kilometers, which gives it sensitivity to the $\sim$ mHz gravitational waves that are expected to arise from a first order electroweak phase transition [343].

It is important to understand how future collider measurements, such as Higgs pair production, and observations of a stochastic GW background can complement each other in exploring new physics yielding a strong first-order electroweak phase transition. The simplest template where these questions can be studied is an extension of the SM by a singlet scalar discussed above. The complementarity between GW and collider measurements has recently been explored in this model by the authors of Refs. [208] and [207], and we summarize the main results here. The left panel of Fig. 3.22 displays the GW spectrum obtained at a benchmark point in this model which is compatible with electroweak precision measurements and all other phenomenological constraints. The mass of the extra singlet is 455 GeV. The total GW signal is shown in red, while the different contributions from sound waves (turbulence) are shown in blue (brown). The color-shaded regions are the experimentally sensitive regions for various GW detectors. The right panel of Fig. 3.22 shows AT-LAS (solid green lines) [66] and CMS (solid brown lines) [67] limits on resonant di-Higgs production for 36.1 fb^{-1} and 35.9 fb^{-1} of data, respectively, combining several final states. A simple rescaling of the current limits to 3000 fb^{-1} at the HL-LHC (13 TeV) is performed to obtain the corresponding dashed line future projections. For the points on the parameter space giving detectable GWs with a signal-to-noise ratio at LISA larger than 10, the resonant cross sections from gluon fusion at NNLO+NNLL are computed using the results in [19]. It is clear that resonant di-Higgs studies at the HL-LHC and GW signals from LISA can play complementary roles in exploring this model in the future.
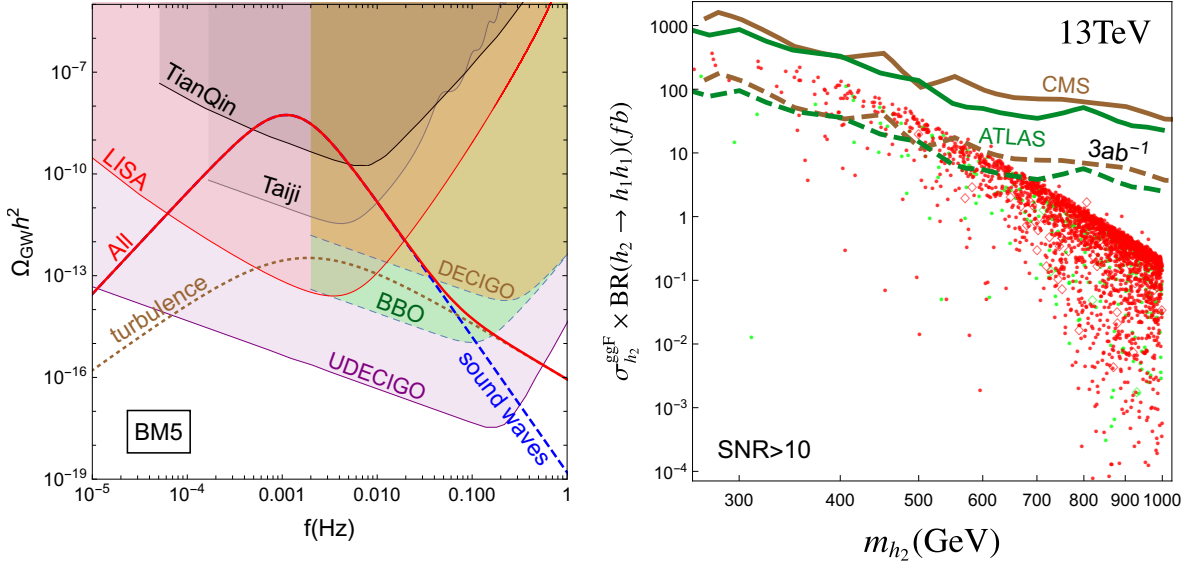
Figure 3.22: Left panel: GW spectrum obtained at a benchmark point in the singlet-extended SM. Figure adapted from Ref. [208]. Right panel: Current and future ATLAS/CMS di-Higgs sensitivity to points predicting a signal-to-noise ratio larger than 10 at LISA. Figure adapted from Ref. [207]. Details in text.

3.7 *HH* and Dark Matter (Missing Energy)

*M. Blanke, S. Kast, J. Thompson, S. Westhoff, J. Zurita*

The final state of two Higgs bosons plus missing transverse energy was originally studied in the context of Goldstino dark matter [344], which is currently the new-physics model that the existing LHC searches [345,346] target. More recently it was realized that *di-Higgs plus E_T* is a signature that also occurs in a plethora of other BSM scenarios including a dark sector [347–354].

In Ref. [355], a detailed analysis of the final state with four *b*-quarks and large missing energy in the High Luminosity phase of the LHC was carried out. Here we provide a summary of the most salient findings and refer the reader to Ref. [355] for further details. The large backgrounds (V + jets, $t\bar{t}$, etc.) and the complex kinematics of the final require a multi-variate analysis (MVA), which we summarize here.

Since many new-physics models can give rise to the same final state, it is important to define physics scenarios that do not depend (crucially) upon the detailed field content, but rather on the masses and couplings that characterise the signature. To this end we have introduced two simplified models targeting two different final-state topologies. Both models feature three new scalar particles, dubbed B, A and χ (invisible), with the production mechanism $gg \rightarrow B \rightarrow AA$, through a dimension-five operator $BG_{\mu\nu}^a G^{\mu\nu a}$. We then have two options for A to decay: either $A \rightarrow h\chi$ for both A bosons (symmetric topology) or $A \rightarrow hh$ and $A \rightarrow \chi\chi$ simultaneously (resonant topology). We restrict ourselves to mass spectra where all these states are produced on-shell. Moreover, we assume all new fields to be SM singlets, and we impose a discrete $\mathbb{Z}_2$ parity under which all SM fields and B are even, χ is always odd and A is even (odd) in the resonant (symmetric) topology. The Feynman diagrams for the $hh + E_T$ final state are shown in Fig. 3.23.

In our study we use the scikit-learn [356] implementation of AdaBoost [357], employing the SAMME.R algorithm to perform a Boosted Decision Tree (BDT) classification (70 trees, maximal depth of 3, learning rate of 0.5, minimum node size of 0.025 of the total weights). We apply a $E_T >$ 200 GeV cut, as we found the inclusive E_T trigger better suited for our purposes than triggering

symmetric topology   resonant topology
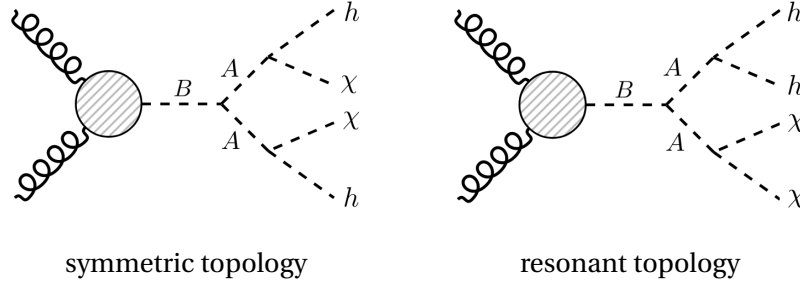
Figure 3.23: Topologies for a scalar resonance B decaying into hh plus $\not{E}_T$.
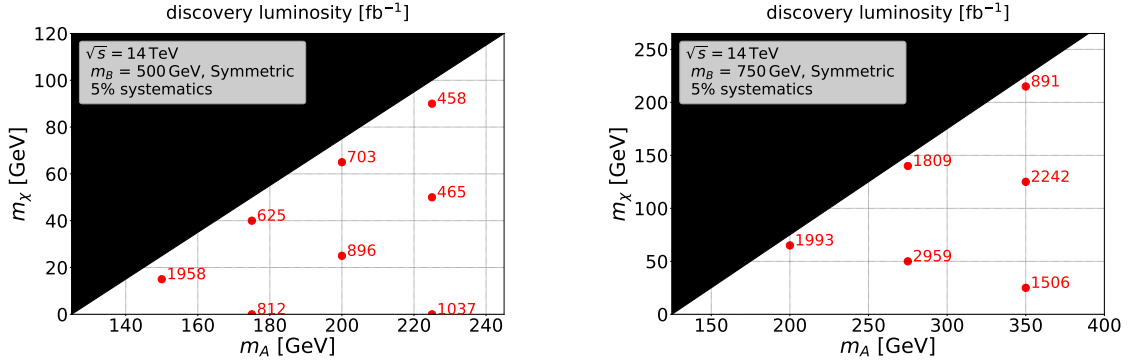
Figure 3.24: Luminosity required for a discovery (in fb^{-1}) at the HL-LHC in the $m_A - m_\chi$ plane for the symmetric model, with $m_B = 500$ GeV (left panel) and $m_B = 750$ GeV (right panel) [355].

on the jets. We employ a modified version of the BDRS algorithm [358], and cluster fat jets with $R = 1.2$ ($R = 0.6$) for the symmetric (resonant) topology, demanding to have at least one b-tagged subjet within each fat jet, and veto events with leptons. The input variables include the p_T, η, ϕ, m of the fat jets and subjets, global variables such as $\not{E}_T$, H_T, the number of fat jets and subjets, and finally variables for the di-fat jet and $\not{E}_T$-fat jet systems, e.g. $\Delta\Phi(J, \not{E}_T)$, $\Delta R(J_1, J_2)$. We define the significance as

$$\Sigma = \frac{S}{\sqrt{\alpha S + B + \beta^2 B^2}},\tag{3.58}$$

where S and B are the number of signal and background events, $\alpha = 0$ (1) for exclusion (discovery) and β is the systematic uncertainty, which we fix here to 5 %. To be conservative we add an additional layer of cautiousness and define *exclusion* as $\Sigma(\alpha = 0) = 3$ (instead of the usual 2) and *discovery* as $\Sigma(\alpha = 1) = 7$ (instead of the usual value of 5). Moreover, in order not to be pushed to very sparsely populated regions of phase space, we also request $S \geq 20$.

We present our results in terms of the scalar masses for a total integrated luminosity of 3 ab^{-1}. In Fig. 3.24, we display the luminosity required to discover the symmetric scenario at the HL-LHC, fixing $m_B = 500$ GeV (left panel) and $m_B = 750$ GeV (right panel). Except for one point, all scenarios are well within the reach of the HL-LHC, and thus we also present, in Fig. 3.25, the results in terms of the minimal cross section that can be discovered with a luminosity of 3 ab^{-1}. The latter has the advantage of providing results that can be readily applied to a larger class of models.

In the resonant model, the planned HL-LHC luminosity is not sufficient to exclude (left) or discover (right) any of the benchmark scenarios, due to the lower production rates.[11] We therefore confine ourselves to presenting the cross sections required to discover a particular resonant bench-

---

[11]This is due to the additional final states, e.g. $WW, ZZ + \not{E}_T$, arising in this model, that can be targeted by complementary searches.
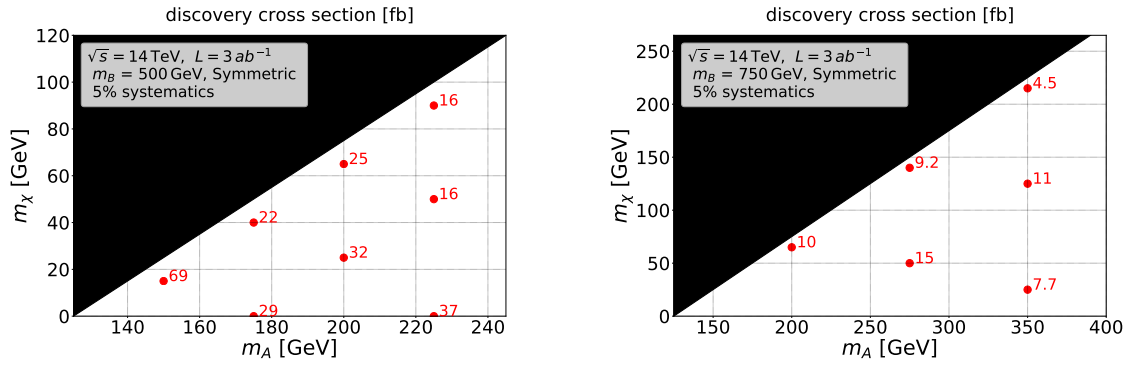
Figure 3.25: Cross sections (in fb) required for a discovery at the HL-LHC in the $m_A - m_\chi$ plane for the symmetric model, with $m_B = 500$ GeV (left panel) and $m_B = 750$ GeV (right panel) [355].
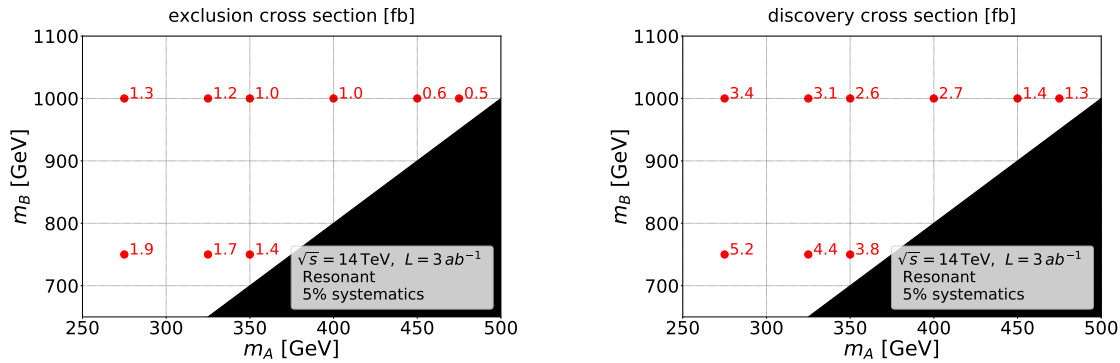

Figure 3.26: Cross sections (in fb) required for exclusion (left) and discovery (right) at the HL-LHC in the $m_A - m_\chi$ plane for the resonant model, with $3\,\mathrm{ab}^{-1}$. Here we have fixed $m_\chi = 25$ GeV, but this parameter is not relevant for the sensitivity provided that $2m_\chi < m_A$ [355].

mark in Fig. 3.26. The mass of the lightest scalar, m_χ, does not affect the sensitivity, since the boost of A does not depend on m_χ or m_h. We therefore present our results in terms of the heavier scalar masses m_A and m_B. From the figure, we see that we can test cross sections in the femtobarn and sub-femtobarn regime. As in the symmetric model, the significance increases when the spectrum is compressed.

We note that in a complete model involving additional couplings, χ could either be the dark matter or a long-lived neutral particle that decays outside the LHC detectors. Dark matter direct detection experiments on the one hand and searches for long-lived particles (see e.g. [359–363]) on the other hand thus serve as complementary probes of the nature of χ.

As a final remark, we would like to stress that we have verified, using `CheckMATE2` [364], that even with the largest possible cross section displayed here, the search for di-Higgs plus E_T is still the most sensitive channel for both symmetric and resonant topologies. We thus encourage the ATLAS and CMS collaborations to expand their di-Higgs portfolio of searches by including a topology-based study of the Higgs pair plus missing transverse energy final state.

3.8 Summary: precision goals for the measurement of the Higgs pair production process in the light of new physics

We can usefully summarize this chapter as a set of goals for the measurement of the Higgs pair production process. While one of the major objectives is certainly the determination of the trilinear Higgs self-coupling, many models have new particles that can be directly searched for in observables related to the Higgs boson. One of the most spectacular signatures of new physics in the Higgs sector is resonant double Higgs production (see Secs. 3.1, 3.3 and 3.4). In models with *s*-channel resonances, the di-Higgs invariant mass spectrum can be distorted compared to the SM distribution, with an additional peak appearing at the mass of the new resonance, as we see, for example, in Fig. 3.4. Care must be taken to incorporate interference effects to correctly interpret results (see Sec. 3.2).

We have furthermore discussed how large the trilinear Higgs self-coupling can realistically be. In Sec. 2.2 we have seen how large the modifications to the di-Higgs production cross section can be in concrete models. We are hence now in the position to give a catalogue of precision goals for the measurement of the di-Higgs production process that might be obtained in future experiments, and the implications of each level for the discovery of effects due to new physics models.

Beyond di-Higgs production, many of the models in Sec. 3.4 have additional scalar particles. These new scalars can also be produced in pairs or in association with the observed Higgs boson, expanding di-Higgs production to di-scalar production. These new modes provide a new, robust phenomenology for colliders. Searches for these new modes are important for fully mapping out the Higgs potential and, in addition to a modified trilinear Higgs self-coupling, even helping to determine if electroweak baryogenesis is the source of the baryon asymmetry of the Universe (see Sec. 3.6).

The above discussion is focused on probing modifications to the Higgs sector and searching for trilinear scalar couplings. However, we have seen in Chapter 2 that other effective operators can substantially modify the di-Higgs production process. In particular, loops of new strongly interacting particles can affect the di-Higgs production cross section, and it is hence important to properly include their effects (see Sec. 3.5).

We now provide an indicative summary of what experimental precision on the di-Higgs measurement is needed to probe the different BSM phenomena we have surveyed in this chapter:

- **Bronze: Precision of 100%:** Measurements at this level are sensitive to models with the largest new physics effects, in which new particles of few hundred GeV mass appear in tree diagrams or as *s*-channel resonances. Depending on the model, the heavy new resonance often has sizeable branching ratios also to VV final states. We have discussed in Sec. 3.1 models with singlets which allow for sizeable branching ratios of a heavy Higgs boson to light Higgs bosons, with values of maximally $BR(H \to hh) = 0.4$ for singlet models with Z_2 symmetry, while larger $BR(H \to hh)$ are possible without Z_2 symmetry.

- **Silver: Precision of 25–50%:** Measurements at this level are sensitive to mixing of the Higgs boson with a heavy scalar with a mass of order 1 TeV. Models of electroweak baryogenesis typically predict this level of deviation in the trilinear Higgs self-coupling. At this level of precision we are able to exclude a physical hypothesis with realistic deviations in the Higgs self-coupling, rather than just eliminating parts of parameter space.

- **Gold: Precision of 5–10%:** Measurements at this level are sensitive to a broad class of loop diagram effects that might be created by light top squarks and or other new particles with

strong coupling to the Higgs sector. Measurements at this level could possibly complement measurements on new particles that could be discovered at the HL-LHC.

- **Platinum: Precision of 1%:** Measurements at percent level are sensitive to typical quantum corrections to the Higgs self-coupling generated by loop diagrams.

In the remainder of this report, we will see how the capabilities of the LHC and of future experiments on the measurement of the di-Higgs production process and the extraction of the Higgs self-coupling align with these goals.

Part II

Status of the measurements at LHC

The Higgs self-coupling can be probed at the LHC directly through Higgs boson pair production or indirectly by exploring the radiative corrections to single Higgs measurements.

Both ATLAS and CMS experiments have developed a wide set of searches to test the SM prediction for the Higgs boson self-coupling. In this Part, we aim to provide an exhaustive overview of the current experimental effort to test the Higgs boson self-coupling through both the double and single Higgs boson productions processes. Direct searches for new resonant states decaying to HH pairs will also be summarised. We hope that the reader will find this overview useful for experimental studies at the LHC and future colliders.

Chapter 4 provides an overview of the online selections (trigger), the detector object reconstruction techniques and the calibration strategies specific for HH final states are reviewed.

Depending on the decay mode of the Higgs boson, a rich variety of signatures is available to probe the production of HH pairs. Chapter 5 presents an overview of the results of the searches for both non-resonant and resonant HH production through gluon-gluon fusion from the ATLAS [365] and CMS [366] experiments, based on the data recorded between 2015 and 2018, corresponding to an integrated luminosity of up to about 126 fb^{-1}.

A discussion on how ATLAS and CMS collaborations could generalize the presentation of the results and possibly allow their re-interpretations under specific models is given in Chapter 6.

The results of all the searches for HH production at the LHC are presented in Chapter 7 under different beyond the SM hypotheses. A first attempt to combine statistically the ATLAS and CMS results is also discussed. When possible, recommendations are provided on how to improve the current measurements and expand the interpretation of the experimental results. The first experimental results from the indirect determination of κ_λ via precision measurements of single Higgs processes, as described in Chapter 2 are also presented and discussed.

Chapter 4

Detector objects, triggers and analysis techniques

Editors: M. A. Kagan, L. Mastrolorenzo

In both ATLAS and CMS, the particles used to reconstruct the Higgs decays are identified by combining the information of several sub-detectors based on different technologies. A detailed description of the ATLAS and CMS detectors, together with a definition of the coordinate system and the relevant kinematic variables, can be found in Ref. [365, 366]. ATLAS and CMS have different concept and detector specifics but similar capabilities.

ATLAS has optimised the detector design to have good stand-alone measurements from each subsystem. Indeed it employees a toroidal magnet field for a stand-alone muon momentum measurement, in addition to the solenoid used for the momentum measurements in the inner detector.

CMS instead has put major emphasis on the tracker system, consisting of all silicon detectors, and relies on a very strong solenoid magnet field to achieve excellent transverse momentum resolution. Both the ATLAS and CMS calorimeter systems have two separate sub-detectors for the reconstruction of electromagnetic and hadronic showers. Both the electromagnetic and hadronic calorimeters for ATLAS have longitudinal and transverse segmentation, while CMS exploits longitudinal segmentation only in the hadronic calorimeter. As a result, while the ATLAS calorimeter allows a good calibration of the energy of hadronic objects and stand-alone reconstruction of the jet direction, CMS has to combine with information from the tracking system in order to achieve similar performance for the jet measurements and pile-up subtraction. Dedicated algorithms are needed in order to identify different particles. Most of them relies on machine learning techniques, such as Neural Networks (NN) or Boosted Decision Tree (BDT), which combine multiple observables at once to achieve good performance [367]. The algorithms are calibrated using data from well understood SM processes and the correction derived are then applied to the simulation to match the observed detector response. In the following we will describe how jets are reconstructed and identified as initiated from b-quarks, as well as the τ and photon reconstruction algorithms. The case when two objects are merged due to the high momentum of the parent particle (boosted objects) is also discussed. In addition, dedicated strategies have been developed to identify final state particles in a very short time to make real time decision whether to save a collision event to disk or discard it. In this Chapter, the online selections (applied at trigger level) and the calibration strategies specific for HH final states (such as kinematic fit) are reviewed. In particular differences between ATLAS and CMS strategies are reported when relevant. Possible improvements and limitations of the current algorithms are also discussed.

4.1   Jet reconstruction

M. Swiatlowski

Quarks and gluons fragment (hadronisation) into a large number of stable particles, which result in narrow cones of hadrons, called "jets". Jets are reconstructed with the anti-k_T [78] clustering algorithm with a distance parameter $R = 0.4$. Due to the differences between the calorimeter and tracking systems, ATLAS and CMS employ different sets of inputs to the jet clustering algorithm. ATLAS uses topological clusters composed of calorimeter cells and applies corrections to the energy measurement based on the longitudinal profile of the energy deposits in the calorimeters, as well as the shape and number of associated inner-detector tracks. CMS, on the other hand, uses "particle flow" objects [368] which exploits the information from all sub-detectors and aims at reconstructing and identifying all stable particles in the event (μ, e, γ, π etc...). The particle flow algorithm matches inner-detector tracks to calorimeter energy depositions and perform a combined energy measurement, weighted by the expected resolutions of each detector. Thus, it compensates the calorimeter energy resolution with the tracker information at low p_T. Moreover the particle flow approach allows for the subtraction of energy deposits originating from pileup improving the jet energy resolution, especially at low p_T.

ATLAS is also considering moving to a particle flow approach for the end of Run 2 analyses [369]. In the meanwhile, in order to reduce the impact of pileup, ATLAS requires a significant fraction of the tracks associated with each jet below a certain p_T threshold to have an origin compatible with the primary vertex, as defined by the jet-vertex-tagger (JVT) algorithm [370].

Techniques are in place to reduce the impact of pileup on the mis-reconstruction of the jet properties, also known as pileup mitigation techniques. Several approaches have been exploited so far. The jet-area method [371] evaluates the average neutral energy density from pileup interactions and subtracts it from the reconstructed jets. The pileup per particle identification (PUPPI) algorithm [372] in CMS assigns a weight to each particle prior to jet clustering based on the likelihood of the particle originating from the hard scattering vertex. Pileup mitigation will present a significant challenge as the colliders move to higher instantaneous luminosity values. Improving the jet resolution by more accurately removing pileup contamination will lead to narrower signal distributions, allowing for increased sensitivity of nearly the entire HH search program, especially as the pileup is expected to grow to more than three times the current levels at the HL-LHC.

The jets reconstructed in the detectors are calibrated to the particle level (excluding neutrinos) using a multi-stage calibration procedure [373,374]. It includes MC corrections taking advantage of MC truth and data-driven approaches used to uniform the detectors response and to provide scale factors to correct for simplified detector simulation.

Searches for new resonances decaying to HH with mass above 1 TeV (high mass), the resulting Higgs bosons have a momentum considerably higher than their mass. Thus, each $H \rightarrow b\bar{b}$ decay is reconstructed more efficiently as one hadronic jet with a larger anti-k_T distance parameter: $R = 1.0$ (ATLAS) or $R = 0.8$ (CMS). As with $R = 0.4$ jets, CMS uses particle flow objects as inputs, whereas ATLAS uses clusters of calorimeter cells only.

The larger jet size leads to increased susceptibility to contamination from underlying events and pileup. Specific algorithms, grooming, are employed to reduce contributions from soft and wide angle radiation by re-clustering the jet constituents, and as a result they help to mitigate pileup effects.

Different "grooming" algorithms are applied to large-radius jets to allow a better identification of the substructure of the $W/Z/H$-initiated jets, resulting from the decay to two partons at LO in

QCD (2-prong decay). The resolution of the H-jet mass is improved by grooming since it filters out contributions from soft and wide angle radiation that affects significantly the estimation of the original invariant mass of the two-prong system.

The optimal choice of the grooming algorithm depends significantly on the specifics of the detector. Few options have been proposed such as trimming [375], employed by ATLAS, pruning [376] and soft-drop [377, 378], used by CMS. A review of the performance of these algorithms can be found in Ref. [379].

ATLAS has recently validated large-radius jets that incorporate combined inner-detector and calorimeter information. These "track-calorimeter-cluster" jets use the improved angular reconstruction of the inner detector and the improved energy measurements of the calorimeters in order to significantly improve the resolution at high p_T.

4.2 Identification of *b*-jets

M. A. Kagan, L. Mastrolorenzo, C. Vernieri

The ability to correctly identify *b*-jets initiated by $H \to b\bar{b}$ decays is crucial to reduce the otherwise overwhelming background from processes involving jets initiated from gluons (g) and light-flavour quarks (u, d, s), and from *c*-quark fragmentation.

The *b*-quark fragmentation process is very peculiar and its properties are fully exploited to achieve good tagging efficiencies. The *b*-quarks hadronise in *B*-hadrons and several hadron particles, mostly pions. In particular, the large lifetime ($c\tau \sim 500~\mu$m) and the relative large mass of *B*-hadrons make *b*-jets unique. A *B*-hadron with $p_\mathrm{T} \approx 50$ GeV will fly about half a centimetre in the transverse plane before decaying. Thus, daughter particles are expected to have a sizeable impact parameter with respect to the *B*-hadron point of origin, the primary collision vertex. In addition, *B*-hadrons are much more massive than anything they decay into, thus the decay products have a momentum of few GeV in the *B* rest of frame. They can be identified by looking for (i) a decay vertex displaced from the primary collision vertex, (ii) tracks with large impact parameter, or distance of closest approach, with respect to the primary collision vertex, (iii) non-isolated leptons from the semi-leptonic decays of *B*-hadrons (soft-leptons). The presence of a lepton in a jet is indeed a good signature of the presence of a *B*-hadron given the high rate of semi-leptonic decays ($\sim 35\%$). Moreover, since the *B*-hadrons retain about 70% of the original *b*-quark momentum [380], usually these leptons have a high p_T relative to the jet p_T which make them easier to identify with respect to other sources of leptons in jets.

The primary source of *b*-jet mis-identification include jets initiated by a charm quark, and light-flavour quark- or gluon-initiated jets that have displaced vertices or large impact-parameter tracks. Jets initiated by *c*-quarks , *c*-jets, are misidentified as *b*-jet due to the relatively large mass and lifetime of charm hadrons, and the presence of charm hadrons in the *B*-hadron decay chain. Light-flavour quark- or gluon-identified jets can be misidentified as *B*-hadrons due to detector resolution effects in the reconstruction of the secondary vertices and the impact parameters, due to the hadron interactions with the material or long-lived particle decays (such as kaon and Λ particles).

Both ATLAS and CMS have dedicated *b*-tagging algorithms which exploit in turn the secondary vertex, impact-parameter, and soft-lepton information [381, 382]. As these algorithms are largely complementary, multi-variate techniques based on neural networks are used to combine these different and complementary sets of information in order to yield the highest performance for a *high-level* tagger. For jets in a $t\bar{t}$ simulated sample with $p_\mathrm{T} > 20$ GeV, with a selection on high-level taggers that results in a 70% *b*-tagging efficiency, ATLAS achieves mis-tag rates of approximately 0.3% for
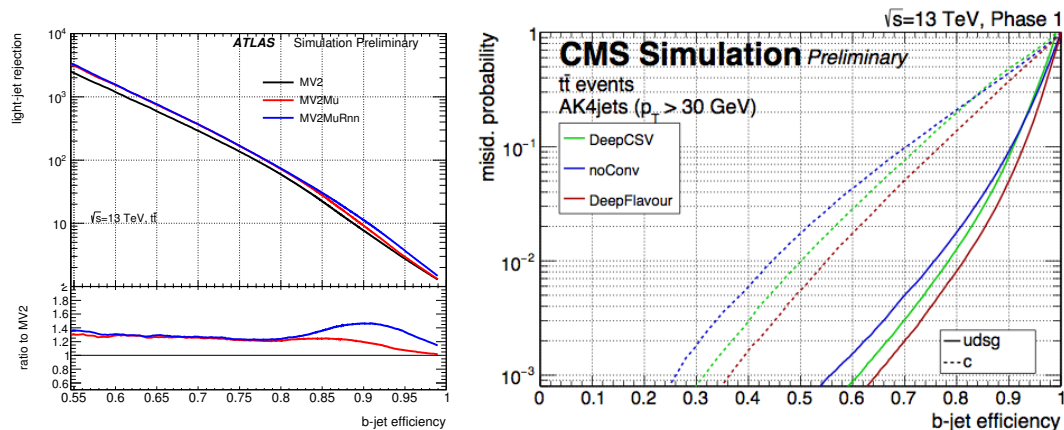
Figure 4.1: Light-flavour and c-jet rejection as a function of *b*-jet efficiency for DNN-based algorithm developed by ATLAS (left) [383]. Comparison between the DeepCSV and DeepFlavour algorithms developed by CMS to identify jets originated by bottom quarks (Right). The plot shows the *b*-tagging efficiency versus the mis-tag rate from light-jets (continuous line) and *c*-jets (dashed line) [385].

light flavoured jets and approximately 11% for charm-initiated jets [383]. The highest performance *b*-tagging algorithm in CMS relies on a deep NN [384], with more hidden layers and more nodes per layer, capable of combining vertexing information, track related variables and the kinematics of jets reconstructed with the particle-flow algorithm, exploiting the correlations between these variables [382, 385]. The performance of the CMS *b*-tagging algorithms has been evaluated for jets with $p_T > 20$ GeV in a simulated sample of $t\bar{t}$ events. For a *b*-tagging efficiency of 68%, the tagger *c*-quark mis-tag rate is 12% and the light-quark mis-tag rate is 1.1%. ATLAS outperforms CMS and this is also related to the different tracking performance.

In Table 4.1 the commissioned working point for some of the CMS and ATLAS taggers most used in the double Higgs boson searches are listed.

Working point	ATLAS Tagger (MV2)			CMS Tagger (Deep CSV)		
	$\epsilon_b(\%)$	$\epsilon_c(\%)$	$\epsilon_l(\%)$	$\epsilon_b(\%)$	$\epsilon_c(\%)$	$\epsilon_l(\%)$
Very loose	85	32	3	–	–	–
Loose	77	20	1	84	40	10
Medium	70	11	0.3	68	12	1.1
Tight	65	6	0.2	50	2	0.1

Table 4.1: Calibrated operating points with relative efficiencies for ATLAS and CMS *b*-tagging algorithms during Run 2, evaluated for jets with $p_T > 20$ GeV from $t\bar{t}$ simulated events [382, 383].

The calibration of the tagging efficiency and mis-tag rates of these algorithms is performed by identifying pure samples of *b*-, *c*-, and light-flavour jets and by measuring the tagging efficiency in $t\bar{t}$ or multi-jet events in data. By comparing to the results from simulation, scale factors can be derived to provide tagging efficiency corrections to the simulation. In ATLAS, scale factors for the *b*-jet tagging efficiency deviate from unity (i.e. no correction) by typically $2 - 4\%$, with uncertainties of $3 - 5\%$ except at low- and high-p_T [386]. ATLAS *c*- and light-flavour-quark mis-tag rate scale factors deviate from unity by typically $2 - 10\%$ and $5 - 30\%$, with uncertainties of $5 - 15\%$ and $30 - 50\%$, respectively [387–389]. In CMS, the measured data-to-simulation scale factors for the tight working point of the DeepCSV algorithm range from 0.9 to 1.0. The relative precision on the scale factors is

1% to 1.5% using jets with $70 < p_T < 100$ GeV and rises to 3% to 5% at the highest considered jet p_T. The relative precision on the light-flavour mis-tag scale factors is 5–10% for the loose working point and 20–30% for the tight working point. For the *c*-quark mis-identification, the relative precision on the scale factor is 3–5% for the loose working point, and 10–38% for the tight working point. Depending on the usage of the *b*-tagging algorithm in physics searches, reshaping scale factors may be needed to correct for the tagger discriminant distribution. For such scale factors related to *c*-jets in resolved topologies, the total uncertainty is 5% to 10%, and the statistical uncertainty in the tagging efficiency dominates over the full jet p_T range.

There are several long-term challenges for *b*-tagging at the HL-LHC. Increased levels of pileup may lead to degradation in tracking performance, both from tracking algorithmic failures producing poor quality or completely fake tracks and from the radiation damage which degrades the pixel detector hit efficiency and resolution. In addition, the larger density of tracks in HL-LHC events can lead to *b*-tagging algorithmic challenges, as identifying the tracks from the *B*-hadron decay and rejecting other tracks becomes increasingly challenging.

4.2.1   Boosted $H \rightarrow b\bar{b}$ taggers

For transverse momenta of the Higgs boson significantly higher than its mass (≈ 250 GeV), the resulting Lorentz boost reduces the angular separation between its decay products. In the case of the decay to *b*-quarks, the Higgs boson is reconstructed as a single large-radius jet ("*H*-jet") and not as two separate jets. Then, the composite nature of such a jet is revealed by analysing its substructure. Several phenomenological studies have explored $H \rightarrow b\bar{b}$ tagging algorithms (or "*H*-tagging") using jet substructure [358], though ultimately the optimal performance comes from using both the substructure information of the fat jet and the track and vertex information related to the *B*-hadrons lifetime [379].

For boosted Higgs-jet identification, ATLAS uses large $R = 1.0$ anti-k_T jets built from calorimeter topological clusters to identify Higgs boson candidates, measure their energy and direction, and estimate a variety of substructure inspired features, for discriminating the $H \rightarrow b\bar{b}$ signal from backgrounds [390]. For identifying *b*-quark candidates, small $R = 0.2$ anti-k_T jets are built from charged particle tracks only, then the aforementioned suite of *b*-tagging algorithms are applied to these jets [390, 391]. Such small radius jets can perform *b*-tagging even in dense environments and at small opening angles between *b*-initiated sub-jets as would be expected in boosted jets. Utilising tracks to build such jets benefits from the better resolution of tracking detectors over calorimeters. New approaches, aimed at providing *b*-tagging for jets where the $b-$quark pair ΔR is smaller than the track jets radius, have also been developed through the use of variable-radius track jets [392].

In CMS different approaches to identify boosted $H \rightarrow b\bar{b}$ candidates have been developed: the subjet *b*-tagging and the double-b tagger [382]. In the first approach the subjets are first defined, using the anti-k_T algorithm with 0.4 distance parameter, and then the standard *b*-tagging is applied to each of the subjets. At high p_T the two subjets start to overlap causing the standard *b*-tagging techniques to break down due to double-counting of tracks and secondary vertices when evaluating the *b*-tag discriminants. The double-b tagger is a dedicated multivariate (BDT) tagging algorithm which does not define subjets. It fully exploits not only the presence of two *B*-hadrons inside the AK8 jet, but also the correlation between the directions of the momenta of the two *B*-hadrons. There are 27 inputs in total which rely on reconstructed tracks, secondary vertices (SV) as well as the two-SV system. The performance achieved in terms of background rejection for a given boosted $b\bar{b}$ tagging algorithm outperforms those reached by reconstructing and tagging individually the two jets for di-jet transverse momentum $p_T > 350 - 400$ GeV.

The algorithm has been updated to use a DNN based architecture, known as "Deep-Double-b" [393], and more observables exploiting the kinematics of the charged particle flow candidates and secondary vertex information. For a given $b\bar{b}$ tagging efficiency of 70%, the inclusive mis-tag rate is reduced more than a factor 2 with respect to the BDT based double-b tagger (from 4% down to 1.2%-1.5%).

Due to the small cross section of producing events with boosted $H \to b\bar{b}$ or $Z \to b\bar{b}$ jets, the efficiencies of these algorithms are measured using QCD multi-jet events enriched in jets from gluon splitting to $b\bar{b}$ ($g \to b\bar{b}$) with topology similar to that of boosted $H \to b\bar{b}$ jets [390, 394].

Recently, CMS and ATLAS have reported the first observation of Z to $b\bar{b}$ in the single jet topology [395, 396], consistent with the SM expectation, in the context of a search of inclusive Higgs boson production at high p_T decaying to $b\bar{b}$.

4.3 Specific Corrections for *b*-jet transverse momentum

N. Chernyavskaya, F. Micheli, L. Mastrolorenzo, C. Vernieri

The most sensitive searches for HH production involve at least one Higgs boson decay to bottom quark-antiquark ($H \to b\bar{b}$). Improving the invariant mass resolution of the b-jet pair plays a critical role for these searches. The jet energy calibration is done as a function of the jet p_T and η, and taking into account the pileup activity of the event, as the p_T density (ρ), which is the corresponding amount of transverse momentum per unit area [371]. The jet energy is calibrated in data using QCD di-jet events, which are mostly gluon-initiated jets, without taking into account the additional details of the jet reconstruction. Typical values for the jet energy resolution are 15–20% at 30 GeV [374, 397].

Jets initiated from b-quarks contain B-hadrons, which have a relatively high probability (35%) to decay to leptons and neutrinos. The presence of neutrinos, which escapes detection, in the B hadron semi-leptonic decay chain results in an even lower response with respect to the light quark/gluon induced jets used in the standard calibration [373, 374]. In addition, due to the soft particles from the decay of heavy hadrons, b-jets deposit over a wider cone than light jets. Therefore, the standard jet energy calibration does not correct for the energy loss caused by escaping neutrinos or out-of-cone energy leakage, and a dedicated energy correction is needed for b-jets.

Both ATLAS and CMS have developed specific strategy to correct the b-jet energy and improve the invariant mass resolution of the reconstructed Higgs boson [398, 399].

Both ATLAS and CMS attempt to correct the b-jet energy, by applying a multi-variate technique similar to that used in CDF [400],

The CMS method [401, 402] uses the regression method to combine various jet and event properties, to get an additional correction beyond the standard CMS jet energy corrections. The regression is essentially a multi-dimensional calibration at the particle level - including neutrinos - which exploits the main b-jet properties. The regression target is the jet p_T at generator level, including the contribution of neutrinos. A specialised BDT is trained on a jet-by-jet basis using a large dataset of simulated b-jets from decay of $t\bar{t}$ pairs. It provides a correction factor that improves both the b-jet energy scale and its resolution.

Inputs are chosen among variables that are correlated with the b-quark energy and well measured. They include detailed jet structure information about tracks and jet constituents which differs from light flavour quarks/gluons jets. Information from B-hadron decays on the reconstructed secondary vertices are used as well as soft lepton from semi-leptonic decay when available, provid-

ing an independent estimate of the b-quark p_T. This multi-dimensional regression then combines information about the secondary vertex and tracks associated to a *b*-jet, jet kinematics, jet composition and individual energy deposits reconstructed by the different CMS sub-detectors, as well as pileup information.

In Run 1 [403] the information carried by the variables related to the missing transverse energy (E_T^{miss}) has been also exploited as input to the regression. In the absence of real E_T^{miss} in the event, it acts as a kinematic constraint for the momentum balance in the transverse plane.

In general, the most discriminating variables are those related to the jet kinematic, due to the fact that most of the power of the regression is derived from the neutrinos involved in the semileptonic *B*-hadron decays.

The average improvement on the mass resolution, measured on simulated signal samples, when the corrected jet energies are used is about 15-25%, resulting in an increase in the analysis sensitivity of 10–20%, depending on the p_T of the reconstructed Higgs boson and on the analysis strategy.

The validation of the regression technique in data has been performed in $Z(\ell\ell) + b\bar{b}$ events, by comparing the Z p_T with the p_T of the $b\bar{b}$ system, and in an $t\bar{t}$-enriched sample targeting the lepton plus jets final state, by looking at the reconstructed top-quark mass distribution [401].

Very recently, the CMS experiment has improved the regression through the use of a DNN [398]. A dedicated loss function is introduced, allowing simultaneous training of an energy correction and a per-jet resolution estimator[1]. The DNN regression improves the *b*-jet resolution by a about 13%. Therefore this improvement generalises well to *b*-jets originating from physics processes different from $t\bar{t}$ production. A larger improvement of roughly 20% is observed for the di-jet invariant mass resolution. The resolution estimator predicted by the DNN and based on quantile estimators is shown to predict the intrinsic jet resolution with an accuracy of better than 20% over a p_T range spanning over one order of magnitude. The DDN-based regression has been validated in data using events arising from dilepton decay of a Z boson in association with *b*-jets. It was confirmed that the improvement coming from *b*-jet energy regression is observed in both data and simulation.

ATLAS proceeds following the same logic to improve the *b*-jet energy resolution. Since muons are not included in the standard ATLAS jet calibration, but are present in roughly 15% of the *B*-hadron decays, *b*-jets receive an additional μ-in-jet correction. If a muon is found within a jet cone of $\Delta R = \sqrt{\Delta\eta^2 + \Delta\phi^2} = 0.4$, the four-momentum of the muon closest to the jet axis is added to the four-momentum of the jet. Additional residual jet p_T corrections are applied to account for escaping neutrinos and equalise the response to jets containing semi-leptonic and hadronic decays of *B*-hadrons ATLAS has also developed a more sophisticated method using a boosted decision tree (BDT) algorithm with a set of inputs similar to those used by CMS [405]. The improvement of the di-jet invariant mass resolution coming from simple average correction and BDT regression is very similar, and it is of the order of 18% with respect to the calibration without including muons [406].

In Fig. 4.2 the impact of the μ-in-jet and the *b*-jet regression based corrections is shown for simulated $H \to b\bar{b}$ events in ATLAS and CMS.

Both ATLAS and CMS have implemented dedicated algorithms to improve the *b*-jet energy resolution using machine-learning techniques. These algorithms will further be developed to meet the conditions of the HL-LHC. For the HL-LHC phase, a major upgrade of the ATLAS and CMS detectors is planned, with new detectors having a higher granularity, extended coverage, and additional timing layers. The high granularity of the detectors and the additional timing information will improve the reconstruction of the *b*-jets by removing spurious tracks from pileup and by improving

---

[1] The loss function combines a Huber function for the energy correction estimation with two quantile estimators [404].
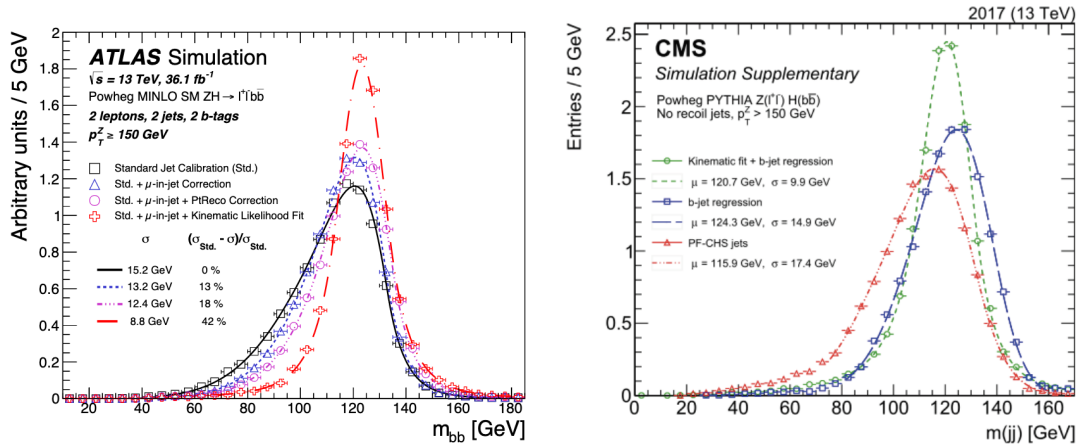
Figure 4.2: Di-jet invariant mass distributions for simulated samples of $Z(\ell\ell)H \rightarrow b\bar{b}$ events, before and after the μ-in-jet energy correction (left) and the regression procedure (right) is applied for ATLAS and CMS respectively [398, 399].

the identification of secondary vertices. The additional information coming from detectors can be used for the training of more sophisticated neural network architectures.

4.4 Hadronic τ object identification

A. Bethani, K. Leney, L. Mastrolorenzo

The τ is the heaviest lepton with a mass of 1.776 GeV and a lifetime $c\tau \sim 87\mu m$. Because of its large mass τ is the only lepton that can decay hadronically. More precisely, in 65% of the cases the τ decays hadronically, typically into either one or three charged mesons (mainly pions) in presence of up to two neutral pions, subsequently decaying into a pair of photons. While leptonic τ-decays are reconstructed as prompt electrons or muons, hadronic decays of a τ-lepton (τ_h) are reconstructed by combining detailed information of the visible decay products, such as tracks and their impact parameters, and energy clusters corresponding to the τ candidate. In both ATLAS and CMS, hadronic τ detector objects are seeded by jets reconstructed with the anti-k_T algorithm, with a distance parameter $R = 0.4$. Further reconstruction in CMS is performed by using the Hadron-Plus-Strips (HPS) [407] method, described further in this section.

The τ reconstruction method used by ATLAS [408, 409] is based on a set of selection criteria, applied to jets to reject those initiated by quarks and gluons. Information from the inner tracker is used to identify the τ vertex and the resulting tracks using the number of hits and the distance of closest approach to the τ vertex, that are compatible with the hadronic τ decays. The energy of the τ object is then obtained using dedicate calibration algorithms.

The τ reconstruction in CMS is based on the HPS algorithm, that combines information from the energy deposited in the calorimeters and from the reconstructed charged tracks. It starts searching for τ lepton decay products within a particle-flow jet, identifying the most abundant τ hadronic decays, classified accordingly to the number of reconstructed charged hadrons and electromagnetic energy deposits: 1-prong (1 charged track assumed to originate from a pion), 3-prongs (3 charged tracks with invariant mass compatible with the mass of the intermediate resonances a_1 or ρ) and 1-prong + π^0 (1 charged track originated from a pion plus electromagnetic deposition).

Both experiments use multi-variate discriminators to reduce mis-identification of quark- and

gluon-initiated jets as τ objects. During the 2015-2017 data taking period, a BDT was used by both experiments and in 2018, ATLAS introduced a τ identification algorithm based on a recurrent NN (RNN) [410]. In physics analyses, different selections on the discriminant output score can be applied according to the desired efficiency. In ATLAS, three working points referred to as loose, medium and tight are provided, corresponding to different cuts on the BDT output score and hence different efficiencies, as listed in Table 4.2. The rejection factors for quark- and gluon-initiated jets is $\mathcal{O}(10^2)$ to $\mathcal{O}(10^3)$ depending on the working point as well as p_T and the number of tracks. In CMS, several multi-variate techniques were probed, with three to six working points. The corresponding efficiencies and background rejection factors are listed in Table 4.2.

Working point	ATLAS		CMS			
	τ eff./ jet $\to \tau$ (1 track)	τ eff. / jet $\to \tau$ (3 tracks)	τ eff.	jet $\to \tau$	e $\to \tau$	$\mu \to \tau$
Loose	60% / 2%	50% / 1%	60%	0.8%	1%	0.1-0.5%
Medium	55% / 0.8%	40% / 0.8%	55%	0.4%	0.2%	
Tight	45% / 0.6%	30% / 0.6%	45%	0.2%	0.1%	0.03-0.4%

Table 4.2: Efficiencies for the different τ hadronic identification working points used by the ATLAS [409,411] and CMS [407] collaborations. Identification efficiency are evaluated using simulated $H \to \tau^+\tau^-$ or a 2 TeV BSM resonance decay to $\tau^+\tau^-$ events. Jet $\to \tau$ mis-identification probabilities for τ objects are evaluated using simulated multi-jet events and reported for inclusive p_T for ATLAS while for 30-60 GeV in the CMS case. e $\to \tau$ and $\mu \to \tau$ mis-identification probabilities are evaluated using $Z/\gamma \to ee/\mu\mu$ events.

The efficiency of the hadronic τ identification criteria has increased enormously since the first data-taking periods in 2010, when the fake rates were more than an order of magnitude larger for similar efficiencies, despite the increase of instantaneous luminosity and concurrent pileup events. Electrons and muons can also be mis-identified as τ objects, and these backgrounds are suppressed using algorithms that combine information from the inner tracker, calorimeters, and muon detectors. The $e \to \tau$ and $\mu \to \tau$ mis-identification probabilities are significantly smaller than for jet$\to \tau$.

The uncertainties on τ identification efficiency correction factor measurement are approximately 5-6% for the sum of the transverse momenta of all charged pions and photons from π^0 (visible transverse momentum) in the 20-60 GeV range [407, 409]. The reconstructed τ energy scale correction factor is measured with a precision of approximately 1.2–2% for ATLAS [409] and less than 1.2% for CMS [407].

4.4.1 Boosted $H \to \tau^+\tau^-$

Reconstructing the di-τ system is an integral part of HH searches that include a $H \to \tau^+\tau^-$ decay. In the case of searches for heavy resonances, it is likely that the di-τ system is produced with very high transverse momentum and the τ decay products are more collimated. The higher the energy of the original state the smaller the angular distance between the two τ objects. The τ reconstruction efficiency drops dramatically as the di-τ p_T increases. The τ reconstruction is seeded by anti-k_t jets with a distance parameter $R = 0.4$, corresponding to the maximal distance between jet axes. Therefore τ pairs within a cone of $\Delta R < 0.4$ are merged into the same jet and can not be reconstructed separately, as for the boosted $H \to b\bar{b}$ reconstruction.

To reconstruct highly boosted τ pairs, a new approach is necessary since they cannot be handled with existing methods by construction. A simple solution would be to reduce the anti-k_T distance parameter, until both τ objects can be reconstructed separately again. This approach does improve the efficiency of a single τ reconstruction in a high-momentum regime. However, in the case of

boosted τ pairs it is very likely one τ to have a significantly higher p_T than the other. In the case the τ pair originates from a scalar particle, as the Higgs boson, then one τ-lepton is likely to give most of its energy to the τ neutrino because of spin conservation and the V-A structure of the electroweak interaction. Therefore a better solution is to reconstruct the boosted τ pair as one object. Both ATLAS and CMS have developed specific tools for the identification of boosted di-τ systems with similar approach. The sub-structure of wide jets is exploited to look for the presence of two τ decays. The large-radius jets are used as seeds for the reconstruction and sub-jets are subsequently identified. ATLAS has employed a multi-variate method [412] to discriminate the boosted di-τ system from other boosted hadronic objects. The observable used as input to the algorithm are similar to those used for standard τ identification, including calorimeter information on the clusters and energy deposits, as well as tracking inputs related to primary and secondary vertices to estimate the τ decay length. Given the distinctive di-τ decay signature, a higher jet background rejection is likely to be achievable for boosted τ-pairs as compared to boosted $H \rightarrow b\bar{b}$.

So far the focus of both experiments has been to identify fully hadronic di-τ system, however everything already stated before applies in the case of the semi-leptonic di-τ decays as well. In this case the wider jet is investigated to look for the presence of a lepton. The identification of boosted semi-leptonic di-τ decays is significantly easier for CMS due to the use of particle flow in the event reconstruction which combines tracker and calorimeter information for particle identification.

CMS has developed a dedicated reconstruction algorithm to reconstruct the Higgs boson decaying to τ leptons. Higgs decaying to τ leptons are clustered as large radius jet (distance parameter of 0.8) and if two subjets with $p_T > 10$ GeV that satisfy the mass drop condition are found, then the two subjets are used as seeds in the standard τ reconstruction and the HPS algorithm is applied on them to identify hadronic taus. The τ leptons selected by the HPS algorithm are then required to have $p_T > 20$ GeV and satisfy a selection on the (MVA) τ-ID isolation. A medium working point is used for the leading τ and a very loose one is used for the second leading τ in fully hadronic events.

For boosted Higgs boson decays into $\mu\tau_h$ and $\tau_h\tau_h$, the corresponding efficiencies are about 80% and 60% and the mis-identification rate 10^{-3} and 10^{-4} respectively, depending on the Higgs boson p_T [413].

4.5   Photon reconstruction

E. Brost, R. Teixeira de Lima

The photon reconstruction algorithm in the ATLAS detector starts by dividing the electromagnetic (EM) calorimeter into angular regions of $\Delta\eta \times \Delta\phi = 0.025 \times 0.025$, a tower, with energy given by the sum of all longitudinal cells within that area. Towers with an energy larger than 2.5 GeV are used as seeds for the cluster reconstruction with the sliding window algorithm [414], which clusters calorimeter cells within fixed-size rectangle, with a window size of 3×5 towers. Clusters are classified as electron, unconverted photons or converted photons according to the presence of matched well reconstructed tracks that are consistent or not with primary vertices in the event. These EM clusters are calibrated to account for different effects, in data and simulation, using the transverse and longitudinal segmentation of the EM calorimeter. The calibration uses $Z \rightarrow e^+e^-$, $Z \rightarrow (e^+e^-, \mu^+\mu^-)\gamma$ and $J/\Psi \rightarrow e^+e^-$ as standard candles. This achieves a relative energy resolution of $\sigma/E = 2.5\%$ (1%) for central unconverted photons with $E_T = 20$ (200) GeV [415].

In the CMS detector, photon and electron clusters are reconstructed based on energy deposits in the CMS electromagnetic calorimeter (ECAL) crystals. Crystals with an energy deposit above that of their immediate neighbours and above the noise threshold are used as seeds for the clustering

algorithm, which works with flexible-sized windows, depending on the energy distribution around the seed crystals [416]. Before the clustering, the ECAL crystal responses are corrected for ageing effects, and inter-calibrated by measuring quantities such as the $\pi^0/\eta \rightarrow \gamma\gamma$ process and the ratio between the energy of electrons with respect to their momenta measured by the CMS trackers. The absolute scale calibration is then performed with $Z \rightarrow e^+e^-$ decays as a function of η. In addition, pileup effects are mitigated with a multi-variate regression technique. The energy resolution is measured in $Z \rightarrow e^+e^-$ events with electrons reconstructed as photons, and achieves a relative resolution of $\sigma_E/E = 1.5\%$ for central electrons with low bremsstrahlung emission [417].

ATLAS identifies photons with respect to jets with high EM activity (such as $\pi^0 \rightarrow \gamma\gamma$ from hadronic showers) with rectangular cuts on expected prompt-photon shower shapes [418]. Due to the longitudinal segmentation of its EM calorimeter, ATLAS uses information based on the energy distribution in the different EM layers for a purer selection. This purer version of the algorithm achieves an efficiency of $85 - 90\%$ ($85 - 95\%$) for unconverted (converted) photons in the range of $30\,\text{GeV} < E_T < 100\,\text{GeV}$ [419]. Additionally, isolation criteria based on vetoing hadronic (track- and calorimeter-based) activity around the cone defined by the photon axis is used to reject $\pi^0 \rightarrow \gamma\gamma$ from nearby jets that have been reconstructed as a single photon. The isolation requirement has a signal efficiency of approximately 98% for SM $HH \rightarrow b\bar{b}\gamma\gamma$ events.

Photon identification in CMS is performed both with rectangular cuts and with a multi-variate approach based on a BDT [417]. Quantities such as the width of the photon shower in the η direction are used to mitigate hadronic background. The CMS photon identification BDT includes variables related to extra activity in the detector in the vicinity of the reconstructed photon, and, in the endcaps, extra information obtained from the CMS preshower detector [2], particularly to identify $\pi^0 \rightarrow \gamma\gamma$ decays. Since in the endcap regions, the angle between the two emerging photons from the decay of a neutral pion is on average smaller. The algorithm was developed during Run 1, focusing on the performance of the CMS $H \rightarrow \gamma\gamma$ analysis. For the Run 2 version of the algorithm, efficiencies on data with $Z \rightarrow e^+e^-$ events, where one of the electrons is reconstructed as a photon, are found to be between 75% and 95% for photons with $E_T > 20\,\text{GeV}$ [420].

4.6 Trigger strategies

J. Alison

Identifying b-jets and τ leptons efficiently at trigger level [421, 422] is critical for two of the most sensitive HH final states, $HH \rightarrow b\bar{b}b\bar{b}$ and $HH \rightarrow b\bar{b}\tau^+\tau^-$. The challenges of properly identifying these objects online are outlined in the following sections.

The ATLAS and CMS triggers consists of two different systems: the L1 Trigger (L1) and the High Level Trigger (HLT). The first uses custom-built programmable hardware to make an accept-reject decision in approximately 2.5-3μs, while the second relies on a shelf processor farm employing the same reconstruction software framework used for the offline reconstruction.

4.6.1 b-jet trigger

J. Alison

The all-hadronic $HH \rightarrow b\bar{b}b\bar{b}$ final state poses a great challenge to the online selection criteria due to the overwhelming rate of QCD multi-jet events. The b-jet properties are exploited at trigger level to keep an acceptable rate without increasing the jet transverse momentum thresholds, reducing

---

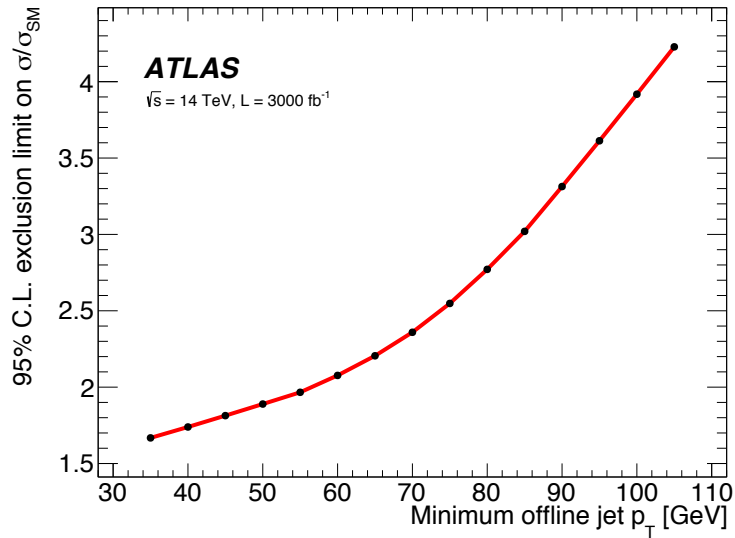[2]The preshower detector is located in front of the ECAL in the endcap regions and has a much finer granularity.

Figure 4.3: Expected upper limit on the $HH \to b\bar{b}b\bar{b}$ cross section as a function of the minimum jet p_{T} threshold [423].

the $HH \to b\bar{b}b\bar{b}$ signal acceptance. The sensitivity of the projected $HH \to b\bar{b}b\bar{b}$ analysis as a function of the jet threshold is shown in Fig. 4.3. An increase of the jet threshold from 60 to 100 GeV reduces the $HH \to b\bar{b}b\bar{b}$ sensitivity by a factor of two. This loss is greatest for events with relatively low m_{HH}, the region most sensitive to λ. It is therefore crucial to identify b-jets at the trigger level with the highest possible efficiency. This is a challenging task for the LHC experiments.

The L1 triggers do not use inner detector tracks and thus provide no separation between b-jets and jets from light-flavour quarks or gluons. As a result, b-jets can only be efficiently collected using relatively inclusive, and consequently high-rate, hadronic L1 triggers. The output rate of these L1 seeds is a major, and often the most severe, constraint for the b-jet triggers. The b-jet identification is carried out in the high-level trigger (HLT), when track information becomes available. Another major limitation to b-jet triggers is the available CPU in the HLT farms to perform track reconstruction. While tracking information is necessary for b-tagging, it is computationally expensive. The large CPU cost, coupled with a high input rate from the inclusive L1 triggers, results in the b-jet triggers demanding a significant fraction of the available HLT CPU. The b-jet triggers have to trade performance for speed in order to fit into the allocated resources. It is also important for the online b-tagging to maintain as much consistency with the offline b-tagging algorithms as possible. Most of the searches for HH require b-jets to be identified both online and offline; any inconsistency in the two identification algorithms leads to a reduced overall efficiency. Maintaining online/offline consistency is particularly challenging as the offline algorithms are constantly evolving – even after the trigger decisions have been made – and are not subject to the CPU constraints in the HLT. The remainder of this section discusses the various inputs to HLT b-tagging and summarises the overall performance. Differences between ATLAS and CMS are highlighted.

Primary vertex (PV) finding is crucial to b-tagging as it defines the reference from which track displacements are measured and it is used to suppress tracks coming from pile-up. Both transverse and longitudinal positions of the PV are needed. The transverse position is determined from the beam spot position. The position of the beam spot is monitored in real-time during data-taking with dedicated HLT triggers. The transverse beam spot width is comparable to the accuracy with which the transverse PV position can be measured, $\mathcal{O}(10\mu m)$. As a result, the PV transverse posi-

tion is approximated with the beam spot position. The longitudinal PV position, however, must be reconstructed on an event-by-event basis. It is used both to reduce the phase-space where tracking is performed, as well as to define the inputs to the b-tagging. Only tracks pointing to the PV are important for b-tagging, so imposing a maximal longitudinal distance between the track and the PV significantly reduces the relevant hit combinations and thus the CPU cost associated to tracking algorithms.

ATLAS and CMS have quite different approaches to reconstruct the online PV. CMS uses an iterative approach that starts with *track-less* vertex finding using jet directions and pixel clusters. Pixel clusters matched to the four leading jets in the event are projected to the beam line. The position of the PV along the beam line is then determined as a maximum in the projected hits positions. This technique is extremely fast and locates the PV along the beam line with an accuracy of about a centimetre. This preliminary estimate of the PV position is then used to seed pixel-only track finding. The PV finding algorithm is then performed again including the pixel tracks, improving the resolution in z to $\sim 100 \mu m$. Tracks reconstructed with a combination of hits from both the pixel and strip detectors, consistent with this PV position are then reconstructed and used to further refine the PV position determination, resulting in a final resolution of around $25 \mu m$, comparable to the offline PV resolution.

The PV finding in ATLAS is done in one step. Track reconstruction is performed using inner detector hits matched to $p_{\mathrm{T}} > 30$ GeV jets found at L1. The hits are required to fall within $\Delta R < 0.2$ from the jet direction. Tracks with $p_{\mathrm{T}} > 1$ GeV are reconstructed using a configuration of the track finding algorithm optimised for speed [421]. In 2017, to reduce the CPU cost, the threshold on the track p_{T} was raised to 5 GeV. These tracks are then used to reconstruct the PV with an accuracy of $\sim 60 \mu m$ along the beam line. The PV position is then used as seed to the track finding algorithm in a wider $\Delta R < 0.4$ area around the jet direction. A more precise and CPU expensive configuration of the track reconstruction algorithm is used at this final stage.

The HLT track efficiency is one place where there is a significant difference in performance between ATLAS and CMS. The online track reconstruction in CMS, as evaluated in simulated $t\bar{t}$ events, has an efficiency that is 10% lower than that of the corresponding offline reconstruction for tracks with p_{T} of 1-10 GeV. In ATLAS for a similar kinematic phase space, the efficiency of the online track reconstruction relative to the offline is better than 98%. This difference in track reconstruction performance translates into a difference in online b-tagging performance between the two experiments.

The b-jet trigger decisions are ultimately made based on the multiplicities of jets passing various p_{T} and b-tagging thresholds. Jet reconstruction, discussed in Sec. 4.1, is thus also critical to the b-jet trigger. The online jet reconstruction follows the procedure used offline as closely as possible. Residual differences in the online/offline performance arise mainly from the different track reconstruction used online and from the jet thresholds applied at L1. Currently neither experiment implements dedicated b-jet p_{T} corrections in the trigger, an obvious potential area for future improvement.

The b-tagging algorithm is the final ingredient for the b-jet triggers. The b-tagging algorithms used by ATLAS and CMS are described in Sec. 4.2. The online algorithms follow those used offline as closely as possible. The primary differences between the online and offline b-tagging arise from differences in the input tracks and from improvements to the offline algorithms that come after the software used in the trigger is frozen. In Run 2, ATLAS used the MV2c algorithm both offline and in the trigger [424]. In the start of Run 2, CMS deployed a version of the CSVv2 [382] algorithm at trigger level. However, during 2018 the CMS trigger moved to the DeepCSV discussed in Sec. 4.2.
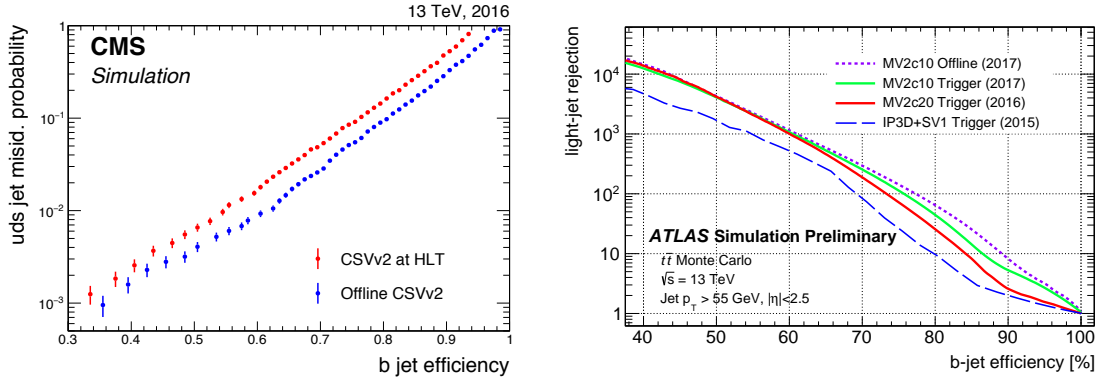
Figure 4.4: Comparison of online and offline *b*-tagging performance for CMS [382] (left) and AT-LAS [424] (right).

The relative performance of the online and offline *b*-tagging algorithms are shown for both AT-LAS and CMS in Fig. 4.4. For a background rejection of 100, the difference in online and offline signal efficiency for ATLAS is ~2%; in CMS, the corresponding difference is ~ 6%. The worse relative online performance for CMS is likely a result of the lower HLT tracking efficiency because the limited availability of pixel tracks.

4.6.2 τ trigger

A. Ferrari, L. Mastrolorenzo

During the Run 2 taking, CMS has developed a new τ trigger algorithm [425] for the L1. The recent micro-TCA (μTCA) technology [426], together with more powerful and dedicated Field Programmable Gate Arrays (FPGA), had being deployed at the L1 trigger during the Phase-I upgrade allowing enhanced calorimeter granularity to be used by the online algorithms[3]. The L1-tau algorithm is based on an innovative dynamic clustering technique (used also to trigger electron and photon at L1 [427]) capable to combine the information coming from the calorimeters to perform a first online identification of the main τ hadronic decay mode (1-prong, 1-prong, 1-prong+π^0, and 3-prongs). Together with a cluster-dedicated calibration and an innovative isolation technique to perform an online PU mitigation, the performances obtained allow to effectively use the L1-tau trigger to seed the acquisition of events with hadronic τ lepton in their final state requiring unprecedentedly low online thresholds. For the different hadronic τ decay modes considered, the trigger efficiency is found to be close to 100% for τ reconstructed online with a p_{T} fairly above the trigger threshold (to avoid energy resolution effect).

In ATLAS, the trigger-level identification of τ objects relies at L1 on the calorimeter information, with a granularity of 0.1×0.1 in η and ϕ [409]. A core region consists of 2×2 trigger towers and requirements are placed on the transverse energy of the two most energetic adjacent towers as well as an isolation region around the core. At the HLT, topological clusters of calorimeters cells are considered within a cone of radius 0.2 around the L1 τ object and they are calibrated using the same method as offline τ objects. Following the use of trigger specific pattern recognition algorithms, requirements of at most 4 and 2 are made on the number of tracks in, respectively, the core ($\Delta R < 0.2$) and isolation ($0.2 < \Delta R < 0.4$) regions. The hits and tracks identified in this fast-tracking procedure then serve as seeds at the HLT, similarly to the offline reconstruction. Finally, the tracking and

---

[3]the granularity corresponds to the single calorimeter trigger tower: 5x5 crystals in ECAL in addition to the corresponding projection in HCAL
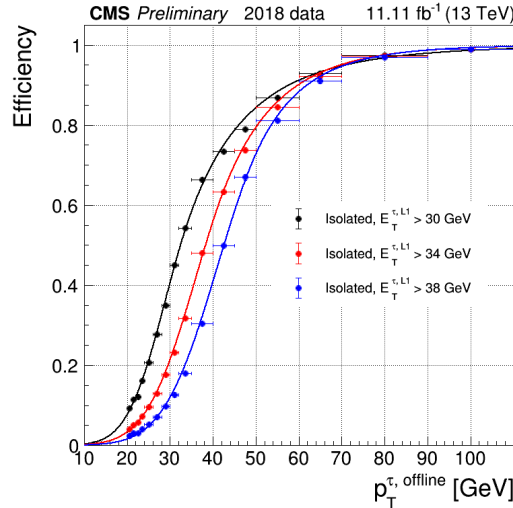
Figure 4.5: Level-1 trigger efficiency of isolated τ-seeds (i.e. requiring the L1 τ candidate to pass a cut on its isolation transverse energy) as a function of the offline τ p_{T} [425].

calorimeter information is used in a BDT algorithm, similarly to that used for offline identification, with minor differences arising from the fact that vertexing information is not available at trigger level. Three working points (loose, medium and tight) are defined for the online τ identification. These working points were tuned to provide target efficiencies of approximately 0.95 (0.70) after their offline counterpart identification is applied for τ leptons with one (three) associated tracks

4.7 *HH* specific analysis techniques

The event topology resulting from the Higgs pair production is very peculiar and it could be further exploited to improve the signal reconstruction, as described in the next two sections.

4.7.1 Kinematic fit procedure
M. Gouzevitch, C .Vernieri

It has been shown (see [428–431] and references therein) that the resolution of the measured objects in the final state of $p - p$ collisions can be improved by forcing well-defined kinematic hypotheses through an event-by-event least square fitting technique. The resulting chi-square of the fit can be interpreted as the probability of the proposed kinematic hypotheses to be true for the observed event.

In the searches for resonances decaying into HH, the Higgs boson mass, as measured by both ATLAS and CMS experiments [432], could be used as a kinematic constraint in the event reconstruction. The kinematic fit procedure is extremely effective for improving the four body invariant mass. Such kinematic constraints are widely used for measurements where a decay proceeds through some known intermediate state. For example, in the case of $HH \rightarrow b\bar{b}b\bar{b}$ the kinematic fit technique aims to fit the measured quantities, i.e. the four b-jet four vectors, to certain hypotheses within their uncertainty, as described in [433]. On an event-by-event basis, it builds a χ^2 function using the four-vectors of the final state objects and their resolutions. The χ^2 is minimised by correcting the measured quantities within their resolutions, fulfilling the kinematic constraints by using Lagrangian multipliers. In this case, the number of degrees of freedom allowed in the fit is

ten, as there are four jets (three degrees of freedom for each jet) and the two constraints from each di-jet invariant mass. The outcome of the kinematic fit is a set of corrections for each of the measured quantities, which translate into in an improved four-body invariant mass resolution. The information provided by the minimised χ^2 is the measure of the probability for the observed event to be compatible with the proposed kinematic. The correction factors are then applied to each jet to improve the four-body invariant mass reconstruction. This procedure uses η, ϕ and p_T information for each jet and their related uncertainty. As the jet angles are measured with a better relative resolution than the jet-p_T, the corrections mainly affect the jet transverse momentum.

The improvement in resolution for the reconstructed signal resonance ranges from 20 to 40% depending on the mass hypothesis for the CMS $HH \to b\bar{b}b\bar{b}$ resonant search [402], resulting in an improvement of the sensitivity of 10–20%. Similar improvements are also observed in CMS $HH \to b\bar{b}\tau^+\tau^-$ searches at 13 TeV [434] or $HH \to b\bar{b}\gamma\gamma$ at 8 TeV [435]. The asymmetry of the corrections, due to the jet momentum resolution across the p_T range considered, results in a linear mass shift as function of the resonant mass. The relative improvement is large for the lowest mass resonant hypotheses, since by construction once the two Higgs boson masses are constrained to the nominal value of the Higgs boson mass, the resolution of the four-body invariant mass $\sim 2m_H + \Delta(E_{H1}, p_{H1}, E_{H2}, p_{H2})$ is dominated by the precision of the $2m_H \sim 250$ GeV term [436].

The application of the kinematic fit could potentially be extended to other final states involving b-jets, to further improve the resolution of the m_{HH} invariant mass on top of the dedicated b-jet specific corrections, as the two methods exploit orthogonal information. Indeed the sensitivity of the CMS search for $HH \to b\bar{b}\tau^+\tau^-$ is enhanced by the use of the kinematic fit, which exploits the four-momenta of both the τ and b-jets and the p_T^{miss} vector in the event, and is performed under the hypothesis of two 125 GeV Higgs bosons decaying into a bottom quark pair and a τ lepton pair. The use of the kinematic fit improves the resolution on m_{HH} by about a factor of two compared to the four-body invariant mass of the reconstructed leptons and jets [434]. The decay products of the τ leptons are assumed to be collinear in the fit, since they are highly boosted as they originate from an object that is heavy when compared to their own mass. In the decay of the two τ leptons, at least two neutrinos are involved and there is no precise measurement of their original energies. For this reason, the τ lepton energies are constrained from the balance of the fitted H boson transverse momentum and the reconstructed transverse recoil, p_T^{miss}, as detailed in Ref. [437].

A simplified version of the kinematic fit is used by the ATLAS $HH \to b\bar{b}\gamma\gamma$ and $HH \to b\bar{b}b\bar{b}$ searches [148, 149], where $m_{b\bar{b}}$ is constrained by a simple multiplicative factor $m_H = 125/m_{b\bar{b}}$ before reconstructing m_{HH}. This improves the m_{HH} resolution, on average, by 30–60% across the resonance mass range of interest as shown in Figure 4.6 and sculpts the non-resonant background in the low m_{HH} range.

The CMS $HH \to b\bar{b}\gamma\gamma$ [438] search applies two different scaling factors for the $m_{\gamma\gamma}$ and $m_{b\bar{b}}$, and approximates the kinematic fit procedure by defining a modified m_{HH} estimator. The so called "reduced" m_{HH} mass [439] is shown in the following equation:

$$\widetilde{M}_X = m_{jj\gamma\gamma} - (m_{b\bar{b}} - m_H) - (m_{\gamma\gamma} - m_H). \tag{4.1}$$

This estimator subtracts the out-of-cone and resolution effects that impact the $m_{b\bar{b}}$ mass more than the jet p_T. While the kinematic fit scales the jet momentum, this method attempts to directly correct the $m_{b\bar{b}}$ mass. The $m_{jj\gamma\gamma}$ is also corrected for the reconstructed $m_{\gamma\gamma}$ value, even if its resolution is much better compared to $m_{b\bar{b}}$. The use of $\widetilde{M}_X$ instead $m_{jj\gamma\gamma}$ improves the m_{HH} reconstruction by 25 to 30 GeV in absolute, that have the most visible effect at mass resonant hypotheses, as shown in Fig. 4.6. For resonant mass of 300 GeV the resolution reduces from roughly 50 to 20
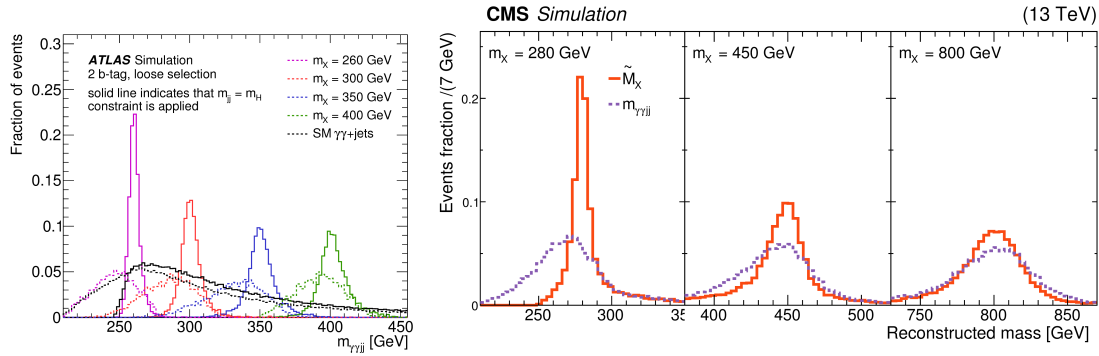
Figure 4.6: Reconstructed m_{HH} with (solid lines) and without (dashed lines) the dijet mass constraint, for a subset of the mass points used for the resonant $HH \to b\bar{b}\gamma\gamma$ searches of ATLAS [149] (left) and CMS (right) [438].

GeV. CMS also uses an $\widetilde{M}_X$ estimator for the boosted $HH \to b\bar{b}b\bar{b}$ searches [440, 441], reporting an improvement of about 10% for the dijet mass resolution.

4.7.2 *HH* vertex reconstruction with $H \to \gamma\gamma$ decay
V. M. M. Cairo, M. Gouzevitch

For $H \to \gamma\gamma$ decays, the Higgs boson mass is computed from the measured photon energies and from their directions relative to the Higgs production vertex.

In general, the hard scatter interaction is identified as the vertex that has the highest total transverse momentum (sumPT) of outgoing charged particles produced in the same $p - p$ collision that generated the Higgs boson.

For single Higgs boson production through gluon-gluon fusion, there are only two photons coming from the primary vertex at LO. Therefore in absence of additional jets, it is hard to identify the vertex because tracks from the primary $p - p$ collision are due only to the underlying events and are soft. In addition to the primary vertex there are many other vertices due to pileup that could spread out in a region of 10 cm along z-axis, therefore it is not possible to identify the right vertex by simply looking at the charged particles.

The di-photon production vertex is then chosen among all reconstructed primary vertex candidates using multivariate techniques based on track and primary vertex information, as well as the directions of the two photons measured in the calorimeter and inner detector (in the case of photon conversion). In this way, the Higgs boson production vertex is correctly identified with an efficiency of about 80% [442, 443] for the ggF production mechanism.

This was optimised in a way that the Higgs boson mass resolution is affected from the wrong vertex identification less than from the photon energy resolution.

The same algorithm used for the identification of the $H \to \gamma\gamma$ primary vertex is then used in the case of $HH \to b\bar{b}\gamma\gamma$ searches, but the presence of $H \to b\bar{b}$ allows to exploit the particles produced in the $H \to b\bar{b}$ hadronization which makes it possible to reconstruct and select the correct event of interest with even higher efficiency than that of the $H \to \gamma\gamma$ case. In fact, similar performance are achieved by both ATLAS and CMS, which are able to identify the primary vertex correctly in up to 99.9% of the simulated signal events [149, 438].

Likewise also in the case of searches for $HH \to \gamma\gamma WW^*$, the presence of high p_T leptons or jets from the W boson decay could contribute to correctly identify the primary vertex together with the constraints derived from $H \to \gamma\gamma$.

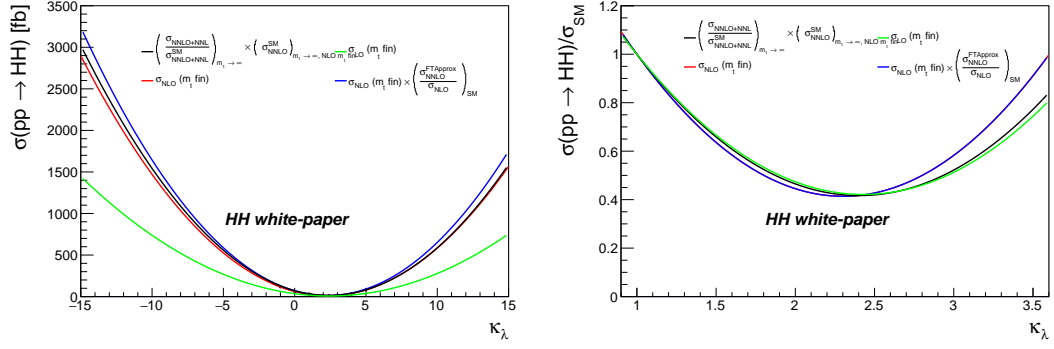Figure 4.7: Left: $pp \to HH$ production cross section as a function of κ_λ. Right: ratio of the $pp \to HH$ to its SM expectation, obtained for $\kappa_\lambda = 1$. Different calculations, as used by the LHC experiments are shown.

computation	a [fb]	b [fb]	c [fb]
LO m_t fin	34.9836	-22.9863	4.72815
NLO m_t fin	62.6094	-44.3898	9.64419
NLO m_t fin × NNLO SM FTApprox	69.9791	-49.6149	10.7794
NLO $m_t \to \infty$ × NNLO+NLL SM (partial m_t fin)	71.3591	-47.7427	9.9315

Table 4.3: Second order polynomial parameters ($a + b \cdot \kappa_\lambda + c \cdot \kappa_\lambda^2$) for different computations as used by the experimental collaborations and new recommendations.

4.7.3   Parameterisation of the HH production cross section as a function of κ_λ.

Chapter 5

Overview of HH searches at the LHC

Editors: J. Alison, B. Di Micco, A. Ferrari, C. Vernieri

The ATLAS and CMS collaborations have exploited a rich variety of signatures to search for HH pair production, exploiting the several Higgs boson decay modes shown in Fig. 5.1.

The feasibility of many of them has been considered in several phenomenological studies. The interested reader can consult Refs. [30, 169, 170, 269, 270, 444–453] and references therein. Sec. 5.1-5.5 present an overview of the results of the searches for both non-resonant and resonant HH production through gluon-gluon fusion from the ATLAS [365] and CMS [366] experiments, based on the data recorded in 2015 and 2016, corresponding to an integrated luminosity of up to about 36 fb^{-1}.

Table 5.1 lists the relevant searches performed by ATLAS and CMS experiments and the corresponding main features. The $HH \to b\bar{b}b\bar{b}$ final state exploits the leading BR for a SM Higgs boson but it suffers from a large multi-jet background. The experimental challenges related to this signature, the current results and potential improvements are discussed in Sec. 5.1. Despite the low branching fraction, the $HH \to b\bar{b}\gamma\gamma$ final state has a very good sensitivity to the SM HH production, thanks to an excellent trigger and reconstruction efficiency of photons, and the excellent invariant mass resolution for the Higgs boson decay to photons, see Sec. 5.2. The $HH \to b\bar{b}\tau^+\tau^-$ final state represents a compromise between the rate and the background contamination. Thanks to the use of multi-variate analysis techniques, the search performed by the ATLAS collaboration yields to the most stringent limit on HH production from an individual channel, as discussed in Sec. 5.3.

The above three final states drive the sensitivity to the SM Higgs boson pair production. However, experiments have also exploited other rare and challenging final states such as $HH \to b\bar{b}VV^*$, where $V = W, Z$ (Sec. 5.4), $HH \to WW^*\gamma\gamma$, $HH \to WW^*WW^*$ and $HH \to \tau^+\tau^-\tau^+\tau^-$ (Sec. 5.5). The current outlook for the non-resonant $HH \to b\bar{b}VV^*$ channel is challenging and provides ample opportunity for improvement. Searches for HH production in final states without b-jets have in general smaller signal yields, but are also typically affected largely by backgrounds processes. As their sensitivity is mainly limited by statistical uncertainties, their sensitivity is expected to scale better with the integrated luminosity, as more refined and sophisticated analysis techniques could be employed.
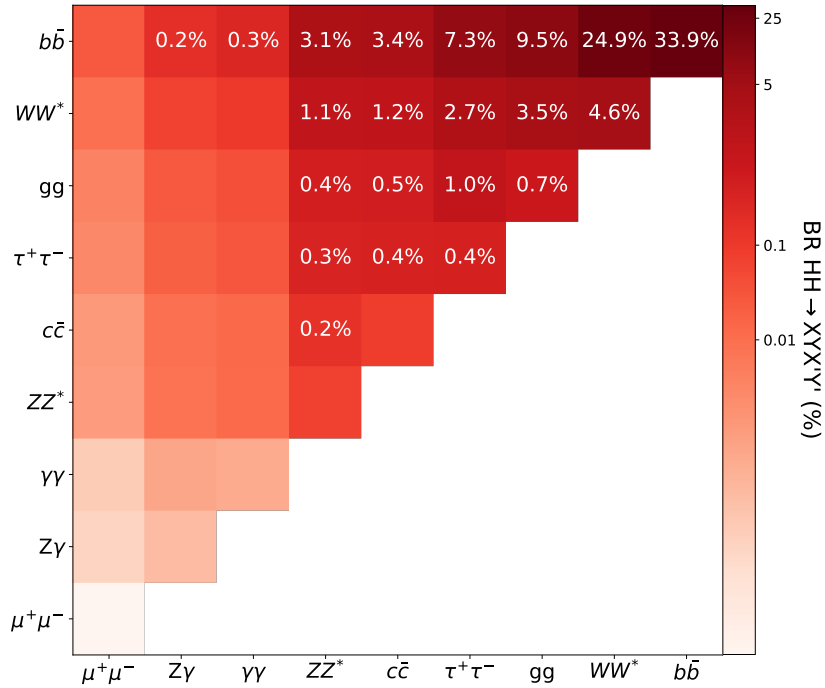
Figure 5.1: Branching fractions of the decay of an HH pair to a selected group of final states. The decay modes are shown on each axis by increasing probability. The numerical values are only shown if larger than 0.1%. The branching fractions of the Higgs boson are evaluated for $m_H = 125.0$ GeV [19].

5.1 $HH \to b\bar{b}b\bar{b}$: status and perspectives

P. Bryant, M. Osherson

Nearly one third of HH events decay via the $b\bar{b}b\bar{b}$ channel, resulting in the experimental signature of four energetic jets which originate from b-quark hadronisation. The main challenge for this signature is the large background from multi-jet final states produced by quantum chromodynamics (QCD) processes, which collectively yield rates exceeding that of the signal by several orders of magnitude. Other non-resonant processes can contribute to the signal signature, such as the production of top quark pairs, and W or Z bosons in association with b-jets.

As discussed in Sec. 2.1.3, most of the impact of modifications of the Higgs boson self-coupling to the m_{HH} distribution is near the $2m_H$ threshold, where the irreducible multi-b-jet background has a significant contribution. Since the start of Run 2, much of the experimental effort has been focusing on extending these searches in the low m_{HH} range, by employing dedicated trigger strategies, consequently loosening the event selection criteria and modelling the substantially increased background acceptance as illustrated in Fig. 5.2. In the most recent ATLAS search, the loosened kinematic selection requirements have increased the background acceptance by a factor of 20, relative to the restricted phase space probed in the first Run 2 result (Fig. 5.2, left). Combined with the integrated luminosity increase, the statistical uncertainty at the peak of the m_{HH} distribution has dropped by an order of magnitude to the percent level in the latest Run 2 result (Fig. 5.2, right). By the end of HL-LHC data-taking, we will require a sub-percent level background model – a daunting task that will require novel data-driven modelling techniques.

In addition to non-resonant HH production via gluon-gluon fusion, ATLAS and CMS searches [148, 454], also searched for resonant HH production in the range $260 < m_{HH} < 3000$ GeV. The momenta and angles between the decay products of such a resonance vary significantly over

Search channel		References	Luminosity	Discriminant
$b\bar{b}b\bar{b}$	ATLAS	[148]	27.5–36.1	m_{HH}
	CMS	[454]	35.9	BDT
$b\bar{b}\gamma\gamma$	ATLAS	[149]	36.1	$m_{\gamma\gamma}/m_{HH}$
	CMS	[438]	35.9	$m_{b\bar{b}}, m_{\gamma\gamma}$ (2D)
$b\bar{b}\tau^+\tau^-$	ATLAS	[150]	36.1	BDT
	CMS	[434]	35.9	BDT/m_{T2}
$b\bar{b}VV^*$	ATLAS	[455]	36.1	e.c.
	CMS	[456]	35.9	DNN
$WW^*\gamma\gamma$	ATLAS	[226]	36.1	$m_{\gamma\gamma}$
	CMS	–	–	–
WW^*WW^*	ATLAS	[457]	36.1	e.c.
	CMS	–	–	–

Table 5.1: Summary of HH search channels with their corresponding references, the integrated luminosity of the dataset used in the analysis and the distribution used to extract the signal (discriminant) - note that e.c. stands for event counting. This table is based on the HH non-resonant and resonant searches performed with the 2015 and 2016 datasets collected by ATLAS and CMS at 13 TeV.

this range. In order to increase the sensitivity of this search, different event selection criteria are used for the two main kinematic regions: (i) "resolved" with four individually reconstructed b-jets which tests resonance mass hypotheses from $2 \times m_H$ up to 1500 GeV; (ii) "boosted" which exploits large-radius jets and substructure techniques (see Sec. 4.1 and Sec.4.2.1) to probe resonance mass hypotheses up to 3 TeV. The resolved regime dominates the sensitivity to SM non-resonant HH production. In addition, the strategy adopted by CMS makes use of a third category, the "semi-resolved". This case, first proposed in Ref. [257], aims to recover potential events which did not enter the other two categories by considering events where one Higgs candidate merges into a single large-radius jet but the other is reconstructed as two individual b-jets. This analysis moderately improves the sensitivity for m_{HH} between 750 and 2000 GeV [441]. For the non-resonant $HH \rightarrow b\bar{b}b\bar{b}$ searches, events are selected online by combining two different trigger selections, both using the b-tagging algorithms to identify b-jets. Events are requested offline to contain four b-tagged jets with $p_T > 30/40$ GeV (CMS/ATLAS). The b-tagging efficiency for jets with p_T in the 60–150 GeV range is approximately 70% (68%) and gradually decreases for lower and higher jet p_T. This corresponds to a light jet mis-tag efficiency of 0.3% (1%) for ATLAS [459] (CMS [382]), see Sec. 4.2 for more details. After these selection criteria are applied, the dominant background processes are multi-b-jet production (85–90%) and top-quark pair production (10–15%). The Z + jets background is estimated to contribute no more than 0.2–0.5% to the total background, and therefore is neglected.

The main challenge for the signal extraction in the $b\bar{b}b\bar{b}$ final state, is to build a precise model of the multi-jet background without a reliable simulation. The simulation of these final states, due to their large cross section, requires the simulation of a large number of events, which is challenging for the available computing resources.

In the following the analysis strategies are presented, Sec. 5.1.1, together with their limitations, Sec. 5.1.2. Finally possible paths forward, where there is clear room for improvement and opportunities for innovation, are discussed, Sec. 5.1.3.

(a) 2015 analysis [458]
≈ 15 events per fb^{-1}
≈ 30% statistical uncertainty at the m_{HH} peak

(b) 2018 analysis [148]
≈ 300 events per fb^{-1}
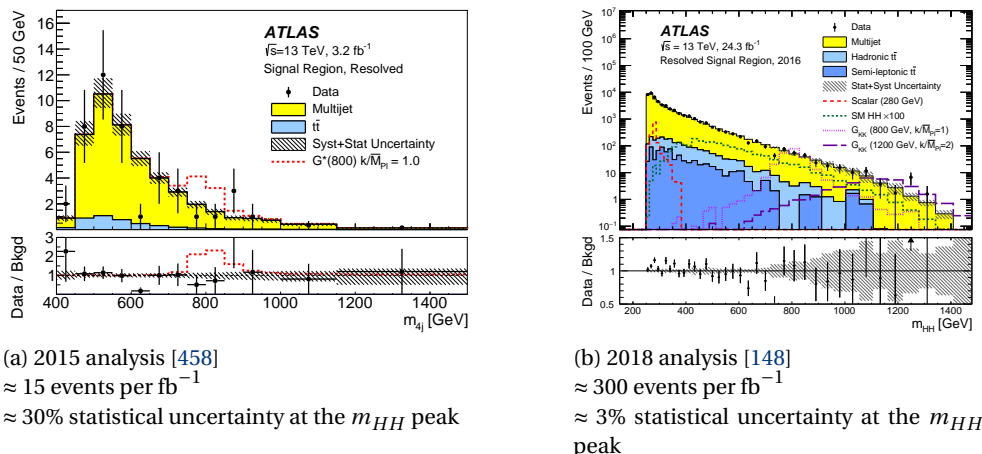≈ 3% statistical uncertainty at the m_{HH} peak

Figure 5.2: Distributions of m_{HH} in the signal region of the ATLAS resolved search for 2015 [458] (left) and 2016 [148] (right) data, compared to the predicted backgrounds. The hatched bands represent the statistical uncertainties. Note the change in y-axis range in the ratio plots.

5.1.1 Analysis strategies

Both ATLAS and CMS analysis strategies rely on multi-jet triggers at L1 with online b-tagging selections applied at the HLT to a subset of the online jets, as described in Sec. 4.6. At L1 the multi-jet trigger selections is required to have a maximum rate of approximately 3 kHz, which demands significant HLT resources for the online b-tagging to reduce trigger rates to roughly 40 Hz. At HLT, CMS requires four jets with $p_T > 30$ GeV and two above 90 GeV, and three online b-tags corresponding to an offline b-tagging efficiency of less than 60%. ATLAS trigger selection requires four jets with $p_T > 35$ GeV, where at least two are b-tagged online with the 60% working point. The CMS trigger efficiency, as evaluated for a resonant signal benchmark as function of m_{HH}, ranges from 10% at the $2m_H$ threshold to 60% above 800 GeV and it is 34% for the non-resonant hypothesis. The ATLAS trigger efficiency is evaluated instead, with respect to the offline requirements and ranges from 65% at the $2m_H$ threshold to $\gtrsim$ 99% above 600 GeV.

The four jets with the highest b-tagging score are paired to reconstruct the two Higgs boson candidates. Given these four jets, there are three possible di-jet pair constructions. Both ATLAS and CMS chose the pairing which minimizes the difference between the di-jet masses. CMS performs this minimization over all three pairings for the non-resonant signal and exploits the smaller angular separation of the two b-jets for resonance mass values above 500 GeV. ATLAS reduces the number of considered pairings by applying a sliding selection on the di-jet opening angle as a function of the reconstructed four body mass. The impact of the sliding selection requirements on the signal is shown in Fig. 5.6. The ATLAS (CMS) approach selects the correct pairing at least 90% (70%) of the time for the non-resonant HH signal hypothesis and across the full range of resonance mass hypotheses (70–95%). A multi-variate classifier able to use all of the di-jet correlation information for all possible pairings would perform better than the ΔR(j,j) sliding requirement, by classifying such events as more background-like than those where none of the pairings are such clear examples of the dominant background.

A requirement on the masses of the Higgs boson candidates is used to define the signal region
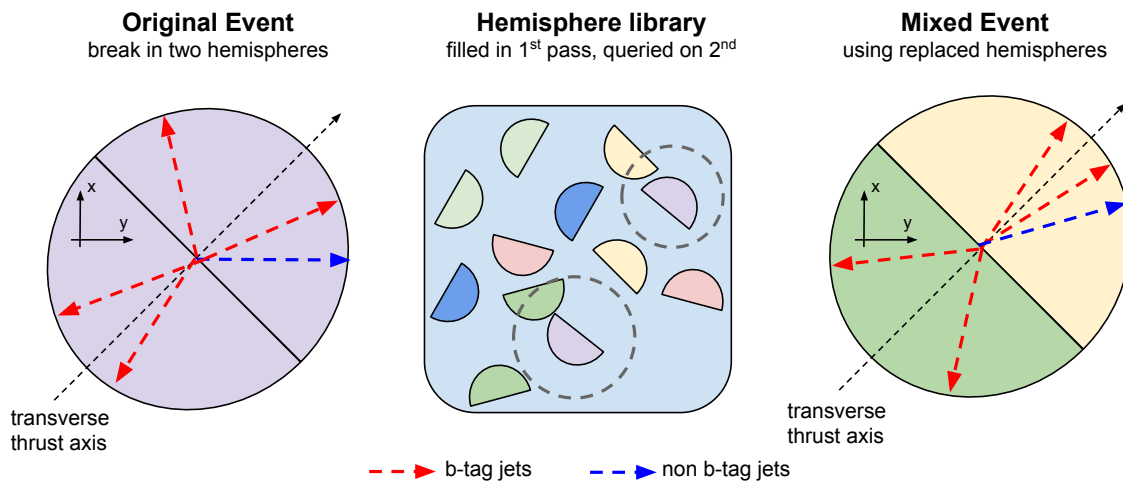
Figure 5.3: Illustration of the hemisphere mixing procedure from [454].

for the ATLAS search which takes into account of the $m_{b\bar{b}}$ resolution:

$$\sqrt{\left(\frac{m_{H1} - 120 \text{ GeV}}{10\% m_{H1} \text{ GeV}}\right)^2 + \left(\frac{m_{H2} - 110 \text{ GeV}}{(10\% m_{H2} \text{ GeV})}\right)^2} < 1.6 \qquad (5.1)$$

Similarly CMS, for the resonant $HH \to b\bar{b}b\bar{b}$ search, defines a circular signal region in the two-dimensional space defined by the reconstructed masses of the two Higgs boson candidates, after the regression based corrections, described in Sec. 4.3, are applied to each b-jet. The m_{HH} resolution is further improved by correcting the momenta of the reconstructed b-quarks imposing the kinematic constraint of the invariant mass of the Higgs boson candidates to be 125 GeV, as described in Sec. 4.7.1. The improvement in resolution for the reconstructed signal resonance ranges from 20 to 40% depending on the resonant mass hypothesis, which results in an improvement of the sensitivity by 10–20%.

Background modelling

The ATLAS analysis strategy derives the model for high b-jet multiplicity events from the low b-jet multiplicity events, with at least two b-jets. This procedure relies on the assumption that the ratio of multi-jet production matrix elements with different b-jet multiplicities does not change sharply in the phase space with di-jets near the Higgs boson mass. This ratio takes into account of the kinematic dependence of the b-tagging efficiency and fake rate as well as the different relative contributions of the underlying matrix elements. The ratio is then used as a weighting factor to correct low b-jet multiplicity events to match high b-jet multiplicity events and should apply equally well across a broad range of phase space with different di-jet masses, in particular they should apply for events with two di-jet pairs near the Higgs boson mass. This assumption is validated in a control region in data, orthogonal to the signal regions used to extract the signal. Shape uncertainties in the multi-jet background are estimated to affect the m_{HH} distribution by 5–30%, by deriving an alternative background model using the same procedure as in the nominal case, but using data from the control region.

For ATLAS, the systematic uncertainty associated to the background model estimate limits the

current result and it will become more important with the full Run 2 integrated luminosity.

The ATLAS background estimation method profits of a dedicated trigger selection with only two b-jet, not available in CMS due to different optimisation choice of the b-jet trigger, that favoured the use of lower p_{T} threshold and a b-jet multiplicity of at least three (see Sec. 4.6 for more details). The CMS collaboration, instead, has developed different background estimation strategies for the resonant and non-resonant HH searches. For the non-resonant signal extraction, the so called "hemisphere mixing" technique is used, where fake events are generated by mixing and matching di-jet systems from separate events [454] as illustrated in Fig. 5.3. This background estimate method does not require the presence of signal depleted control region in data, but it aims at creating an artificial background data set using the whole original data set as input. Thus, rather than a model of a single distribution, a full model of the original data is produced.

The *transverse thrust axis* is defined as the axis that maximises the sum of the absolute values of the projections of jets transverse momenta along the axis itself. The event space is divided into hemispheres by cutting along the axis perpendicular to the transverse thrust axis. Artificial events are then built, by picking hemispheres from different events that are similar to the two hemispheres that made up the original event. The matching algorithm is designed to create fake events with the same kinematic structure as the background process while washing out the correlated structure of the signal process. Because of this, the resulting artificial data sets are unaffected by the presence of a small signal contamination in the original data. This has been verified with signal injection tests. A BDT classifier, using the XGBOOST library [460], is employed to separate signal (including other BSM non-resonant hypotheses) from background processes. The resulting artificial samples are used to provide a background model in the training of a BDT classifier (training sample), an independent set for its validation and optimisation (validation sample), and a third set used to extract the predicted shape of the optimised BDT (application sample). The BDT exploits the b-tagging scores, kinematic information of both the HH system and Higgs candidates, as well as the angles between the HH system and the leading Higgs boson, for a total of 25 inputs. The BDT distribution for data and the artificial model are compared in control regions and a systematic bias is detected. Thus, the background template is corrected for the bias evaluated from this comparison.

A search for SM $HH \rightarrow b\bar{b}b\bar{b}$ signal is then performed for an excess in the tail of the BDT output distribution.

Minor background contamination arising from $t\bar{t}H$, ZH, $b\bar{b}H$ do not show a signal-like BDT distribution and their effect is found to be negligible in the selected data at the current level of the search sensitivity. The systematic uncertainty associated to the shape and normalisation of the background model affects the final result by about 9% and 30% respectively.

For the resonant signal extraction, a simultaneous fit to the m_{HH} spectrum in the signal region is used. The background model is validated in data in dedicated control regions with reduced b-tag multiplicity [402]. Since the $t\bar{t}$ contribution to the background exhibits a shape very similar to that for the multi-jet process, it is implicitly included in the data driven estimate. The systematic uncertainty associated with the choice of the parametric background model is evaluated with pseudo-datasets, generated from an alternative function and fitted with the nominal function to evaluate the bias in the reconstructed signal strength. The measured bias impacts the expected limit by 0.3–1.5 %.

Data-driven methods to estimate the backgrounds (dominantly multi-jet) are also used in the boosted and semi-resolved regimes. The ATLAS result are obtained with the same approach exploited for the resolved analysis. The CMS results instead, rely on the smooth dependence, in background jets, of the specialised double$-b$ tagging efficiency on the jet mass, introduced in Sec. 4.2.1.
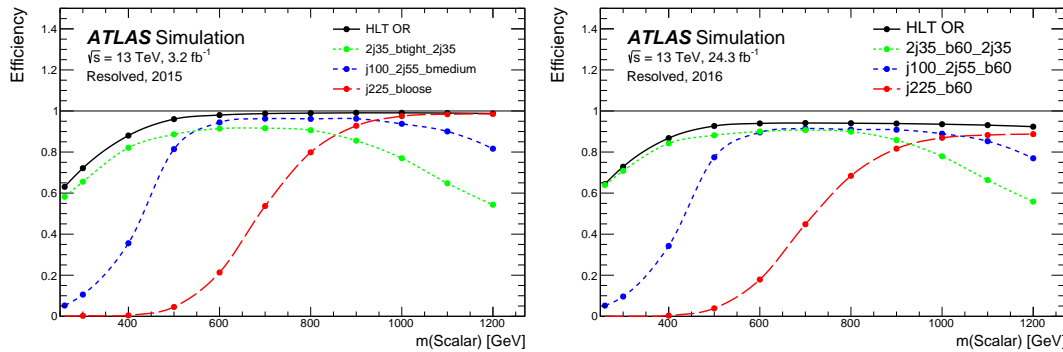
Figure 5.4: The ATLAS event-level trigger efficiencies for the various signal $HH \to b\bar{b}b\bar{b}$ hypotheses [148].

This rate can be derived in sidebands of the Higgs boson mass and interpreted as a ratio of events passing to events failing the requirement, so that it can be applied to events with the correct mass, but failing the double-b tagging requirement. The dominant uncertainty in these searches is the uncertainty associated to the substructure requirements for large-radius jet algorithms, which can be as large as 20%.

5.1.2 Limitations of current analysis strategies

Both the ATLAS and CMS experiments face significant challenges related to the hardware and software triggers. The current trigger efficiencies are limited at L1 for events with $m_{HH} \lesssim 500$ GeV as illustrated in Fig. 5.4.

At the HLT trigger level, maintaining good tracking performance to efficiently reconstruct secondary vertices without using excessive CPU resources is extremely challenging, as discussed in Sec. 4.6. The required CPU time to perform online b-tagging grows non-linearly with pileup. In fact, in the year 2017 and 2018 the trigger thresholds were increased and tracking algorithms optimised to cope with high instantaneous luminosities, but new techniques will be required to accommodate for the luminosity targets of Run 3. While ATLAS focused on providing a unified analysis strategy for resonant and non-resonant $HH \to b\bar{b}b\bar{b}$ searches, CMS has developed independent strategies and optimised the signal extraction for low-, intermediate- and high-mass resonances.

Both the ATLAS and CMS approaches suffer from statistically limited control regions in data. The assumptions that go into generating a background model from data do not necessarily hold to a higher degree of precision than can be tested outside of the signal region. Such uncertainties are difficult to be quantitatively assessed, particularly when they have non-trivial effects on distributions beyond their normalisation.

The recent ATLAS result [148] attempted to address this by deriving the background model twice, using orthogonal kinematic selections, and using the resulting variation of the background prediction in the signal region to derive systematic uncertainties. In principle this method accounts for biases in the model due to the extrapolation into the signal region by making one model derivation region kinematically "closer" to the signal region. It also naturally provides a full spectrum (and in principle, high dimensional) uncertainty in the final discriminant distribution with the proper bin-to-bin correlations. Ideally one would chop the phase space into many orthogonal regions, each progressively closer to the signal region, such that trends in the extrapolation of the models across phase space could be extracted. Unfortunately, these attempts quickly become limited by
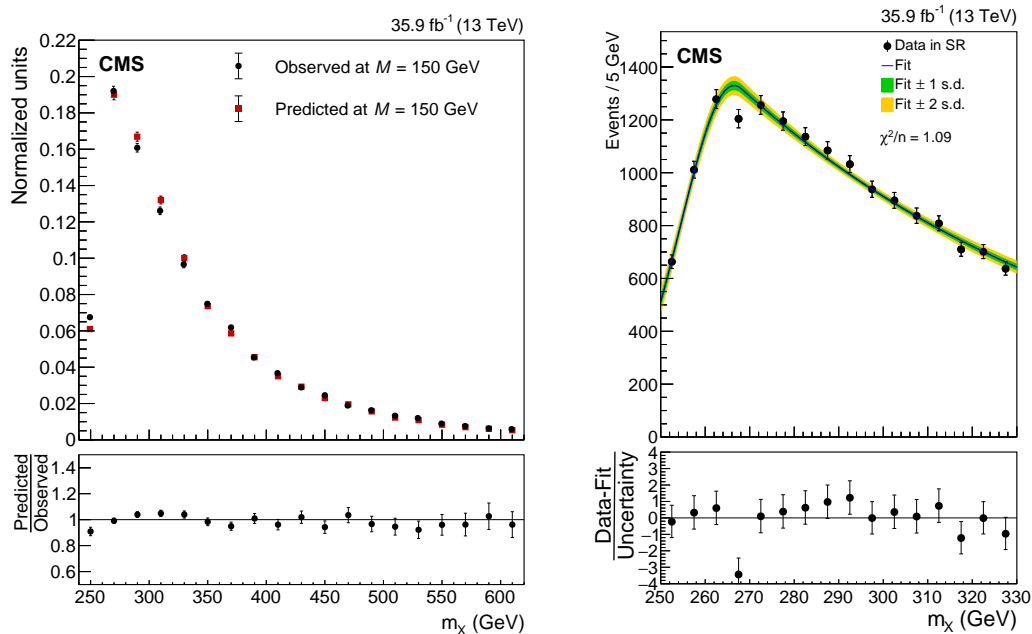
Figure 5.5: These plots illustrate the validation and result of the CMS background modelling of the HH mass spectrum [402]. Left: observed and predicted HH mass spectrum in a validation region centred around $m_{b\bar{b}} = 150$ GeV. Right: A fit to the background-only hypothesis of the m_{HH} distribution in the signal region in data.

the need to validate each model at the statistical precision anticipated in the signal region. If this requirement is not kept, large systematic uncertainties are required to cover the lack of precision in the model validation. These issues are compounded when trying to model higher dimensional target spaces to improve the sensitivity and model independence of searches.

One of the primary limitations of the current ATLAS background model is the algorithm used to derive the correction factors from low to high b-jet multiplicity. The method iteratively weights multiple one dimensional distributions, which are selected to encapsulate the primary differences in the scattering processes with as few variables as possible. This avoids the statistical limitations of high dimensional histograms but may not correctly account for (anti)correlations between the reweighted distributions. With the integrated luminosity of 27.5 fb^{-1} used in [148] one could argue hints of such effects are becoming visible and a new strategy will almost certainly be required for analyses of the full Run 2 data set.

In the low mass phase space near the kinematic threshold $m_{HH} \gtrsim 250$ GeV, the CMS and ATLAS searches suffer from the reliability of any potential excess on top of a sharply peaking background, as shown in Fig. 5.5.

The CMS background model prediction is validated by comparing the prediction for the signal region and the actual signal region in a kinematic sideband defined by moving the Higgs boson mass window from 120 to 150 GeV. ATLAS used a similar background validation method, looking at signal-region-like select $m_{b\bar{b}}$ Higgs shifted both below and above the actual Higgs boson mass. The background shape has a strong dependence on the di-jet mass selection, as it is shown in Fig. 3 of [461] for CMS, but it is properly modelled.

The ATLAS background strategy and the functional fits used by CMS can easily accommodate sub-dominant background sources like $t\bar{t}$, H/Z+jets and diboson processes using simulated samples. In the ATLAS approach the simulated backgrounds processes are used in a two step process.
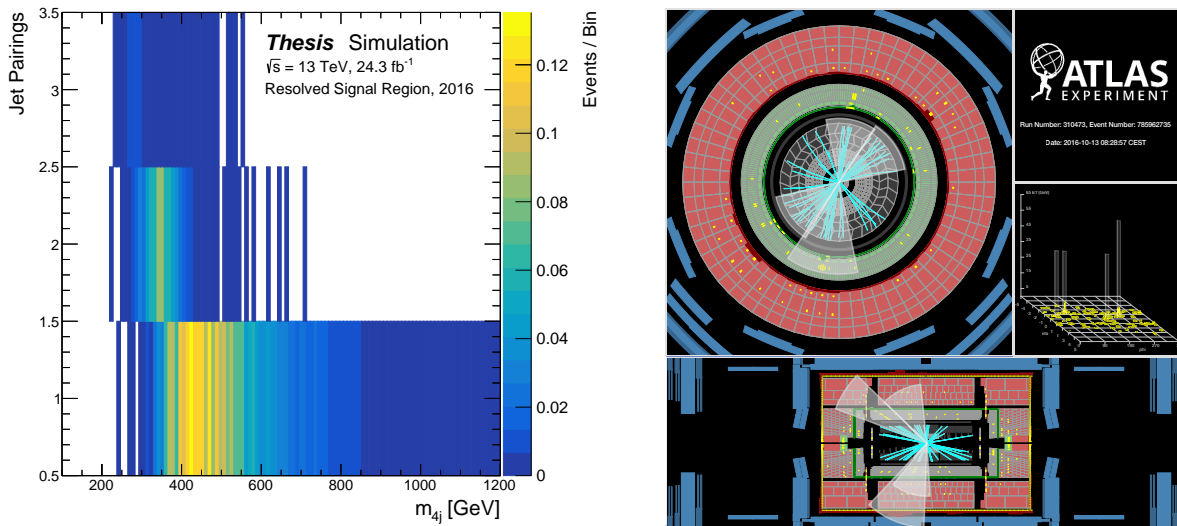
Figure 5.6: Left: Distribution of the number of jet pairings which pass the $\Delta R(j,j)$ selection as a function of the reconstructed m_{HH} for simulated SM HH events [462]. Right: An event collected by ATLAS during 2016 data taking with m_{HH} =272 GeV which passes the signal region selection from [148]. Of the three possible pairings, the two with large di-jet opening angles pass the $\Delta R(j,j)$ sliding requirement, while the third pairing with both opening angles approximately equal to twice the jet radius fails. This third pairing is consistent with the topology of the dominant two to two gluon scattering background where the two outgoing gluons split to $b\bar{b}$ pairs and results in a low mass large radius jets.

First, they are run through the data driven background modelling procedure so that they can then be subtracted from the background model procedure as applied to data. This gives a multi-jet background estimate where the other processes have been removed. Next, the simulated backgrounds are added back into the background model to give the total background.

The hemisphere mixing method has been successfully used in the search based on the 2016 dataset. With the increasing statistics, the need for an accurate modelling of the $t\bar{t}$ and electroweak processes will become more relevant. It is not clear that the hemisphere mixing approach used for the CMS non-resonant result can appropriately model the event level correlations of these processes. Indeed the hemisphere mixing technique relies on its ability to remove the event level correlations of the HH signal process to avoid signal contamination in the background model. This same dilution of event level correlation could subtly impact the $t\bar{t}$ and electroweak backgrounds such that their contamination in the high signal purity bins of the BDT output is underestimated.

Furthermore, to avoid tricky statistical issues, the hemisphere mixing, Sec. 5.1.1, can only use each source event once, limiting the statistical precision of the background model to that of the true background. If the statistical uncertainty of the published ATLAS background model is set to $\sqrt{N}$ in each bin of the final discriminant, the sensitivity to SM HH production is reduced by 33%. This is unsurprising because the ATLAS result [148] is statistically limited: the sensitivity of a measurement where the background and data have the same statistical uncertainty scales with $1/\sqrt{\mathscr{L}}$.

5.1.3 Potential improvements

All final states with b-jets are likely to gain from dedicated b-jet energy regressions and calibrations. In the $b\bar{b}b\bar{b}$ case improvements in the b-jet energy scale reduce the mass resolution for both

Higgs bosons allowing for tighter signal region definitions with the same signal efficiency. CMS has demonstrated this in their most recent resonant search [402] where the Higgs boson mass resolution for different resonance mass hypotheses improved by 6-12%. The tighter optimal signal region definitions then improved the search sensitivity by 5-20%.

One promising approach to construct a multi-jet model from lower b-jet multiplicity data is to reweight using a single multivariate classifier output distribution rather than several one dimensional kinematic distributions or sparse high dimensional histograms. The classifier would be trained to separate low b-jet multiplicity data from high b-jet multiplicity data without any flavour tagging information. In principle this should appropriately account for (anti)correlations between the classifier input variables and provide a better high dimensional model of the four b-jet data. ATLAS has already released a search for Higgsino pair production [345] using a BDT based reweighting scheme using the same event selection as Ref. [148].

Multivariate reweighting provides a possible solution to the curse of dimensionality in extrapolating a multi-jet model across b-jet multiplicity but does not address the assumption that the reweighting can be extrapolated across the kinematic phase space. This assumption could instead be independently verified in a tri-jet sample, if triggers exist to collect such a sample. The extrapolation across phase space could also be tested in a synthetic sample like that generated by the CMS hemisphere mixing procedure. Furthermore, at low values of m_{HH} the signal contamination in events with exactly three b-jets would be negligible and could be used to validate the background procedure with substantially higher statistics than the four b-jet sample. One would have to use caution with data containing three b-jets, with $m_{HH} \gtrsim 500\,\text{GeV}$ data, as it could offer significant sensitivity to new physics and should be explored as an additional signal selection.

The most obvious approach to improve any search is to perform combined fits with more regions, more dimensions or on especially trained multivariate classifiers. All of these approaches require well understood high dimensional background models. The following variables, in addition to the Higgs boson candidate masses and m_{HH}, should be investigated:

- Angular correlations like the pseudorapidity separation between Higgs boson candidates $\Delta\eta(H_1, H_2)$ provide discrimination between scalar and tensor resonances and low-mass Higgsino pair production.

- The (b-)jet multiplicity to target VBF HH production (VBF jet η difference and di-jet mass are also relevant in this case).

- Correlations in other di-jet constructions (in contrast to the Higgs boson candidate construction) may provide a handle in separating the signal from the dominant two-to-two gluon scattering background for $m_{HH} \lesssim 400\,\text{GeV}$. This combinatoric background can be seen in Fig. 5.6 where, depending on the chosen jet pairing, the displayed event can look like a HH event with back-to-back b-jets from each Higgs boson or a di-gluon event where each gluon splits to a low-mass collimated $b\bar{b}$ pair.

With the full Run 2 dataset of about 300 fb^{-1}, it may already be feasible to perform dedicated measurements of SM ZZ and ZH production in the $b\bar{b}b\bar{b}$ final state.

$$\frac{\sigma(pp \to ZZ \to b\bar{b}b\bar{b})}{\sigma(pp \to HH \to b\bar{b}b\bar{b})} \approx \frac{15\,\text{pb} \times 0.15^2}{33\,\text{fb} \times 0.58^2} \approx 31$$

$$\frac{\sigma(pp \to ZH \to b\bar{b}b\bar{b})}{\sigma(pp \to HH \to b\bar{b}b\bar{b})} \approx \frac{880\,\text{fb} \times 0.15}{33\,\text{fb} \times 0.58} \approx 7$$

Measurements of these processes would serve to validate the background model and reduce the impact of the systematic uncertainties. The same measurements in the $b\bar{b}\tau^+\tau^-$ final state would benefit from even larger ratios. The techniques used to generalise the HH search to these measurements will also be useful in developing generalised $b\bar{b}b\bar{b}$ searches for additional exotic particles in processes like $Y \to XH \to b\bar{b}b\bar{b}$.

5.2 $HH \to b\bar{b}\gamma\gamma$: status and perspectives

E. Brost, R. Teixeira de Lima, M. Gouzevitch

5.2.1 Overview

The $HH \to b\bar{b}\gamma\gamma$ final state has the lowest branching fraction among the most sensitive channels, just 0.3%, but it provides a high signal-to-background ratio by reducing multi-jet events with the identification of two high quality photons. The analysis strategies developed for $HH \to b\bar{b}\gamma\gamma$, closely follow those for the SM $H \to \gamma\gamma$ analyses.
Two isolated photons with $p_{\text{T}} > 25$ GeV provide an excellent handle for the triggers. This provides a clear advantage in this final state for $m_{HH} < 400$ GeV, compared to the ones with higher branching fractions, but with trigger strategies requiring higher momenta particles, such as $HH \to b\bar{b}b\bar{b}$.
Furthermore,the presence of the $H \to \gamma\gamma$ photons provides a clear strategy for event selection and signal extraction. As a consequence, the ATLAS and CMS analyses of Run 2 dataset [149, 438] ($\approx$36fb^{-1}) have many similarities.
ATLAS excludes SM HH production at 95% confidence level with cross sections higher than 0.73 pb (expected 0.93 pb) while CMS 0.79 pb (expected 0.63 pb). Limits are also set on the modifier of the Higgs self-coupling, with ATLAS constraining $-8.2 < \kappa_\lambda < 13.2$ and CMS $-11 < \kappa_\lambda < 17$. However, small changes in strategy can lead to significant improvements to sensitivity to SM and BSM HH production. Therefore, it is important to understand the details of each analysis strategy.

5.2.2 Signal modelling

The $HH \to b\bar{b}\gamma\gamma$ final state benefits from having a fully reconstructable final state. In contrast with other final states, such as $HH \to b\bar{b}b\bar{b}$ and other fully hadronic channels, there are no combinatoric issues in the identification of the Higgs boson candidates. Therefore, one expects to see clear peaks consistent with the Higgs boson mass in both the di-jet and di-photon invariant mass spectra. Due to the good energy resolution and low reconstruction uncertainties for photons at the LHC experiments, the di-photon mass resolution is small relative to the di-jet mass, with $\sigma_{\gamma\gamma}/\text{M}_{\gamma\gamma} = 1.3\%(1.5)$ for the most sensitive signal region in the CMS (ATLAS) search. CMS quotes $\text{M}_{\text{jj}}/\sigma_{\text{jj}} = 15\%$ for that same category after applying the b-jet energy regression, derived using $HH \to b\bar{b}b\bar{b}$ signal events as described in Sec. 4.3.

In order to avoid issues with the statistical precision of the simulated samples, both the ATLAS and CMS searches model the peaks from Higgs boson decays with the double-sided Crystal-Ball (DSCB) function for $m_{\gamma\gamma}$ (ATLAS and CMS) and m_{jj} (CMS). The DSCB function is chosen for its Gaussian core and power-law asymmetric tails:

$$f(x;\mu,\sigma,\alpha_L,p_L,\alpha_R,p_R) = N \cdot \begin{cases} A_L \cdot \left(B_L - \frac{x-\mu}{\sigma}\right)^{-p_L} & \text{for } \frac{x-\mu}{\sigma} > -\alpha_L, \\ A_R \cdot \left(B_R + \frac{x-\mu}{\sigma}\right)^{-p_R} & \text{for } \frac{x-\mu}{\sigma} > \alpha_R, \\ e^{\frac{(x-\mu)^2}{\sigma^2}} & \text{for } \frac{x-\mu}{\sigma} < -\alpha_L \\ & \text{and } \frac{x-\mu}{\sigma} > \alpha_R \end{cases}, \qquad (5.2)$$

where A_L, A_R, B_L, B_R are normalization constants defined by:

$$A_k = \left(\frac{p_k}{|\alpha_k|}\right)^{p_k} \cdot e^{-\frac{\alpha^2}{2}}, \tag{5.3}$$

$$B_k = \frac{p_k}{|\alpha_k|} - |\alpha_k|. \tag{5.4}$$

One of the main benefits of using the DSCB function to model the Higgs boson is the ability to describe the effects of systematic uncertainties in its shape with extra parameters in Eq.(5.2). Therefore, scale and resolution effects can be mapped into variations of the mean and width of the DSCB Gaussian core, respectively, keeping the tail parameters fixed. This description simplifies the final steps of the searches, which involve unbinned parametric fits to describe the continuous background and extract the signal.

The DSCB parameters are determined from a fit to the simulated $HH \to b\bar{b}\gamma\gamma$ signal. In ATLAS, the fit is performed in the $m_{\gamma\gamma}$ distribution, while in CMS, the fit is performed simultaneously in the $m_{\gamma\gamma}$ and m_{jj} distributions[1], with $f(m_{\gamma\gamma}, m_{jj}) = g(m_{\gamma\gamma}) \times h(m_{jj})$ where $g(x)$ and $h(x)$ are DSCB functions, Eq. (5.2). The modelling of the $m_{\gamma\gamma}$ and m_{jj} distributions is shown in Fig. 5.7.
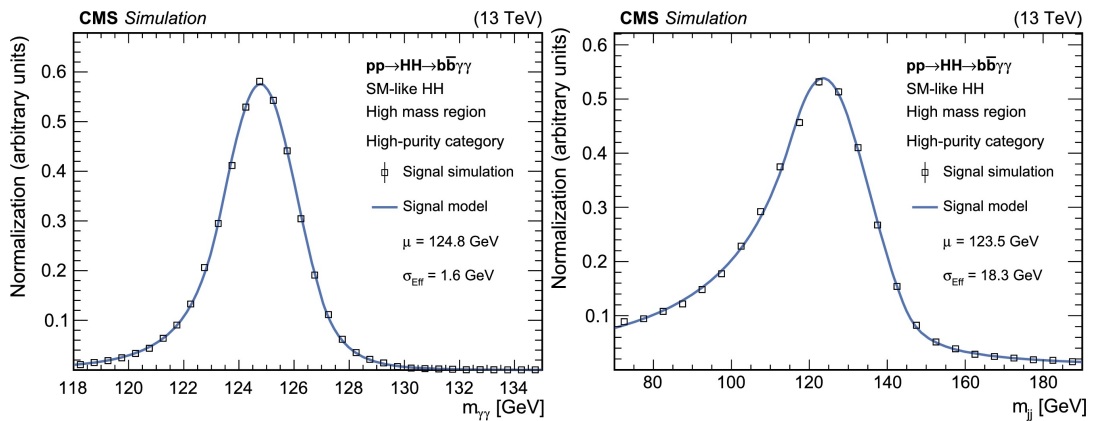
Figure 5.7: $m_{\gamma\gamma}$ (left) and m_{jj} (right) signal modelling in the CMS $HH \to b\bar{b}\gamma\gamma$ analysis. The blue lines represent the double-sided Crystal Ball parametric fit to the SM HH signal simulation (squares) [438].

The ATLAS and CMS searches use slightly different strategies to simulate the $HH \to b\bar{b}\gamma\gamma$ signal. The ATLAS non-resonant signal is modeled at approximate NLO, using MG5_aMC@NLO [52], reweighted in m_{HH} to take into account the full top quark mass dependence, and parton showering uses HERWIG++ [463]. CMS models the non-resonant $HH \to b\bar{b}\gamma\gamma$ signal at LO in MG5_aMC@NLO, and parton showering uses PYTHIA [93]. A comparison of non-resonant $HH \to b\bar{b}\gamma\gamma$ production at LO and NLO is shown in Fig. 5.8. The transverse momenta of the jets is harder in the LO simulation, and therefore the signal acceptance is higher at LO.

5.2.3   Event selection and reconstruction

The online selection strategy for the $HH \to b\bar{b}\gamma\gamma$ analyses follows closely the approaches from the $H \to \gamma\gamma$ analyses, utilising the $H \to \gamma\gamma$ targeted di-photon triggers. These triggers offer lower online thresholds on the photon p_T than the jet corresponding triggers thanks to the good quality of the trigger-level reconstructed photons.

---

[1]It has been checked using simulations that the correlations between the two distributions are negligible.
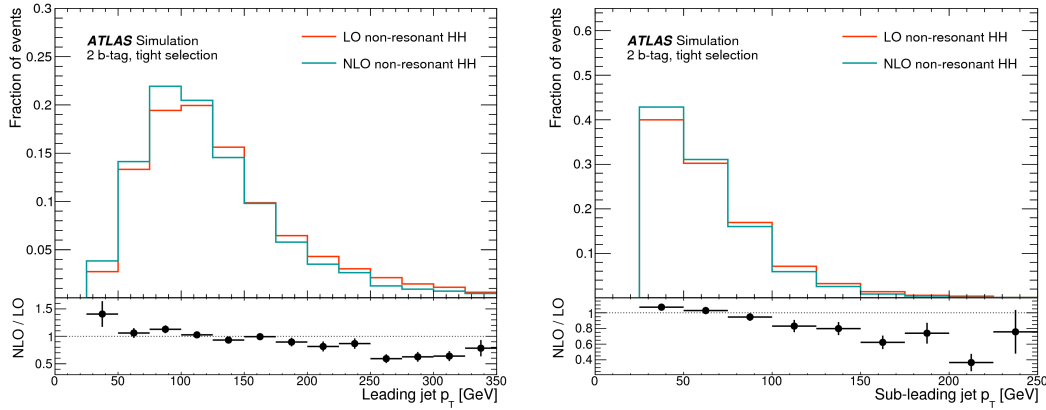
Figure 5.8: Comparison of ATLAS $HH \to b\bar{b}\gamma\gamma$ signal at LO (orange) and NLO (green) for the transverse momenta of the leading (left) and sub-leading jets (right) [149].

In ATLAS, the di-photon trigger requires two clusters of energy deposits in the electromagnetic calorimeter with transverse energy above 35 GeV and 25 GeV for the leading and sub-leading cluster, respectively. These clusters are required to have shapes that are consistent with photon-initiated electromagnetic showers and that are isolated from other electromagnetic activity [464]. The CMS di-photon trigger requires the leading (sub-leading) transverse isolated energy deposit to be above 30 (18) GeV, and that the invariant mass of the di-cluster system be above 90 GeV [465]. Both ATLAS and CMS triggers are nearly fully efficient for the $H \to \gamma\gamma$ and $HH \to b\bar{b}\gamma\gamma$ photons that pass the kinematic requirements. The offline object selection of the $HH \to b\bar{b}\gamma\gamma$ analyses is seeded by finding good quality photons and jets, which must be consistent with the hadronisation of the b-quarks. The overall strategies of the ATLAS and CMS analyses are similar, and begin by selecting photons close to their trigger thresholds, with extra criteria inspired by $H \to \gamma\gamma$ analyses - such as $E_T^\gamma / m_{\gamma\gamma}$ requirements, which preserve the shape of the $m_{\gamma\gamma}$ distribution.

One important distinction between the ATLAS and CMS $HH \to b\bar{b}\gamma\gamma$ analyses is their use of the b-tagging information (see Sec. 4.2) to classify event categories. The ATLAS $HH \to b\bar{b}\gamma\gamma$ search categorises events according to the number of b-jets:

(i) two b-tags, defined by selecting events with exactly two jets which pass the 70% efficient b-tagging working point;

(ii) one b-tag, exactly one jet passes the 60% efficient b-tagging working point.

Events with more than two b-tagged jets are vetoed in order to be orthogonal with the $HH \to b\bar{b}b\bar{b}$ analysis, and those with no b-tagged jets are not considered as signal events. The $H \to b\bar{b}$ candidate is then reconstructed with the two b-tagged jets, in the two b-tag region, and with the b-tagged plus an extra jet, in the one b-tag region. This extra jet is selected with a BDT trained with kinematic information of each possible $H \to b\bar{b}$ candidate reconstructed with the b-tagged jet and the non-b-tagged jets in the event. More details of this approach will be discussed in Sec. 5.2.7. After the $H \to b\bar{b}$ candidate is defined, loose and tight jet selections are defined, depending on the p_T of the jets: loose if the leading jet $p_T > 40$ GeV; tight if the leading jet has $p_T > 100$ GeV and the sub-leading $p_T > 30$ GeV.

CMS exploits the full distribution of the probability that the jets are b-tagged (the b-tagging score). First, the $H \to b\bar{b}$ candidate is reconstructed using the jets with the highest b-tagging score and their scores are then used as inputs for the multivariate event categorisation, described in Sec. 5.2.7. The angular correlations between the four objects used to reconstruct the $H \to \gamma\gamma$ and

$H \to b\bar{b}$ candidates, the helicity angles, are also exploited by the event categorisation algorithm to classify signal versus $\gamma\gamma$+jets background events.

Helicity angles have been historically used in analyses such as the SM $H \to ZZ^* \to l^+l^-l^+l^-$ searches and subsequent measurements, as they have been shown to distinguish between different spin and parity hypotheses for the Higgs boson [466]. Some of these angles are also sensitive to the tensor structure of a resonance production mechanism [467]. Similar to the four-lepton final state, the $HH \to b\bar{b}\gamma\gamma$ analysis also profits from having four final state objects that can be used to measure such angles.

Three helicity angles have been found to bring the most sensitivity in the CMS $HH \to b\bar{b}\gamma\gamma$ search, as shown in Fig. 5.9. They are defined in the Collins-Soper (CS) references frame [468]. The CS frame boosts to the rest frame of the Higgs bosons and defines fixed axes such that measured variables are sensitive to spin and CP properties of the Higgs boson. It minimises the dependence of the angles on the transverse momentum of the HH system, as follows:

- $|\cos(\theta_{HH}^{\mathrm{CS}})|$: θ_{HH} is the angle between the momentum of the $H \to \gamma\gamma$ candidate and the line that bisects the acute angle between the colliding protons.
- $|\cos(\theta_{\gamma\gamma}^{\mathrm{CS}})|$, $|\cos(\theta_{jj}^{\mathrm{CS}})|$: $\theta_{\gamma\gamma}^{\mathrm{CS}}$ and $\theta_{jj}^{\mathrm{CS}}$ are the angles between the Higgs bosons and their decay products in the CS reference frame. The two photons or jets used to define the angle are chosen randomly.
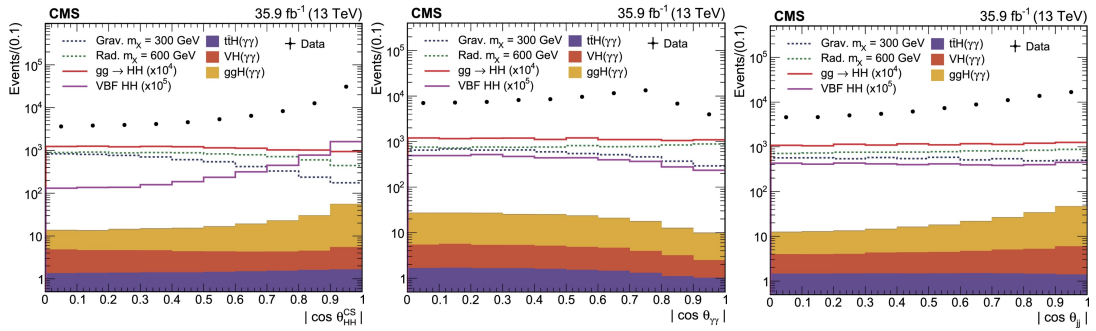
Figure 5.9: Distributions of the three helicity angles for data (dots), γ+jets background, different signal hypotheses and three single Higgs boson samples ($t\bar{t}H$, VH, and ggF) after the selections on photons and jets [438] have been applied.

The output of this algorithm classifies events as more signal- or continuum-background-like, separating events into high, medium and low purity categories. Only the two highest purity categories are used for the signal extraction.

The $HH \to b\bar{b}\gamma\gamma$ final state can be fully reconstructed and the m_{HH} spectrum is a particularly important observable for the resonant $HH \to b\bar{b}\gamma\gamma$ searches. The m_{HH} estimator described in Sec. 4.7.1 is actually used for the signal extraction.

5.2.4 Background modelling

Searches for $HH \to b\bar{b}\gamma\gamma$ are affected by both backgrounds from single Higgs boson production and by non-resonant backgrounds with continuum $m_{\gamma\gamma}$ spectra.

The dominant backgrounds to the $b\bar{b}\gamma\gamma$ final state are those in which two objects identified as photons (either prompt photons or jets misidentified as photons) are produced in association with jets (referred to as γ+jets). The simulation of these final states poses a major challenge because of large effects from higher orders in QCD. Furthermore, the knowledge of the fragmentation effects

for a jet misidentified as a photon is quite limited. For these reasons, these contributions are modelled entirely from data in both ATLAS and CMS $HH \to b\bar{b}\gamma\gamma$ searches with maximum-likelihood fits to parametric shapes.

However, the choice of a specific function, or families of functions, for the background modelling leads to extra systematic uncertainties related to possible biases in the signal estimate. This uncertainty is derived by generating pseudo-data from a certain function choice (truth function) and performing the signal extraction with another function of choice (fit function). There are then two alternative approaches: either by testing different truth functions against the fit function, from which an uncertainty due to this choice can be extracted; or the number of degrees of freedom can be increased in the fit function to reduce the bias of fitting different truth function to a negligible level (defined formally as a maximum of 14% of the statistical uncertainty[2]).

With the large amount of data to be analysed in the next iterations of these searches, this uncertainty might become the dominant one, justifying the pursuit of alternative background estimation methods, such as Gaussian Processes (GPs) [469] and envelope [470] methods.

In the GPs approach, instead of defining the parametric description $f(x)$, where x is the fitted observable (in this case $m_{\gamma\gamma}$ or $m_{jj\gamma\gamma}$), $f(x)$ is modelled as a Gaussian and the correlation between two points x and x' is given by a *covariance kernel* $\Sigma(x, x')$. The choice of the fit function becomes the physics inspired definition of a covariance kernel, which could encode detector specific information, such as energy resolution and scale uncertainties when fitting the invariant mass distribution. Moreover, the GPs fit is enough flexible to allow for any function that respects the covariance relation defined by the kernel.

The envelope method includes the bias uncertainties in the fitting procedure. All possible parametrisations of the background are considered while performing the maximum likelihood fit, with a penalty proportional to their number of degrees of freedom.

Single Higgs boson processes, with two additional jets and with a subsequent decay of the Higgs boson to two photons, are 5–14% of the total background. Additional jets can be effectively initiated by b-quarks, or by lighter quarks and misidentified as a b-jet. The SM single Higgs boson background contribution is estimated using a parametric model fitted to simulated samples. The SM single Higgs boson background is particularly challenging for the $b\bar{b}\gamma\gamma$ searches, as the $m_{\gamma\gamma}$ peak, which is the most important handle for signal discrimination, appears as a background feature. However, other event characteristics that are dependent on the Higgs boson production mechanism can be exploited. Some of these features might also be helpful to reduce the continuous background, therefore a combined background mitigation procedure can be devised. The CMS parametric fit of $m_{\gamma\gamma}$ and m_{jj} distributions, described in Sec. 5.2.5, mitigates the impact of the single Higgs boson background. Alternatively a machine learning based multi-classification algorithm, exploiting kinematic properties of the four-body system and other event observables, such as the number of jets and b-jets, and missing transverse momentum, could be investigated.

New physics may enhance single Higgs production too, both HH and $t\bar{t}H$ can be enhanced by modifications to the Higgs-top Yukawa coupling. Performing a simultaneous signal extraction of the $HH \to b\bar{b}\gamma\gamma$ and $t\bar{t}H \to \gamma\gamma$ signals could account of this possible scenario. The ability to constrain the SM single $H \to \gamma\gamma$ backgrounds will play an important role in the future.

---

[2]The bias is estimated by how much the definition of standard deviation around the unbiased expected signal strength (μ) has to be inflated to cover 68.3% of the bias expected μ, in alternative of adding a bias term that corrects the bias μ. A 14% bias with respect to the unbiased standard deviation, requires to inflate the definition of standard deviation by 1%, which is much smaller than the systematic uncertainties in the analysis.

5.2.5   Signal extraction

The signal extraction in the $HH \to b\bar{b}\gamma\gamma$ searches is similar to the procedure used in the SM $H \to \gamma\gamma$ measurements, to take advantage of the excellent mass resolution of the $H \to \gamma\gamma$ channel, by fitting the resonant $H \to \gamma\gamma$ peak on top of the continuous and monotonically falling background. For $HH \to b\bar{b}\gamma\gamma$ searches, the presence of the $H \to b\bar{b}$ resonant peak becomes an extra handle to constrain or reduce background processes. The ATLAS and CMS analyses signal extraction strategies differ particularly in the usage of the $H \to b\bar{b}$ mass spectrum.

The ATLAS approach is an unbinned, maximum-likelihood fit to the $m_{\gamma\gamma}$ distribution and the $H \to b\bar{b}$ resonance is used to reduce the background by requiring the compatibility of m_{jj} peak with the Higgs hypothesis ($80/90 < m_{jj} < 140$ GeV for the loose/tight selection). The relative contribution of $\gamma\gamma$, γj, jγ and jj produced in associations with jets, to the continuum background is determined from data by varying the photon identification and isolation criteria. The functional form used to model the background is then chosen using events simulated with SHERPA [85]. The accuracy of the simulation is tested in events passing all the event selection requirements but failing the b-tagging and a correction factor, up to 5%, is derived as function of $m_{\gamma\gamma}$ and applied in the one and two b-tag categories. The $\gamma\gamma b\bar{b}$ is the dominant contribution to the continuum background in the two b-tag category ($\approx 80\%$), while $\gamma\gamma$bj ($\approx 60\%$) dominates in the one b-tag category, as shown in Fig. 5.10.
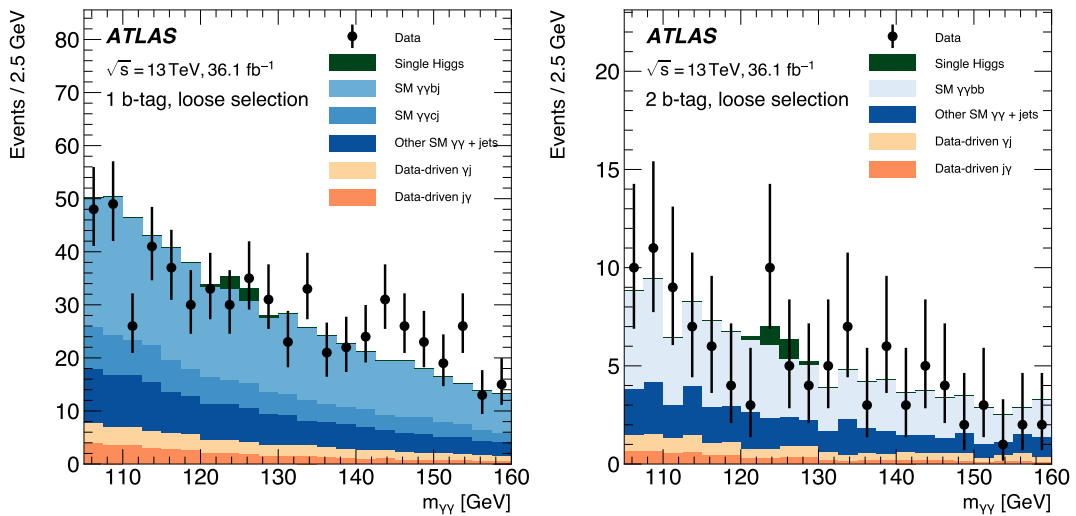
Figure 5.10: The expected number of background events for the continuum $\gamma\gamma$+jets production, other continuum γ+j production (orange) and single Higgs boson production (green) is compared to the observed data (black points) for the $m_{\gamma\gamma}$ distribution in the one (left) and two b-tag (right) categories [149].

The full background fit is shown in Fig. 5.11, for the loose and tight selections in the two b-tag category.

In the CMS analysis, the signal extraction is performed simultaneously in the $m_{\gamma\gamma}$ and m_{jj} distributions (2D fit). It assumes that the background can be described by a two dimensional parametric function and that can be factorised, similarly to the parametric signal model described in Sec. 5.2.2. This hypothesis is tested by checking if possible correlations between $m_{\gamma\gamma}$ and m_{jj} would be statistically significant with the typical expected number of background events in the analysis signal regions. The validity of this assumption is therefore dependent on the size of the dataset, and has to be checked again with the increase of the integrated luminosity. The projections in $m_{\gamma\gamma}$ and
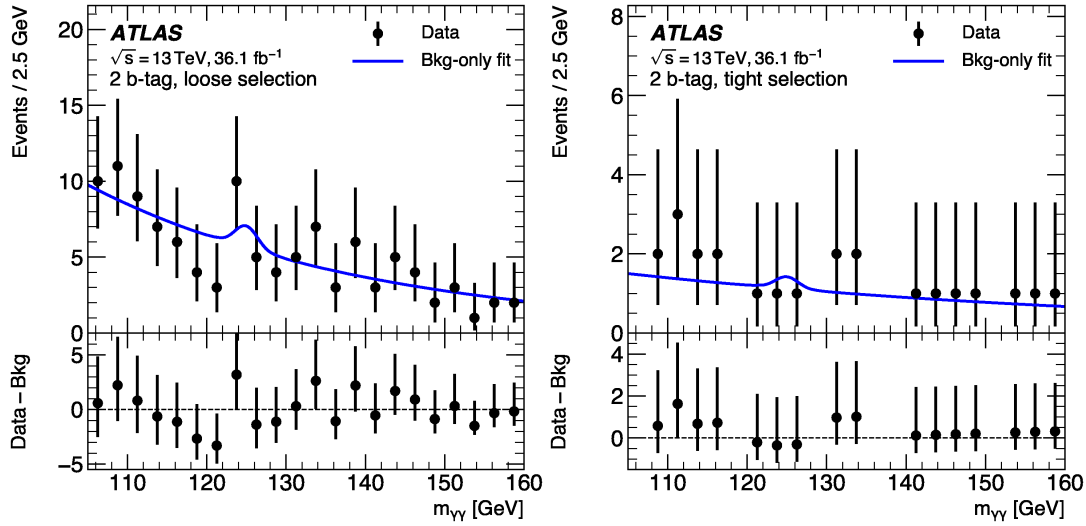
Figure 5.11: $m_{\gamma\gamma}$ distributions for the two b-tag category after the loose (left) and tight (right) event selection requirements are applied [149].

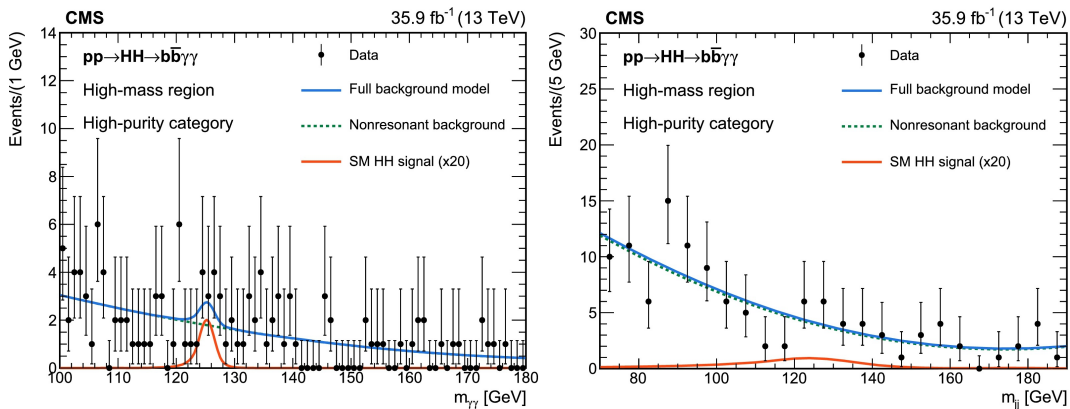m_{jj} distributions for the most sensitive categories to the SM HH production are shown in Fig. 5.12.

Figure 5.12: $m_{\gamma\gamma}$ and m_{jj} projections of the 2D maximum-likelihood fit for the signal extraction, in the most sensitive category to the SM HH production [438].

The ATLAS approach simplifies the continuum background description, as it does not depend on the accuracy of the $m_{\gamma\gamma}$–m_{jj} correlations modelling, for both the signal and background hypotheses. On the other hand, the CMS 2D fit approach constrains better the non-resonant background exploiting fully the m_{jj} distribution and it improves the search sensitivity by $\approx 10\%$.

5.2.6 Systematic uncertainties

The $HH \to b\bar{b}\gamma\gamma$ searches are currently limited by the statistics of the Run 2 dataset. Theoretical uncertainties on the PDF and scale variations are applied to the non-resonant signal model and they amount to 3–6%. Uncertainties on the normalisation of single Higgs boson background processes are also taken into account, corresponding to 1–20%.

Photon trigger efficiency, as well as photon energy scale and resolution uncertainties impact the signal model and acceptance by 1–5%. The largest experimental uncertainties come from the jet energy scale and resolution (1–5%), and from flavour-tagging uncertainty (10–20%).

ATLAS additionally applies an uncertainty due to the continuum background fitting process,

and a 100% uncertainty on the ggF and WH single Higgs boson production modes in events with extra heavy-flavour particles.

5.2.7   Machine learning in $HH \to b\bar{b}\gamma\gamma$: use and challenges

Both ATLAS and CMS analyses use machine learning methods for event categorisation and signal classification. ATLAS uses a BDT method for the selection of the $H \to b\bar{b}$ candidate, when only one jet is b-tagged. The b-tagged plus non-b-tagged jet pairings are built for the signal (only one pairing is correct) and the continuum background (no pairing is correct) using simulated events. The BDT is trained to classify correct and incorrect pairings based on the kinematic information of the paired jets: paired jets p_T^j, di-jet p_T and b-tagging information, m_{jj}, paired jets η^j, di-jet η^{jj}, $\Delta\eta$ between the paired jets. The ranking of the jets according to the closest match between the di-jet mass and the Higgs boson mass, highest jet p_T^j and highest di-jet p_T is exploited as well. Each di-jet pairing in an event is given a BDT score, the di-jet with the highest score is then selected to reconstruct the $H \to b\bar{b}$ candidate.

In the CMS analysis, a BDT is trained for signal classification against the continuum background. The training variables are: the b-tagging scores of the jets that form the $H \to b\bar{b}$ candidate, the three helicity angles and the HH transverse balance variables $p_T^{jj}/m_{jj\gamma\gamma}$ and $p_T^{\gamma\gamma}/m_{jj\gamma\gamma}$. The training is performed with the ensemble of all non-resonant HH production hypotheses (SM plus the shape benchmark used for BSM reinterpretations as explained in Sec. 2.4) as signal. This choice allows for the final classifier performance to be generalised to various BSM HH production hypotheses. Events that pass all the analysis selection criteria except the identification and isolation requirements for one photon candidate, are used as background events for the training. This choice is validated by comparing the input distributions in the training dataset with the signal selection events that fall outside of a mass window of 30 GeV around the Higgs boson mass in $m_{\gamma\gamma}$.

A common issue with classifiers trained with specific target signals is how their performance can be generalised to other signal hypotheses, for which the kinematic properties might change substantially. Both ATLAS and CMS searches deal with this challenge by defining different kinematic regimes with the four-body invariant mass, populated by different signal hypotheses and background compositions, in which dedicated training or cut based analyses can be performed. In addition, CMS chooses to use an ensemble of different signal simulated samples as the signal hypothesis for the BDT training to guarantee a uniformity of the sensitivity to different final states.

A different approach, already used by other HH analyses such as the CMS $HH \to b\bar{b}VV^*$ search, is to train a discriminant based on a parameterised neural network (NN). The NN training is performed as a function of a certain model parameter, such as the X resonance mass when looking for resonant $X \to HH \to b\bar{b}\gamma\gamma$ signals, or the Higgs boson self-coupling modifier κ_λ. The performance for each individual model parameter is similar to the performance of a network trained using that single hypothesis as the target signal. Therefore, the parameterised NN effectively trains different NNs for each model parameter in a single training procedure. Additionally, this NN is also able to interpolate between the model parameters used for training.

5.3 $HH \to b\bar{b}\tau^+\tau^-$: status and perspectives

K. Leney

The $HH \to b\bar{b}\tau^+\tau^-$ final state has a branching fraction of 7.3% for a SM Higgs boson with mass of 125 GeV and a relatively small background contribution from other SM processes, compared to the

$HH \to b\bar{b}b\bar{b}$ search. Three final states of the τ-lepton pair are combined for the $HH \to b\bar{b}\tau^+\tau^-$ searches: $\tau\tau \to e\tau_h$, $\tau\tau \to \mu\tau_h$, and $\tau\tau \to \tau_h\tau_h$. These three final states all together account for 88% of $\tau\tau$ decays. The case where both τ-leptons decay to lighter charged leptons ($\ell = e/\mu$) and their associated neutrinos account for the remaining 12% of $\tau\tau$ decays, but this category of events have not been considered by either the ATLAS or CMS experiments yet [150, 434].

The reconstruction of $HH \to b\bar{b}\tau^+\tau^-$ events poses several challenges, including the reconstruction of hadronic objects: b-jets and hadronically decaying τ-leptons, τ_h (as described in sections 4.2 and 4.4), the rejection of objects that mimic these, and the reduction of backgrounds. The most irreducible backgrounds are $Z \to \tau\tau$ produced in association with heavy-flavour jets, $t\bar{t}$ pairs and multi-jet processes, in which quark- and gluon-initiated jets are misidentified as τ_h. Single Higgs boson production, particularly in association with a Z boson or a top pair, is becoming an important background contribution as the size of the available dataset increases.

5.3.1 Analysis strategies

K. Androsov, A. Bethani, A. Betti, H. Fox, M. Gallinaro, K. Leney

At the trigger level, both the ATLAS and CMS experiments require the presence of an isolated lepton or hadronic τ object, depending on the final state.

For the fully hadronic channel ($\tau_h\tau_h$), CMS requires di-τ triggers, while ATLAS uses both single- and di-τ triggers, described in Sec. 4.6. For the semi-leptonic channels ($\ell\tau_h$), ATLAS uses single lepton and lepton-plus-τ on line selections, while CMS uses only single lepton triggers. This use of lepton-plus-τ triggers by ATLAS allows the use of lower p_T thresholds for the analysis object selection, which result in a 3% gain on the final sensitivity for the semi leptonic channels.

Similar trigger strategies are planned for the future, however the increased instantaneous luminosity will force the lepton and jet p_T thresholds to be raised unless new techniques, exploiting track information for instance, are used.

In order to reconstruct a $HH \to b\bar{b}\tau^+\tau^-$ candidate event, it is necessary to identify any electron or muon from a leptonic τ decay, one or two hadronically decaying τ leptons (τ_h), the jets originating from the two b-quarks, and the missing transverse momentum of the event. The latter arises predominantly from the neutrinos accompanying the τ-lepton decays, although neutrinos in semi-leptonic B-hadron decays may also contribute. Both collaborations use a medium operating point for hadronic τ identification, as described in Sec. 4.

In addition to the hadronic τ objects, electrons or muons, the presence of two jets within the tracker acceptance is required. Jets may be required to be tagged as originating from the hadronisation of b-quarks. The operating point used in the ATLAS and CMS analyses provides approximately 70% b-tagging efficiency with a mis-identification rate of approximately 0.3% and 1%, respectively, for light-flavoured jets. The optimisation of the b-jet tagging efficiency and the requirement on the number of b-jets, depends on the background suppression. In the ATLAS search, both jets are required to be b-tagged, while in the CMS analysis events are split into three exclusive categories depending on the number of b-tagged jets (0, 1, or 2).

In the CMS analysis, further classification into "resolved" and "boosted" categories is used in the case of resonant HH production, for invariant mass values (m_{HH}) above 700 GeV [434], where high p_T $H \to b\bar{b}$ candidates are reconstructed more efficiently as a large-radius jet, as described in section 4.2.1. The event is classified as boosted if it contains at least one AK8 jet of invariant mass larger than 30 GeV and $p_T > 170$ GeV that is composed of two sub-jets. Otherwise, the event is classified as resolved. In order to improve the resolution and to enhance the sensitivity of the resonant analysis, the invariant mass is reconstructed using a kinematic fit, as detailed in Sec. 4.7.1.

Different observables related to the event kinematic are used to discriminate between signal and background, with various differences depending on the signal model and the considered $H \rightarrow \tau^+\tau^-$ decay mode.

In both the resonant and non-resonant production modes, m_{HH} is one of the most discriminating variables for background rejection. An essential part of reconstructing the HH mass is to first reconstruct the mass of the two sub-systems, $m_{\tau\tau}$ and $m_{b\bar{b}}$. The $m_{b\bar{b}}$ is improved by applying dedicated b-jet specific energy corrections as discussed in Sec. 4. Accurately reconstructing the mass of a resonance decaying to a pair of τ-leptons is challenging because of the presence of multiple neutrinos from τ-lepton decays, which lead to a kinematic description of the system that is under-constrained. The "collinear approximation" is a simple but frequently used technique to address this problem. It is based on the observation that the neutrinos are produced nearly collinear with the corresponding visible τ-lepton decay and that all the missing transverse energy in the event comes from the neutrinos of the τ-lepton decays. Then, $m_{\tau\tau}$ is directly calculated from the masses and momenta of the visible products of the τ-lepton. This technique gives a reasonable mass resolution, when the two neutrino momenta are not back-to-back or when the di-tau system transverse momentum is large enough to compensate the resolution effects on the reconstructed missing transverse energy. In order to better reconstruct $m_{\tau\tau}$, both the ATLAS and CMS collaborations have developed algorithms including dynamic likelihood techniques [471, 472] to account for the invisible part of the four-momentum due to the neutrinos. The Missing Mass Calculator (MMC) [473] is used by ATLAS, whereas the Secondary Vertex Fit (SVfit) [474, 475] is used by CMS. Both algorithms calculate the best estimate of the $\tau\tau$ invariant mas on an event by event basis, using constraints from the measurements of the visible decay products and the missing transverse energy.

In the case of the MMC algorithm, the estimate exploits the fact that the solutions of the under constrained kinematic system are not all equally probable. Then, additional constraints from the τ kinematics are applied. In this case, the distance ΔR between the neutrino(s) and the visible decay products is parametrised and provides a probability density function that is then incorporated in a global event likelihood. The most probable value provides the final estimation of $m_{\tau\tau}$.

In a similar way, the SVfit $m_{\tau\tau}$ values are reconstructed by combining the measured observables, the x and y components of the missing transverse energy, with a probability model, that includes terms for the τ decay kinematics. The model makes a prediction for the probability to observe the missing transverse energy values measured in the event, given a parameterisation of the kinematics of the τ pair decay and it provides a probability density function as a function of the unknown parameters. The best estimate for the $m_{\tau\tau}$ is the value that maximises this probability.

After selecting events compatible with a di-τ plus b-jets final state, the ATLAS search requires that the MMC-based $m_{\tau\tau}$ be above 60 GeV, while CMS uses an elliptical selection in the $m_{\tau\tau}$-$m_{b\bar{b}}$ plane around the SM Higgs boson mass:

$$\frac{(m_{\tau\tau} - 116\,\text{GeV})^2}{(35\,\text{GeV})^2} + \frac{(m_{b\bar{b}} - 111\,\text{GeV})^2}{(45\,\text{GeV})^2} < 1 \tag{5.5}$$

ATLAS uses three categories of signal events, based on the trigger selection, while CMS defines nine categories in total depending on the τ final state and number of b-jets: $(e\tau_{\text{h}}, \mu\tau_{\text{h}}, \tau_{\text{h}}\tau_{\text{h}}) \times$ (one b-jet, two b-jets, boosted). For both experiments, the most sensitive category is the $\tau_{\text{h}}\tau_{\text{h}}$ where both jets pass the b-tagging requirements.

Both experiments use BDTs trained on different kinematic variables to improve the analysis sensitivity. ATLAS uses BDTs to separate the signal from multi-jet, $t\bar{t}$ and $Z+b$-jet backgrounds. The

input variables include angular information, the full di-τ mass including neutrinos, $m_{b\bar{b}}$ corrected for neutrinos in semi-leptonic B-decays (see Sec. 4.3), m_{HH} and in the leptonic category also thee transverse mass.

ATLAS uses BDTs for all categories of signal events, while CMS uses a BDT only in the semi leptonic resolved categories. Furthermore, while ATLAS uses the output BDT scores directly to extract the signal, CMS applies a cut on the BDT output score and then uses the m_{HH} distribution as the final discriminant for the resonance search, and the "stransverse mass" (m_{T2}) for the non-resonant analysis. The m_{T2} variable exploits the fact that the stransverse mass of the $t \rightarrow Wb$ system is constrained by the top quark mass, and therefore m_{T2} is bounded for the $t\bar{t}$ background (without resolution effects), while this is not the case for the $HH \rightarrow b\bar{b}\tau^+\tau^-$ signal [269].

The MMC-based $m_{\tau\tau}$ and m_{T2} distributions are shown for the $\tau_h\tau_h$ and two b-jets category in Fig. 5.13 for simulated signal and background events.
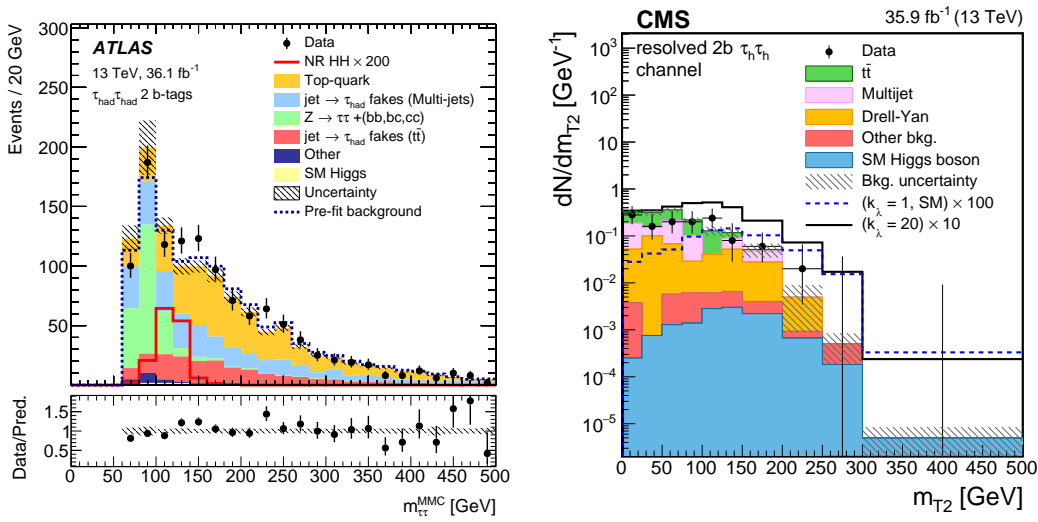
Figure 5.13: The distribution of the MMC-based $m_{\tau\tau}$ (left) [150] and m_{T2} (right) variables in the $\tau_h\tau_h$ and two b-jets category [434].

5.3.2 Modelling of background contributions

K. Androsov, A. Bethani, A. Betti, H. Fox, M. Gallinaro, K. Leney

One of the main backgrounds in the $HH \rightarrow b\bar{b}\tau^+\tau^-$ search comes from $t\bar{t}$ events with $\ell + \tau_h$ final states $\left(t\bar{t} \rightarrow W(\rightarrow \ell\nu)b\, W(\rightarrow \tau_h\nu\nu)\bar{b} \right)$, or lepton and jet final states $(t\bar{t} \rightarrow W(\rightarrow \ell\nu)\bar{b}\, W(\rightarrow q\bar{q})\bar{b})$ where the jet is incorrectly reconstructed as a τ_h object. Due to the relatively large top quark pair production cross section (≈ 832 pb at $\sqrt{s} = 13$ TeV [476, 477]) and final states similar to the signal process, this is the dominant source of background. In both experiments the $t\bar{t}$ model relies on simulation, where ATLAS uses the POWHEG-BOX generator [72] with a NNLO+NNLL precision for the cross section, whereas CMS uses the POWHEG 2.0 generator [478] with a NLO precision for the cross section. In ATLAS, the component of the $t\bar{t}$ background in which the reconstructed τ_h objects are matched to a hadronically decaying τ-lepton at truth level is estimated from simulation. Its normalisation is further constrained in data using the low BDT output score region of the $\tau_\ell\tau_h$ channel. In the $\tau_\ell\tau_h$ channel the component of $t\bar{t}$ in which the reconstructed τ_h object is mis-identified is estimated in an entirely data-driven way. In the $\tau_h\tau_h$ channel, the simulation is corrected using a τ fake-rate derived from data.

Events with a boosted $H \rightarrow b\bar{b}$ candidate are assigned to a dedicated boosted category in the

CMS analysis. A BDT discriminant based on the kinematic differences between the HH and $t\bar{t}$ processes is used in the lepton+jet final states in order to reduce the large amount of $t\bar{t}$ background.

The production of Z bosons in association with heavy-flavour jets provides a significant background to the $HH \to b\bar{b}\tau^+\tau^-$ signal process. Both experiments take the shape of $Z/\gamma^* \to \tau^+\tau^-$+jets from simulation and normalise it using control regions defined in the data. ATLAS uses the SHERPA generator while CMS uses MG5_aMC@NLO [52, 84].

The modelling of this background is limited by the current understanding of the hadronisation of jets initiated from b or c quarks. Cross section predictions for this background do not match the observations in data, and large correction factors need to be applied. In both ATLAS and CMS experiments these are derived from control regions dominated by $Z \to \mu\mu$+jets events. In both cases, the selection is similar to that of the signal region, and an additional cut on $m_{\mu\mu}$ is applied. ATLAS applies an additional selection on the b-tagged jet pair invariant mass $m_{b\bar{b}}$ in order to reduce the SM ZH process and provides a single normalisation factor that is used to correct the $Z + b\bar{b}/bc/c\bar{c}$ processes. CMS performs a simultaneous fit in the three categories and provides three normalisation factors, depending on the number of b-jets from the hard process: Z + 0, 1 or at least 2 b-jets at the generator level.

The scale factors and their uncertainties are applied to the $Z/\gamma^* \to \ell^+\ell^-$ simulated processes and are propagated to the background estimation to correctly account for higher-order effects. The use of finer granularity event categories may further constrain these sources of background and reduce their associated uncertainties.

In the ATLAS searches, fake factors are derived in control regions with inverted isolation requirements on the light lepton ($\tau_\ell\tau_h$ channel) or events where the two τ objects have the same-sign charge ($\tau_h\tau_h$ channel). The fake factors are then applied to a template region where reconstructed τ_h objects fail the nominal ID requirements, but still pass a very loose requirement on the τ ID BDT score (in order to maintain a selection of jets that have τ_h-like properties). The fake factors are binned in p_T and number of associated tracks.

For all channels in the CMS search, control regions are constructed by inverting the requirements on the sign of the τ_h-pair charge product, and the τ_h isolation. The three control regions are therefore defined as: same sign (SS) isolated, opposite sign (OS) anti-isolated, SS anti-isolated. The shape of the multi-jet template is estimated from the SS isolated region, while the normalisation is estimated as the ratio of the yields of OS anti-isolated and SS anti-isolated regions multiplied by the yield in the SS isolated region.

5.3.3 Limitations of the current result and perspectives
M. Gallinaro, T. Vickey

For the non-resonant $HH \to b\bar{b}\tau^+\tau^-$ production, observed limits of 12.7 and 31.4 times the rate predicted by the SM have been set by the ATLAS and CMS experiments respectively. A BDT was not used in the CMS $\tau_h\tau_h$ or boosted channels, since following the semi-leptonic resolved analysis strategy of cutting on the BDT output score and using the m_{HH} variable as the final discriminant was not feasible in these channels, due to limited statistics in the final selection. This approach of cutting on the BDT output score leads to a larger statistical uncertainty on the final result, and additionally makes it harder to constrain the nuisance parameters associated to background processes.

Another source of the difference in the results obtained by the two experiments is that the CMS selection has significantly lower efficiency for the signal in all categories due to less efficient b-tagging. This effect is amplified in the two b-jet categories. For example, in the most sensitive $\tau_h\tau_h$ two b-jet category the expected yield of non-resonant SM HH events is 0.75±0.14 events (0.55±0.10

in the last two bins of the BDT) in ATLAS, while CMS expects 0.21 events in their signal region. These limitations have a direct impact on the signal extraction strategy chosen by CMS and on the sensitivity of the final limits.

As the result of (i) the limited statistics in the final selection for CMS, (ii) the absence of a multivariate analysis for the most sensitive category and (iii) the choice of selecting events based on the BDT score instead of the extracting the signal from its distribution, the final signal sensitivity obtained by CMS is considerably weaker, by a factor 1.7, than the result obtained by ATLAS.

An independent study using CMS data [479] has shown that results comparable to those published by ATLAS can be obtained if multivariate techniques are used for all three channels and if the signal is extracted using the continuous BDT score. This confirms that by improving the analysis strategy CMS results could reach similar sensitivity to those reported by the ATLAS experiment.

Although the analyses are currently dominated by statistical uncertainties on the data, the impact of systematic uncertainties will become increasingly important as the size of the available dataset increases. The dominant source of systematic uncertainties are the multi-jet and $t\bar{t}$ background normalisation, which are 5–30% depending on the final state and category and 10–17% respectively; the knowledge of the τ_h and b-tagging efficiency, which impact the overall signal normalisation up to 10–16% and 6–8% respectively the ATLAS and CMS non-resonant searches.

Reducing these uncertainties is therefore an important way to improve the sensitivity of the $HH \to b\bar{b}\tau^+\tau^-$ searches in the future.

5.4 $HH \to b\bar{b}VV^*$: status and perspectives

J. H. Kim, S. Shrestha

The $HH \to b\bar{b}WW^*$ final state has the second largest branching fraction, providing desirable statistics and leaving much flexibility to consider all its different sub-channels, depending on the W decay mode: fully hadronic, semi-leptonic and di-lepton final states. In addition, in the fully hadronic and di-lepton state, this channel has the same final state objects as $b\bar{b}ZZ^*$, which could provide additional sensitivity. Given the large statistics, the $HH \to b\bar{b}VV^*$ channel, where V is either W or Z, is quite important, necessitating a careful study. However, it has been relatively overlooked, mostly due to the large $t\bar{t}$ background. The current outlook for the non-resonant $HH \to b\bar{b}VV^*$ channel is challenging and provides ample opportunity for improvement. In this section, we summarise the current experimental status and explore potential solutions to improve sensitivity in this channel.

Double Higgs production could also be used as a probe of a new scalar particle S, ubiquitous in many well-motivated extensions of the SM [260, 480]. The new scalar can mix with the Higgs boson acquiring couplings with the SM particles. If the S mass is larger than twice the Higgs mass, S can decay into two Higgs bosons, and it manifests as a resonance in the HH invariant mass. On the other hand, if S is lighter than twice the Higgs mass, the resonant double-Higgs production is forbidden. In this particular scenario, the mixed non-resonant HS production [337] provides an alternative window to search for an evidence of new physics. The S boson will dominantly decay into two on-shell W or Z bosons. Therefore, for both mass regimes, the $HH \to b\bar{b}VV^*$ channel is ranked high in terms of branching fractions, with a higher priority of the $HH \to b\bar{b}WW^*$ decay chain.

ATLAS has reported results of a search for Higgs boson pair production where one Higgs boson decays via $H \to b\bar{b}$, and the other decays via $H \to WW^*$ with subsequent decays of the W bosons into $\ell\nu q\bar{q}$, where ℓ is either an electron or a muon [455]. One of the W bosons is off-shell.

The small contamination from leptonic τ decays is not explicitly vetoed in the analysis. CMS has reported results in the final state with two leptons such that it is sensitive to both $b\bar{b}WW^*$ and $b\bar{b}ZZ^*$ channels, again with one of the gauge bosons being off-shell [456].

5.4.1 $HH \rightarrow b\bar{b}WW^*$ ($\ell\nu q\bar{q}$)

For the analysis of this channel data were collected using a set of single lepton triggers (triggers requiring the presence of at least one high p_T electron or muon) with increasing lepton p_T thresholds through the data taking as function of the instantaneous luminosity, in order to keep the total event rate below the requirements of the data acquisition system. Events are required to contain at least one reconstructed electron or muon matching a trigger-lepton candidate. In order to ensure that the leptons originate from the interaction point, requirements on the transverse and longitudinal impact parameters of the leptons relative to the primary vertex are imposed.

Four different event selections have been optimised for: non-resonant HH, resonant HH production for resonance masses below 600 GeV, in the 600-1500 GeV mass range, and above 1500 GeV. For the latter category the $H \rightarrow b\bar{b}$ candidates are reconstructed as large-radius jets and identified with boosted reconstruction technique described in Sec. 4.2.1. The b-jets are identified using operating points such that the b-tagging efficiency is 85% and 77% in the resolved and boosted case respectively.

The dominant background process for both boosted and resolved searches is the top-quark background, which ranges from more than 50% to 90% depending on the kinematic regime. All the background processes are estimated from simulation, except the normalisation of the $t\bar{t}$ process and the multi-jet background which are derived from data. Exploiting kinematic constraints, in particular the masses of the W and Higgs bosons, each event can be fully reconstructed despite the presence of one neutrino in the final state.

The invariant mass of the HH system (m_{HH}) after applying all selection requirements for the resolved analysis is shown in Fig. 5.14. Data are generally found to be in good agreement with the expected background predictions within the total uncertainty. The dominant systematic uncertainties for the resolved regime are $t\bar{t}$ modelling (18%), flavour tagging (30%), JES/JER (20%) and data samples in control regions (60%). In the resolved analysis, a counting experiment is performed after applying all selection requirements, which include a requirement on m_{HH} in the searches for resonant HH production. In the boosted analysis, the fully reconstructed m_{HH} shape is used to extract the signal.

The resolved and boosted analyses have non trivial overlap of events. In fact, a set of energy deposits in the calorimeter can be reconstructed both as two separate jets and one large-radius jet. The expected limit in the boosted analysis is higher than that from the resolved analysis for masses greater than 1300 GeV in the case of the scalar interpretation, and for masses greater than 800 GeV in the spin-2 hypothesis.

For the non-resonant signal hypothesis the observed (expected) upper limit on the $\sigma(pp \rightarrow HH) \times \mathcal{B}(HH \rightarrow b\bar{b}WW^*)$ at 95% CL is:

$$\sigma(pp \rightarrow HH) \times \mathcal{B}(HH \rightarrow b\bar{b}WW^*) < 2.5 \left(2.5^{+1.0}_{-0.7}\right) \text{pb},$$

which corresponds to 300 (300^{+100}_{-80}) times the cross section predicted by the SM.

These results from ATLAS are dominated by large backgrounds and associated systematic uncertainties. Additionally, further optimization of the trigger and the computation of the neutrino longitudinal momentum are needed. It will also be interesting to see how the sensitivity improves
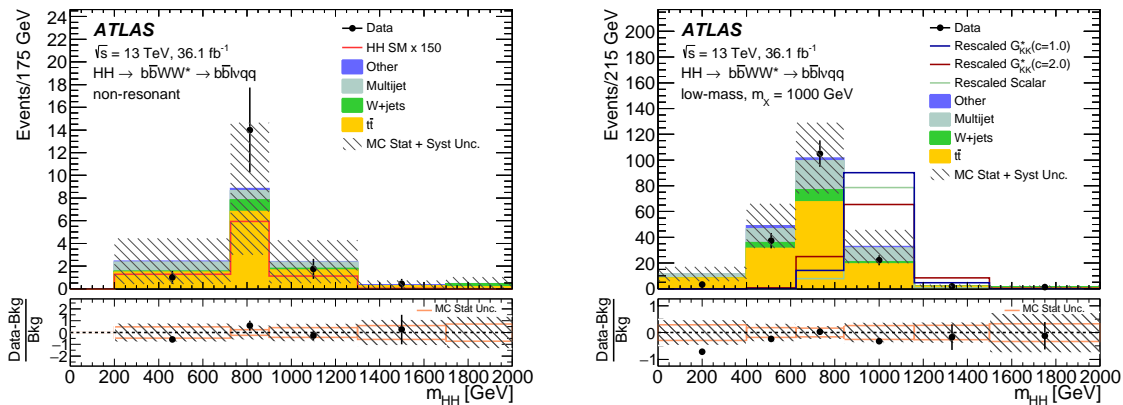
Figure 5.14: Distributions of m_{HH} for the non-resonant HH search (left) and for the search of a resonance (right) using the selections of the resolved analysis. The lower panel shows the fractional difference between data and the total expected background with the corresponding statistical and total uncertainty. The signal distributions are scaled arbitrary for presentation [455].

when adding fully-hadronic and di-lepton channels. Finally, techniques discussed in Sec. 5.4.3 and multivariate analysis also appear promising and should definitely be explored in the next iteration of this search.

5.4.2 $HH \to b\bar{b}VV^*$ ($\ell\nu\ell\nu$)

B. Di Micco, S. Shrestha

For the di-lepton analysis, data were collected in Run 2 with a set of di-lepton triggers[3] with asymmetric p_{T} thresholds. Events with two oppositely charged leptons are selected using asymmetric p_{T} requirements, chosen to be above the corresponding trigger thresholds, for leading and subleading leptons of 25 GeV and 15 GeV for *ee* and events with one electron and one muon where the muon has a higher p_{T} than the electron (μe), 20 GeV and 10 GeV for $\mu\mu$ events, and 25 GeV and 10 GeV for events with one electron and one muon where the electron has a higher p_{T} than the muon ($e\mu$). Electrons in the pseudo-rapidity range $|\eta| < 2.5$ and muons in the range $|\eta| < 2.4$ are considered.

Jets are required to be separated from a selected lepton by a distance of $\Delta R > 0.3$ and are considered to be *b*-tagged if they pass the working point of the algorithm at which the efficiency is 70%, see Sec. 4.2.

The top-quark background is the single most-dominant background, which accounts for almost 85–90% of the total background and is estimated from simulation. The Drell-Yan production in the same flavour channels amounts to 7–10% of the total and is estimated with data-driven techniques. Other backgrounds have almost negligible contribution.

Deep neural network (DNN) discriminators are used to improve the signal to background separation. As the dominant background process ($t\bar{t}$ production) is irreducible, the DNNs rely on information related to event kinematics. The variables provided as input to the DNNs exploit the presence in the signal of two Higgs bosons decaying into two *b*-jets on one side, and two leptons and two neutrinos on the other, which results in different kinematics for the di-lepton and di-jet systems between signal and background processes. Two parameterised DNNs are trained: one for the resonant search and one for the non-resonant search. In order to extract the best fit signal cross sections, a binned maximum likelihood fit is performed using templates built from the DNN output distributions in the three m_{jj} regions and in the three channels (e^+e^-, $\mu^+\mu^-$, and $e^{\pm}\mu^{\pm}$).

---

[3]Di-lepton triggers require the presence of two leptons at level 1 and at HLT.

The major uncertainty source is the top-background modelling (5–13%), followed by simulated sample size (up to 20%). The results obtained by CMS are in agreement, within uncertainties, with the SM predictions. For the SM HH hypothesis, the data exclude a product of the cross section and branching ratio of 72 fb, corresponding to 79 times the SM prediction. The expected exclusion is 81^{+42}_{-25} fb, corresponding to 89^{+47}_{-28} times the SM prediction.

ATLAS has also presented preliminary results in this channel [481] using an integrated luminosity of 139 fb^{-1}, only for the non-resonant signal model. The analysis follows a similar approach of the CMS analysis using a DNN to separate signal from $t\bar{t}$, $Z \to e^+e^-, \mu^+\mu^-$ ($Z \to ll$) and $Z \to \tau^+\tau^-$. The DNN produces four outputs: $p_{HH}, p_{t\bar{t}}, p_{Z \to ll}$ and $p_{Z \to \tau^+\tau^-}$. The four DNN outputs are combined in a single variable using the relation:

$$d_{HH} = ln\left(\frac{p_{HH}}{p_{Z \to ll} + p_{Z \to \tau^+\tau^-} + p_{t\bar{t}}}\right)$$

The observed (expected) results are upper limits at 95% CL equal to 40 (29) times the SM cross section that, when the different integrated luminosity is taken into account, are slightly better than the CMS results.

The results from CMS are dominated by large $t\bar{t}$ background and associated systematic uncertainties, that already exceed the statistical precision. It will be interesting to see how sensitivity improves when adding fully hadronic and single lepton $H \to WW^*$ final states. Finally, techniques discussed in Section 5.4.3, in addition to the already used multivariate analysis, also appear to be promising and should be explored in the next iteration of the analysis.

5.4.3   New kinematic observables for $HH \to b\bar{b}WW^*$

V. D'Amico, B. Di Micco, J.H. Kim, K. Kong, K. T. Matchev, M. Park

The sensitivity to double Higgs boson production in the $HH \to b\bar{b}WW^*$ final state, where both W bosons decay leptonically, could be improved by the use of two novel kinematic observables, *Topness* and *Higgsness* [453, 482, 483]. These functions, which could be generalised to other final states as well, capture features of the dominant $t\bar{t}$ background and the HH signal events, respectively, and result to be effective in separating these two different event topologies. For the $HH \to b\bar{b}WW^*$ ($\ell\nu\ell\nu$) final state other two observables are combined, the subsystem M_{T2} (or subsystem M_2) [484–486] for $t\bar{t}$ production and the subsystem $\sqrt{\hat{s}}_{\min}$ (or subsystem M_1) [486–488] for HH production. The M_{T2} variable is defined as:

$$M_{T2}^2 \equiv M_2^2 = \min_{\not{p}_{T1}+\not{p}_{T2}=\not{p}_T}\left[\max\{m_T^2\left(p_{Tl^-},\not{p}_1\right), m_T^2\left(p_{Tl^+},\not{p}_2\right)\}\right] \tag{5.6}$$

where $\not{p}_{T1}$ and $\not{p}_{T2}$ are the neutrino transverse momenta, $\not{p}_T$ is the the measured missing transverse momentum, $\not{p}_1$ and $\not{p}_2$ are the neutrino four-momenta. The minimisation is performed on the eight components of the two neutrino four momenta with the constraint that the sum of their transverse momenta is equal to the measured missing transverse momentum. The M_1 variable is defined as:

$$M_1 = \sqrt{M_{\text{vis}}^2 + |\vec{p}_T|^2} + |\vec{\not{p}}_T| \quad M_{\text{vis}}^2 = E_{\text{vis}}^2 - |\vec{p}_{T\,\text{vis}}|^2 - p_{z\,\text{vis}}^2 \tag{5.7}$$

where E_{vis} and $\vec{p}_{T,\text{vis}}$ are the sum of the energy and of the transverse momenta of all visible particles respectively.

The *Topness* variable quantifies the degree of consistency of the event kinematic with the dilepton $t\bar{t}$ production, with six unknowns (the three-momenta of the two neutrinos, $\vec{p}_\nu$ and $\vec{p}_{\bar{\nu}}$) and

plot under approval from
the ATLAS collaboration

Figure 5.15: The $m_{l\nu}$ invariant mass for the $HH \to b\bar{b}WW^*$ channel. The on-shell mass is defined as the mass of the heavier W boson, while the off-shell mass is the mass of the lighter W boson.

four on-shell constraints, m_t, $m_{\bar{t}}$, m_{W^+} and m_{W^-}. An estimate of the neutrino momenta can be obtained by minimising the following quantity:

$$\chi^2_{ij} \equiv \min_{\not{p}_T = \vec{p}_{\nu T} + \vec{p}_{\bar{\nu} T}} \left[\frac{\left(m^2_{b_i \ell^+ \nu} - m^2_t\right)^2}{\sigma^4_t} + \frac{\left(m^2_{\ell^+ \nu} - m^2_W\right)^2}{\sigma^4_W} + \frac{\left(m^2_{b_j \ell^- \bar{\nu}} - m^2_t\right)^2}{\sigma^4_t} + \frac{\left(m^2_{\ell^- \bar{\nu}} - m^2_W\right)^2}{\sigma^4_W} \right] \tag{5.8}$$

subjected to the missing transverse momentum constraint, $\not{p}_T = \vec{p}_{\nu T} + \vec{p}_{\bar{\nu} T}$. Since there is a two-fold ambiguity in the pairing of a b-quark and a lepton, *Topness* is defined as the smaller of the two χ^2:

$$T \equiv \min\left(\chi^2_{12}, \chi^2_{21}\right). \tag{5.9}$$

In double Higgs boson production, a selection on the invariant mass $m_{b\bar{b}}$ is used to identify $H \to b\bar{b}$ candidates and to reduce the SM backgrounds. *Higgsness* characterises the decay of the other Higgs boson, $H \to WW^* \to \ell^+\ell^-\nu\bar{\nu}$. It is defined as follows:

$$H \equiv \min\left[\frac{\left(m^2_{\ell^+\ell^-\nu\bar{\nu}} - m^2_H\right)^2}{\sigma^4_{h_\ell}} + \frac{\left(m^2_{\nu\bar{\nu}} - m^2_{\nu\bar{\nu},\text{peak}}\right)^2}{\sigma^4_\nu} + \min\left(\frac{\left(m^2_{\ell^+\nu} - m^2_W\right)^2}{\sigma^4_W} + \right. \right.$$

$$\left. \left. + \frac{\left(m^2_{\ell^-\bar{\nu}} - m^2_{W^*,\text{peak}}\right)^2}{\sigma^4_{W_*}} , \frac{\left(m^2_{\ell^-\bar{\nu}} - m^2_W\right)^2}{\sigma^4_W} + \frac{\left(m^2_{\ell^+\nu} - m^2_{W^*,\text{peak}}\right)^2}{\sigma^4_{W_*}} \right) \right], \tag{5.10}$$

where m_{W^*} is the invariant mass of the lepton-neutrino pair coming from the off-shell W. The m_{W^*} distribution has an end-point at around $m_H - m_W$, (see Fig. 5.15), and its peak is located at

$$m^{\text{peak}}_{W^*} = \frac{1}{\sqrt{3}} \sqrt{2\left(m^2_H + m^2_W\right) - \sqrt{m^4_H + 14 m^2_H m^2_W + m^4_W}} . \tag{5.11}$$

Note also that $m^{\text{peak}}_{\nu\bar{\nu}} = m^{\text{peak}}_{\ell\ell} \approx 30$ GeV is the location of the peak in the $d\sigma/dm_{\nu\bar{\nu}}$ or $d\sigma/dm_{\ell\ell}$
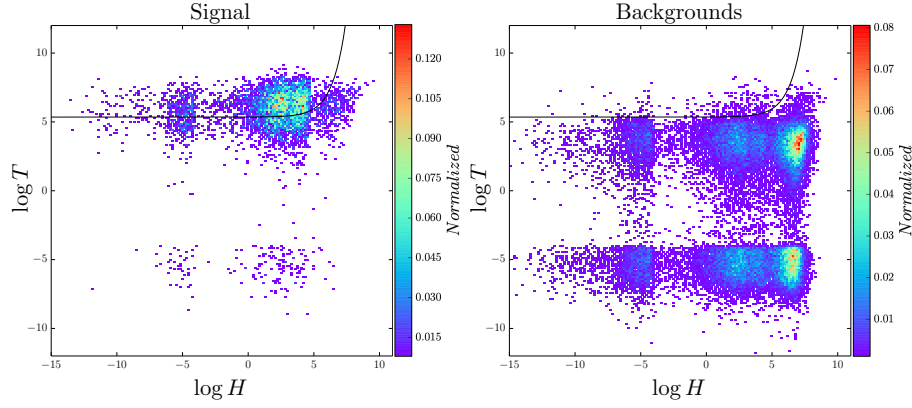
Figure 5.16: Distribution of $(\log H, \log T)$ for simulated signal (HH) and backgrounds ($t\bar{t}$, $t\bar{t}H, t\bar{t}V$, $\ell\ell bj$, $b\bar{b}\tau^+\tau^-$ and others) events after loose selection requirements as defined in Ref. [453].

distribution [453, 489]. The σ parameters in Eq. (5.8) and (5.10) stand for the experimental uncertainties and intrinsic particle widths. In principle, they can be treated as free parameters, and tuned by a neutral network or a boosted decision tree. For the studies shown in the following the values $\sigma_t = 5$ GeV, $\sigma_W = 5$ GeV, $\sigma_{W^*} = 5$ GeV, $\sigma_{h_\ell} = 2$ GeV, and $\sigma_v = 10$ GeV have been used.

The *Higgsness* and *Topness* distributions are shown in Fig. 5.16 for simulated signal and all backgrounds ($t\bar{t}$, $t\bar{t}H$, $t\bar{t}V$, $\ell\ell bj$, $b\bar{b}\tau^+\tau^-$ and others) events. Simulated signal and background events include for parton shower and hadronisation simulation, as well as semi-realistic detector effects, as described in Ref. [453, 482]

The dominant $t\bar{t}$ events are expected to be on the lower right corner with smaller *Topness* and larger *Higgsness*. The HH events are, on the other hand, expected to have smaller *Higgsness* and larger *Topness*. A selection in the $(\log H, \log T)$ is then used to separate signal and backgrounds.

Along with *Higgsness* and *Topness*, the M_{T2} variable, Eq. (5.6) could be exploited for both the $H \rightarrow b\bar{b}$ ($M_{T2}^{(b)}$) and leptonic ($M_{T2}^{(\ell)}$) [485] candidates, as well as $\hat{s}_{\min}^{(\ell\ell)}$ for $H \rightarrow WW^* \rightarrow \ell^+\ell^-\nu\bar{\nu}$ [487, 488]. In the case of $M_{T2}^{(b)}$, the two W bosons play the role of two missing neutrinos. The $M_{T2}^{(b)}$ and $M_{T2}^{(\ell)}$ distributions are shown in Fig. 5.17 (upper panels). The vertical lines at $M_{T2}^{(b)} = 190$ GeV and $M_{T2}^{(\ell)} = 6$ GeV represent optimised cuts, suppressing $t\bar{t}$ and $b\bar{b}\tau^+\tau^-$ (Drell-Yan) backgrounds, respectively.

The $\hat{s}_{\min}^{(v)}$ variable [486–488] is defined as:

$$\hat{s}_{\min}^{(v)} = m_v^2 + 2\left(\sqrt{|\vec{P}_T^v|^2 + m_v^2}|\vec{\not{p}}_T| - \vec{P}_T^v \cdot \vec{\not{p}}_T\right), \tag{5.12}$$

where the script (v) represents a set of visible particles under consideration. The m_v and $\vec{P}_T^v$ denote their invariant mass and transverse momentum, respectively.

The $\hat{s}_{\min}^{(v)}$ variable provides the minimum value of the Mandelstam invariant mass $\hat{s}$ which is consistent with the observed visible four-momentum vector. Figure 5.17 (lower-left panel) demonstrates that the $\sqrt{\hat{s}_{\min}^{(\ell\ell)}}$ distribution has an endpoint at around m_H for HH events. All other backgrounds, however, extend above this point. This justifies the use of $\sqrt{\hat{s}_{\min}^{(\ell\ell)}} < 130$ GeV as a cut to reduce the backgrounds. Figure 5.17 (lower-right panel) shows distributions of $\sqrt{\hat{s}_{\min}^{(b\bar{b}\ell\ell)}}$ and the true $\sqrt{\hat{s}}$ for HH and $t\bar{t}$ events. First, one can observe that $\sqrt{\hat{s}_{\min}^{(b\bar{b}\ell\ell)}}(HH)$ provides a good measure of the true $\sqrt{\hat{s}}(HH)$, while $\sqrt{\hat{s}_{\min}^{(b\bar{b}\ell\ell)}}(t\bar{t})$ peaks lower, near the $2m_t$ threshold. Secondly, both $\sqrt{\hat{s}}(HH)$ and $\sqrt{\hat{s}}(t\bar{t})$ peak at ~ 400 GeV. This implies that while the two top quarks are produced near threshold ($2m_t$), the two Higgs bosons are produced well above the corresponding $2m_H$ threshold. Conse-
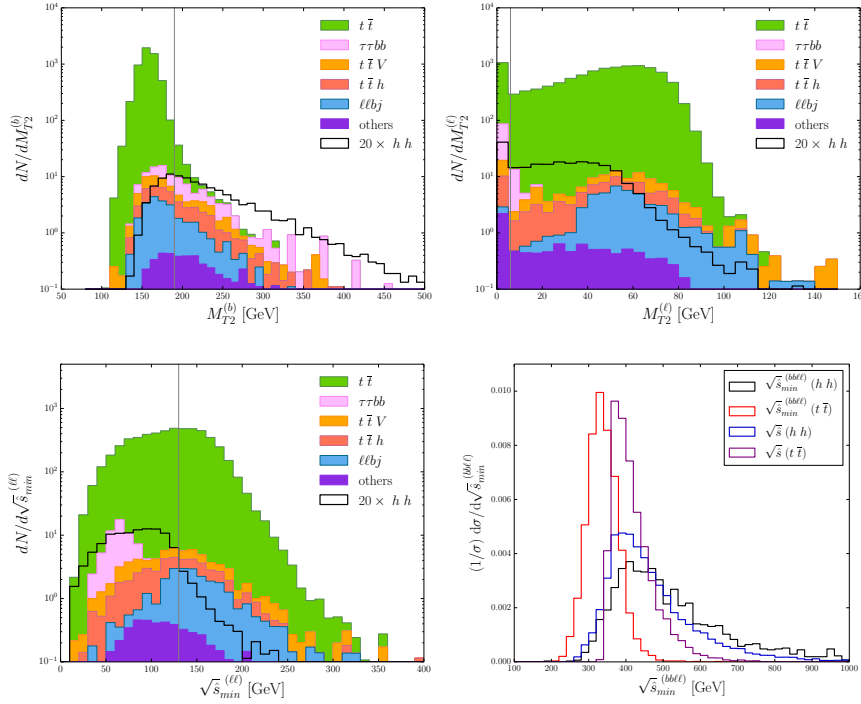
Figure 5.17: Distributions of $M_{T2}^{(b)}$, $M_{T2}^{(\ell)}$ and $\sqrt{\hat{s}}_{\min}^{(\ell\ell)}$ for the signal (HH) and all backgrounds ($t\bar{t}$, $t\bar{t}H$, $t\bar{t}V$, $\ell\ell bj$, $b\bar{b}\tau^+\tau^-$ and others) events [453, 482]. The vertical lines at $M_{T2}^{(b)} = 190$ GeV, $M_{T2}^{(\ell)} = 6$ GeV and $\sqrt{\hat{s}}_{\min}^{(\ell\ell)} = 130$ GeV show the optimised cuts. The lower-right panel shows the distributions of $\sqrt{\hat{s}}_{\min}^{(bb\ell\ell)}$ as defined in Eq. (5.12) as compared to the $\sqrt{\hat{s}} \equiv M_1$ for the HH and $t\bar{t}$ events.

quently, the two top quarks are more or less at rest, while the two Higgs bosons are expected to be relatively boosted and their decay products tend to be more collimated. This observation motivates the use of simple kinematic variables such as $\Delta R_{\ell\ell}$, $\Delta R_{b\bar{b}}$, $m_{\ell\ell}$ and $m_{b\bar{b}}$ to further separate signal and background events [453, 482].

The new observables presented in this section are quite general and can be easily applied to different topologies. For the $HH \to b\bar{b}WW^*$ ($\ell\nu jj$) final state, the *Topness* variable is defined through Eq. (5.9) where

$$\chi_{ij}^2 \equiv \min_{p_z^\nu} \left[\frac{\left(m_{b_i\ell\nu}^2 - m_t^2\right)^2}{\sigma_t^4} + \frac{\left(m_{\ell\nu}^2 - m_W^2\right)^2}{\sigma_W^4} + \frac{\left(m_{b_jjj}^2 - m_t^2\right)^2}{\sigma_t^4} + \frac{\left(m_{jj}^2 - m_W^2\right)^2}{\sigma_W^4} \right]. \tag{5.13}$$

In this expression p_z^ν is the longitudinal neutrino momentum, b_1 and b_2 are the b-jets in the final state, jj is the di-jet system, $m_{b_i\ell\nu}$ is the invariant mass of the lepton, neutrino, b-jet system and

plot under approval from
the ATLAS collaboration

plot under approval from
the ATLAS collaboration

Figure 5.18: The *Higgness* and the *Topness* variables for signal (left) and $t\bar{t}$ (right). The signal has been simulated with MG5_AMC@NLO using the FTApprox approximation and with a HERWIG++ parton-shower simulation. The $t\bar{t}$ background has been simulated with POWHEG with a PYTHIA8 parton-shower simulation.

$m_{b_j j j}$ that of the b-jet plus di-jet system. The *Higgness* is defined by the identity:

$$
H \equiv \min_{p_z^v} \left[\frac{\left(m_{\ell v jj}^2 - m_h^2\right)^2}{\sigma_h^4} + \min \left(\frac{\left(m_{\ell v}^2 - m_W^2\right)^2}{\sigma_W^4} + \frac{\left(m_{jj}^2 - m_{W_{\text{peak}}^*}^2\right)^2}{\sigma_{W^*}^4}, \right.\right. \tag{5.14}
$$

$$
\left.\left. \frac{\left(m_{jj}^2 - m_W^2\right)^2}{\sigma_W^4} + \frac{\left(m_{lv}^2 - m_{W_{\text{peak}}^*}^2\right)^2}{\sigma_{W^*}^4} \right) \right]
$$

The distribution of the *Higgness* and *Topness* variables are shown in Fig. 5.18 for simulated signal and $t\bar{t}$ events.

5.5   *HH*, other signatures: status and perspectives

C. Veelken

Searches for HH production in channels without b-jets have in general smaller signal yields, but are typically less contaminated by backgrounds than those with b-jets. As the sensitivity of searches without b-jets is mainly limited by statistical uncertainties, we expect that their sensitivity will scale better with the integrated luminosity than the b-jets final states. ATLAS has recently investigated both the $HH \to \gamma\gamma WW^*$ [226, 490] and $HH \to WW^* WW^*$ [457] final states, while CMS has studied for the first time $HH \to \tau^+\tau^-\tau^+\tau^-$ [491]. The branching fractions of these channels for SM HH bosons are $9.85 \cdot 10^{-4}$, $4.67 \cdot 10^{-2}$, and $4.00 \cdot 10^{-3}$, respectively. Phenomenological studies of the $HH \to \gamma\gamma WW^*$ and $HH \to WW^* WW^*$ channels have been published in Refs. [452] and [452, 492–495], respectively.

5.5.1 $HH \rightarrow \gamma\gamma WW^*$

Events in the $HH \rightarrow \gamma\gamma WW^*$ channel are selected in the final state $\gamma\gamma\ell\nu jj$, covering 34.3% of the total $HH \rightarrow \gamma\gamma WW^*$ signal. The search looks for both SM non-resonant and resonant HH production in the mass range between 260 and 500 GeV [226, 490]. The signal is extracted by means of a maximum-likelihood fit to the distribution in mass of the photon pair, $m_{\gamma\gamma}$. In the non-resonant analysis and in the search for resonances of mass 400 GeV and higher, the p_T of the di-photon system, $p_T^{\gamma\gamma}$, is required to exceed 100 GeV, in order to reduce backgrounds. Within a mass window centred on $m_H = 125.09$ GeV and of size equal to 2 times the experimental resolution on $m_{\gamma\gamma}$, 7 events are observed in the data, in agreement with an expected background of 6.1 ± 2.3 events. In the search for resonances of mass below 400 GeV, where no $p_T^{\gamma\gamma} > 100$ GeV cut is applied, 33 events are observed in the data, while 24 ± 5.0 events are expected from background processes. The expected signal contribution from SM non-resonant HH production amounts to $3.8\cdot10^{-2}$ ($4.6\cdot10^{-2}$) in case the requirement on $p_T^{\gamma\gamma}$ is applied (not applied). The distributions in $m_{\gamma\gamma}$, obtained when no cut on $p_T^{\gamma\gamma}$ is applied and with the $p_T^{\gamma\gamma} > 100$ GeV cut applied, are shown in Figure 5.19. The event yields, as well as the distributions in $m_{\gamma\gamma}$, observed in the data agree with the SM expectation in both cases. As no evidence for a HH signal is observed, the analysis proceeds by setting an upper limit on the HH signal cross section. The observed (expected) limit on the cross section for non-resonant HH production with SM kinematics amounts to 230 (160) times the SM prediction. In the corresponding Run 1 analysis, 4 events were observed in the signal mass window of the $m_{\gamma\gamma}$ distribution, compared to 1.65 ± 0.47 events expected from background processes and $7.2\cdot10^{-3}$ signal events expected from SM non-resonant HH production, and an observed (expected) upper limit of 1150 (680) times the SM cross section was set.
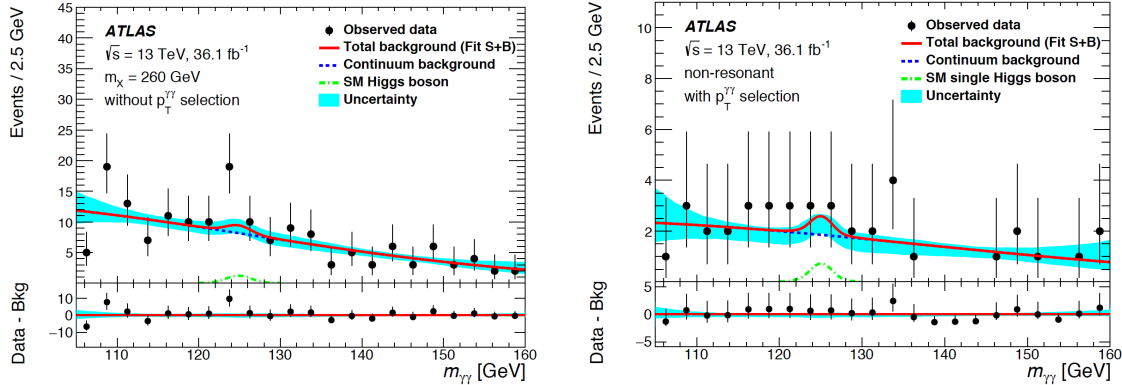
Figure 5.19: Distribution in $m_{\gamma\gamma}$ observed in the ATLAS analysis of $HH \rightarrow \gamma\gamma WW^*$, compared to the expected contribution from SM single Higgs boson plus SM non-resonant HH production (dash-dotted line) and other backgrounds (dashed line), when no cut on the p_T of the di-photon system is applied (left) and with a cut of $p_T^{\gamma\gamma} > 100$ GeV applied (right) [226].

5.5.2 $HH \rightarrow WW^*WW^*$

The ATLAS analysis of $HH \rightarrow WW^*WW^*$ [457] selects events in a combination of final states with 2, 3, and 4 leptons. In the di-lepton channel, the contamination from background processes is reduced by requiring the two leptons to be of the same charge. The combination of the 2, 3, and 4 lepton final states covers 10.7% of the total $HH \rightarrow WW^*WW^*$ signal. Similar to the $HH \rightarrow \gamma\gamma WW^*$ analysis, the analysis of the $HH \rightarrow WW^*WW^*$ final states exploits both SM non-resonant and BSM resonant production in the mass range 260 to 500 GeV. In addition, the presence of heavy scalars S of mass $135 < m_S < 165$ GeV originating from the decay of resonances X of mass $280 < m_X < 340$ GeV,

$X \rightarrow SS$ is probed. An automatic optimisation of event selection criteria ("rectangular cuts"), implemented in the package TMVA [367], is employed in order to enhance the ratio of signal over background events, before the signal gets extracted by means of a maximum likelihood fit to the event yields in nine event categories. Events selected in the di-lepton channel are analysed in three event categories, containing events with either two electrons (ee), two muons ($\mu\mu$), or one electron plus one muon ($e\mu$), respectively. In the 3 lepton channel, events containing zero and events containing one or more pairs of leptons of the same flavour and opposite charge are analysed separately. Events selected in the 4 lepton channel are analysed in four event categories, based on the multiplicity of same flavour and opposite charge lepton pairs and the mass of the 4 lepton system. The event yields observed in the data is compared to the SM expectation for the HH signal and for background processes in Figure 5.20. The data is in agreement with the SM expectation. The analysis proceeds by setting upper limits on the HH signal cross section. The combined fit of the nine event categories yields an observed (expected) limit on the cross section for non-resonant HH production with SM kinematics of 160 (230) times the SM prediction.
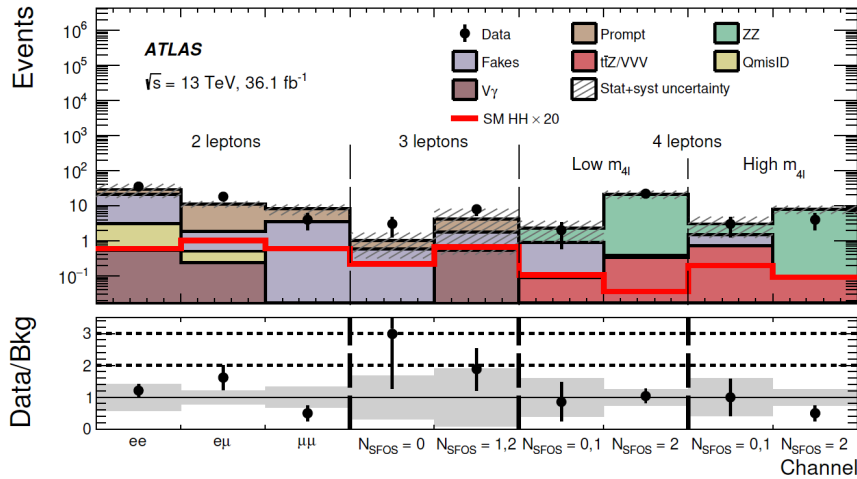
Figure 5.20: Event yields observed in the ATLAS analysis of $HH \rightarrow WW^*WW^*$ [457], compared to the expected contribution of background processes and to a non-resonant HH signal of SM kinematics and production rate amounting to 20 times the SM value. The symbol N_{SFOS} denotes the number of lepton pairs of same-flavour and opposite-charge, while the low and high $m_{4\ell}$ categories refer to events in which the mass of the 4 lepton system is below and above 180 GeV, respectively.

5.5.3 $HH \rightarrow \tau^+\tau^-\tau^+\tau^-$

The CMS search for $HH \rightarrow \tau^+\tau^-\tau^+\tau^-$ [491] is performed in the final state with 2 leptons and 2 τ_h, corresponding to 31.2% of the total $HH \rightarrow \tau^+\tau^-\tau^+\tau^-$ signal. The analysis is performed in six event categories, based on the flavour of the leptons (ee, $\mu\mu$, $e\mu$) and on their charge (same-sign, opposite-sign). Events containing pairs of leptons of the same flavour, opposite charge, and mass within the range 70 to 110 GeV are rejected, in order to remove background arising from $Z/\gamma^* \rightarrow \ell^+\ell^-$ Drell-Yan production. The multi-jet background is estimated from data, while the contribution of other backgrounds is modelled using the MC simulation. The signal extraction is based on a maximum-likelihood fit to the distribution in mass of the 2 leptons plus 2 τ_h system in case of the three event categories containing opposite-sign lepton pairs. In the event categories with same-sign lepton pairs, the small number of background events precludes the usage of a shape analysis and the event yields are instead used as input to the maximum-likelihood fit ("cut and

count" analysis). The analysis is still blinded. Based on the expected signal acceptance and efficiency and on the expected background contamination, the analysis is expected to be sensitive to resonant HH signals produced with a cross section of order 10 pb.

5.5.4 Potential improvements

A common feature of the three channels $HH \rightarrow \gamma\gamma WW^*$, WW^*WW^*, and $\tau^+\tau^-\tau^+\tau^-$ is that their sensitivity is limited by small signal yields and sizeable statistical uncertainties with the present data. Significant gains in analysis sensitivity have been achieved in the "established" channels $HH \rightarrow b\bar{b}b\bar{b}$, $b\bar{b}\gamma\gamma$, and $b\bar{b}\tau^+\tau^-$ during LHC Runs 1 and 2, thanks to improvements in the analysis methods (up to a factor 2-3 improvement in sensitivity for the same luminosity). Significant potential exists to likewise improve the sensitivity of the "new" channels $HH \rightarrow \gamma\gamma WW^*$, WW^*WW^*, and $\tau^+\tau^-\tau^+\tau^-$.

In the $HH \rightarrow \gamma\gamma WW^*$ channel, potential improvements include the use of multivariate methods to enhance the separation of the HH signal from backgrounds, the reconstruction of the mass of the HH system by means of an algorithm similar to the "High Mass Estimator" (HME) algorithm developed for the analysis of resonant HH production in $HH \rightarrow b\bar{b}WW^*$, described in Ref. [203], the replacement of the $p_T^{\gamma\gamma} > 100$ GeV cut by event categories based on $p_T^{\gamma\gamma}$, and the extension of the analysis to the $\gamma\gamma\ell\nu\ell\nu$ and $\gamma\gamma jjjj$ final states.

Potential improvements to the sensitivity of the $HH \rightarrow WW^*WW^*$ channel comprise the substitution of the "rectangular cuts" that are employed for separating the HH signal from backgrounds by more modern multivariate methods such as BDTs or NNs, and by upgrading the analysis from a "cut and count" approach to a shape analysis, based on the output of a BDT or NN. Besides improving the separation of the HH signal from the background, we expect that a shape analysis based on the output of the BDT or NN will have the further benefit of providing useful constraints to the systematic uncertainties, compared to the simple "cut and count" approach. Non-prompt and fake leptons constitute a sizeable source of background in particular in the final state with 2 leptons of the same charge, where it amounts to 30-40% of all backgrounds. We expect significant reductions of this background may be achievable thanks to anticipated improvements in the identification of leptons with multivariate methods in the future.

Potential improvements to the sensitivity of the $HH \rightarrow \tau^+\tau^-\tau^+\tau^-$ channel are expected from extending the analysis to cover further final states (4 leptons, 3 leptons plus 1 τ_h, 1 lepton plus 3 τ_h, 4 τ_h) and to determine reducible backgrounds other than multi-jet production from data instead of from the MC simulation. The latter is expected to not only reduce the systematic uncertainties, but also the statistical uncertainties on the background expectation, as samples of backgrounds with large cross sections, for example Drell-Yan production, have a higher event statistics already in the LHC Run 2 data, compared to the event statistics presently available by MC simulation. Moreover, the current CMS analysis of HH production in the final state with 2 leptons and 2 τ_h neglects the signal contribution arising from the decays $HH \rightarrow \tau^+\tau^- WW^*$ and WW^*WW^*. We expect these decays to provide a significant contribution to the overall HH signal yield.

A further improvement in the sensitivity of the $HH \rightarrow \tau^+\tau^-\tau^+\tau^-$ channel may be achieved by using an algorithm for reconstructing the mass of the HH system, presented at the workshop. The algorithm is based on a dynamical likelihood approach [471,472] and represents an extension of the SVfit algorithm [474, 475] that is used in the CMS $HH \rightarrow b\bar{b}\tau^+\tau^-$ analysis presented in section 5.3. Measurements of the energies and momenta of the visible τ decay products and of the missing transverse energy are combined in a probability model for the $HH \rightarrow \tau^+\tau^-\tau^+\tau^-$ decay with constraints on the mass of each $\tau^+\tau^-$ pair to equal $m_H = 125.09$ GeV. Details of the algorithm are given

in Ref. [496]. The algorithm achieves a resolution on m_{HH}, the mass of the HH system, of 22% (7%) in simulated $HH \to \tau^+\tau^-\tau^+\tau^-$ signal events in which the Higgs boson pair originates from the decay of a narrow resonance X of mass $m_X = 300$ (500) GeV and produces a final state with 2 leptons and $2\,\tau_h$. The quoted resolutions include the effect that the algorithm chooses an incorrect assignment of the 2 leptons and $2\,\tau_h$ to the first and second H boson in 13% (2%) of simulated signal events at $m_X = 300$ (500) GeV, which causes the Higgs mass constraint to be applied to the wrong combinations of leptons and τ_h, thereby degrading the resolution on m_{HH}. In case the algorithm could be improved to always choose the correct assignment, the resolution on m_{HH} would improve to 4% (6%) for signal events of $m_X = 300$ (500) GeV. Distributions in the ratio of reconstructed to true mass of the HH system are shown in Figure 5.21, separately for simulated $HH \to \tau^+\tau^-\tau^+\tau^-$ signal events in which the correct assignment ("correct pairing") is chosen and events in which the incorrect assignment ("spurious pairing") is chosen by the algorithm.
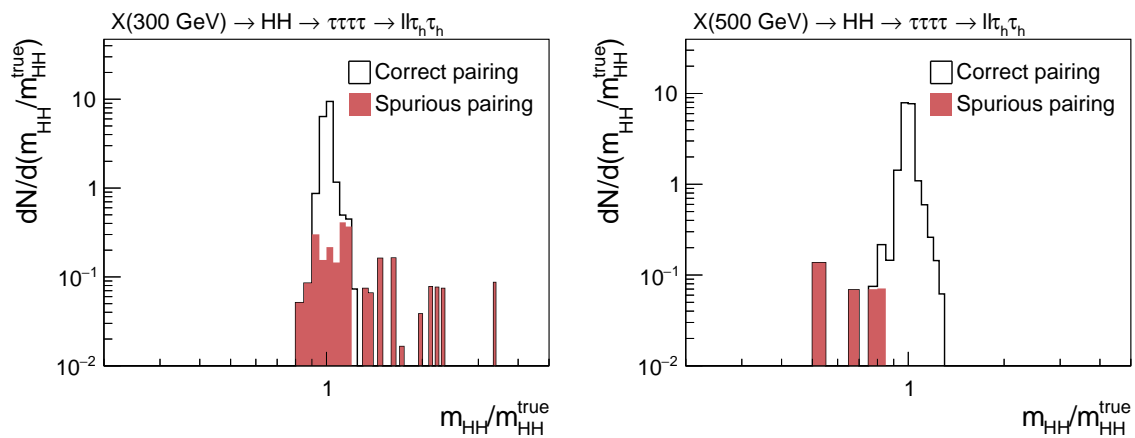
Figure 5.21: Distributions in the ratio of reconstructed to true mass of the HH system, m_{HH}/m_{HH}^{true}, in simulated $HH \to \tau^+\tau^-\tau^+\tau^-$ signal events of true HH mass 300 GeV (left) and 500 GeV (right) [496]. The x-axis ranges from 0.2 to 5.

In summary, we expect that the sensitivity of channels without b-jets will increase faster compared to the sensitivity of channels with b-jets as more LHC data becomes available in the future and more refined and sophisticated analysis techniques get utilised in the new channels. In our view, it is a worthwhile effort to study the feasibility of these new channels in preparation for the upcoming HL-LHC data-taking period.

5.6   *HH* production in the VBF mode

T. J. Burch

At the current LHC centre of mass energy of 13 TeV, the VBF HH production cross section is an order of magnitude smaller than the gluon-gluon fusion (ggF) process, which is the predominant mode studied so far in this review (see the detailed discussion in Chapter I and in particular Table 1.1). Being initiated by quarks rather than gluons, the signature of the VBF production mode differs greatly from ggF. Its distinctive topology is characterized by the presence of two separated quarks in the final state, which are reconstructed as high energetic jets in the forward region of the detector with large separation across the beam direction. Both the large invariant mass (m_{jj}) and rapidity separation of the outgoing VBF jets are particularly effective in isolating this peculiar signature.

The VBF HH production proceeds at tree level through the three Feynman diagrams shown in

Fig. 5.23. The left, middle, and right diagrams scale with c_{2V}, $c_V{}^2$ and $c_V c_3$, respectively, where c_{2V} and c_V are the coefficients of the *HHVV* and *HVV* couplings, normalized to their SM values.

A study of this process at the LHC and future colliders with $\sqrt{s} = 100$ TeV, to explore the sensitivity to higher-dimension operators, is reported in Ref. [451]. Here the emphasis was on the large m_{HH} domain, where the behaviour of the longitudinal-longitudinal component of the amplitude is characterized by the destructive interference between the first two diagrams:

$$A(V_L V_L \rightarrow HH) \sim \frac{\hat{s}}{v^2}(\delta_c) + \mathcal{O}(m_W^2/\hat{s}) \tag{5.15}$$

where:

$$\delta_c = c_{2V}^2 - c_V \tag{5.16}$$

The quantity δ_c vanishes in the SM as well as in BSM extensions where the Higgs boson belongs to an SU(2) doublet, and the growth of the amplitude with energy is suppressed. The study of the high m_{HH} behaviour is therefore a powerful probe of δ_c and of the gauge structure of the Higgs sector.

While the constraints on c_V are currently derived by searches for single Higgs boson VBF production at $1.21^{+0.22}_{-0.21}$ times the value predicted by the SM [115], the other two couplings are far less constrained. The HHVV vertex is unconstrained from current data, hence searches for VBF *HH* production provide the only direct probe to the associated parameter. Furthermore, enhancements of this coupling with respect to its SM prediction may yield to a significant increase of the VBF *HH* cross section, by as much as two orders of magnitude at twice the value predicted by the SM, as shown in Fig. 5.22 [451]. Such an enhancement would be noticeable with the full Run 2 data. Furthermore the VBF *HH* production probes the Higgs self-coupling as well, resulting in an additional constraint.

A phenomenological study that exploits the $b\bar{b}b\bar{b}$ final state is reported in Ref. [451], applying boosted jet tagging techniques – justified by the high p_{T} of the Higgs bosons in the relevant kinematic region – to minimise the dominant background processes. An example of the impact of $\delta_c \neq 0$ is shown in Fig. 10.13 of Sec. 10.8, for VBF *HH* production at future colliders. In that figure the di-Higgs mass spectrum, the rapidity separation and invariant mass of the VBF jets, in the SM and in a $c_V = 1$, $c_{2V} = 0.8$ scenario are compared to the expected backgrounds (in the parton-level simulation). These observables have long been used in searches for single Higgs boson through VBF production at the LHC. After the detector simulation of fully showered events, Ref. [451] carried out a detailed study of the shape of the mass distribution, reporting that at the LHC with an integrated luminosity of $300\mathrm{fb}^{-1}$ the c_{2V} coupling can be measured with about 40% precision at the 68% CL. This results in a strong motivation to extend the current searches to the *HH* VBF production mode during Run 2 and 3, although this analysis of the $b\bar{b}b\bar{b}$ final state shows clearly that the VBF channel is less sensitive than ggF to the Higgs boson self-coupling[4].

In the CMS $HH \rightarrow b\bar{b}\gamma\gamma$ search [438], a VBF signal model has been considered for the first time experimentally. However, signal events in this analysis were chosen via a BDT trained on ggF *HH* events, thereby limiting the potential for sensitivity improvement. The efficiency times acceptance for SM-like VBF *HH* events using this model is 13%, with 10% in the high mass region (greater than 350 GeV) and 3% in the low mass region (below 350 GeV). Ultimately, considering this VBF *HH* signal in the analysis designed to target ggF $HH \rightarrow b\bar{b}\gamma\gamma$ improves the sensitivity by 1.3% (while the VBF *HH* cross section represents 5% of the total one). Figure 5.25 illustrates the small impact of including a VBF signal on the overall sensitivity of the search for ggF $HH \rightarrow b\bar{b}\gamma\gamma$ in CMS. A

---

[4]The sensitivity to κ_λ arises from the threshold region $m_{HH} \sim 2m_H$ where multi-jet background buries the signal even for large modifications of the Higgs couplings with respect to their SM values.
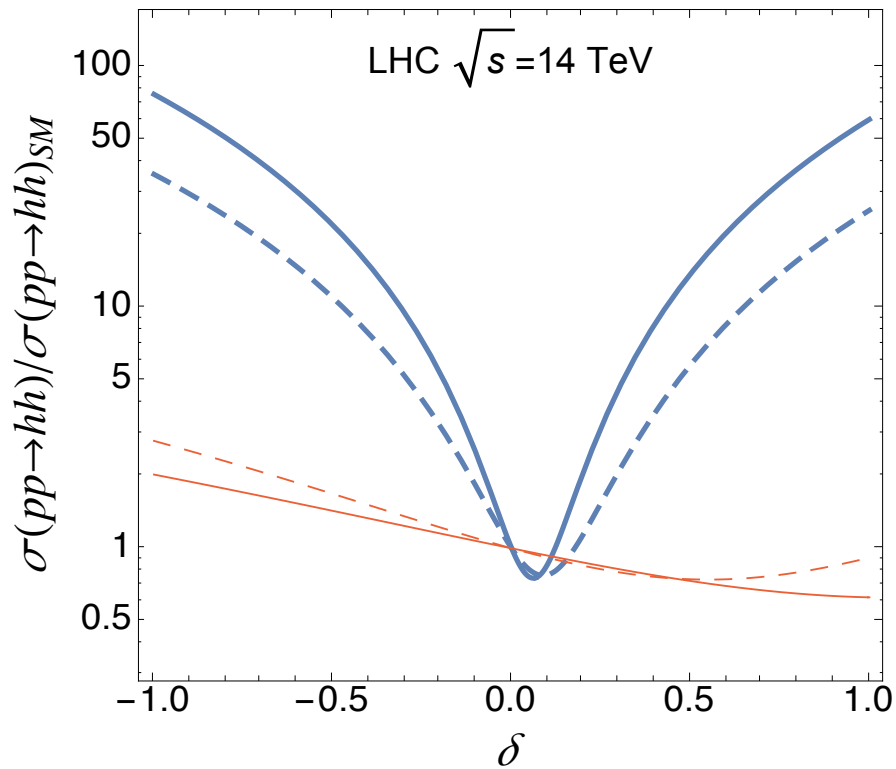
Figure 5.22: VBF HH production cross section as a function of the coupling deviation from the SM value for the $HHVV$ (HHH) vertex in blue (red). The solid line is after acceptance cuts, the dashed line is after analysis cuts applied on the rapidity difference and m_{jj} [451].
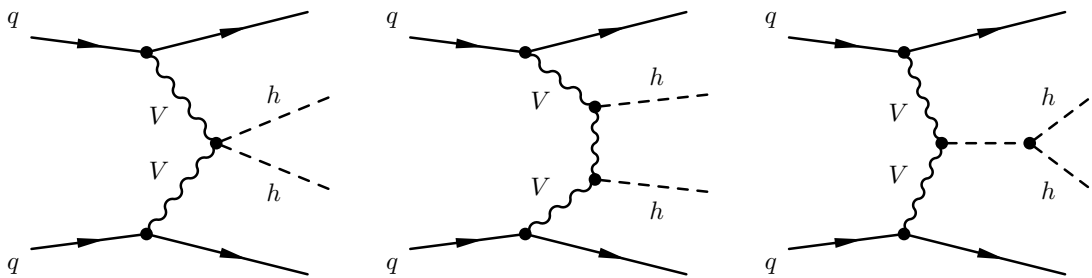

Figure 5.23: Leading order Feynman diagrams for Higgs pair production via vector boson fusion. The HHVV vertex (left), corresponding to the c_{2V} coupling, is not probed by single Higgs boson processes. The HVV vertex (center) corresponds to the c_V coupling, is constrained by single Higgs boson measurements. The HHH vertex (right) involves the Higgs boson self-coupling.
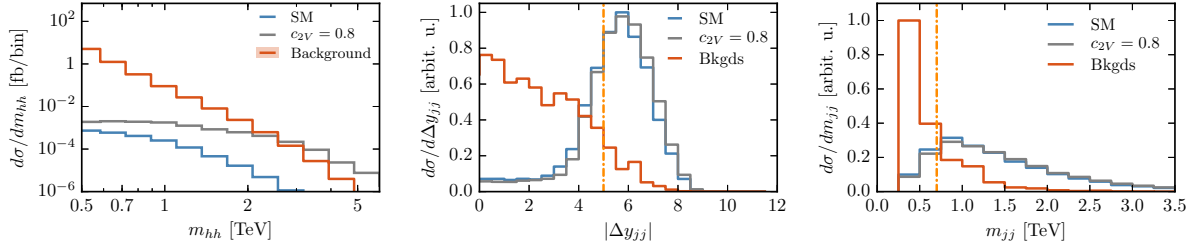
Figure 5.24: Distribution of the m_{HH}, the difference in rapidity $|\Delta y_{jj}|$ (left) and invariant mass m_{jj} (right) of the VBF jets associated to a HH pair in a phenomenological study [451] at 14 TeV. Distributions are also shown for a c_{2V} value at 0.8 times the SM prediction. The background includes multi-jet events, $t\bar{t}$ and Higgs boson production via ggF where additional radiation can mimic VBF jets.
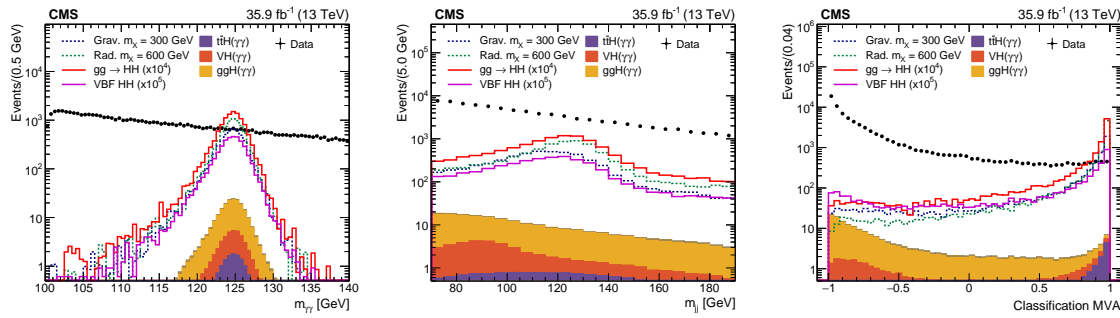
Figure 5.25: Higgs candidate $m_{\gamma\gamma}$ (left) and m_{jj} (middle) distributions, as well as the BDT classifier score (right) in the CMS $HH \to b\bar{b}\gamma\gamma$ analysis after kinematic selection criteria are applied. The contribution of the VBF HH process is shown in pink, normalized to 10^5 times its cross section [438].

dedicated category with event selections designed to specifically target VBF production will lead to a much better improvement of the sensitivity when combined with an analysis targeting ggF HH production, due to the aforementioned signal purity obtainable in such a category. In addition to taking advantage of VBF specific m_{jj} and $\Delta\eta$ distributions, different m_{HH} regimes can be used in order to isolate VBF production from the dominant ggF production mode: at large values of m_{HH}, VBF production is enhanced relative to the ggF production of HH pairs [447]. Given the difficulty of measuring SM HH production due to its small cross section, any such gain is invaluable in improving an analysis. Furthermore, should HH production be observed due to a BSM enhancement, such a model would be vital in understanding the source and nature of that said enhancement.

The very first experimental search targeting VBF HH production has been presented by ATLAS in the $b\bar{b}b\bar{b}$ final state [405], using the data collected during 2016–2018 and corresponding to an integrated luminosity of 126fb^{-1}. The analysis strategy follows very closely the analogous search in the same final state for the ggF initiated process and described in Sec. 5.1. The main differences are the use of a multivariate jet energy regression, described in Sec. 4.3, to correct the energy of b-jets which improves by about 10% the jet energy resolution; and of course of VBF specific selection requirements. The event selection requires at least four central ($|\eta| < 2$) b-tagged jets with $p_T > 40$ GeV and at least two forward ($|\eta| > 2$) jets with $p_T > 30$ GeV to ensure compatibility with the VBF HH production mode. The two forward jets with highest p_T have to satisfy requirements on both their angular separation, $|\Delta\eta| > 5$, and their invariant mass, $m_{jj} > 1$ TeV. In addition to the VBF HH production, also the VHH process, resulting in the $HHjj$ topology has been taken into account, although it is found to have a negligible contribution after the VBF specific event selection

requirements.

This search sets 95% CL upper limit on the non-resonant VBF HH production cross section of 1600 fb, where the expected value is 1000 fb. The results are also interpreted as a function of c_{2V}, while c_V and κ_λ are set to their SM values. The observed (expected) excluded range is $c_{2V} <$ -1.00 and $c_{2V} > 2.67$ ($c_{2V} <$-1.07 and $c_{2V} > 2.78$), which is not sensitive yet to the SM prediction ($c_{2V} = 1$). This search tests large deviations of c_{2V} from their SM predictions, which result in a harder m_{HH} spectrum and higher momentum for the b-jets from the Higgs boson decay.

Similarly to the searches for resonant ggF Higgs boson pair production, VBF HH production involving an intermediate resonance may be considered. This kind of search would be complementary to the ggF searches, as in this case the vector bosons are the ones coupling to the new resonance, which then decays to a pair of Higgs bosons. However, this production mode is not particularly well studied (see Ref. [240] for an analysis in the context of a model with warped extra dimensions), since its very small cross section poses a question on the ability of the LHC to impose significant constraints through this type of search. Nevertheless, the VBF HH search reported in Ref. [405] has been interpreted also in the context of resonant production and results are reported in the resonance mass range of 260–1000 GeV, where two classes of signals have been tested to perform a rather inclusive search under both the narrow and broad hypotheses for the resonance width.

Chapter 6

Results presentation

Editors: M. S. Neubauer, M. Swiatlowski

Experimental collaborations typically publish the results of their BSM searches in the context of particular models. The CLs method [497] is used to derive exclusion limits on some model parameter space, by comparing the compatibility of the data to background-only and signal plus background hypotheses. Then, a test statistics from the likelihood ratio is used to discriminate between the two hypotheses. Reasonably well motivated, but somehow arbitrary benchmark models are often used for the signal hypothesis. Examples include generic resonances decaying to HH of spin-0 [260,480] or spin-2 with particular choices of the natural width [235], as well as the SM HH process with the production cross section re-scaled by an arbitrary factor. The observed (and expected) upper cross section limits in the context of these models are often the final result of the publication, and the specific values obtained are often published as HEPData [498].

Often the theoretical community devises new models to which existing searches might be sensitive. Given the lengths of time between experimental publications (and the difficulty from experimental collaborations to interpret their data in all available models) theorists might want to assess the sensitivity of existing published results to their model. If the hypothesised signal is sufficiently similar to those already presented in benchmark models used by the experiments (in width, resulting kinematic, etc.), the results on the benchmarks can be directly applied. On the other hand, if the properties of the signal differ significantly, the current presentation of results for HH searches via specific benchmarks leave few options for re-interpretation.

There are several methods to explore to fully exploit the scientific potential of the experimental results. This section describes some possibilities discussed by the community and their relative strength. LHC experiments are encouraged to provide more information in their publications to allow possible re-interpretations of their results within the particle physics community. The impact of the available experimental results would consequently increase by allowing a more rapid testing of exciting new theoretical predictions.

6.1 Examples from other BSM searches

The difficulty of the re-interpretation of the Higgs pair production searches lies in their sophisticated profile likelihood fits. As these analyses fit a full distribution (m_{HH} or an MVA score, typically), it is difficult to provide an upper limit on the cross section without an assumption on the shape of the signal distributions.

A possible alternative is to use a simpler approach, such as event counting after the application of analysis cut, "cut and count", that is less dependent from the signal shape, since this information is not directly used in the likelihood fit. Instead, a simple implementation of the analysis selections, along with parameterised efficiency provided by the experimental collaborations, is sufficient to calculate a predicted signal yield, which can be compared to the model-independent cross section upper limits. The physics groups of both ATLAS and CMS experiments searching for SUSY and exotics new particles, provide information that is interpretable in this manner for many of their searches [499, 500]. A number of frameworks to facilitate combination of such results and to allow for the fast testing of models against different experimental results are available, such as CHECK-MATE [364] and GAMBIT [501]. In particular, GAMBIT provides a framework for quickly simulating a provided signal model, testing its yields in a variety of encoded signal regions from a variety of analyses, and for testing the compatibility of a signal to the data by calculating the combined likelihood over these analyses (assuming complete orthogonality between different analyses) by summing over the various individual log likelihoods. For example, GAMBIT has recently re-interpreted and combined several ATLAS and CMS SUSY searches to set new constraints on chargino and neutralino production at the LHC, showing a small excess that individual analyses published by the experimental collaborations were not sensitive to [502]. This result enables the experimental groups to focus on a potential hint of new physics revealed by the existing data.

While some searches are amenable to simple, re-interpretable "cut and count" approaches, some sensitivity would be lost by the HH searches if this approach were to be taken. This is because the shape of the signal distributions provides important information for the discrimination against background. Adopting this approach for the presentation of di-Higgs results is therefore disfavoured.

Another commonly used method for generic result presentation is utilised by several ATLAS and CMS searches for di-jet resonances [503], where the signal is extracted by fitting the di-jet mass distribution, similarly to HH searches. Results are provided in the context of specific models and, additionally, experimental efficiencies and upper cross section limits on generic gaussian-shaped signals of various widths are also provided in HEPData. These allow to map the experimental results to various classes of models, as most resonant signals will look similar to a Gaussian with some width which depends on the details of the model. An example from ATLAS's 13 TeV di-jet resonance search is shown in Fig.6.1 [504]. This was used to re-interpret the results in the context of stop production in R-parity violating models [505], allowing for the strongest observed limits on stop particles at the LHC, as shown by the red lines in Fig. 6.2. This approach is particularly promising for the presentation of HH results, as many interesting BSM models predict resonant signals whose shapes are approximately Gaussian. However, for non-resonant signals, where the shapes are not as easy to parameterise this method would not work. Moreover, MVA techniques would limit the use of such simple signal parameterisation.

The CMS Collaboration, in the context of SUSY searches, has adopted a new way of share the results with the HEP community by publishing "simplified" likelihoods [506][1]. The covariance matrices for the various elements of the uncertainties on the background model are published along with the recipes for reconstructing the likelihood. An example is shown in Fig. 6.3, and an example of the results one can obtain using the simplified likelihood compared to the full likelihood for a dark matter search are shown in Fig. 6.4. The likelihood can therefore cover arbitrarily complicated functions and numbers of signal regions. This method is promising for the presentation of di-Higgs results, as a full description of the m_{HH} distribution and the relationship of the uncertainties among

---

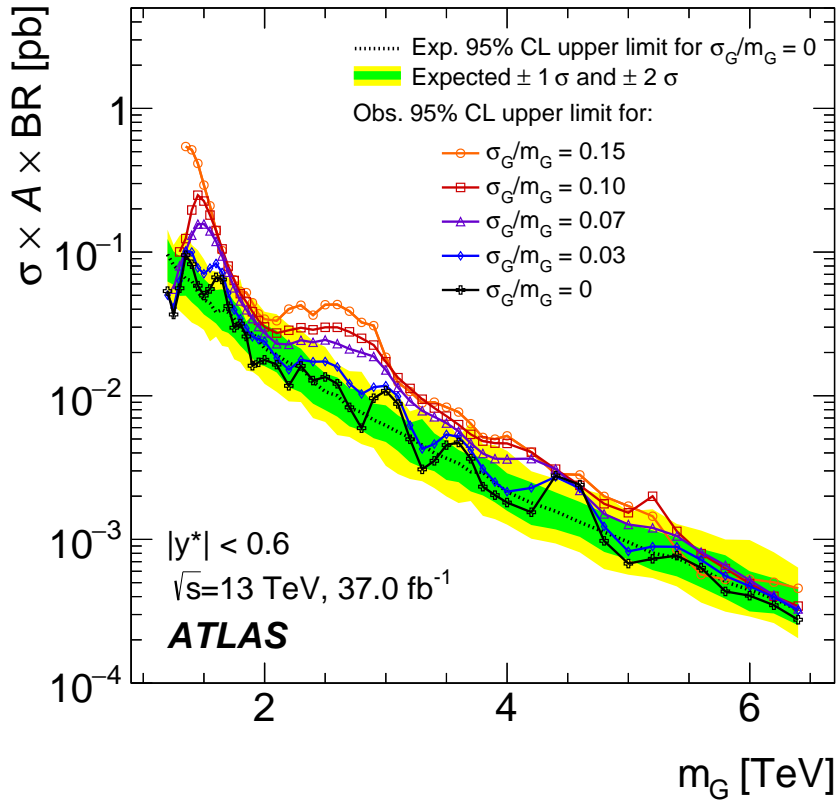[1]See also [507] for important considerations regarding systematic uncertainties.

Figure 6.1: Upper cross section limits on generic gaussian-shaped resonances decaying to di-jets as a function of the mean mass, for various widths hypotheses [504].
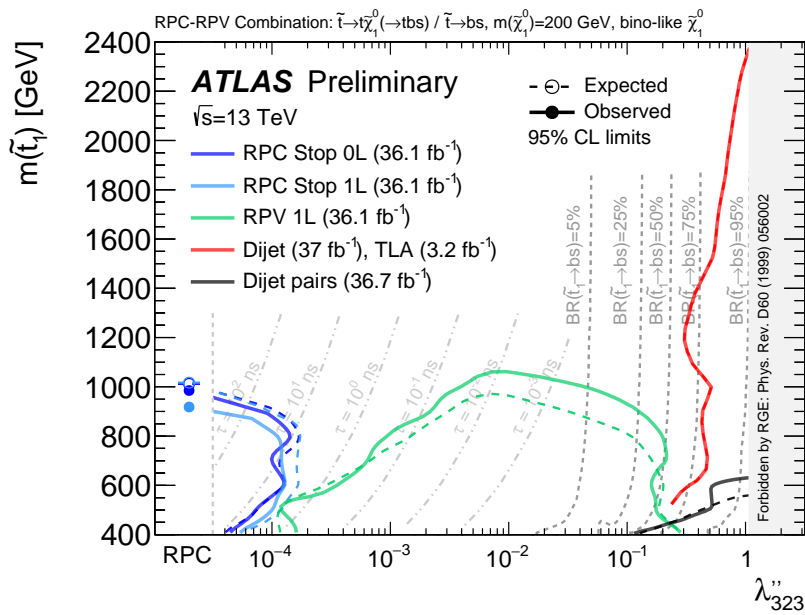

Figure 6.2: ATLAS SUSY results, re-interpreted in the context of long-lived and prompt *R*-parity violating models [505]. The excluded stop mass is shown as a function of the λ''_{323} RPV coupling parameter. The red line is the limit from the di-jet resonance research, re-interpreted using the Gaussian limit strategy.

Figure 6.3: The covariance of backgrounds in various search regions, which can be used to calculate a simplified likelihood function [506].

bins can be succinctly encapsulated in the covariance matrix.

6.2   Options for the future

One possibility to improve the re-interpretability of the published results is to simply make available the statistical objects and the code used to develop the profile likelihood for each specific search. These fits are usually interpreted in the ROOFIT framework [508]. The full information on the signal and background shapes and a complete list of systematic uncertainties affecting both is contained in the so called "workspace" within ROOT files. Although the binary format of these containers utilised by ROOFIT makes the replacement of the signal model with an arbitrary shape difficult.

PYHF [509] is a ROOT-free implementation of the underlying HISTFACTORY [510] probability distribution functions that addresses this issue by describing the workspace in human-readable JSON [511] format.

Another similar and promising avenue is RECAST [512], currently used by the ATLAS Collaboration. It provides a container-based archiving system for the full implementation (selection and statistical analysis) of a search. For an analysis preserved in the RECAST framework, a set of LHE files describing a specific BSM signal can be provided and the full simulation and statistical interpretation can be run automatically, producing a final CLs value for a particular BSM signal. This is very useful for collaborations to quickly re-spin analyses using their full simulation and analyses methods. Figure 6.5 shows an example from the ATLAS SUSY re-interpretation effort in RPV scenarios [505], where the blue lines were obtained entirely using the RECAST framework implementation of an existing Run 2 search for gluinos in final states with many b-jets [513].

The use of RECAST is currently limited internally to the collaborations. Any additional interpretation of the published results would need to go through the normal approval and publication process within the ATLAS collaboration. Some effort is being invested to streamline these processes for simple interpretations, but this remains a difficult prospect. So while RECAST would provide the most accurate re-interpretations possible (by using the full, official detector simulations and no
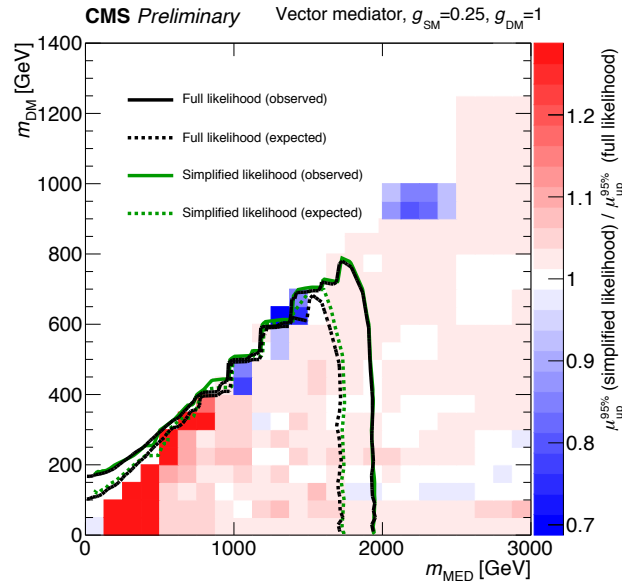
Figure 6.4: The expected and observed limits, for an example dark matter model, where the fit uses either the full, experimental likelihood or the simplified likelihood [506].
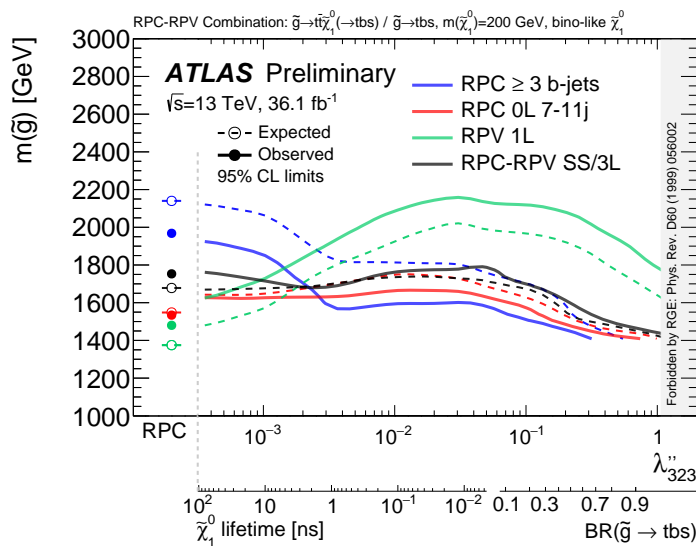

Figure 6.5: ATLAS SUSY results, re-interpreted in the context of long-lived and prompt R-parity violating models [505]. The excluded gluino mass is shown as a function of the λ''_{323} RPV coupling parameter. The blue lines, corresponding to a 36.1fb^{-1} search for gluinos in final states with many b-jets [513], were obtained entirely using the RECAST framework.

compromises in the statistical analysis), the suitability as a tool for commonplace re-interpretation is limited, at least in its current form.

6.3 Machine-learning vs interpretability

A potential challenge, especially as analyses techniques become more sophisticated, is how to re-interpret results obtained with multi-variate analyses (MVAs) such as Boosted Decision Trees (BDTs), or Neural Networks (NNs). While truth-level distributions produced without full detector simulation (or, smeared distributions produced via a partial simulation such as DELPHES [514]) may be sufficient to re-produce the characteristics of simple analyses, the more complicated MVA approach may encode aspects of the detector that are more difficult to reproduce.

While this is a valid concern, the level of agreement between the truth-level and fully simulated samples can be assessed directly by the experimental collaborations. In some cases, such as the ATLAS SUSY stop 1-lepton search [515], this has already been done, and the agreement between the fully-simulated and truth-level inputs, run through the same Boosted Decision Tree, agree to within 10%. As the accuracy of most re-interpretation approaches is similar, this shows that at least in some cases, using a BDT does not necessarily preclude re-interpretation. This same analysis in fact published the XML configuration files used by the TMVA [367] implementation of the BDT, allowing for others to easily re-run exactly the same selection. Similar possibilities exist for NNs from a KERAS model [516], for example, where the model can be saved in JSON or YAML [517] formats. Publishing the full configuration of the MVA is an approach that other analyses could follow to ensure the results can continue to live beyond the initial publication.

6.4 Considerations for non-resonant signatures and EFT

Re-interpretation is important for both resonant and non-resonant HH signatures. The discussion so far has focused on resonant signatures, but most applies transparently to the non-resonant signatures as well. As long as results are described as cross section upper limits on known models, or likelihoods are published where arbitrary signals can be included directly, limits on new signal types can be calculated or extracted. Of course, depending on the particular model to be tested the assumptions of the analysis may not be optimal, but the sensitivity of a given analysis to a particular non-resonant signal can always be derived.

There are several other approaches to consider as well, especially in the context of EFT, discussed in Chapter 2), which can generate a large variety of potential signal dynamics. As described in Sec. 2.4, CMS and the authors of [178] have proposed the use of shape benchmarks to form a basis of possible signals for an HEFT analysis. CMS interprets the results of the non resonant HH searches for each of these shape benchmark hypotheses, and theorists can study their own particular model and identify the shape benchmark which best describes the signal, allowing a quick and simple extraction of the upper limit on the cross section. This approach has the advantage of making the cross section limit setting trivial in the case the signal under test is sufficiently similar to a benchmark. On the contrary, it cannot be used for a particularly unique signal which is not included by any of the benchmarks.

Experiments provide upper limits to the HH cross section production for different benchmarks. Anyone who has interest to explore a particular portion of the EFT phase space can use those benchmarks to obtain an estimate of how strongly this portion is constrained by HH data. A map of the EFT phase space to the specific shape benchmarks can be derived with a dedicated tool available at
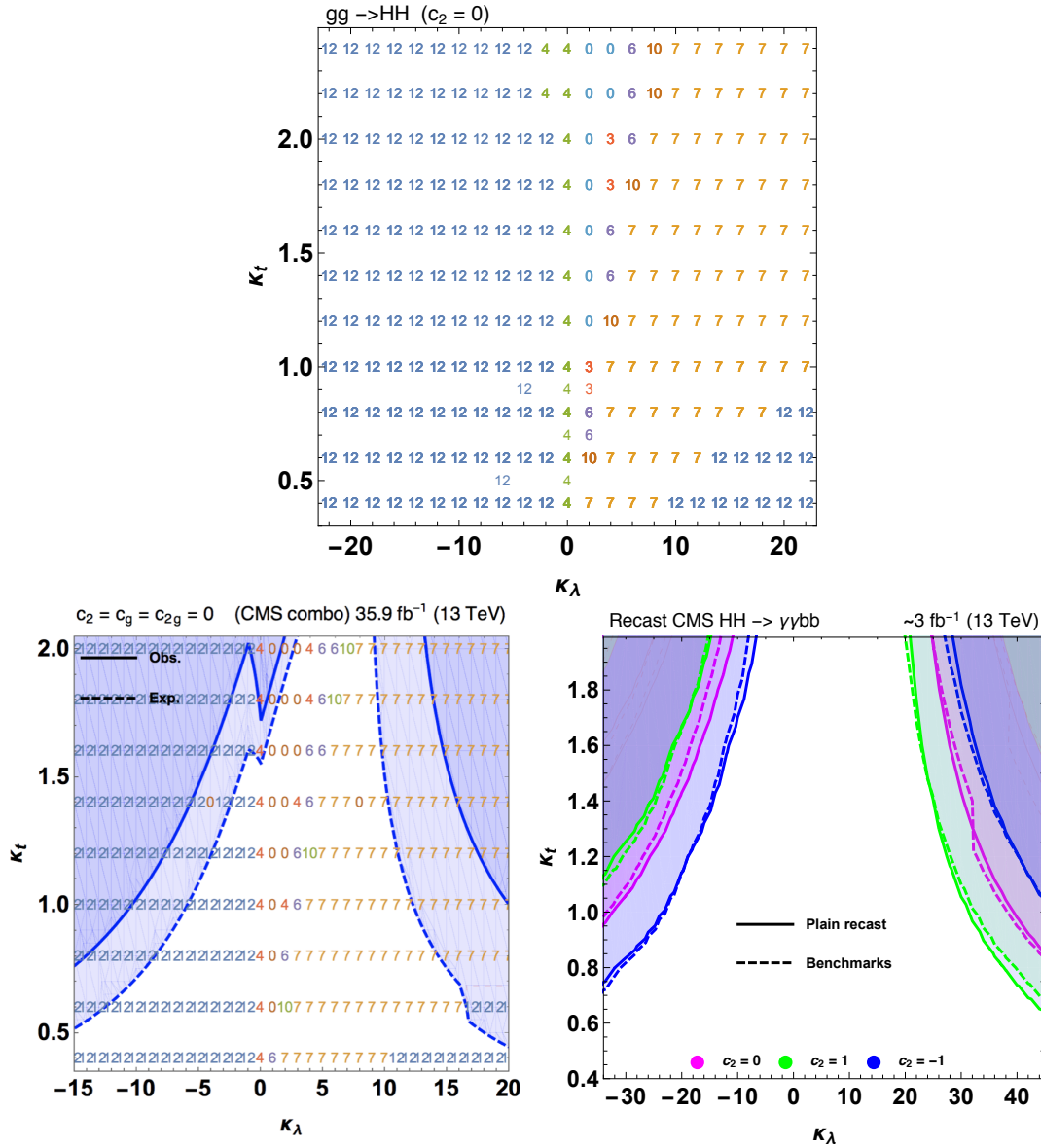
Figure 6.6: Mapping of benchmarks into $\kappa_\lambda \times \kappa_t$ phase space (top) obtained using recast tool http://rosetta.hepforge.org/ [171]; benchmark mapping and excluded region of the EFT parameter phase space obtained using CMS combined limits on the benchmarks [67] (bottom-left); upper limits obtained using benchmark mapping compared to the upper limit obtained using directly EFT shapes (bottom-right) [171];

http://rosetta.hepforge.org/ [171]. This map can be then used to estimate the upper limits on each combination of EFT parameters

An example of this procedure is shown in Fig. 6.6, where the map between κ_t, κ_λ and the shape benchmarks is provided on the top. The exclusion limits derived by the CMS collaboration will be discussed in Sec. 7.2 and in Fig. 7.5 the upper limit for each benchmark by combining different final states is shown. Benchmark limits are then reported on the EFT map and compared to theory predictions in bottom-left of Fig. 6.6. This allows to estimate the excluded regions on EFT parameters. The comparison for a particular case between the exclusion limits derived with an EFT analysis and with the shape benchmarks is provided in bottom-right. It was obtained by a simple counting experiment based on 8 TeV CMS data, using a recast of public results [171]. The observed difference

was rather small.

If an excess is present in the data related to a non-resonant production it is possible to spot it in one of the benchmarks. For example just looking at the upper limits on the SM-like production may hide an excess at very low or very high m_{HH} values incompatible with the SM. A detailed analysis could be then be performed on different EFT points that belong to a given cluster using their real m_{HH} shapes [109].

The Simplified Template Cross Section Method (STXS) described in Sec. 7.6 takes a similar approach for single Higgs measurements by defining simple fiducial regions for cross section measurements of Higgs properties and kinematics. As single Higgs boson production has been convincingly observed in many channels and phase space regions, these are cross section measurements and not just upper limits. Many of these regions, for example those for $t\bar{t}H$ production with high p_{T} Higgs bosons, are potentially sensitive to deviations from the SM values of the self-coupling parameter. Generically, EFTs can cause simultaneous changes in several of these fiducial regions, but because the results are presented as easily interpretable measured cross sections, it is possible to determine the compatibility of a particular EFT model with the data. This can play an important role for understanding which EFT model should be explored by the experimental collaborations, as obviously excluded phase space points can be ruled out before expensive simulation is performed.

6.5   Conclusions and recommendations

We have reviewed several ways of enabling di-Higgs searches published by the experimental collaborations to be re-interpreted after their publication within the HEP community. With the timescale between publications potentially increasing as the LHC datasets grow, the ability to re-interpret existing searches will be critical to allow the LHC data to be used to their full potential in a timely manner in the coming years. Several different options are possible, but experimental collaborations are encouraged to consider the following:

(i) if possible, provide the full likelihood developed by the analyses, preferably in an easy to modify format such as the PYHF JSON;

(ii) if the first item is not possible, consider providing covariance matrices which allow for the reproduction of the likelihoods used by the searches to some degree of accuracy. This requires potentially more work from the analysis teams, with smaller accuracy for re-interpretations, so it is less preferred than the first option;

(iii) where possible, provide the full configuration of the machine learning algorithms used by analyses. Ideally these would be accompanied by a detailed comparison between fully simulated samples and truth-level samples, so that re-interpretations can assess the applicability of using the MVA without the full detector simulation.

By following these practices, the impact of the searches for BSM signals published by the LHC experiments will increase beyond their initial publications, and the results will be fully exploited within the HEP community for years to come.

Chapter 7

LHC results

Editors: B. Di Micco, J. Schaarschmidt

7.1 *HH* results and combination: status and perspectives

The ATLAS and CMS collaborations have searched for Higgs boson pair production at 8 and 13 TeV, as reviewed in detail in Chapter 5. These searches have tested both resonant and non-resonant *HH* production for new physics contributions. In particular for the non-resonant case, results have been provided either by assuming the SM prediction for the *HH* kinematic and that only the total cross section is affected by BSM contributions, or by assuming BSM effects would impact only the Higgs boson self-coupling while all the other couplings are unaffected and equal to their SM values.

Although observing non-resonant *HH* production at the level predicted by the SM is likely not possible until the end of the HL-LHC data taking, it nevertheless remains extremely important to probe this process with current dataset to constrain BSM models allowing for large increase of the *HH* production cross section.

The *HH* decay final states that have been studied are described in detail in the previous chapters. Here all results and their combination are summarised and discussed.

The combination is performed by building a single likelihood function using all signal and background normalisation regions, correlating properly theoretical and experimental systematic uncertainties and ensure consistency in the definition of the parameters of interest, for resonant searches, sometime different mass values are probed by different channels, therefore an interpolation procedure needs to be applied in order to properly test each mass point.

7.2 Non-resonant production mode

ATLAS has searched for the non resonant production in the $HH \to b\bar{b}\gamma\gamma$, $HH \to b\bar{b}b\bar{b}$, $HH \to b\bar{b}\tau^+\tau^-$, $HH \to b\bar{b}WW^*$, $HH \to WW^*\gamma\gamma$ and $HH \to WW^*WW^*$ final states. For the $HH \to b\bar{b}WW^*$ final state, only the single lepton channel has been included in the combination. CMS has instead combined searches in the $HH \to b\bar{b}\gamma\gamma$, $HH \to b\bar{b}b\bar{b}$, $HH \to b\bar{b}\tau^+\tau^-$ and $HH \to b\bar{b}VV^*$ channels, using only the di-lepton channel for $HH \to b\bar{b}VV^*$. The 95% CL expected and observed upper limits on the signal strength $\mu = \sigma_{HH}/\sigma_{HH}^{SM}$ are reported in Table 7.1 for each individual final state. Their combination has allowed the two experiments to set an observed (expected) upper limit on *HH* production at 6.9 (10), 22.2 (13) times the SM, for ATLAS and CMS respectively, using data

collected in 2015 and 2016 at 13 TeV [66, 67] .

Search channel	Collaboration	95% CL Upper Limit	
		observed	expected
$b\bar{b}b\bar{b}$	ATLAS	13	21
	CMS	75	37
$b\bar{b}\gamma\gamma$	ATLAS	20	26
	CMS	24	19
$b\bar{b}\tau^+\tau^-$	ATLAS	12	15
	CMS	32	25
$b\bar{b}VV^*\,(\ell\nu\ell\nu)^*$	ATLAS	40	29
	CMS	79	89
$b\bar{b}WW^*\,(\ell\nu qq)$	ATLAS	305	305
	CMS	–	–
$WW^*\gamma\gamma$	ATLAS	230	160
	CMS	–	–
WW^*WW^*	ATLAS	160	120
	CMS	–	–
Combined	ATLAS	6.9	10
	CMS	22	13

Table 7.1: List of HH searches at the LHC based on the $p-p$ data collected by ATLAS and CMS at 13 TeV and corresponding to about 36 fb^{-1}. Observed and expected upper limits on the SM HH production cross section are normalised to the SM prediction [19]. The ATLAS search for $b\bar{b}VV^*$ ($\ell\nu\ell\nu$) is not included in the combination and uses 139fb^{-1} of integrated luminosity.

The best final state for the non-resonant HH production is $b\bar{b}\tau^+\tau^-$ in ATLAS, and $b\bar{b}\gamma\gamma$ in CMS. The expected upper limit on non-resonant SM HH production cross section for ATLAS decreases by 71% with respect to the best single channel ($b\bar{b}\tau^+\tau^-$), and for CMS by 68%, with respect to the best limit provided by the $b\bar{b}\gamma\gamma$ channel. This shows that the combination significantly outperform single channel performance, as a result of the comparable sensitivity of the $HH \rightarrow b\bar{b}\gamma\gamma$, $HH \rightarrow b\bar{b}\tau^+\tau^-$ and $HH \rightarrow b\bar{b}b\bar{b}$ final states in particular.

The difference between the ATLAS and CMS performances in each channel, is the result of different optimisation of the experimental analysis strategies. ATLAS employs BDT discriminators for all the analysis categories in the $HH \rightarrow b\bar{b}\tau^+\tau^-$ search, boosting the sensitivity of this final state with respect to the analogues CMS search. Likewise CMS uses a sophisticated MVA categorisation for the $b\bar{b}\gamma\gamma$ search, while the equivalent ATLAS search does not. Future improvements in the analysis techniques would lead to a further increase of the sensitivity, in addition to the larger integrated luminosity that will become available. Besides $b\bar{b}\tau^+\tau^-$ and $b\bar{b}\gamma\gamma$, in ATLAS also the $b\bar{b}b\bar{b}$ is one of the main final state contributing to the combined result, thanks to the good b-tagging performance and improved b-jet triggers (see Sec. 4.2 and 4.6). Both the ATLAS and CMS experiments have used the value of 33.53 fb as the HH production cross section predicted by the SM, it has been recently updated from Ref. [19]. A more recent evaluation recommends a value of 31.05 fb (see Table 1.1), this was used to derive the HL-LHC projections [29] reported in Chapter 8. For more details on the theoretical prediction, see Chapter 1. The impact of systematic uncertainties is currently not negligible. ATLAS has evaluated the expected sensitivity to the SM non-resonant production in the ideal case where no systematic uncertainties are considered and quotes an improvement of about 13% on the upper limit.

As described in Sec. 2.1.3 it is possible to consider special classes of new physics model that modify only the κ_λ parameter, affecting only the Higgs boson self-coupling. Any modification to

the κ_λ value would affect both the HH production cross section and decay kinematics. These effects are fully simulated for each κ_λ value considered in the scan performed by the ATLAS and CMS collaborations. Modifications to the Higgs boson decay branching fractions through one loop electroweak corrections (see Sec. 2.3.2) are not considered in the analyses of the two collaborations, although they can modify the results up to 10%. Figure 7.1 shows the upper limit on $\sigma(pp \rightarrow HH)$ for a given value of κ_λ published by the ATLAS and CMS collaborations.
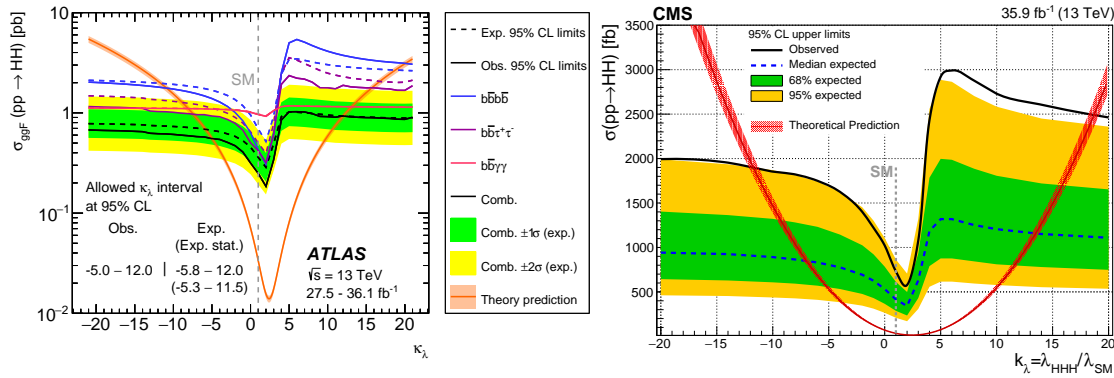
Figure 7.1: Expected and observed 95% CL upper limits on the HH production cross section as a function of κ_λ for ATLAS (left) and CMS (right) [66, 67]. The SM expectation and its uncertainty are also reported. All other Higgs boson couplings are set to their SM values.

The shape of the upper limit curve follows the signal acceptance, shown in Fig. 7.2, for the $HH \rightarrow b\bar{b}\tau^+\tau^-$ and $HH \rightarrow b\bar{b}\gamma\gamma$ case. In the $b\bar{b}b\bar{b}$ search also the invariant mass of the four b-jets, which is used to extract the signal, is affected by κ_λ, while The BDT score and the $m_{\gamma\gamma}$ distributions used to extract the signal in the $HH \rightarrow b\bar{b}\tau^+\tau^-$ and $HH \rightarrow b\bar{b}\gamma\gamma$ analysis respectively, do not show a κ_λ dependence as strong as in the $b\bar{b}b\bar{b}$ final state. The dependence of the signal acceptance from κ_λ is shown in Fig. 7.2. The maximum of the acceptance is obtained for $\kappa_\lambda \sim 2$, where the cross
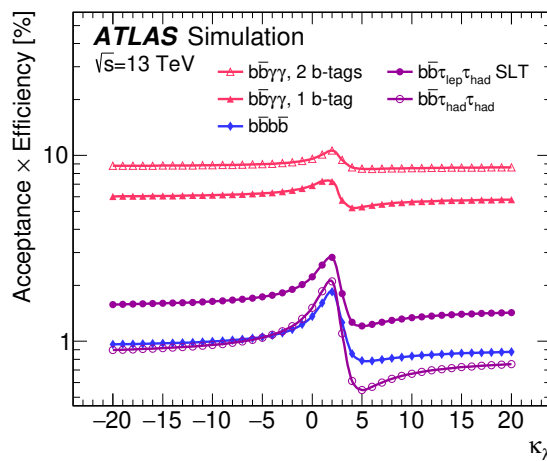
Figure 7.2: HH signal acceptance as a function of κ_λ for the ATLAS $HH \rightarrow b\bar{b}b\bar{b}$, $HH \rightarrow b\bar{b}\tau^+\tau^-$ and $HH \rightarrow b\bar{b}\gamma\gamma$ searches [66].

section is minimum as shown in Fig. 7.1. This κ_λ value corresponds to the maximum destructive interference between the box and the triangle diagrams, resulting in a harder m_{HH} spectrum (see Fig. 1.13 and Fig. 2.3) that increases the signal acceptance. For $|\kappa_\lambda| > 10$ the triangle diagram becomes dominant and the upper limit becomes symmetric in κ_λ. The ATLAS and CMS combined
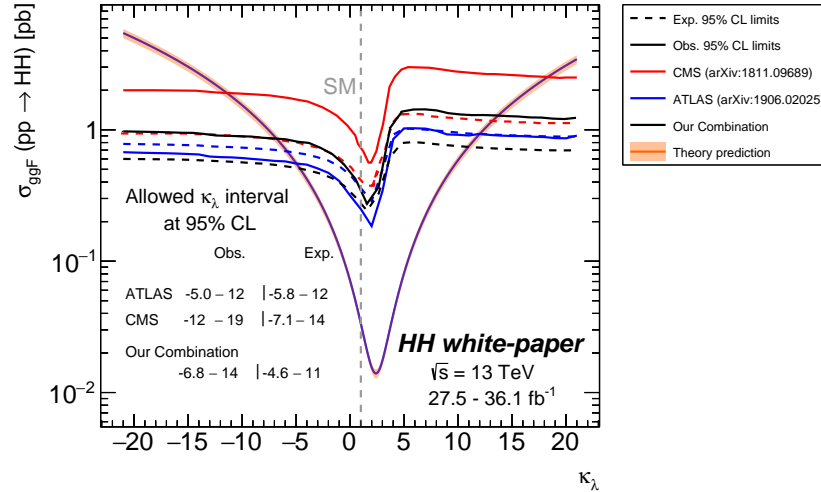
Figure 7.3: 95% CL upper limits on the $\sigma(pp \rightarrow HH)$ cross section as a function of κ_λ. The ATLAS and CMS limits are shown together their statistical combination.

upper limits on the HH cross section as function of κ_λ are shown in Fig. 7.3. The combination of the ATLAS and CMS results is also shown. It has been derived from the published ATLAS and CMS expected and observed upper limits, assuming that the likelihoods have gaussian shape and that, for each of the two experiments, the observed and expected likelihoods differ only by a shift on the mean value, while they have the same width. The combination of ATLAS and CMS results has been performed without including correlation of systematic errors between the two experiments. Due to the 2σ excess in CMS results, the combined observed result is slightly worse than the ATLAS one.

The corresponding intervals where the κ_λ is observed (expected) to be constrained at 95% CL are listed in Table 7.2 for the main channels.

Final state	collaboration	allowed κ_λ interval at 95% CL	
		observed	expected
$b\bar{b}b\bar{b}$	ATLAS	-11 – 20	-12 – 19
	CMS	-23 – 30	-15 – 23
$b\bar{b}\tau^+\tau^-$	ATLAS	-7.3 – 16	-8.8 – 17
	CMS	-18 – 26	-14 – 22
$b\bar{b}\gamma\gamma$	ATLAS	-8.1 –13	-8.2 – 13
	CMS	-11 – 17	-8.0 – 14
Combined	ATLAS	-5.0 – 12	-5.8 – 12
	CMS	-12 – 19	-7.1 – 14
Our combination	Both experiments	-6.8 – 14	-4.6 – 11

Table 7.2: The observed and expected 95% CL intervals on κ_λ for the combination and the individual final states analysed for non-resonant HH production at 13 TeV with about 36 fb^{-1}. All other Higgs boson couplings are set to their SM values [66, 67]. The $b\bar{b}b\bar{b}$ CMS values are obtained by extrapolating the published CMS values outside the published range [-20,20].

As discussed in Chapter 2, BSM contributions could be constrained in a model independent approach using the EFT approach. In the HEFT model (Sec. 2.1.3) five anomalous Higgs boson couplings (Eq. 2.19) relevant for HH production are identified: $c_{hhh} \equiv \kappa_\lambda$, $c_t \equiv \kappa_t$ and three additional interaction vertexes c_{tt}, c_{gghh} and c_{ggh}.

When imposing no new interactions in the model: $c_{tt} = c_{gghh} = c_{ggh} = 0$, the $pp \rightarrow HH$ cross section depends only from κ_t and κ_λ through the diagrams in Fig. 1.1 (a). The BSM amplitude of
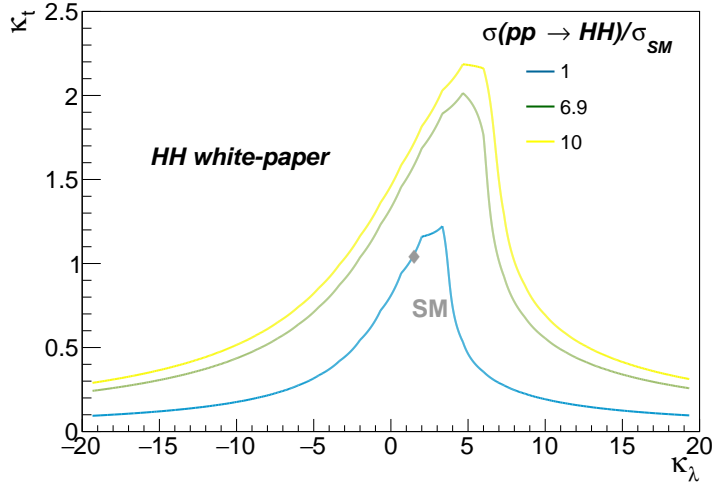
Figure 7.4: Contour level of $\sigma(pp \to HH)/\sigma_{\mathrm{SM}}$ as function of κ_t, κ_λ, under the assumption of no additional Higgs coupling vertices, as derived in Eq.7.2. The diamond indicates the SM predicted value. The reference values of 6.9 and 10 correspond to the best available observed and expected upper limits on the $\sigma(pp \to HH)$ cross section as measured by the ATLAS experiment.

the process can then be written as:

$$\mathscr{A} = \kappa_t^2 \mathscr{A}_1 + \kappa_t \kappa_\lambda \mathscr{A}_2$$

where $\mathscr{A}_1$ and $\mathscr{A}_2$ are given by the SM top-box and triangle diagrams. The cross section is proportional to $|\mathscr{A}|^2$ therefore the following expression holds:

$$\sigma_{pp \to HH}(\kappa_t, \kappa_\lambda) \propto \left(\kappa_t^4 \overline{|\mathscr{A}_1|^2} + 2\kappa_t^3 \kappa_\lambda \overline{\Re \mathscr{A}_1 \mathscr{A}_2^*} + \kappa_t^2 \kappa_\lambda^2 \overline{|\mathscr{A}_2|^2} \right) \tag{7.1}$$

where with the overline we indicate the average of the quantity over the phase space of the process, factorising κ_t^4 we obtain

$$\sigma_{pp \to HH}(\kappa_t, \kappa_\lambda) \propto \kappa_t^4 \left[\overline{|\mathscr{A}_1|^2} + 2\left(\frac{\kappa_\lambda}{\kappa_t}\right) \overline{\Re \mathscr{A}_1 \mathscr{A}_2^*} + \left(\frac{\kappa_\lambda}{\kappa_t}\right)^2 \overline{|\mathscr{A}_2|^2} \right] \tag{7.2}$$

From this expression it is clear that it is impossible to extract κ_λ constraints from HH production without assumptions on κ_t, this is more evident in the representation in Fig. 7.4. The κ_t and κ_λ parameters can be constrained also using single Higgs measurements as described in Sec. 7.6, these measurements impose a different correlation pattern between κ_t and κ_λ, therefore a future combination of single H and HH measurements is expected to provide a more model independent determination of κ_λ.

A five dimensional scan of the HEFT couplings is computationally excessive, therefore a clustering strategy has been developed to group together possible combinations of coupling values that present similar kinematic properties as discussed in detail in Sec. 2.4. Twelve clusters have been identified, in addition to the SM ($\kappa_\lambda = 1$) and the $\kappa_\lambda = 0$ scenarios. Within each cluster, the representative points in the EFT space shown in Table 2.2 are identified as benchmarks. Each benchmark predicts a different m_{HH} distribution as shown in Fig. 2.11, that affects the signal acceptance and the final discriminant of the analyses determining different sensitivities for different benchmark points. The CMS experiment has adopted this approach and provided the observed and expected exclusion limits on the HH cross section for the different EFT benchmarks, which are shown in
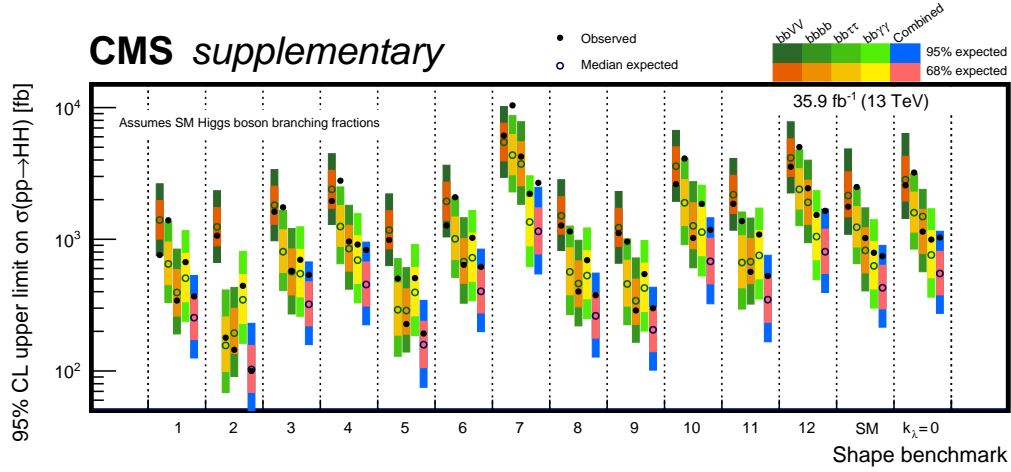
Fig. 7.5.

Figure 7.5: The 95% CL upper limits on the non-resonant HH cross section for different EFT bench-mark topologies (bins 1 to 12). Each benchmark represents a possible modification in both the pre-dicted rate and kinematic distributions. The last two bins show the 95% CL upper limits for $\kappa_\lambda = 1$ (SM) and 0. Each of the four final states is shown separately together with their combination [67].

7.3   Resonant HH production mode

In addition to the non-resonant production, searches for resonant HH are performed in the m_{HH} range from 250 to 3000 GeV, for spin-0 under the narrow width approximation[1] and spin-2 reso-nances (see Sec. 3.3).

For the resonant hypothesis the ATLAS and CMS collaborations have both analysed the $b\bar{b}b\bar{b}$, $b\bar{b}WW^*$, $b\bar{b}\tau^+\tau^-$ and $b\bar{b}\gamma\gamma$ channels. ATLAS has also included WW^*WW^* and $WW^*\gamma\gamma$, while CMS $b\bar{b}VV^*$ has investigated the di-lepton final state. No evidence for a signal is observed, and upper limits at 95% CL have been set on the production cross section for spin-0 resonances and they are shown in Fig. 7.6. In the same figure limits obtained by the combination of all channels are also shown. The most sensitive channels for both the ATLAS and CMS collaborations are $b\bar{b}b\bar{b}$, $b\bar{b}\tau^+\tau^-$ and $b\bar{b}\gamma\gamma$. Their sensitivity for the ATLAS and CMS experiments are compared in Fig. 7.7.

The spin-2 model has been tested for several values of the $k/\bar{M}_{\rm pl}$, namely < 0.5 from CMS and 1.0 and 2.0 from ATLAS, as shown in Fig. 7.8. As $k/\bar{M}_{\rm pl}$ increases, the resonance width becomes larger and the narrow width approximation, used by the CMS collaboration, is valid only for $k/\bar{M}_{\rm pl} < 0.5$. The ATLAS analyses take into account the natural width of the resonance in the simulation of the signal processes.

At higher resonance masses, the $b\bar{b}b\bar{b}$ channel dominates the sensitivity in both experiments, thanks to the large branching fraction of $H \to b\bar{b}$, the good signal efficiency and the decreasing background at high m_{HH} value. Also the boosted $b\bar{b}\tau^+\tau^-$ final state, which has been investigated by CMS, significantly contributes to the combination for resonance masses above 1 TeV. ATLAS has also investigated $b\bar{b}WW^*$ in the single lepton final state [455] in a regime where the $H \to b\bar{b}$ system is boosted and the WW decay is resolved, but it is not as competitive as the $b\bar{b}b\bar{b}$ final state at high mass. CMS additionally has explored the $b\bar{b}WW^*$ single lepton channel where both Higgs bosons are boosted, and demonstrated good sensitivity for resonances below 1.5 TeV in mass [520]. All this

---

[1]The width of the signal mass distribution is much smaller of the experimental resolution
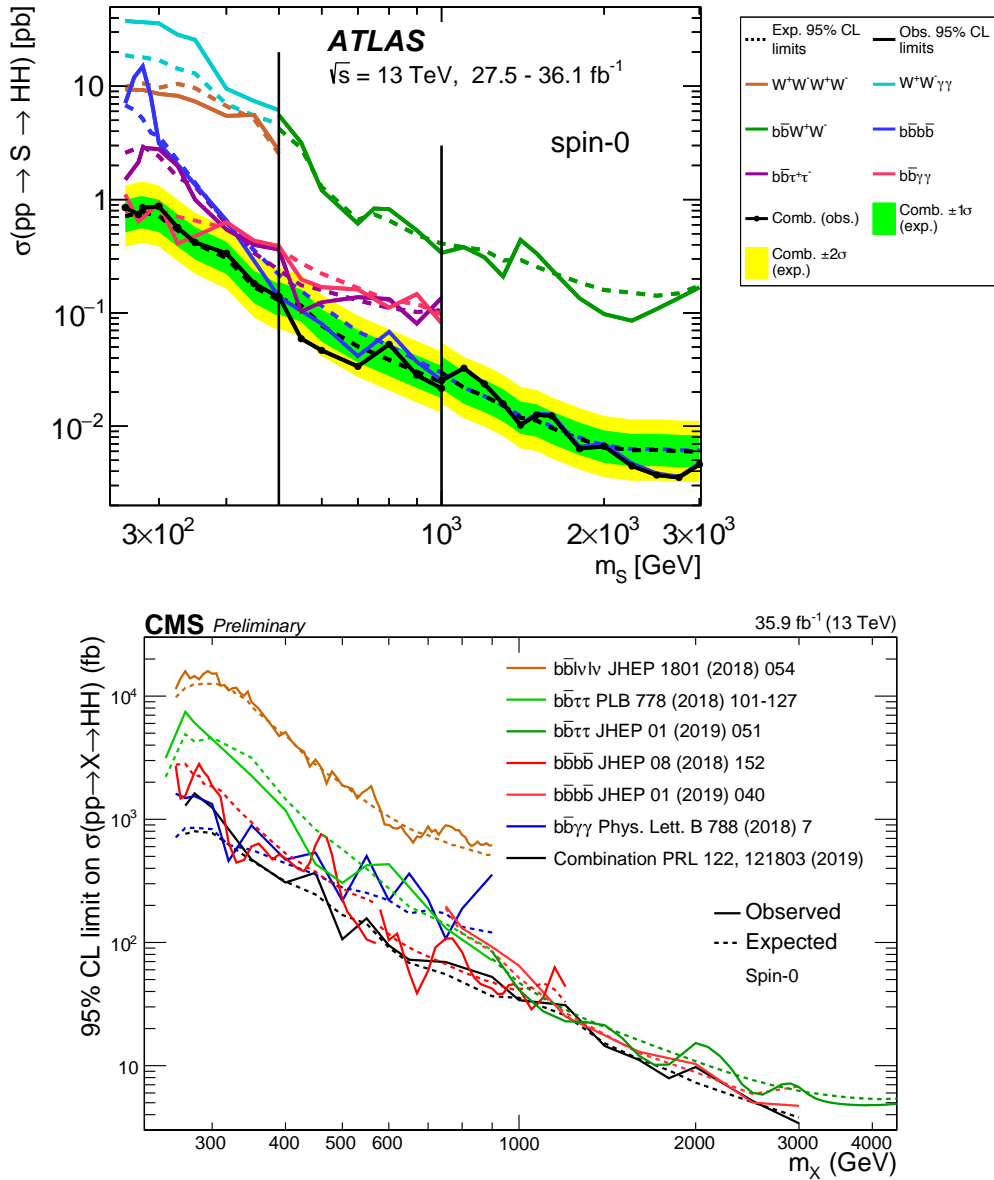
Figure 7.6: Expected and observed 95% CL exclusion limits on the production cross section of a narrow, spin zero resonance (S or X) decaying into a pair of Higgs bosons. Top: ATLAS combination and breakdown by final state for m$_S$ <3 TeV [66]; Bottom: CMS combination and breakdown by final state for m$_S$ <3 TeV [67].

has been possible thanks to the developments of dedicated techniques used to identify boosted $H \rightarrow b\bar{b}$ events, as discussed in Sec. 4.1 and Sec. 4.2.1.
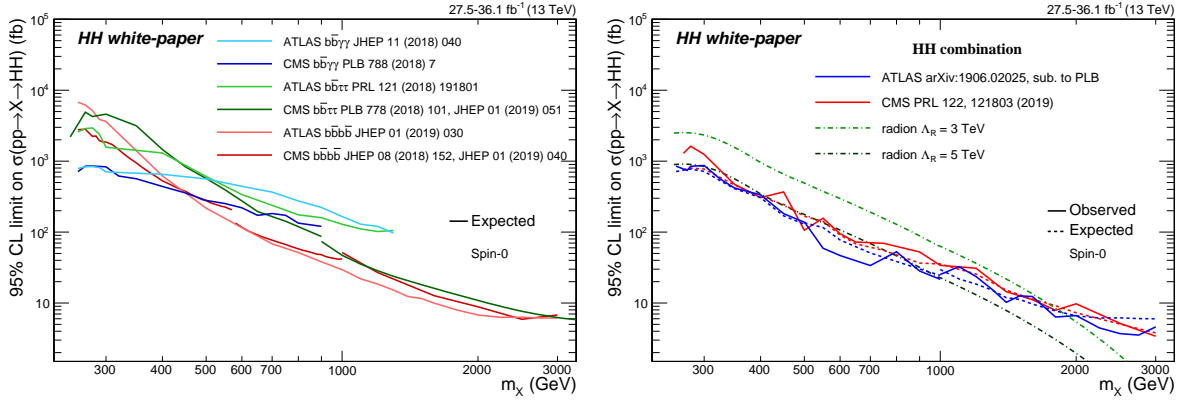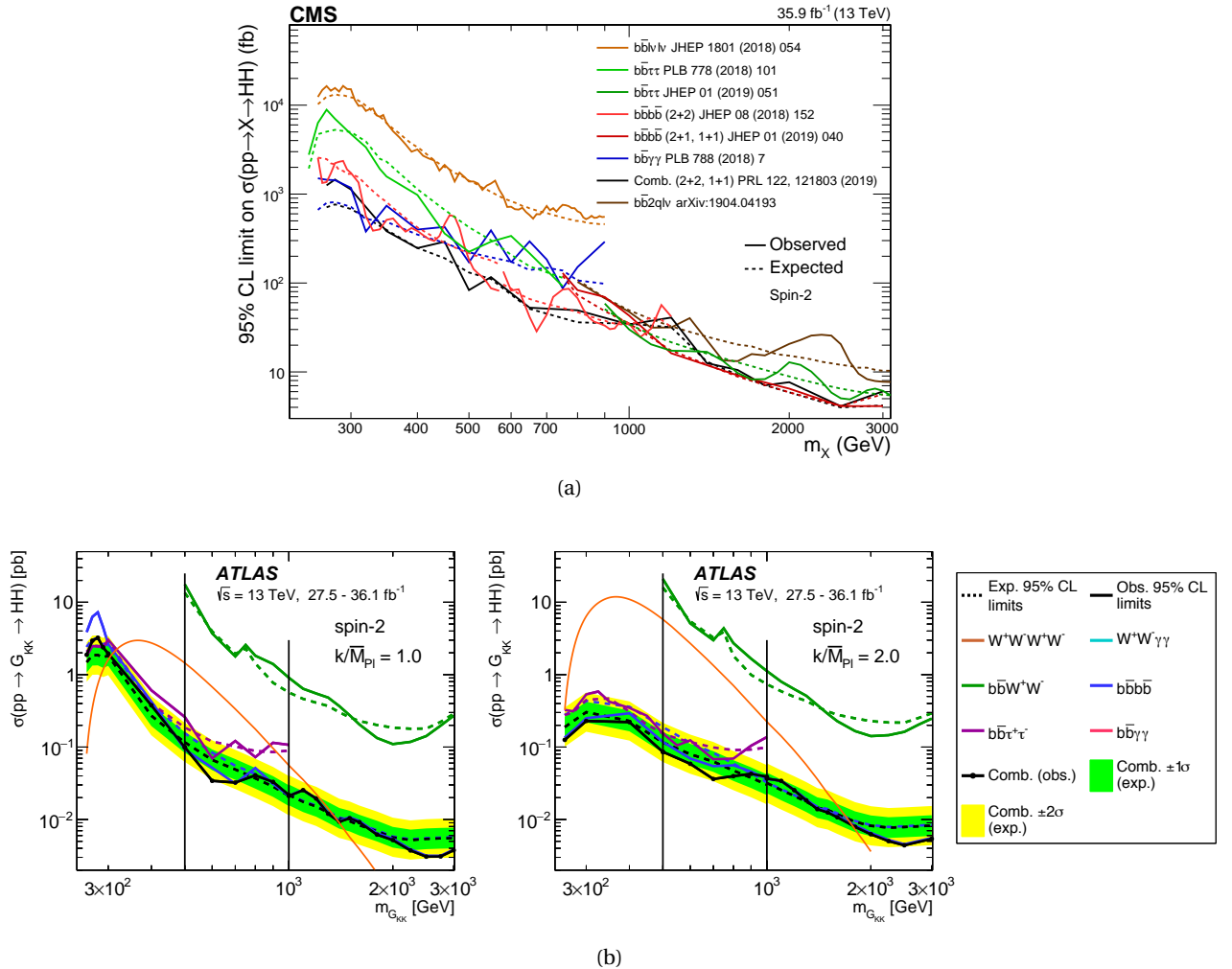
Figure 7.7: Left: expected 95% CL upper limits on the resonant production cross section of a narrow, spin-0 resonance (S or X) decaying into a pair of Higgs bosons for the most sensitive channels: $b\bar{b}b\bar{b}$, $b\bar{b}\tau^{+}\tau^{-}$ and $b\bar{b}\gamma\gamma$. Right: expected and observed 95% CL combined exclusion limits on the resonant spin-0 HH production. A theory prediction from bulk radion model is overlaid [518, 519].

(a)

(b)

Figure 7.8: Expected and observed 95% CL exclusion limits on the production cross section of a spin-2 resonance decaying into a pair of Higgs bosons. Top left: CMS combination and breakdown by final state with $k/\bar{M}_{pl} = 0.5$ [67]; Top right: ATLAS combination and breakdown by final state for $k/\bar{M}_{pl} = 1.0$ [66]; Bottom left: ATLAS combination and breakdown by final state for $k/\bar{M}_{pl} = 2.0$ [66].

7.4   Interpretation in complete models

The ATLAS collaboration has provided interpretations of spin-0 resonance limits in two models, the hMSSM model (Sec. 3.4.3) and the EWK-singlet model (Sec. 3.1, with a Z_2 symmetry). The exclusion limits in the model parameter space are shown in Fig. 7.9 and Fig. 7.10 respectively. The interpretation is derived in the narrow width approximation, in this sense results are valid only when the scalar resonance width is much smaller than the detector resolution. This happens when $\Gamma_S/m_S < 2\%$ in the $b\bar{b}\gamma\gamma$ case, 5% in the $b\bar{b}\tau^+\tau^-$ case and 10% in the $b\bar{b}b\bar{b}$ case. Regions where $\Gamma_S/m_S > 2\%$ have been removed from Fig. 7.9, while in Fig. 7.10 regions where $\Gamma_S/m_S > 10\%$ were removed and are indicated with a dashed region, while only the $b\bar{b}b\bar{b}$ and $b\bar{b}\tau^+\tau^-$ channels are combined when $\Gamma_S/m_S > 2\%$ and only $b\bar{b}b\bar{b}$ results are shown for $\Gamma_S/m_S > 5\%$.
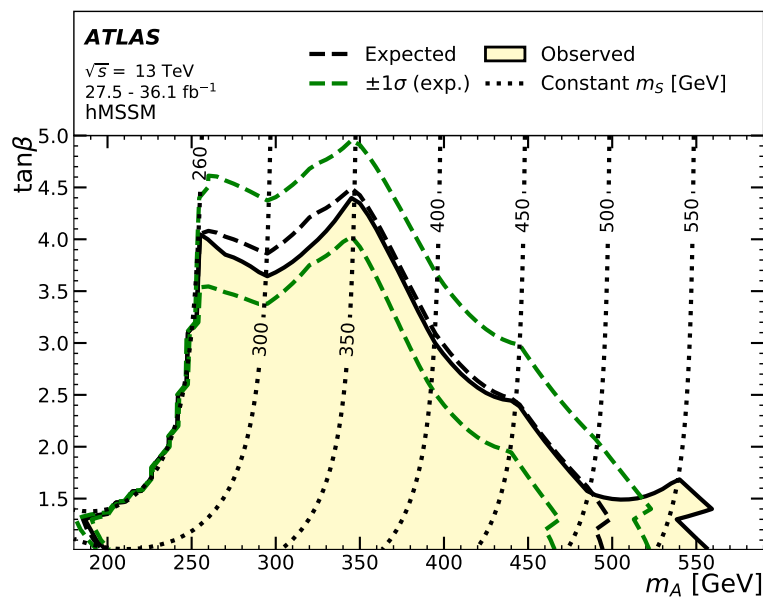
Figure 7.9: Expected and observed 95% CL exclusion limits in the $\tan\beta$-m_A parameter space of the hMSSM model [66].
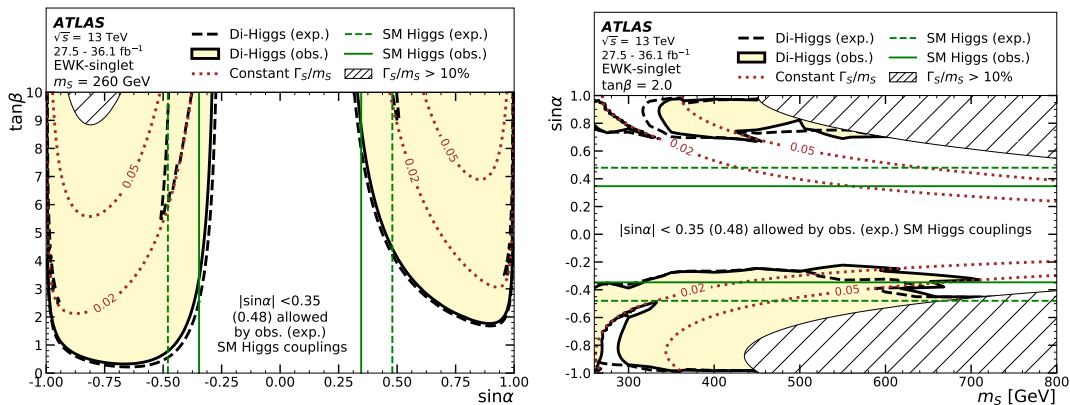
Figure 7.10: Expected and observed 95% CL exclusion limits in the: $\sin\alpha$-$\tan\beta$ parameter space for $m_S = 260$ Gev (left), and the $\sin\alpha$-m_S parameter space for $\tan\beta = 2$ of the EWK-singlet model [66].

7.5   Impact of systematic errors and concluding remarks

In general,results presented in this chapter are, based on 27.5–36.1 fb^{-1} $p-p$ collision data, are limited by the size of the available dataset rather than systematic uncertainties. The overall impact of systematic uncertainties and their leading contributions are shown for the ATLAS analyses in Table 7.3[2].

Upper limit percentage variation	NR	Spin-0		Spin-2 $k/\overline{M}_{Pl} = 1$		Spin-2 $k/\overline{M}_{Pl} = 2$	
		1 TeV	3 TeV	1 TeV	3 TeV	1 TeV	3 TeV
Simulation statistics	3%	1%	-	2%	-	1%	-
Background modelling	5%	7%	9%	11%	15%	16%	21%
Signal theory	1%	-	-	-	1%	-	-
Tau	2%	-	-	-	-	1%	-
Jet	-	1%	2%	2%	3%	5%	4%
b-tagging	1%	2%	-	3%	-	4%	-
All	13%	12%	11%	19%	18%	29%	25%

Table 7.3: Percentage variations of the upper limits on the cross section of various signal models due to systematic uncertainties for the ATLAS analysis [66][3]. The variations are calculated by computing the ratio between the difference of the upper limits obtained including all systematic uncertainties with the one obtained by removing the systematic uncertainty under study, and the nominal upper limit including all systematic uncertainties. The variations from the six leading systematic uncertainties and from all systematic uncertainties ("All") are listed. The row "All" is obtained by removing all systematic uncertainties. When the fractional change is less than 1%, "-" is shown. "NR" indicates the non-resonant signal model.

Assuming that systematic errors will remain sub-dominant while keeping the current analysis sensitivity, an expected limit of 5 times the SM prediction is reachable with the analysis of the full Run 2 dataset by the ATLAS and CMS collaborations.

In the non-resonant analysis the dominant sources of systematic uncertainties are associated to the background estimation methods, especially for the modelling of the multi-jet component in the $b\bar{b}b\bar{b}$ and $b\bar{b}\tau^{+}\tau^{-}$ analyses, for which no reliable simulation is yet available. The data-driven approaches used extrapolate the multi-jet parameterisation from signal-free control regions in data. The precision of these data-driven methods is expected to improve with the increasing size of the available dataset, while the uncertainty associated to the extrapolation technique is an intrinsic limitation of this approach.

Other sources that contribute to systematic uncertainties are related to objects reconstruction and identification. Both ATLAS and CMS experiments are working on more precise evaluations of these object-related uncertainties and improvements on this subject are expected in the future. Further contributions are the uncertainty on the integrated luminosity and the limited MC statistics. For the latter, future progress in fast simulation techniques and truth level filtering techniques will allow to generate larger simulated samples and therefore hopefully mitigate these statistical limitations.

For searches of high mass resonances, where the signal is expected to appear on the tails of steeply falling invariant mass distribution of the non-resonant background, the analyses are now strongly limited by the number of events available in the current dataset.

---

[2]The related CMS publications do not provide this information, but we don't expect large differences in systematic uncertainties between the ATLAS and CMS searches.

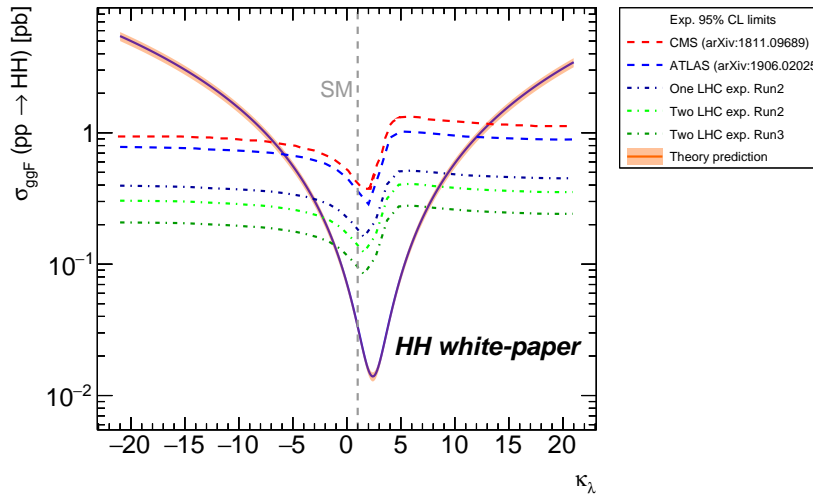[3]The table is extracted from the auxiliary material available on the ATLAS webpage https://atlas.web.cern.ch/Atlas/GROUPS/PHYSICS/PAPERS/HDBS-2018-58/

Figure 7.11: Expected limit on the $pp \to HH$ cross section as a function of κ_λ for one of the two LHC experiments and their combination estimated for the Run 2 integrated luminosity (140fb^{-1}) and the Run 2 and 3 (300fb^{-1}).

In the future, more final states will be combined. The orthogonality between the various searches must be carefully ensured, especially when combining similar final states, such as $b\bar{b}WW^*$, $b\bar{b}ZZ^*$ and $b\bar{b}\tau^+\tau^-$. They can all result in a signature with two b-jets, two leptons and missing transverse energy.

A potential combination of ATLAS and CMS based on the full Run 2 dataset will be considered, which increases the sensitivity significantly compared to single-experiment results as shown in Fig. 7.3. The treatment of systematic uncertainties and correlations between ATLAS and CMS needs to be carefully studied. A useful reference is the ATLAS and CMS Higgs coupling combination [177] and the procedure for this combination outlined in [521] by the LHC Higgs Combination Group. Theoretical uncertainties on the signal process should be correlated, likewise simulation-based background uncertainties may be correlated, while the data-driven background uncertainties should not. A harmonised treatment of the signal process in terms of MC generators, theoretical uncertainties, as well as the same mass points, will facilitate such a combination.

By combining the ATLAS and CMS data, the expected upper limit on the non-resonant cross section should reach down to 3.5 times the SM prediction at the end of Run 2 (140fb^{-1}), and to 2.4 times the SM at the end of Run 3 (300fb^{-1}). If instead the impact of the systematic uncertainties will not change, the sensitivity at the end of Run 3 would reach about 5 times the SM expectation, and it would be completely systematic dominated. Concerning κ_λ, Fig. 7.11 shows the expected limit on the $pp \to HH$ cross section as a function of κ_λ using Run 2 and Run 3 extrapolations assuming negligible systematic errors. Without important improvements to the analyses but assuming it will be possible to reduce the impact of the systematic errors, κ_λ is expected to be constrained in the interval $-1.2 < \kappa_\lambda < 7.5$ at 95% CL at the end of Run 3.

7.6 Constraints on κ_λ from single Higgs boson measurements

B. Di Micco, S. Manzoni, C. Vernieri

In addition to the direct determination of the Higgs self-coupling through the study of Higgs boson pair production, an indirect measurement is also possible exploring the NLO electroweak (EW) corrections to single Higgs measurements, as discussed in detail in Sec. 2.3.2. The first experimen-

Measurement	Reference	$\mathscr{L}$
$t\bar{t}H$ ($H \to b\bar{b}$ and multileptons final states)	[522, 523]	36.1 . fb^{-1}
$H \to \gamma\gamma$ (including $t\bar{t}H$)	[442, 464, 524]	79.8fb^{-1}
$H \to ZZ^*$ (including $t\bar{t}H$)	[525, 526]	79.8 fb^{-1}
VH $H \to b\bar{b}$	[399, 527]	79.8 fb^{-1}
$H \to WW^*$	[528]	36.1 fb^{-1}
$H \to \tau^+\tau^-$	[529]	36.1 fb^{-1}

Table 7.4: List of the ATLAS measurements of Higgs production and decay modes, combined to derive a constraint on the value of the Higgs boson self-coupling, κ_λ. The measurements used in this analysis are based on data collected at 13 TeV corresponding to an integrated luminosity of up to 79.8fb^{-1}.

tal constraint on κ_λ from single Higgs measurements has been determined by the ATLAS experiment [134], by fitting data from single Higgs boson analyses taking into account the NLO κ_λ dependence of the cross section and the branching fractions of the ggF, VBF, WH, ZH and $t\bar{t}H$ production modes and the $\gamma\gamma$, WW, ZZ, $\tau\tau$ and $b\bar{b}$ decay modes, as listed in Table 7.4. Differential information has also been exploited through the use of the Simplified Template Cross Section (STXS) categories (described in Sec. 6.4).

Each analysis separates the measured events into orthogonal kinematic and topological categories depending on the reconstructed final state. These categories partially account for the kinematic dependence and they have been optimised to maximise the sensitivity to their associated truth-level region. Although the gluon-gluon fusion production mode is subdivided in bins of jet multiplicity and transverse momentum of the Higgs boson, p_T^H, differential corrections are not yet available[4] and therefore the corresponding STXS bins related share the same parameterisation as for the inclusive ggF production. Nevertheless, such contributions have been evaluated in the Heavy Top Quark expansion [176], that is valid for $p_T^H << m_t$, i.e. $p_T^H < 150$ GeV (see Sec. 2.3.2) and result to be small. The $t\bar{t}H$ production mode is considered inclusively in one single bin, as no differential measurement is available yet. The $gg \to ZH$ cross section is not parameterised as a function of κ_λ, because the theoretical computation is still missing and it should contribute mostly in high p_T^H regions where the sensitivity to κ_λ is expected to be small.

The values of the kinematic dependent C_1 linear coefficients, Eq.(2.34), that parameterise the sensitivity of the measurement to κ_λ have been derived for each STXS region defined in the measurement. The values obtained are reported in Table 7.5.

The NLO EW K-factors , that includes one loop EWK correction not involving κ_λ, are computed inclusively for each production mode and not in STXS bins, as in the regions of phase space where these corrections are most significant (typically for high Higgs boson transverse momentum), the sensitivity to the Higgs boson trilinear coupling is minimal [131]. The selection efficiencies have been evaluated as function of κ_λ and a negligible dependency has been found, thus they are assumed to be constant. The exception is $t\bar{t}H$ production mode, which shows a 10% increase for $\kappa_\lambda < -10$, but in this interval the reduction of the cross section due to the κ_λ dependence is about 80%, therefore largely dominating over the efficiency variation. This assumption will be re-evaluated in the ggF production mode once a complete computation of the differential NLO EW corrections will become available.

A likelihood fit is performed to constrain the value of the Higgs boson self-coupling κ_λ, while all

---

[4]They would involve higher order calculations including two loop corrections

STXS region		VBF	WH	ZH
		$C_1^i \times 100$		
VBF+V(had)H	VBF-cuts + $p_T^{j1} < 200$ GeV, $\leq 2j$	0.63	0.91	1.07
	VBF-cuts + $p_T^{j1} < 200$ GeV, $\geq 3j$	0.61	0.85	1.04
	VH-cuts + $p_T^{j1} < 200$ GeV	0.64	0.89	1.10
	no VBF/VH-cuts, $p_T^{j1} < 200$ GeV	0.65	1.13	1.28
	$p_T^{j1} > 200$ GeV	0.39	0.23	0.28
$qq \rightarrow H\ell\nu$	$p_T^V < 150$ GeV		1.15	
	$150 < p_T^V < 250$ GeV, $0j$		0.18	
	$150 < p_T^V < 250$ GeV, $\geq 1j$		0.33	
	$p_T^V > 250$ GeV		0	
$qq \rightarrow H\ell\ell$	$p_T^V < 150$ GeV			1.33
	$150 < p_T^V < 250$ GeV, $0j$			0.20
$qq \rightarrow H\nu\nu$	$150 < p_T^V < 250$ GeV, $\geq 1j$			0.39
	$p_T^V > 250$ GeV			0

Table 7.5: C_1^i coefficients for each region of the STXS scheme for the VBF, WH and ZH production modes. The definition of the STXS regions can be found in Ref. [134] . In the VBF categories, "VBF-cuts" [19] indicates selections applied to target the VBF di-jet topology, with requirements on the di-jet invariant mass (m_{jj}) and the difference in pseudorapidity between the two jets; the additional $\leq 2j$ and $\geq 3j$ region separation is performed indirectly by requesting $p_T^{Hjj} \lesssim 25$ GeV. "VH-cuts" select the $W, Z \rightarrow jj$ decays, requiring an m_{jj} value close to the vector boson mass [19]. The C_1^i coefficients of the $p_T^V > 250$ GeV regions are negligible, O(10^{-6}), and are set to 0.
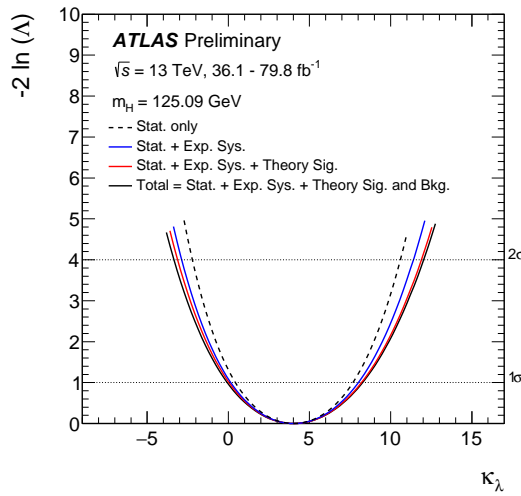
Figure 7.12: The profile likelihood scan performed as a function of κ_λ on data [134].

other Higgs boson coupling are set to their SM values ($\kappa_{i,F} = \kappa_{i,V} = 1$ in Eq. 2.32 and 2.35). Thus, for a large variety of BSM scenarios, where new physics modifies only the Higgs boson self-coupling, the constraints on κ_λ derived through the combination of single Higgs measurements can be directly compared to the constraints set by double Higgs production measurements. The profile likelihood scan performed as a function of κ_λ is shown in Fig. 7.12. The central value and uncertainty of the modifier of the trilinear Higgs boson self-coupling is determined to be:

$$\kappa_\lambda = 4.0^{+4.3}_{-4.1} = 4.0^{+3.7}_{-3.6}(\text{stat.})^{+1.6}_{-1.5}(\text{exp.})^{+1.3}_{-0.9}(\text{sig.th.})^{+0.8}_{-0.9}(\text{bkg.th.}) \tag{7.3}$$

where the total uncertainty is decomposed into components for statistical, experimental and theory uncertainties on signal and background modelling. The 95% CL allowed interval for κ_λ is $-3.2 < \kappa_\lambda < 11.9$ (observed) and $-6.2 < \kappa_\lambda < 14.4$ (expected). This interval is competitive with the one obtained from the direct HH searches using an integrated luminosity of 36.1 fb^{-1}, which is $-5.2 < \kappa_\lambda < 12.1$ (observed) and $-5.8 < \kappa_\lambda < 12.0$ (expected). The dominant contributions to the κ_λ sensitivity derive from the di-boson decay channels $\gamma\gamma$, ZZ, WW and from the ggF and $t\bar{t}H$ production modes. The differential information currently provided by the STXS binning in the VBF, WH and ZH production modes does not improve the sensitivity to κ_λ significantly. However, differential information should help most in the $t\bar{t}H$ production mode. A dedicated optimisation of the kinematic binning, including the most sensitive ggF and $t\bar{t}H$ production modes, still needs to be fully theoretically and experimentally explored and might improve the sensitivity in the future.

While the sensitivity on κ_λ derived from single Higgs processes in an exclusive fit is comparable to those from HH direct searches, the constraints become significantly weaker when BSM deformations to the single Higgs couplings are taken properly into account. Two additional fit configurations with a simultaneous fit to $(\kappa_\lambda, \kappa_V)$ or to $(\kappa_\lambda, \kappa_F)$ have been considered. These fits target BSM scenarios where new physics could affect only the Yukawa type terms ($\kappa_V = 1$) of the SM or only the couplings to vector bosons ($\kappa_F = 1$), in addition to the Higgs boson self-coupling (κ_λ) [272]. This set of results provides a rough indication of the simultaneous sensitivity to both Higgs boson self-coupling and single Higgs boson couplings with the data statistics currently available for the input analyses.

Figure 7.13 shows negative log-likelihood contours on $(\kappa_\lambda, \kappa_V)$ and $(\kappa_\lambda, \kappa_F)$. The constraining power of the measurement is reduced by including additional degrees of freedom to the fit. In particular, the sensitivity to κ_λ is degraded by 50% (on the expected lower 95% C.L. exclusion limit) when determining simultaneously κ_V and κ_λ.

Similarly, the sensitivity to κ_λ from double Higgs measurements completely vanishes if the coupling to the top quark (κ_t) is left free to float, due to a κ_t^4 dependence of the total $pp \to HH$ cross section (see Sec. 7.2 and Fig. 7.4). Therefore a determination of κ_λ which would take into account BSM contributions affecting κ_t, κ_F or κ_V would be possible only through a simultaneous analysis of both single and double Higgs measurements. As the experimental sensitivity increases, the addition of more differential information, in particular for $t\bar{t}H$ and ggF, would allow the inclusion of more relevant EFT operators in the analysis, as κ_t and c_{gg} (cf. discussion at the end of Sec. 2.3.2).
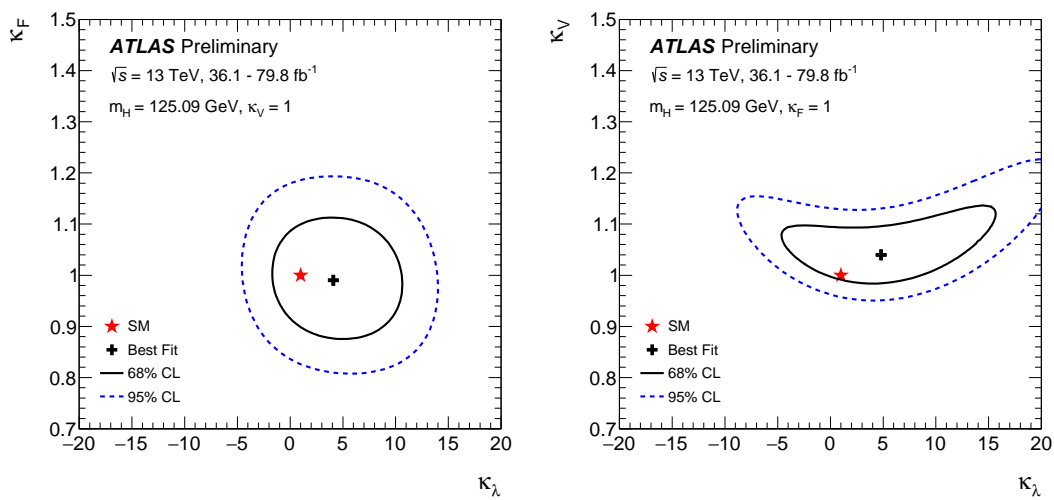
Figure 7.13: Negative log-likelihood contours at 68% and 95% CL as function of (κ_λ, κ_F) under the assumption of $\kappa_V = 1$ (left), and as function of (κ_λ, κ_V) under the assumption of $\kappa_F = 1$) (right). The best fit value is indicated by a cross while the SM hypothesis is indicated by a star [134].

Acknowledgements

Bibliography

[1] P. W. Higgs, *Broken symmetries, massless particles and gauge fields*, Phys. Lett. **12** (1964) 132–133.

[2] P. W. Higgs, *Broken Symmetries and the Masses of Gauge Bosons*, Phys. Rev. Lett. **13** (1964) 508–509.

[3] P. W. Higgs, *Spontaneous Symmetry Breakdown without Massless Bosons*, Phys. Rev. **145** (1966) 1156–1163.

[4] F. Englert and R. Brout, *Broken Symmetry and the Mass of Gauge Vector Mesons*, Phys. Rev. Lett. **13** (1964) 321–323.

[5] G. S. Guralnik, C. R. Hagen, and T. W. B. Kibble, *Global Conservation Laws and Massless Particles*, Phys. Rev. Lett. **13** (1964) 585–587.

[6] T. W. B. Kibble, *Symmetry breaking in nonAbelian gauge theories*, Phys. Rev. **155** (1967) 1554–1561.

[7] ATLAS Collaboration, *Observation of a new particle in the search for the Standard Model Higgs boson with the ATLAS detector at the LHC*, Phys. Lett. B **716** (2012) 1–29, arXiv:1207.7214 [hep-ex].

[8] CMS Collaboration, *Observation of a new boson at a mass of 125 GeV with the CMS experiment at the LHC*, Phys. Lett. B **716** (2012) 30–61, arXiv:1207.7235 [hep-ex].

[9] M. Shaposhnikov and C. Wetterich, *Asymptotic safety of gravity and the Higgs boson mass*, Phys. Lett. B **683** (2010) 196–200, arXiv:0912.0208 [hep-th].

[10] F. L. Bezrukov and M. Shaposhnikov, *The Standard Model Higgs boson as the inflaton*, Phys. Lett. B **659** (2008) 703–706, arXiv:0710.3755 [hep-th].

[11] I. Masina and A. Notari, *The Higgs mass range from Standard Model false vacuum Inflation in scalar-tensor gravity*, Phys. Rev. D **85** (2012) 123506, arXiv:1112.2659 [hep-ph].

[12] N. Cabibbo, L. Maiani, G. Parisi, and R. Petronzio, *Bounds on the Fermions and Higgs Boson Masses in Grand Unified Theories*, Nucl. Phys. B **158** (1979) 295–305.

[13] D. Buttazzo, G. Degrassi, P. P. Giardino, G. F. Giudice, F. Sala, A. Salvio, and A. Strumia, *Investigating the near-criticality of the Higgs boson*, JHEP **12** (2013) 089, arXiv:1307.3536 [hep-ph].

[14] G. Degrassi, S. Di Vita, J. Elias-Miro, J. R. Espinosa, G. F. Giudice, G. Isidori, and A. Strumia, *Higgs mass and vacuum stability in the Standard Model at NNLO*, JHEP **08** (2012) 098, arXiv:1205.6497 [hep-ph].

[15] T. Plehn and M. Rauch, *The quartic higgs coupling at hadron colliders*, Phys. Rev. D **72** (2005) 053008, `arXiv:0507321 [hep-ph]`.

[16] T. Binoth, S. Karg, N. Kauer, and R. Rückl, *Multi-Higgs boson production in the Standard Model and beyond*, Phys. Rev. D **74** (2006) 113008, `arXiv:0608057 [hep-ph]`.

[17] B. Fuks, J. H. Kim, and S. J. Lee, *Probing Higgs self-interactions in proton-proton collisions at a center-of-mass energy of 100 TeV*, Phys. Rev. D **93** (2016) 035026, `arXiv:1510.07697 [hep-ph]`.

[18] F. Maltoni, E. Vryonidou, and M. Zaro, *Top-quark mass effects in double and triple Higgs production in gluon-gluon fusion at NLO*, JHEP **1411** (2014) 079, `arXiv:1408.6542 [hep-ph]`.

[19] LHC Higgs Cross Section Working Group Collaboration, *Handbook of LHC Higgs Cross Sections: 4. Deciphering the Nature of the Higgs Sector*, `arXiv:1610.07922 [hep-ph]`.

[20] E. N. Glover and J. van der Bij, *Higgs Boson Pair Production Via Gluon Fusion*, Nucl. Phys. B **309** (1988) 282.

[21] T. Plehn, M. Spira, and P. M. Zerwas, *Pair production of neutral Higgs particles in gluon-gluon collisions*, Nucl. Phys. B **479** (1996) 46–64, `arXiv:9603205 [hep-ph]`. [Erratum: Nucl. Phys.B531,655(1998)].

[22] S. Borowka, N. Greiner, G. Heinrich, S. Jones, M. Kerner, J. Schlenk, U. Schubert, and T. Zirke, *Higgs Boson Pair Production in Gluon Fusion at Next-to-Leading Order with Full Top-Quark Mass Dependence*, Phys. Rev. Lett. **117** (2016) 012001, `arXiv:1604.06447 [hep-ph]`. [Erratum: Phys. Rev. Lett.117,no.7,079901(2016)].

[23] S. Borowka, N. Greiner, G. Heinrich, S. P. Jones, M. Kerner, J. Schlenk, and T. Zirke, *Full top quark mass dependence in Higgs boson pair production at NLO*, JHEP **10** (2016) 107, `arXiv:1608.04798 [hep-ph]`.

[24] J. Baglio, F. Campanario, S. Glaus, M. Mühlleitner, M. Spira, and J. Streicher, *Gluon fusion into Higgs pairs at NLO QCD and the top mass scheme*, Eur. Phys. J. C **79** (2019) 459, `arXiv:1811.05692 [hep-ph]`.

[25] D. de Florian and J. Mazzitelli, *Two-loop virtual corrections to Higgs pair production*, Phys. Lett. B **724** (2013) 306–309, `arXiv:1305.5206 [hep-ph]`.

[26] D. de Florian and J. Mazzitelli, *Higgs Boson Pair Production at Next-to-Next-to-Leading Order in QCD*, Phys. Rev. Lett. **111** (2013) 201801, `arXiv:1309.6594 [hep-ph]`.

[27] J. Grigo, K. Melnikov, and M. Steinhauser, *Virtual corrections to Higgs boson pair production in the large top quark mass limit*, Nucl. Phys. B **888** (2014) 17–29, `arXiv:1408.2422 [hep-ph]`.

[28] D. de Florian, M. Grazzini, C. Hanga, S. Kallweit, J. M. Lindert, P. Maierhöfer, J. Mazzitelli, and D. Rathlev, *Differential Higgs Boson Pair Production at Next-to-Next-to-Leading Order in QCD*, JHEP **09** (2016) 151, `arXiv:1606.09519 [hep-ph]`.

[29] M. Grazzini, G. Heinrich, S. Jones, S. Kallweit, M. Kerner, J. M. Lindert, and J. Mazzitelli, *Higgs boson pair production at NNLO with top quark mass effects*, JHEP **05** (2018) 059, `arXiv:1803.02463 [hep-ph]`.

[30] J. Baglio, A. Djouadi, R. Gröber, M. M. Mühlleitner, J. Quevillon, and M. Spira, *The measurement of the Higgs self-coupling at the LHC: theoretical status*, JHEP **04** (2013) 151, arXiv:1212.5581 [hep-ph].

[31] L.-S. Ling, R.-Y. Zhang, W.-G. Ma, L. Guo, W.-H. Li, and X.-Z. Li, *NNLO QCD corrections to Higgs pair production via vector boson fusion at hadron colliders*, Phys. Rev. D **89** (2014) 073001, arXiv:1401.7754 [hep-ph].

[32] F. A. Dreyer and A. Karlberg, *Vector-Boson Fusion Higgs Pair Production at N^3LO*, Phys. Rev. D **98** (2018) 114016, arXiv:1811.07906 [hep-ph].

[33] F. A. Dreyer and A. Karlberg, *Fully differential Vector-Boson Fusion Higgs Pair Production at Next-to-Next-to-Leading Order*, Phys. Rev. D **99** (2019) 074028, arXiv:1811.07918 [hep-ph].

[34] H. T. Li and J. Wang, *Fully Differential Higgs Pair Production in Association With a W Boson at Next-to-Next-to-Leading Order in QCD*, Phys. Lett. B **765** (2017) 265–271, arXiv:1607.06382 [hep-ph].

[35] H. T. Li, C. S. Li, and J. Wang, *Fully differential Higgs boson pair production in association with a Z boson at next-to-next-to-leading order in QCD*, Phys. Rev. D **97** (2018) 074026, arXiv:1710.02464 [hep-ph].

[36] R. Frederix, S. Frixione, V. Hirschi, F. Maltoni, O. Mattelaer, et al., *Higgs pair production at the LHC with NLO and parton-shower effects*, Phys. Lett. B **732** (2014) 142–149, arXiv:1401.7340 [hep-ph].

[37] S. Dawson, S. Dittmaier, and M. Spira, *Neutral Higgs boson pair production at hadron colliders: QCD corrections*, Phys. Rev. D **58** (1998) 115012, arXiv:9805244 [hep-ph].

[38] J. R. Ellis, M. K. Gaillard, and D. V. Nanopoulos, *A Phenomenological Profile of the Higgs Boson*, Nucl. Phys. B **106** (1976) 292.

[39] M. A. Shifman, A. I. Vainshtein, M. B. Voloshin, and V. I. Zakharov, *Low-Energy Theorems for Higgs Boson Couplings to Photons*, Sov. J. Nucl. Phys. **30** (1979) 711–716.

[40] T. Inami, T. Kubota, and Y. Okada, *Effective Gauge Theory and the Effect of Heavy Quarks in Higgs Boson Decays*, Z. Phys. C **18** (1983) 69–80.

[41] M. Spira, A. Djouadi, D. Graudenz, and P. M. Zerwas, *Higgs boson production at the LHC*, Nucl. Phys. B **453** (1995) 17–82, arXiv:9504378 [hep-ph].

[42] B. A. Kniehl and M. Spira, *Low-energy theorems in Higgs physics*, Z. Phys. C **69** (1995) 77–88, arXiv:9505225 [hep-ph].

[43] K. G. Chetyrkin, B. A. Kniehl, and M. Steinhauser, *Hadronic Higgs decay to order α_s^4*, Phys. Rev. Lett. **79** (1997) 353–356, arXiv:9705240 [hep-ph].

[44] M. Krämer, E. Laenen, and M. Spira, *Soft gluon radiation in Higgs boson production at the LHC*, Nucl. Phys. B **511** (1998) 523–549, arXiv:9611272 [hep-ph].

[45] Y. Schröder and M. Steinhauser, *Four-loop decoupling relations for the strong coupling*, JHEP **01** (2006) 051, arXiv:0512058 [hep-ph].

[46] P. A. Baikov, K. G. Chetyrkin, and J. H. Kühn, *Five-Loop Running of the QCD coupling constant*, Phys. Rev. Lett. **118** (2017) 082002, `arXiv:1606.08659 [hep-ph]`.

[47] M. Spira, *Effective Multi-Higgs Couplings to Gluons*, JHEP **10** (2016) 026, `arXiv:1607.05548 [hep-ph]`.

[48] M. Gerlach, F. Herren, and M. Steinhauser, *Wilson coefficients for Higgs boson production and decoupling relations to* $\mathcal{O}\left(\alpha_s^4\right)$, `arXiv:1809.06787 [hep-ph]`.

[49] G. Altarelli and G. Parisi, *Asymptotic Freedom in Parton Language*, Nucl. Phys. B **126** (1977) 298–318.

[50] D. Y. Shao, C. S. Li, H. T. Li, and J. Wang, *Threshold resummation effects in Higgs boson pair production at the LHC*, JHEP **07** (2013) 169, `arXiv:1301.1245 [hep-ph]`.

[51] D. de Florian and J. Mazzitelli, *Higgs pair production at next-to-next-to-leading logarithmic accuracy at the LHC*, JHEP **09** (2015) 053, `arXiv:1505.07122 [hep-ph]`.

[52] J. Alwall, R. Frederix, S. Frixione, V. Hirschi, F. Maltoni, et al., *The automated computation of tree-level and next-to-leading order differential cross sections, and their matching to parton shower simulations*, JHEP **1407** (2014) 079, `arXiv:1405.0301 [hep-ph]`.

[53] J. Grigo, J. Hoff, K. Melnikov, and M. Steinhauser, *On the Higgs boson pair production at the LHC*, Nucl. Phys. B **875** (2013) 1–17, `arXiv:1305.7340 [hep-ph]`.

[54] J. Grigo, J. Hoff, and M. Steinhauser, *Higgs boson pair production: top quark mass effects at NLO and NNLO*, Nucl. Phys. B **900** (2015) 412–430, `arXiv:1508.00909 [hep-ph]`.

[55] G. Degrassi, P. P. Giardino, and R. Gröber, *On the two-loop virtual QCD corrections to Higgs boson pair production in the Standard Model*, Eur. Phys. J. C **76** (2016) 411, `arXiv:1603.00385 [hep-ph]`.

[56] G. Heinrich, S. P. Jones, M. Kerner, G. Luisoni, and E. Vryonidou, *NLO predictions for Higgs boson pair production with full top quark mass dependence matched to parton showers*, JHEP **08** (2017) 088, `arXiv:1703.09252 [hep-ph]`.

[57] S. Jones and S. Kuttimalai, *Parton Shower and NLO-Matching uncertainties in Higgs Boson Pair Production*, JHEP **02** (2018) 176, `arXiv:1711.03319 [hep-ph]`.

[58] L. F. Richardson, *The approximate arithmetical solution by finite differences of physical problems including differential equations, with an application to the stresses in a masonry dam*, Philosophical Transactions of the Royal Society A **210** (1911) 307.

[59] J. Fleischer and O. V. Tarasov, *Calculation of Feynman diagrams from their small momentum expansion*, Z. Phys. C **64** (1994) 413–426, `arXiv:9403230 [hep-ph]`.

[60] R. Gröber, A. Maier, and T. Rauh, *Reconstruction of top-quark mass effects in Higgs pair production and other gluon-fusion processes*, JHEP **03** (2018) 020, `arXiv:1709.07799 [hep-ph]`.

[61] R. Bonciani, G. Degrassi, P. P. Giardino, and R. Gröber, *Analytical Method for Next-to-Leading-Order QCD Corrections to Double-Higgs Production*, Phys. Rev. Lett. **121** (2018) 162003, `arXiv:1806.11564 [hep-ph]`.

[62] J. Davies, G. Mishima, M. Steinhauser, and D. Wellmann, *Double-Higgs boson production in the high-energy limit: planar master integrals*, JHEP **03** (2018) 048, `arXiv:1801.09696 [hep-ph]`.

[63] J. Davies, G. Mishima, M. Steinhauser, and D. Wellmann, *Double Higgs boson production at NLO in the high-energy limit: complete analytic results*, JHEP **01** (2019) 176, `arXiv:1811.05489 [hep-ph]`.

[64] X. Xu and L. L. Yang, *Towards a new approximation for pair-production and associated-production of the Higgs boson*, JHEP **01** (2019) 211, `arXiv:1810.12002 [hep-ph]`.

[65] D. De Florian and J. Mazzitelli, *Soft gluon resummation for Higgs boson pair production including finite M_t effects*, JHEP **08** (2018) 156, `arXiv:1807.03704 [hep-ph]`.

[66] ATLAS Collaboration, *Combination of searches for Higgs boson pairs in pp collisions at $\sqrt{s} = 13$ TeV with the ATLAS detector*, `arXiv:1906.02025 [hep-ex]`. Submitted to PLB.

[67] CMS Collaboration, *Combination of searches for Higgs boson pair production in proton-proton collisions at $\sqrt{s} = 13$ TeV*, Phys. Rev. Lett. **122** (2019) 121803, `arXiv:1811.09689 [hep-ex]`.

[68] G. Heinrich, S. P. Jones, M. Kerner, G. Luisoni, and L. Scyboz, *Probing the trilinear Higgs boson coupling in di-Higgs production at NLO QCD including parton shower effects*, JHEP **06** (2019) 066, `arXiv:1903.08137 [hep-ph]`.

[69] G. Buchalla, M. Capozi, A. Celis, G. Heinrich, and L. Scyboz, *Higgs boson pair production in non-linear Effective Field Theory with full m_t-dependence at NLO QCD*, JHEP **09** (2018) 057, `arXiv:1806.05162 [hep-ph]`.

[70] P. Nason, *A New method for combining NLO QCD with shower Monte Carlo algorithms*, JHEP **11** (2004) 040, `arXiv:0409146 [hep-ph]`.

[71] S. Frixione, P. Nason, and C. Oleari, *Matching NLO QCD computations with Parton Shower simulations: the POWHEG method*, JHEP **11** (2007) 070, `arXiv:0709.2092 [hep-ph]`.

[72] S. Alioli, P. Nason, C. Oleari, and E. Re, *A general framework for implementing NLO calculations in shower Monte Carlo programs: the POWHEG BOX*, JHEP **06** (2010) 043, `arXiv:1002.2581 [hep-ph]`.

[73] J. Butterworth et al., *PDF4LHC recommendations for LHC Run II*, J. Phys. G **43** (2016) 023001, `arXiv:1510.03865 [hep-ph]`.

[74] S. Dulat, T.-J. Hou, J. Gao, M. Guzzi, J. Huston, P. Nadolsky, J. Pumplin, C. Schmidt, D. Stump, and C. P. Yuan, *New parton distribution functions from a global analysis of quantum chromodynamics*, Phys. Rev. D **93** (2016) 033006, `arXiv:1506.07443 [hep-ph]`.

[75] L. A. Harland-Lang, A. D. Martin, P. Motylinski, and R. S. Thorne, *Parton distributions in the LHC era: MMHT 2014 PDFs*, Eur. Phys. J. C **75** (2015) 204, `arXiv:1412.3989 [hep-ph]`.

[76] NNPDF Collaboration, *Parton distributions for the LHC Run II*, JHEP **04** (2015) 040, `arXiv:1410.8849 [hep-ph]`.

[77] A. Buckley, J. Ferrando, S. Lloyd, K. Nordström, B. Page, M. Rüfenacht, M. Schönherr, and G. Watt, *LHAPDF6: parton density access in the LHC precision era*, Eur. Phys. J. C **75** (2015) 132, arXiv:1412.7420 [hep-ph].

[78] M. Cacciari, G. P. Salam, and G. Soyez, *The anti-k_T jet clustering algorithm*, JHEP **04** (2008) 063, arXiv:0802.1189 [hep-ph].

[79] M. Cacciari and G. P. Salam, *Dispelling the N^3 myth for the k_t jet-finder*, Phys. Lett. B **641** (2006) 57–61, arXiv:0512210 [hep-ph].

[80] M. Cacciari, G. P. Salam, and G. Soyez, *FastJet User Manual*, Eur. Phys. J. C **72** (2012) 1896, arXiv:1111.6097 [hep-ph].

[81] R. Gröber, M. Mühlleitner, M. Spira, and J. Streicher, *NLO QCD Corrections to Higgs Pair Production including Dimension-6 Operators*, JHEP **09** (2015) 092, arXiv:1504.06577 [hep-ph].

[82] D. de Florian, I. Fabre, and J. Mazzitelli, *Higgs boson pair production at NNLO in QCD including dimension 6 operators*, JHEP **10** (2017) 215, arXiv:1704.05700 [hep-ph].

[83] *Les Houches 2019: Physics at TeV Colliders Standard Model Working Group Report*, in preparation.

[84] V. Hirschi and O. Mattelaer, *Automated event generation for loop-induced processes*, JHEP **10** (2015) 146, arXiv:1507.00020 [hep-ph].

[85] T. Gleisberg, S. Hoeche, F. Krauss, M. Schonherr, S. Schumann, F. Siegert, and J. Winter, *Event generation with SHERPA 1.1*, JHEP **02** (2009) 007, arXiv:0811.4622 [hep-ph].

[86] J. R. Andersen et al., *Les Houches 2017: Physics at TeV Colliders Standard Model Working Group Report*, arXiv:1803.07977 [hep-ph].

[87] S. Alioli, P. Nason, C. Oleari, and E. Re, *NLO Higgs boson production via gluon fusion matched with shower in POWHEG*, JHEP **04** (2009) 002, arXiv:0812.0578 [hep-ph].

[88] E. Bagnaschi, R. V. Harlander, H. Mantler, A. Vicini, and M. Wiesemann, *Resummation ambiguities in the Higgs transverse-momentum spectrum in the Standard Model and beyond*, JHEP **01** (2016) 090, arXiv:1510.08850 [hep-ph].

[89] S. Alioli, F. Caola, G. Luisoni, and R. Röntsch, *ZZ production in gluon fusion at NLO matched to parton-shower*, Phys. Rev. D **95** (2017) 034042, arXiv:1609.09719 [hep-ph].

[90] S. Frixione and B. R. Webber, *Matching NLO QCD computations and parton shower simulations*, JHEP **06** (2002) 029, arXiv:0204244 [hep-ph].

[91] G. Ferrera and J. Pires, *Transverse-momentum resummation for Higgs boson pair production at the LHC with top-quark mass effects*, JHEP **02** (2017) 139, arXiv:1609.01691 [hep-ph].

[92] T. Sjostrand, S. Mrenna, and P. Z. Skands, *A Brief Introduction to PYTHIA 8.1*, Comput.Phys.Commun. **178** (2008) 852–867, arXiv:0710.3820 [hep-ph].

[93] T. Sjostrand, S. Ask, J. R. Christiansen, R. Corke, N. Desai, P. Ilten, S. Mrenna, S. Prestel, C. O. Rasmussen, and P. Z. Skands, *An Introduction to PYTHIA 8.2*, Comput. Phys. Commun. **191** (2015) 159–177, arXiv:1410.3012 [hep-ph].

[94] S. Schumann and F. Krauss, *A Parton Shower Algorithm Based on Catani-Seymour Dipole Factorisation*, JHEP **0803** (2008) 038, `arXiv:0709.1027 [hep-ph]`.

[95] S. Höche and S. Prestel, *The midpoint between dipole and parton showers*, Eur. Phys. J. C **75** (2015) 461, `arXiv:1506.05057 [hep-ph]`.

[96] R. Corke and T. Sjostrand, *Improved Parton Showers at Large Transverse Momenta*, Eur. Phys. J. C **69** (2010) 1–18, `arXiv:1003.2384 [hep-ph]`.

[97] R. Corke and T. Sjostrand, *Interleaved Parton Showers and Tuning Prospects*, JHEP **03** (2011) 032, `arXiv:1011.1759 [hep-ph]`.

[98] B. Cabouat and T. Sjostrand, *Some Dipole Shower Studies*, Eur. Phys. J. C **78** (2018) 226, `arXiv:1710.00391 [hep-ph]`.

[99] S. Weinberg, *Phenomenological Lagrangians*, Physica **A96** (1979) no. 1-2, 327–340.

[100] M. Carena and H. E. Haber, *Higgs Boson Theory and Phenomenology*, Prog. Part. Nucl. Phys. **50** (2003) 63–152, `arXiv:0208209 [hep-ph]`.

[101] R. Contino, *The Higgs as a Composite Nambu-Goldstone Boson,* in *Physics of the large and the small, TASI 09, proceedings of the Theoretical Advanced Study Institute in Elementary Particle Physics, Boulder, Colorado, USA, 1-26 June 2009*, pp. 235–306. 2011. `arXiv:1005.4269 [hep-ph]`.

[102] G. Panico and A. Wulzer, *The Composite Nambu-Goldstone Higgs*, Lect. Notes Phys. **913** (2016) pp.1–316, `arXiv:1506.01961 [hep-ph]`.

[103] B. Grzadkowski, M. Iskrzynski, M. Misiak, and J. Rosiek, *Dimension-Six Terms in the Standard Model Lagrangian*, JHEP **10** (2010) 085, `arXiv:1008.4884 [hep-ph]`.

[104] G. F. Giudice, C. Grojean, A. Pomarol, and R. Rattazzi, *The Strongly-Interacting Light Higgs*, JHEP **06** (2007) 045, `arXiv:0703164 [hep-ph]`.

[105] R. Contino, M. Ghezzi, C. Grojean, M. Muhlleitner, and M. Spira, *Effective Lagrangian for a light Higgs-like scalar*, JHEP **07** (2013) 035, `arXiv:1303.3876 [hep-ph]`.

[106] W. Buchmuller and D. Wyler, *Effective Lagrangian Analysis of New Interactions and Flavor Conservation*, Nucl. Phys. B **268** (1986) 621–653.

[107] F. Goertz, A. Papaefstathiou, L. L. Yang, and J. Zurita, *Higgs boson pair production in the D=6 extension of the SM*, JHEP **04** (2015) 167, `arXiv:1410.3471 [hep-ph]`.

[108] A. Azatov, R. Contino, G. Panico, and M. Son, *Effective field theory analysis of double Higgs boson production via gluon fusion*, Phys. Rev. D **92** (2015) 035001, `arXiv:1502.00539 [hep-ph]`.

[109] A. Carvalho, M. Dall'Osso, P. De Castro Manzano, T. Dorigo, F. Goertz, M. Gouzevich, and M. Tosi, *Analytical parametrization and shape classification of anomalous HH production in the EFT approach*, `arXiv:1608.06578 [hep-ph]`.

[110] R. Contino, C. Grojean, D. Pappadopulo, R. Rattazzi, and A. Thamm, *Strong Higgs Interactions at a Linear Collider*, JHEP **02** (2014) 006, `arXiv:1309.7038 [hep-ph]`.

[111] S. Di Vita, C. Grojean, G. Panico, M. Riembau, and T. Vantalon, *A global view on the Higgs self-coupling*, JHEP **09** (2017) 069, `arXiv:1704.01953 [hep-ph]`.

[112] S. Di Vita, G. Durieux, C. Grojean, J. Gu, Z. Liu, G. Panico, M. Riembau, and T. Vantalon, *A global view on the Higgs self-coupling at lepton colliders*, JHEP **02** (2018) 178, `arXiv:1711.03978 [hep-ph]`.

[113] M. E. Peskin and T. Takeuchi, *A New constraint on a strongly interacting Higgs sector*, Phys. Rev. Lett. **65** (1990) 964–967.

[114] A. Falkowski and F. Riva, *Model-independent precision constraints on dimension-6 operators*, JHEP **02** (2015) 039, `arXiv:1411.0669 [hep-ph]`.

[115] ATLAS Collaboration, *Combined measurements of Higgs boson production and decay using up to 80 fb^{-1} of proton–proton collision data at $\sqrt{s}$ = 13 TeV collected with the ATLAS experiment*, ATLAS-CONF-2018-031, 2018.

[116] CMS Collaboration, *Combined measurements of Higgs boson couplings in proton-proton collisions at $\sqrt{s}$ = 13 TeV*, Eur. Phys. J. C **79** (2019) 421, `arXiv:1809.10733 [hep-ex]`.

[117] V. A. Kuzmin, V. A. Rubakov, and M. E. Shaposhnikov, *On the Anomalous Electroweak Baryon Number Nonconservation in the Early Universe*, Phys. Lett. B **155** (1985) 36.

[118] M. E. Shaposhnikov, *Possible Appearance of the Baryon Asymmetry of the Universe in an Electroweak Theory*, JETP Lett. **44** (1986) 465–468. [Pisma Zh. Eksp. Teor. Fiz.44,364(1986)].

[119] C. Grojean, G. Servant, and J. D. Wells, *First-order electroweak phase transition in the standard model with a low cutoff*, Phys. Rev. D **71** (2005) 036001, `arXiv:0407019 [hep-ph]`.

[120] A. Noble and M. Perelstein, *Higgs self-coupling as a probe of electroweak phase transition*, Phys. Rev. D **78** (2008) 063518, `arXiv:0711.3018 [hep-ph]`.

[121] D. E. Morrissey and M. J. Ramsey-Musolf, *Electroweak baryogenesis*, New J. Phys. **14** (2012) 125003, `arXiv:1206.2942 [hep-ph]`.

[122] A. Katz and M. Perelstein, *Higgs Couplings and Electroweak Phase Transition*, JHEP **07** (2014) 108, `arXiv:1401.1827 [hep-ph]`.

[123] P. Huang, A. J. Long, and L.-T. Wang, *Probing the Electroweak Phase Transition with Higgs Factories and Gravitational Waves*, Phys. Rev. D **94** (2016) 075008, `arXiv:1608.06619 [hep-ph]`.

[124] A. Falkowski and R. Rattazzi, *Which EFT*, `arXiv:1902.05936 [hep-ph]`.

[125] F. Maltoni, E. Vryonidou, and C. Zhang, *Higgs production in association with a top-antitop pair in the Standard Model Effective Field Theory at NLO in QCD*, JHEP **10** (2016) 123, `arXiv:1607.05330 [hep-ph]`.

[126] M. McCullough, *An Indirect Model-Dependent Probe of the Higgs Self-Coupling*, Phys. Rev. D **90** (2014) 015001, `arXiv:1312.3322 [hep-ph]`. [Erratum: Phys. Rev.D92,no.3,039903(2015)].

[127] M. Gorbahn and U. Haisch, *Indirect probes of the trilinear Higgs coupling: $gg \to h$ and $h \to \gamma\gamma$*, JHEP **10** (2016) 094, `arXiv:1607.03773 [hep-ph]`.

[128] G. Degrassi, P. P. Giardino, F. Maltoni, and D. Pagani, *Probing the Higgs self coupling via single Higgs production at the LHC*, JHEP **12** (2016) 080, `arXiv:1607.04251 [hep-ph]`.

[129] W. Bizon, M. Gorbahn, U. Haisch, and G. Zanderighi, *Constraints on the trilinear Higgs coupling from vector boson fusion and associated Higgs production at the LHC*, JHEP **07** (2017) 083, `arXiv:1610.05771 [hep-ph]`.

[130] T. Barklow, K. Fujii, S. Jung, M. E. Peskin, and J. Tian, *Model-Independent Determination of the Triple Higgs Coupling at e+e- Colliders*, Phys. Rev. D **97** (2018) 053004, `arXiv:1708.09079 [hep-ph]`.

[131] F. Maltoni, D. Pagani, A. Shivaji, and X. Zhao, *Trilinear Higgs coupling determination via single-Higgs differential measurements at the LHC*, Eur. Phys. J. C **77** (2017) 887, `arXiv:1709.08649 [hep-ph]`.

[132] F. Maltoni, D. Pagani, and X. Zhao, *Constraining the Higgs self-couplings at e^+e^- colliders*, JHEP **07** (2018) 087, `arXiv:1802.07616 [hep-ph]`.

[133] CMS Collaboration, *Constraints on the Higgs boson self-coupling from ttH+tH, H→ γγ differential measurements at the HL-LHC*, CMS-PAS-FTR-18-020, 2018.

[134] ATLAS Collaboration, *Constraint of the Higgs boson self-coupling from Higgs boson differential production and decay measurements*, ATL-PHYS-PUB-2019-009, 2019.

[135] A. Falkowski, *Higgs Basis: Proposal for an EFT basis choice for LHC HXSWG*, . `https://cds.cern.ch/record/2001958`.

[136] P. Sikivie, L. Susskind, M. B. Voloshin, and V. I. Zakharov, *Isospin Breaking in Technicolor Models*, Nucl. Phys. B **173** (1980) 189–207.

[137] J. Gasser and H. Leutwyler, *Chiral Perturbation Theory to One Loop*, Annals Phys. **158** (1984) 142.

[138] J. Gasser and H. Leutwyler, *Chiral Perturbation Theory: Expansions in the Mass of the Strange Quark*, Nucl. Phys. B **250** (1985) 465–516.

[139] G. Buchalla, O. Catà, and C. Krause, *Complete Electroweak Chiral Lagrangian with a Light Higgs at NLO*, Nucl. Phys. B **880** (2014) 552–573, `arXiv:1307.5017 [hep-ph]`. [Erratum: Nucl. Phys.B913,475(2016)].

[140] G. Buchalla, O. Cata, A. Celis, and C. Krause, *Note on Anomalous Higgs-Boson Couplings in Effective Field Theory*, Phys. Lett. B **750** (2015) 298–301, `arXiv:1504.01707 [hep-ph]`.

[141] J. de Blas, O. Eberhardt, and C. Krause, *Current and Future Constraints on Higgs Couplings in the Nonlinear Effective Theory*, JHEP **07** (2018) 048, `arXiv:1803.00939 [hep-ph]`.

[142] A. Delgado, K. Lane, and A. Martin, *A Light Scalar in Low-Scale Technicolor*, Phys. Lett. B **696** (2011) 482–486, `arXiv:1011.0745 [hep-ph]`.

[143] W. D. Goldberger, B. Grinstein, and W. Skiba, *Distinguishing the Higgs boson from the dilaton at the Large Hadron Collider*, Phys. Rev. Lett. **100** (2008) 111802, `arXiv:0708.1463 [hep-ph]`.

[144] K. Agashe, R. Contino, and A. Pomarol, *The Minimal composite Higgs model*, Nucl. Phys. B **719** (2005) 165–187, `arXiv:0412089 [hep-ph]`.

[145] K. Haba, S. Matsuzaki, and K. Yamawaki, *Holographic Techni-dilaton, or Conformal Higgs,* in *Strong coupling gauge theories in LHC era. Proceedings, International Workshop, SCGT 09, Nagoya, Japan, December 8-11, 2009*, pp. 401–403. 2011. `arXiv:1003.2841 [hep-ph]`.

[146] J. Galloway, M. A. Luty, Y. Tsai, and Y. Zhao, *Induced Electroweak Symmetry Breaking and Supersymmetric Naturalness*, Phys. Rev. D **89** (2014) 075003, `arXiv:1306.6354 [hep-ph]`.

[147] S. Chang, J. Galloway, M. Luty, E. Salvioni, and Y. Tsai, *Phenomenology of Induced Electroweak Symmetry Breaking*, JHEP **03** (2015) 017, `arXiv:1411.6023 [hep-ph]`.

[148] ATLAS Collaboration, *Search for pair production of Higgs bosons in the $b\bar{b}b\bar{b}$ final state using proton-proton collisions at $\sqrt{s} = 13$ TeV with the ATLAS detector*, JHEP **01** (2019) 030, `arXiv:1804.06174 [hep-ex]`.

[149] ATLAS Collaboration, *Search for Higgs boson pair production in the $\gamma\gamma b\bar{b}$ final state with 13 TeV pp collision data collected by the ATLAS experiment*, JHEP **11** (2018) 040, `arXiv:1807.04873 [hep-ex]`.

[150] ATLAS Collaboration, *Search for Resonant and Nonresonant Higgs Boson Pair Production in the $b\bar{b}\tau^+\tau^-$ Decay Channel in pp Collisions at $\sqrt{s} = 13$ TeV with the ATLAS Detector*, Phys. Rev. Lett. **121** (2018) 191801, `arXiv:1808.00336 [hep-ex]`.

[151] V. Barger, T. Han, P. Langacker, B. McElrath, and P. Zerwas, *Effects of genuine dimension-six Higgs operators*, Phys. Rev. D **67** (2003) 115001, `arXiv:0301097 [hep-ph]`.

[152] L. Di Luzio, R. Grober, and M. Spannowsky, *Maxi-sizing the trilinear Higgs self-coupling: how large could it be?*, Eur. Phys. J. C **77** (2017) 788, `arXiv:1704.02311 [hep-ph]`.

[153] C. P. Burgess, V. Di Clemente, and J. R. Espinosa, *Effective operators and vacuum instability as heralds of new physics*, JHEP **01** (2002) 041, `arXiv:0201160 [hep-ph]`.

[154] J. Baglio and C. Weiland, *The triple Higgs coupling: A new probe of low-scale seesaw models*, JHEP **04** (2017) 038, `arXiv:1612.06403 [hep-ph]`.

[155] L. Di Luzio, G. Isidori, and G. Ridolfi, *Stability of the electroweak ground state in the Standard Model and its extensions*, Phys. Lett. B **753** (2016) 150–160, `arXiv:1509.05028 [hep-ph]`.

[156] F. Goertz, J. F. Kamenik, A. Katz, and M. Nardecchia, *Indirect Constraints on the Scalar Di-Photon Resonance at the LHC*, JHEP **05** (2016) 187, `arXiv:1512.08500 [hep-ph]`.

[157] L. Di Luzio, J. F. Kamenik, and M. Nardecchia, *Implications of perturbative unitarity for scalar di-boson resonance searches at LHC*, Eur. Phys. J. C **77** (2017) 30, `arXiv:1604.05746 [hep-ph]`.

[158] S. Borowka, C. Duhr, F. Maltoni, D. Pagani, A. Shivaji, and X. Zhao, *Probing the scalar potential via double Higgs boson production at hadron colliders*, JHEP **04** (2019) 016, `arXiv:1811.12366 [hep-ph]`.

[159] S. Chang and M. A. Luty, *The Higgs Trilinear Coupling and the Scale of New Physics*, `arXiv:1902.05556 [hep-ph]`.

[160] F. Goertz, *Electroweak Symmetry Breaking without the μ^2 Term*, Phys. Rev. D **94** (2016) 015013, `arXiv:1504.00355 [hep-ph]`.

[161] D. Lopez-Val and T. Robens, *Δr and the W-boson mass in the singlet extension of the standard model*, Phys. Rev. D **90** (2014) 114018, arXiv:1406.1043 [hep-ph].

[162] J. E. Camargo-Molina, B. O'Leary, W. Porod, and F. Staub, **Vevacious***: A Tool For Finding The Global Minima Of One-Loop Effective Potentials With Many Scalars*, Eur. Phys. J. C **73** (2013) 2588, arXiv:1307.1477 [hep-ph].

[163] F. Staub, *SARAH*, arXiv:0806.0538 [hep-ph].

[164] F. Staub, *SARAH 4 : A tool for (not only SUSY) model builders*, Comput. Phys. Commun. **185** (2014) 1773–1790, arXiv:1309.7223 [hep-ph].

[165] R. S. Gupta, H. Rzehak, and J. D. Wells, *How well do we need to measure the Higgs boson mass and self-coupling?*, Phys. Rev. D **88** (2013) 055024, arXiv:1305.6397 [hep-ph].

[166] A. Dobado, M. J. Herrero, W. Hollik, and S. Penaranda, *Selfinteractions of the lightest MSSM Higgs boson in the large pseudoscalar mass limit*, Phys. Rev. D **66** (2002) 095016, arXiv:0208014 [hep-ph].

[167] M. Carena, J. R. Espinosa, M. Quiros, and C. E. M. Wagner, *Analytical expressions for radiatively corrected Higgs masses and couplings in the MSSM*, Phys. Lett. B **355** (1995) 209–221, arXiv:9504316 [hep-ph].

[168] F. Goertz, *Indirect Handle on the Down-Quark Yukawa Coupling*, Phys. Rev. Lett. **113** (2014) 261803, arXiv:1406.0102 [hep-ph].

[169] M. J. Dolan, C. Englert, and M. Spannowsky, *Higgs self-coupling measurements at the LHC*, JHEP **10** (2012) 112, arXiv:1206.5001 [hep-ph].

[170] F. Goertz, A. Papaefstathiou, L. L. Yang, and J. Zurita, *Higgs Boson self-coupling measurements using ratios of cross sections*, JHEP **06** (2013) 016, arXiv:1301.3492 [hep-ph].

[171] A. Carvalho, F. Goertz, K. Mimasu, M. Gouzevitch, and A. Aggarwal, *On the reinterpretation of non-resonant searches for Higgs boson pairs*, arXiv:1710.08261 [hep-ph].

[172] G. Degrassi, M. Fedele, and P. P. Giardino, *Constraints on the trilinear Higgs self coupling from precision observables*, JHEP **04** (2017) 155, arXiv:1702.01737 [hep-ph].

[173] G. D. Kribs, A. Maier, H. Rzehak, M. Spannowsky, and P. Waite, *Electroweak oblique parameters as a probe of the trilinear Higgs boson self-interaction*, Phys. Rev. D **95** (2017) 093004, arXiv:1702.07678 [hep-ph].

[174] M. Cepeda et al., *Higgs Physics at the HL-LHC and HE-LHC*, arXiv:1902.00134 [hep-ph].

[175] W. Bizoń, U. Haisch, and L. Rottoli, *Constraints on the quartic Higgs self-coupling from double-Higgs production at future hadron colliders*, arXiv:1810.04665 [hep-ph].

[176] M. Gorbahn and U. Haisch, *Two-loop amplitudes for Higgs plus jet production involving a modified trilinear Higgs coupling*, JHEP **04** (2019) 062, arXiv:1902.05480 [hep-ph].

[177] ATLAS, CMS Collaboration, *Measurements of the Higgs boson production and decay rates and constraints on its couplings from a combined ATLAS and CMS analysis of the LHC pp collision data at $\sqrt{s} = 7$ and 8 TeV*, JHEP **08** (2016) 045, arXiv:1606.02266 [hep-ex].

[178] A. Carvalho, M. Dall'Osso, T. Dorigo, F. Goertz, C. A. Gottardo, and M. Tosi, *Higgs Pair Production: Choosing Benchmarks With Cluster Analysis*, JHEP **04** (2016) 126, `arXiv:1507.02245 [hep-ph]`.

[179] A. Barrientos Bendezu and B. A. Kniehl, *Pair production of neutral Higgs bosons at the CERN large hadron collider*, Phys. Rev. D **64** (2001) 035006, `arXiv:0103018 [hep-ph]`.

[180] B. Batell, M. McCullough, D. Stolarski, and C. B. Verhaaren, *Putting a Stop to di-Higgs Modifications*, JHEP **09** (2015) 216, `arXiv:1508.01208 [hep-ph]`.

[181] A. Agostini, G. Degrassi, R. Grober, and P. Slavich, *NLO-QCD corrections to Higgs pair production in the MSSM*, JHEP **04** (2016) 106, `arXiv:1601.03671 [hep-ph]`.

[182] M. Gillioz, R. Grober, C. Grojean, M. Muhlleitner, and E. Salvioni, *Higgs Low-Energy Theorem (and its corrections) in Composite Models*, JHEP **10** (2012) 004, `arXiv:1206.7120 [hep-ph]`.

[183] R. Grober, M. Muhlleitner, and M. Spira, *Signs of Composite Higgs Pair Production at Next-to-Leading Order*, JHEP **06** (2016) 080, `arXiv:1602.05851 [hep-ph]`.

[184] A. Azatov, C. Grojean, A. Paul, and E. Salvioni, *Resolving gluon fusion loops at current and future hadron colliders*, JHEP **09** (2016) 123, `arXiv:1608.00977 [hep-ph]`.

[185] H. Davoudiasl, R. Kitano, T. Li, and H. Murayama, *The New minimal standard model*, Phys. Lett. B **609** (2005) 117–123, `arXiv:0405097 [hep-ph]`.

[186] R. Schabinger and J. D. Wells, *A Minimal spontaneously broken hidden sector and its impact on Higgs boson physics at the large hadron collider*, Phys. Rev. D **72** (2005) 093007, `arXiv:0509209 [hep-ph]`.

[187] B. Patt and F. Wilczek, *Higgs-field portal into hidden sectors*, `arXiv:0605188 [hep-ph]`.

[188] V. Barger, P. Langacker, M. McCaskey, M. J. Ramsey-Musolf, and G. Shaughnessy, *LHC Phenomenology of an Extended Standard Model with a Real Scalar Singlet*, Phys. Rev. D **77** (2008) 035005, `arXiv:0706.4311 [hep-ph]`.

[189] M. Bowen, Y. Cui, and J. D. Wells, *Narrow trans-TeV Higgs bosons and H→ hh decays: Two LHC search paths for a hidden sector Higgs boson*, JHEP **03** (2007) 036, `arXiv:0701035 [hep-ph]`.

[190] M. J. Dolan, C. Englert, and M. Spannowsky, *New Physics in LHC Higgs boson pair production*, Phys. Rev. D **87** (2013) 055002, `arXiv:1210.8166 [hep-ph]`.

[191] G. M. Pruna and T. Robens, *The Higgs Singlet extension parameter space in the light of the LHC discovery*, Phys. Rev. D **88** (2013) 115012, `arXiv:1303.1150 [hep-ph]`.

[192] B. Cooper, N. Konstantinidis, L. Lambourne, and D. Wardrope, *Boosted hh → b̄bb̄b: A new topology in searches for TeV-scale resonances at the LHC*, Phys. Rev. D **88** (2013) 114005, `arXiv:1307.0407 [hep-ex]`.

[193] J. M. No and M. Ramsey-Musolf, *Probing the Higgs Portal at the LHC Through Resonant di-Higgs Production*, Phys. Rev. D **89** (2014) 095031, `arXiv:1310.6035 [hep-ph]`.

[194] C.-Y. Chen, S. Dawson, and I. M. Lewis, *Exploring resonant di-Higgs boson production in the Higgs singlet model*, Phys. Rev. D **91** (2015) 035015, `arXiv:1410.5488 [hep-ph]`.

[195] V. Martín Lozano, J. M. Moreno, and C. B. Park, *Resonant Higgs boson pair production in the* $hh \to b\bar{b}\,WW \to b\bar{b}\ell^+\nu\ell^-\bar{\nu}$ *decay channel*, JHEP **08** (2015) 004, arXiv:1501.03799 [hep-ph].

[196] S. Dawson and I. M. Lewis, *NLO corrections to double Higgs boson production in the Higgs singlet model*, Phys. Rev. D **92** (2015) 094023, arXiv:1508.05397 [hep-ph].

[197] S. I. Godunov, A. N. Rozanov, M. I. Vysotsky, and E. V. Zhemchugov, *Extending the Higgs sector: an extra singlet*, Eur. Phys. J. C **76** (2016) 1, arXiv:1503.01618 [hep-ph].

[198] L.-C. Lü, C. Du, Y. Fang, H.-J. He, and H. Zhang, *Searching heavier Higgs boson via di-Higgs production at LHC Run-2*, Phys. Lett. B **755** (2016) 509–522, arXiv:1507.02644 [hep-ph].

[199] T. Robens and T. Stefaniak, *Status of the Higgs Singlet Extension of the Standard Model after LHC Run 1*, Eur. Phys. J. C **75** (2015) 104, arXiv:1501.02234 [hep-ph].

[200] F. Bojarski, G. Chalons, D. Lopez-Val, and T. Robens, *Heavy to light Higgs boson decays at NLO in the Singlet Extension of the Standard Model*, JHEP **02** (2016) 147, arXiv:1511.08120 [hep-ph].

[201] T. Robens and T. Stefaniak, *LHC Benchmark Scenarios for the Real Higgs Singlet Extension of the Standard Model*, Eur. Phys. J. C **76** (2016) 268, arXiv:1601.07880 [hep-ph].

[202] K. Nakamura, K. Nishiwaki, K.-y. Oda, S. C. Park, and Y. Yamamoto, *Di-higgs enhancement by neutral scalar as probe of new colored sector*, Eur. Phys. J. C **77** (2017) 273, arXiv:1701.06137 [hep-ph].

[203] T. Huang, J. M. No, L. Pernié, M. Ramsey-Musolf, A. Safonov, M. Spannowsky, and P. Winslow, *Resonant di-Higgs boson production in the* $b\bar{b}WW$ *channel: Probing the electroweak phase transition at the LHC*, Phys. Rev. D **96** (2017) 035007, arXiv:1701.04442 [hep-ph].

[204] J. Chang, C.-R. Chen, and C.-W. Chiang, *Higgs boson pair productions in the Georgi-Machacek model at the LHC*, JHEP **03** (2017) 137, arXiv:1701.06291 [hep-ph].

[205] I. M. Lewis and M. Sullivan, *Benchmarks for Double Higgs Production in the Singlet Extended Standard Model at the LHC*, Phys. Rev. D **96** (2017) 035037, arXiv:1701.08774 [hep-ph].

[206] S. Dawson and M. Sullivan, *Enhanced di-Higgs boson production in the complex Higgs singlet model*, Phys. Rev. D **97** (2018) 015022, arXiv:1711.06683 [hep-ph].

[207] A. Alves, T. Ghosh, H.-K. Guo, K. Sinha, and D. Vagie, *Collider and Gravitational Wave Complementarity in Exploring the Singlet Extension of the Standard Model*, JHEP **04** (2019) 052, arXiv:1812.09333 [hep-ph].

[208] A. Alves, T. Ghosh, H.-K. Guo, and K. Sinha, *Resonant Di-Higgs Production at Gravitational Wave Benchmarks: A Collider Study using Machine Learning*, JHEP **12** (2018) 070, arXiv:1808.08974 [hep-ph].

[209] M. Carena, Z. Liu, and M. Riembau, *Probing the electroweak phase transition via enhanced di-Higgs boson production*, Phys. Rev. D **97** (2018) 095032, arXiv:1801.00794 [hep-ph].

[210] D. O'Connell, M. J. Ramsey-Musolf, and M. B. Wise, *Minimal Extension of the Standard Model Scalar Sector*, Phys. Rev. D **75** (2007) 037701, arXiv:0611014 [hep-ph].

[211] S. Dawson and I. M. Lewis, *Singlet Model Interference Effects with High Scale UV Physics*, Phys. Rev. D **95** (2017) 015004, arXiv:1605.04944 [hep-ph].

[212] M. Bauer, A. Butter, J. Gonzalez-Fraile, T. Plehn, and M. Rauch, *Learning from a Higgs-like scalar resonance*, Phys. Rev. D **95** (2017) 055011, arXiv:1607.04562 [hep-ph].

[213] M. Chala, G. Durieux, C. Grojean, L. de Lima, and O. Matsedonskyi, *Minimally extended SILH*, JHEP **06** (2017) 088, arXiv:1703.10624 [hep-ph].

[214] A. Ilnicka, T. Robens, and T. Stefaniak, *Constraining Extended Scalar Sectors at the LHC and beyond*, Mod. Phys. Lett. A **33** (2018) 1830007, arXiv:1803.03594 [hep-ph].

[215] Gfitter Group Collaboration, *The global electroweak fit at NNLO and prospects for the LHC and ILC*, Eur. Phys. J. C **74** (2014) 3046, arXiv:1407.3792 [hep-ph].

[216] ALEPH, DELPHI, L3, OPAL, LEP Electroweak Collaboration, *Electroweak Measurements in Electron-Positron Collisions at W-Boson-Pair Energies at LEP*, Phys. Rept. **532** (2013) 119–244, arXiv:1302.3415 [hep-ex].

[217] CDF Collaboration, *Precise measurement of the W -boson mass with the Collider Detector at Fermilab*, Phys. Rev. D **89** (2014) 072003, arXiv:1311.0894 [hep-ex].

[218] ATLAS Collaboration, *Measurement of the W -boson mass in pp collisions at $\sqrt{s}$ = 7 TeV with the ATLAS detector*, Eur. Phys. J. C **78** (2018) 110, arXiv:1701.07240 [hep-ex]. [Erratum: Eur. Phys. J.C78,no.11,898(2018)].

[219] Particle Data Group Collaboration, *Review of Particle Physics*, Phys. Rev. D **98** (2018) 030001.

[220] P. Bechtle, O. Brein, S. Heinemeyer, G. Weiglein, and K. E. Williams, *HiggsBounds: Confronting Arbitrary Higgs Sectors with Exclusion Bounds from LEP and the Tevatron*, Comput. Phys. Commun. **181** (2010) 138–167, arXiv:0811.4169 [hep-ph].

[221] P. Bechtle, O. Brein, S. Heinemeyer, G. Weiglein, and K. E. Williams, *HiggsBounds 2.0.0: Confronting Neutral and Charged Higgs Sector Predictions with Exclusion Bounds from LEP and the Tevatron*, Comput. Phys. Commun. **182** (2011) 2605–2631, arXiv:1102.1898 [hep-ph].

[222] P. Bechtle, O. Brein, S. Heinemeyer, O. Stål, T. Stefaniak, et al., *Recent Developments in HiggsBounds and a Preview of HiggsSignals*, PoS **CHARGED2012** (2012) 024, arXiv:1301.2345 [hep-ph].

[223] P. Bechtle, O. Brein, S. Heinemeyer, O. Stal, T. Stefaniak, G. Weiglein, and K. E. Williams, HiggsBounds − 4*: Improved Tests of Extended Higgs Sectors against Exclusion Bounds from LEP, the Tevatron and the LHC*, Eur. Phys. J. C **74** (2014) 2693, arXiv:1311.0055 [hep-ph].

[224] P. Bechtle, S. Heinemeyer, O. Stal, T. Stefaniak, and G. Weiglein, *Applying Exclusion Likelihoods from LHC Searches to Extended Higgs Sectors*, Eur. Phys. J. C **75** (2015) 421, arXiv:1507.06706 [hep-ph].

[225] P. Bechtle, S. Heinemeyer, O. Stal, T. Stefaniak, and G. Weiglein, *HiggsSignals: Confronting arbitrary Higgs sectors with measurements at the Tevatron and the LHC*, Eur. Phys. J. C **74** (2014) 2711, arXiv:1305.1933 [hep-ph].

[226] ATLAS Collaboration, *Search for Higgs boson pair production in the $\gamma\gamma WW^*$ channel using pp collision data recorded at $\sqrt{s} = 13$ TeV with the ATLAS detector*, Eur. Phys. J. C **78** (2018) 1007, arXiv:1807.08567 [hep-ex].

[227] ATLAS Collaboration, *Combination of searches for heavy resonances decaying into bosonic and leptonic final states using 36 fb^{-1} of proton-proton collision data at $\sqrt{s} = 13$ TeV with the ATLAS detector*, Phys. Rev. D **98** (2018) 052008, arXiv:1808.02380 [hep-ex].

[228] E. Maina, *Interference effects in Heavy Higgs production via gluon fusion in the Singlet Extension of the Standard Model*, JHEP **06** (2015) 004, arXiv:1501.02139 [hep-ph].

[229] N. Kauer and C. O'Brien, *Heavy Higgs signal–background interference in $gg \to VV$ in the Standard Model plus real singlet*, Eur. Phys. J. C **75** (2015) 374, arXiv:1502.04113 [hep-ph].

[230] N. Kauer, A. Lind, P. Maierhöfer, and W. Song, *Higgs interference effects at the one-loop level in the 1-Higgs-Singlet extension of the Standard Model*, JHEP **07** (2019) 108, arXiv:1905.03296 [hep-ph].

[231] J. Campbell, M. Carena, R. Harnik, and Z. Liu, *Interference in the $gg \to h \to \gamma\gamma$ On-Shell Rate and the Higgs Boson Total Width*, Phys. Rev. Lett. **119** (2017) 181801, arXiv:1704.08259 [hep-ph]. [Addendum: Phys. Rev. Lett.119,no.19,199901(2017)].

[232] M. Carena and Z. Liu, *Challenges and opportunities for heavy scalar searches in the $t\bar{t}$ channel at the LHC*, JHEP **11** (2016) 159, arXiv:1608.07282 [hep-ph].

[233] G. Brooijmans et al., *Les Houches 2017: Physics at TeV Colliders New Physics Working Group Report*, arXiv:1803.10379 [hep-ph].

[234] *HPAIR, Michael Spira's website*, http://tiger.web.psi.ch/hpair/.

[235] L. Randall and R. Sundrum, *A Large mass hierarchy from a small extra dimension*, Phys. Rev. Lett. **83** (1999) 3370–3373, arXiv:9905221 [hep-ph].

[236] C. Csaki, M. L. Graesser, and G. D. Kribs, *Radion dynamics and electroweak physics*, Phys. Rev. D **63** (2001) 065002, arXiv:0008151 [hep-th].

[237] H. M. Lee, M. Park, and V. Sanz, *Gravity-mediated (or Composite) Dark Matter*, Eur. Phys. J. C **74** (2014) 2715, arXiv:1306.4107 [hep-ph].

[238] A. Falkowski and J. F. Kamenik, *Diphoton portal to warped gravity*, Phys. Rev. D **94** (2016) 015008, arXiv:1603.06980 [hep-ph].

[239] S. J. Huber and Q. Shafi, *Fermion masses, mixings and proton decay in a Randall-Sundrum model*, Phys. Lett. B **498** (2001) 256–262, arXiv:0010195 [hep-ph].

[240] G. Brooijmans et al., *Les Houches 2013: Physics at TeV Colliders: New Physics Working Group Report*, arXiv:1405.1617 [hep-ph].

[241] ATLAS Collaboration, *Searches for heavy ZZ and ZW resonances in the $\ell\ell qq$ and $\nu\nu qq$ final states in pp collisions at $\sqrt{s} = 13$ TeV with the ATLAS detector*, JHEP **03** (2018) 009, arXiv:1708.09638 [hep-ex].

[242] B. M. Dillon and V. Sanz, *Kaluza-Klein gravitons at LHC2*, Phys. Rev. D **96** (2017) 035008, arXiv:1603.09550 [hep-ph].

[243] A. L. Fitzpatrick, J. Kaplan, L. Randall, and L.-T. Wang, *Searching for the Kaluza-Klein Graviton in Bulk RS Models*, JHEP **09** (2007) 013, `arXiv:0701150 [hep-ph]`.

[244] B. M. Dillon, C. Han, H. M. Lee, and M. Park, *KK graviton resonance and cascade decays in warped gravity*, Int. J. Mod. Phys. A **32** (2017) 1745006, `arXiv:1606.07171 [hep-ph]`.

[245] H. M. Lee, M. Park, and V. Sanz, *Gravity-mediated (or Composite) Dark Matter Confronts Astrophysical Data*, JHEP **05** (2014) 063, `arXiv:1401.5301 [hep-ph]`.

[246] C. Han, H. M. Lee, M. Park, and V. Sanz, *The diphoton resonance as a gravity mediator of dark matter*, Phys. Lett. B **755** (2016) 371–379, `arXiv:1512.06376 [hep-ph]`.

[247] A. Carrillo-Monteverde, Y.-J. Kang, H. M. Lee, M. Park, and V. Sanz, *Dark Matter Direct Detection from new interactions in models with spin-two mediators*, JHEP **06** (2018) 037, `arXiv:1803.02144 [hep-ph]`.

[248] T. D. Rueter, T. G. Rizzo, and J. L. Hewett, *Gravity-Mediated Dark Matter Annihilation in the Randall-Sundrum Model*, JHEP **10** (2017) 094, `arXiv:1706.07540 [hep-ph]`.

[249] ATLAS Collaboration, *Search for heavy particles decaying into a top-quark pair in the fully hadronic final state in pp collisions at $\sqrt{s}$ = 13 TeV with the ATLAS detector*, Phys. Rev. D **99** (2019) 092004, `arXiv:1902.10077 [hep-ex]`.

[250] ATLAS Collaboration, *Search for heavy particles decaying into top-quark pairs using lepton-plus-jets events in proton-proton collisions at $\sqrt{s}$ = 13 TeV with the ATLAS detector*, Eur. Phys. J. C **78** (2018) 565, `arXiv:1804.10823 [hep-ex]`.

[251] ATLAS Collaboration, *Search for WW/WZ resonance production in $\ell\nu qq$ final states in pp collisions at $\sqrt{s}$ = 13 TeV with the ATLAS detector*, JHEP **03** (2018) 042, `arXiv:1710.07235 [hep-ex]`.

[252] A. Ahmed, B. M. Dillon, B. Grzadkowski, J. F. Gunion, and Y. Jiang, *Implications of the absence of high-mass radion signals*, Phys. Rev. D **95** (2017) 095019, `arXiv:1512.05771 [hep-ph]`.

[253] H. Davoudiasl, G. Perez, and A. Soni, *The Little Randall-Sundrum Model at the Large Hadron Collider*, Phys. Lett. B **665** (2008) 67–71, `arXiv:0802.0203 [hep-ph]`.

[254] K. L. McDonald, *Little Randall-Sundrum Model and a Multiply Warped Spacetime*, Phys. Rev. D **77** (2008) 124046, `arXiv:0804.0654 [hep-th]`.

[255] B. M. Dillon, D. P. George, and K. L. McDonald, *Regarding the Radion in Randall-Sundrum Models with Brane Curvature*, Phys. Rev. D **94** (2016) 064045, `arXiv:1605.03087 [hep-ph]`.

[256] B. M. Dillon, B. K. El-Menoufi, S. J. Huber, and J. P. Manuel, *Rapid holographic phase transition with brane-localized curvature*, Phys. Rev. D **98** (2018) 086005, `arXiv:1708.02953 [hep-th]`.

[257] M. Gouzevitch, A. Oliveira, J. Rojo, R. Rosenfeld, G. P. Salam, et al., *Scale-invariant resonance tagging in multijet events and new physics in Higgs pair production*, JHEP **1307** (2013) 148, `arXiv:1303.6636 [hep-ph]`.

[258] W.-J. Zhang, W.-G. Ma, R.-Y. Zhang, X.-Z. Li, L. Guo, and C. Chen, *Double Higgs boson production and decay in Randall-Sundrum model at hadron colliders*, Phys. Rev. D **92** (2015) 116005, `arXiv:1512.01766 [hep-ph]`.

[259] J. F. Gunion, H. E. Haber, G. L. Kane, and S. Dawson, *The Higgs Hunter's Guide*, Front. Phys. **80** (2000) 1–404.

[260] G. C. Branco, P. M. Ferreira, L. Lavoura, M. N. Rebelo, M. Sher, and J. P. Silva, *Theory and phenomenology of two-Higgs-doublet models*, Phys. Rept. **516** (2012) 1–102, arXiv:1106.0034 [hep-ph].

[261] D. Fontes, J. C. Romao, and J. P. Silva, $h \to Z\gamma$ *in the complex two Higgs doublet model*, JHEP **12** (2014) 043, arXiv:1408.2534 [hep-ph].

[262] A. W. El Kaffas, P. Osland, and O. M. Ogreid, *CP violation, stability and unitarity of the two Higgs doublet model*, Nonlin. Phenom. Complex Syst. **10** (2007) 347–357, arXiv:0702097 [hep-ph].

[263] H. E. Haber and O. Stål, *New LHC benchmarks for the $\mathcal{CP}$ -conserving two-Higgs-doublet model*, Eur. Phys. J. C **75** (2015) 491, arXiv:1507.04281 [hep-ph]. [Erratum: Eur. Phys. J.C76,no.6,312(2016)].

[264] J. Baglio, O. Eberhardt, U. Nierste, and M. Wiebusch, *Benchmarks for Higgs Pair Production and Heavy Higgs boson Searches in the Two-Higgs-Doublet Model of Type II*, Phys. Rev. D **90** (2014) 015008, arXiv:1403.1264 [hep-ph].

[265] P. Basler, S. Dawson, C. Englert, and M. Mühlleitner, *Showcasing HH production: Benchmarks for the LHC and HL-LHC*, Phys. Rev. D **99** (2019) 055048, arXiv:1812.03542 [hep-ph].

[266] D. Fontes, M. Muhlleitner, J. C. Romao, R. Santos, J. P. Silva, and J. Wittbrodt, *The C2HDM revisited*, JHEP **02** (2018) 073, arXiv:1711.09419 [hep-ph].

[267] U. Baur, T. Plehn, and D. L. Rainwater, *Probing the Higgs selfcoupling at hadron colliders using rare decays*, Phys. Rev. D **69** (2004) 053004, arXiv:0310056 [hep-ph].

[268] U. Baur, T. Plehn, and D. L. Rainwater, *Examining the Higgs boson potential at lepton and hadron colliders: A Comparative analysis*, Phys. Rev. D **68** (2003) 033001, arXiv:0304015 [hep-ph].

[269] A. J. Barr, M. J. Dolan, C. Englert, and M. Spannowsky, *Di-Higgs final states augMT2ed – selecting hh events at the high luminosity LHC*, Phys. Lett. B **728** (2014) 308–313, arXiv:1309.6318 [hep-ph].

[270] D. E. Ferreira de Lima, A. Papaefstathiou, and M. Spannowsky, *Standard model Higgs boson pair production in the ($b\bar{b}$)($b\bar{b}$) final state*, JHEP **08** (2014) 030, arXiv:1404.7139 [hep-ph].

[271] D. Wardrope, E. Jansen, N. Konstantinidis, B. Cooper, R. Falla, and N. Norjoharuddeen, *Non-resonant Higgs-pair production in the $b\bar{b}\,b\bar{b}$ final state at the LHC*, Eur. Phys. J. C **75** (2015) 219, arXiv:1410.2794 [hep-ph].

[272] M. Carena, H. E. Haber, I. Low, N. R. Shah, and C. E. M. Wagner, *Alignment limit of the NMSSM Higgs sector*, Phys. Rev. D **93** (2016) 035013, arXiv:1510.09137 [hep-ph].

[273] S. Baum and N. R. Shah, *Two Higgs Doublets and a Complex Singlet: Disentangling the Decay Topologies and Associated Phenomenology*, JHEP **12** (2018) 044, arXiv:1808.02667 [hep-ph].

[274] U. Ellwanger, C. Hugonie, and A. M. Teixeira, *The Next-to-Minimal Supersymmetric Standard Model*, Phys. Rept. **496** (2010) 1–77, arXiv:0910.1785 [hep-ph].

[275] H. Georgi and D. V. Nanopoulos, *Suppression of Flavor Changing Effects From Neutral Spinless Meson Exchange in Gauge Theories*, Phys. Lett B **82** (1979) 95–96.

[276] J. F. Donoghue and L. F. Li, *Properties of Charged Higgs Bosons*, Phys. Rev. D **19** (1979) 945.

[277] L. Lavoura and J. P. Silva, *Fundamental CP violating quantities in a SU(2) x U(1) model with many Higgs doublets*, Phys. Rev. D **50** (1994) 4619–4624, arXiv:9404276 [hep-ph].

[278] F. J. Botella and J. P. Silva, *Jarlskog - like invariants for theories with scalars and fermions*, Phys. Rev. D **51** (1995) 3870–3875, arXiv:9411288 [hep-ph].

[279] G. C. Branco, L. Lavoura, and S. J.P., *CP violation.* Oxford University Press, Oxford, UK, 1999.

[280] J. F. Gunion and H. E. Haber, *The CP conserving two Higgs doublet model: The Approach to the decoupling limit*, Phys. Rev. D **67** (2003) 075019, arXiv:0207010 [hep-ph].

[281] W. Altmannshofer, M. Carena, N. R. Shah, and F. Yu, *Indirect Probes of the MSSM after the Higgs Discovery*, JHEP **01** (2013) 160, arXiv:1211.1976 [hep-ph].

[282] M. Carena, J. Osborne, N. R. Shah, and C. E. M. Wagner, *Supersymmetry and LHC Missing Energy Signals*, Phys. Rev. D **98** (2018) 115010, arXiv:1809.11082 [hep-ph].

[283] D. Dicus, A. Stange, and S. Willenbrock, *Higgs decay to top quarks at hadron colliders*, Phys. Lett. B **333** (1994) 126–131, arXiv:9404359 [hep-ph].

[284] R. Barcelo and M. Masip, *Extra Higgs bosons in $t\bar{t}$ production at the LHC*, Phys. Rev. D **81** (2010) 075019, arXiv:1001.5456 [hep-ph].

[285] V. Barger, W.-Y. Keung, and B. Yencho, *Azimuthal Correlations in Top Pair Decays and The Effects of New Heavy Scalars*, Phys. Rev. D **85** (2012) 034016, arXiv:1112.5173 [hep-ph].

[286] Y. Bai and W.-Y. Keung, *Can vanishing mass-on-shell interactions generate a dip at colliders?*, Int. J. Mod. Phys. A **30** (2015) 1550120, arXiv:1407.6355 [hep-ph].

[287] S. Jung, J. Song, and Y. W. Yoon, *Dip or nothingness of a Higgs resonance from the interference with a complex phase*, Phys. Rev. D **92** (2015) 055009, arXiv:1505.00291 [hep-ph].

[288] N. Craig, F. D'Eramo, P. Draper, S. Thomas, and H. Zhang, *The Hunt for the Rest of the Higgs Bosons*, JHEP **06** (2015) 137, arXiv:1504.04630 [hep-ph].

[289] S. Gori, I.-W. Kim, N. R. Shah, and K. M. Zurek, *Closing the Wedge: Search Strategies for Extended Higgs Sectors with Heavy Flavor Final States*, Phys. Rev. D **93** (2016) 075038, arXiv:1602.02782 [hep-ph].

[290] A. Djouadi, L. Maiani, G. Moreau, A. Polosa, J. Quevillon, and V. Riquer, *The post-Higgs MSSM scenario: Habemus MSSM?*, Eur. Phys. J. **C73** (2013) 2650, arXiv:1307.5205 [hep-ph].

[291] A. Djouadi and J. Quevillon, *The MSSM Higgs sector at a high M_{SUSY}: reopening the low tanβ regime and heavy Higgs searches*, JHEP **10** (2013) 028, arXiv:1304.1787 [hep-ph].

[292] L. Maiani, A. D. Polosa, and V. Riquer, *Bounds to the Higgs Sector Masses in Minimal Supersymmetry from LHC Data*, Phys. Lett. **B724** (2013) 274–277, arXiv:1305.2172 [hep-ph].

[293] A. Djouadi, L. Maiani, A. Polosa, J. Quevillon, and V. Riquer, *Fully covering the MSSM Higgs sector at the LHC*, JHEP **06** (2015) 168, `arXiv:1502.05653 [hep-ph]`.

[294] E. Bagnaschi et al., *Benchmark scenarios for low* tan β *in the MSSM*, LHCHXSWG-2015-002 (2015) .

[295] G. Lee and C. E. M. Wagner, *Higgs bosons in heavy supersymmetry with an intermediate m_A*, Phys. Rev. **D92** (2015) no. 7, 075032, `arXiv:1508.00576 [hep-ph]`.

[296] G. Chalons, A. Djouadi, and J. Quevillon, *The neutral Higgs self-couplings in the (h)MSSM*, Phys. Lett. **B780** (2018) 74–80, `arXiv:1709.02332 [hep-ph]`.

[297] S. Liebler, M. Mühlleitner, M. Spira, and M. Stadelmaier, *The hMSSM approach for Higgs self-couplings revisited*, Eur. Phys. J. **C79** (2019) no. 1, 65, `arXiv:1810.10979 [hep-ph]`.

[298] M. Maniatis, *The Next-to-Minimal Supersymmetric extension of the Standard Model reviewed*, Int. J. Mod. Phys. A **25** (2010) 3505–3602, `arXiv:0906.0777 [hep-ph]`.

[299] H. Georgi and M. Machacek, *Doubly charged Higgs bosons*, Nucl. Phys. B **262** (1985) 463–477.

[300] M. S. Chanowitz and M. Golden, *Higgs Boson Triplets With $M(W) = M(Z) \cos\theta_w$*, Phys. Lett. B **165** (1985) 105–108.

[301] K. Hartling, K. Kumar, and H. E. Logan, *GMCALC: a calculator for the Georgi-Machacek model*, `arXiv:1412.7387 [hep-ph]`.

[302] M. Aoki and S. Kanemura, *Unitarity bounds in the Higgs model including triplet fields with custodial symmetry*, Phys. Rev. D **77** (2008) 095009, `arXiv:0712.4053 [hep-ph]`. [Erratum: Phys. Rev.D89,no.5,059902(2014)].

[303] K. Hartling, K. Kumar, and H. E. Logan, *The decoupling limit in the Georgi-Machacek model*, Phys. Rev. D **90** (2014) 015007, `arXiv:1404.2640 [hep-ph]`.

[304] CMS Collaboration, *Observation of electroweak production of same-sign W boson pairs in the two jet and two same-sign lepton final state in proton-proton collisions at $\sqrt{s}$ = 13 TeV*, Phys. Rev. Lett. **120** (2018) 081801, `arXiv:1709.05822 [hep-ex]`.

[305] A. Belyaev, M. Drees, O. J. Eboli, J. Mizukoshi, and S. Novaes, *Supersymmetric Higgs pair production at hadron colliders*, Phys. Rev. D **60** (1999) 075008, `arXiv:9905266 [hep-ph]`.

[306] E. Asakawa, D. Harada, S. Kanemura, Y. Okada, and K. Tsumura, *Higgs boson pair production in new physics models at hadron, lepton, and photon colliders*, Phys. Rev. D **82** (2010) 115002, `arXiv:1009.4670 [hep-ph]`.

[307] G. D. Kribs and A. Martin, *Enhanced di-Higgs Production through Light Colored Scalars*, Phys. Rev. D **86** (2012) 095023, `arXiv:1207.4496 [hep-ph]`.

[308] T. Enkhbat, *Scalar leptoquarks and Higgs pair production at the LHC*, JHEP **1401** (2014) 158, `arXiv:1311.4445 [hep-ph]`.

[309] Z. Heng, L. Shang, Y. Zhang, and J. Zhu, *Pair production of 125 GeV Higgs boson in the SM extension with color-octet scalars at the LHC*, JHEP **1402** (2014) 083, `arXiv:1312.4260 [hep-ph]`.

[310] J.-J. Liu, W.-G. Ma, G. Li, R.-Y. Zhang, and H.-S. Hou, *Higgs boson pair production in the little Higgs model at hadron collider*, Phys. Rev. D **70** (2004) 015001, `arXiv:0404171 [hep-ph]`.

[311] C. O. Dib, R. Rosenfeld, and A. Zerwekh, *Double Higgs production and quadratic divergence cancellation in little Higgs models with T parity*, JHEP **0605** (2006) 074, `arXiv:0509179 [hep-ph]`.

[312] A. Pierce, J. Thaler, and L.-T. Wang, *Disentangling Dimension Six Operators through Di-Higgs Boson Production*, JHEP **0705** (2007) 070, `arXiv:0609049 [hep-ph]`.

[313] W. Ma, C.-X. Yue, and Y.-Z. Wang, *Pair production of neutral Higgs bosons from the left-right twin Higgs model at the ILC and LHC*, Phys. Rev. D **79** (2009) 095010, `arXiv:0905.0597 [hep-ph]`.

[314] X.-F. Han, L. Wang, and J. M. Yang, *Higgs-pair Production and Decay in Simplest Little Higgs Model*, Nucl. Phys. B **825** (2010) 222–230, `arXiv:0908.1827 [hep-ph]`.

[315] S. Dawson, E. Furlan, and I. Lewis, *Unravelling an extended quark sector through multiple Higgs production?*, Phys. Rev. D **87** (2013) 014007, `arXiv:1210.6663 [hep-ph]`.

[316] L. Edelhäuser, A. Knochel, and T. Steeger, *Applying EFT to Higgs Pair Production in Universal Extra Dimensions*, JHEP **11** (2015) 062, `arXiv:1503.05078 [hep-ph]`.

[317] C.-R. Chen and I. Low, *Double take on new physics in double Higgs boson production*, Phys. Rev. D **90** (2014) 013018, `arXiv:1405.7040 [hep-ph]`.

[318] P. Huang, A. Joglekar, M. Li, and C. E. M. Wagner, *Corrections to di-Higgs boson production with light stops and modified Higgs couplings*, Phys. Rev. D **97** (2018) 075001, `arXiv:1711.05743 [hep-ph]`.

[319] G. D. Kribs, T. Plehn, M. Spannowsky, and T. M. P. Tait, *Four generations and Higgs physics*, Phys. Rev. D **76** (2007) 075016, `arXiv:0706.3718 [hep-ph]`.

[320] C.-Y. Chen, S. Dawson, and E. Furlan, *Vectorlike fermions and Higgs effective field theory revisited*, Phys. Rev. D **96** (2017) 015006, `arXiv:1703.06134 [hep-ph]`.

[321] S. Dawson and E. Furlan, *A Higgs Conundrum with Vector Fermions*, Phys. Rev. D **86** (2012) 015021, `arXiv:1205.4733 [hep-ph]`.

[322] J. Aguilar-Saavedra, R. Benbrik, S. Heinemeyer, and M. Pérez-Victoria, *Handbook of vectorlike quarks: Mixing and single production*, Phys. Rev. D **88** (2013) 094010, `arXiv:1306.0572 [hep-ph]`.

[323] S. Dawson, A. Ismail, and I. Low, *What's in the loop? The anatomy of double Higgs production*, Phys. Rev. D **91** (2015) 115008, `arXiv:1504.05596 [hep-ph]`.

[324] J. M. Frere, D. R. T. Jones, and S. Raby, *Fermion Masses and Induction of the Weak Scale by Supergravity*, Nucl. Phys. B **222** (1983) 11–19.

[325] M. Claudson, L. J. Hall, and I. Hinchliffe, *Low-Energy Supergravity: False Vacua and Vacuous Predictions*, Nucl. Phys. B **228** (1983) 501–528.

[326] T. Falk, K. A. Olive, L. Roszkowski, and M. Srednicki, *New constraints on superpartner masses*, Phys. Lett. B **367** (1996) 183–187, `arXiv:9510308 [hep-ph]`.

[327] A. Kusenko, P. Langacker, and G. Segre, *Phase transitions and vacuum tunneling into charge and color breaking minima in the MSSM*, Phys. Rev. D **54** (1996) 5824–5834, `arXiv:9602414 [hep-ph]`.

[328] D. Chowdhury, R. M. Godbole, K. A. Mohan, and S. K. Vempati, *Charge and Color Breaking Constraints in MSSM after the Higgs Discovery at LHC*, JHEP **02** (2014) 110, `arXiv:1310.1932 [hep-ph]`. [Erratum: JHEP03,149(2018)].

[329] N. Blinov and D. E. Morrissey, *Vacuum Stability and the MSSM Higgs Mass*, JHEP **03** (2014) 106, `arXiv:1310.4174 [hep-ph]`.

[330] A. Djouadi, *The Anatomy of electro-weak symmetry breaking. II. The Higgs bosons in the minimal supersymmetric model*, Phys. Rept. **459** (2008) 1–241, `arXiv:0503173 [hep-ph]`.

[331] M. R. Buckley and D. Hooper, *Are There Hints of Light Stops in Recent Higgs Search Results?*, Phys. Rev. D **86** (2012) 075008, `arXiv:1207.1445 [hep-ph]`.

[332] D. Carmi, A. Falkowski, E. Kuflik, T. Volansky, and J. Zupan, *Higgs After the Discovery: A Status Report*, JHEP **10** (2012) 196, `arXiv:1207.1718 [hep-ph]`.

[333] M. Badziak and C. E. M. Wagner, *Enhancing the Higgs associated production with a top quark pair*, JHEP **05** (2016) 123, `arXiv:1602.06198 [hep-ph]`.

[334] M. Badziak and C. E. M. Wagner, *Enhanced Higgs associated production with a top quark pair in the NMSSM with light singlets*, JHEP **02** (2017) 050, `arXiv:1611.02353 [hep-ph]`.

[335] A. G. Cohen, D. B. Kaplan, and A. E. Nelson, *Baryogenesis at the weak phase transition*, Nucl. Phys. B **349** (1991) 727–742.

[336] C. Wainwright and S. Profumo, *The Impact of a strongly first-order phase transition on the abundance of thermal relics*, Phys. Rev. D **80** (2009) 103517, `arXiv:0909.1317 [hep-ph]`.

[337] C.-Y. Chen, J. Kozaczuk, and I. M. Lewis, *Non-resonant Collider Signatures of a Singlet-Driven Electroweak Phase Transition*, JHEP **08** (2017) 096, `arXiv:1704.05844 [hep-ph]`.

[338] S. Profumo, M. J. Ramsey-Musolf, and G. Shaughnessy, *Singlet Higgs phenomenology and the electroweak phase transition*, JHEP **08** (2007) 010, `arXiv:0705.2425 [hep-ph]`.

[339] D. Curtin, P. Meade, and C.-T. Yu, *Testing Electroweak Baryogenesis with Future Colliders*, JHEP **11** (2014) 127, `arXiv:1409.0005 [hep-ph]`.

[340] M. Kamionkowski, A. Kosowsky, and M. S. Turner, *Gravitational radiation from first order phase transitions*, Phys. Rev. D **49** (1994) 2837–2851, `arXiv:9310044 [astro-ph]`.

[341] LIGO Scientific, Virgo Collaboration, *Observation of Gravitational Waves from a Binary Black Hole Merger*, Phys. Rev. Lett. **116** (2016) no. 6, 061102, `arXiv:1602.03837 [gr-qc]`.

[342] LISA Collaboration, *Laser Interferometer Space Antenna*, `arXiv:1702.00786 [astro-ph.IM]`.

[343] C. Caprini et al., *Science with the space-based interferometer eLISA. II: Gravitational waves from cosmological phase transitions*, JCAP **1604** (2016) no. 04, 001, `arXiv:1512.06239 [astro-ph.CO]`.

[344] K. T. Matchev and S. D. Thomas, *Higgs and Z boson signatures of supersymmetry*, Phys. Rev. D **62** (2000) 077702, `arXiv:9908482 [hep-ph]`.

[345] ATLAS Collaboration, *Search for pair production of higgsinos in final states with at least three b-tagged jets in $\sqrt{s}$ = 13 TeV pp collisions using the ATLAS detector*, Phys. Rev. D **98** (2018) 092002, `arXiv:1806.04030 [hep-ex]`.

[346] CMS Collaboration, *Search for Higgsino pair production in pp collisions at $\sqrt{s}$ = 13 TeV in final states with large missing transverse momentum and two Higgs bosons decaying via $H \to b\bar{b}$*, Phys. Rev. D **97** (2018) 032007, `arXiv:1709.04896 [hep-ex]`.

[347] Z. Kang, P. Ko, and J. Li, *New Physics Opportunities in the Boosted Di-Higgs-Boson Plus Missing Transverse Energy Signature*, Phys. Rev. Lett. **116** (2016) 131801, `arXiv:1504.04128 [hep-ph]`.

[348] J. M. No, *Looking through the pseudoscalar portal into dark matter: Novel mono-Higgs and mono-Z signatures at the LHC*, Phys. Rev. D **93** (2016) 031701, `arXiv:1509.01110 [hep-ph]`.

[349] Z. Kang, P. Ko, and J. Li, *New Avenues to Heavy Right-handed Neutrinos with Pair Production at Hadronic Colliders*, Phys. Rev. D **93** (2016) 075037, `arXiv:1512.08373 [hep-ph]`.

[350] I. Brivio, M. B. Gavela, L. Merlo, K. Mimasu, J. M. No, R. del Rey, and V. Sanz, *ALPs Effective Field Theory and Collider Signatures*, Eur. Phys. J. C **77** (2017) 572, `arXiv:1701.05379 [hep-ph]`.

[351] E. Arganda, J. L. Díaz-Cruz, N. Mileo, R. A. Morales, and A. Szynkman, *Search strategies for pair production of heavy Higgs bosons decaying invisibly at the LHC*, Nucl. Phys. B **929** (2018) 171–192, `arXiv:1710.07254 [hep-ph]`.

[352] C.-R. Chen, Y.-X. Lin, H.-C. Wu, and J. Yue, *Boosted Higgs-pair production associated with large E_T^{miss}: a signal of Z′*, `arXiv:1804.00405 [hep-ph]`.

[353] E. Bernreuther, J. Horak, T. Plehn, and A. Butter, *Actual Physics behind Mono-X*, SciPost Phys. **5** (2018) no. 4, 034, `arXiv:1805.11637 [hep-ph]`.

[354] A. Titterton, U. Ellwanger, H. U. Flaecher, S. Moretti, and C. H. Shepherd-Themistocleous, *Exploring Sensitivity to NMSSM Signatures with Low Missing Transverse Energy at the LHC*, JHEP **10** (2018) 064, `arXiv:1807.10672 [hep-ph]`.

[355] M. Blanke, S. Kast, J. M. Thompson, S. Westhoff, and J. Zurita, *Spotting hidden sectors with Higgs binoculars*, JHEP **04** (2019) 160, `arXiv:1901.07558 [hep-ph]`.

[356] F. Pedregosa et al., *Scikit-learn: Machine Learning in Python*, J. Machine Learning Res. **12** (2011) 2825–2830, `arXiv:1201.0490 [cs.LG]`.

[357] Y. Freund and R. E. Schapire, *A Decision-Theoretic Generalization of On-Line Learning and an Application to Boosting*, J. Comput. Syst. Sci. **55** (1997) no. 1, 119–139.

[358] J. M. Butterworth, A. R. Davison, M. Rubin, and G. P. Salam, *Jet substructure as a new Higgs search channel at the LHC*, Phys. Rev. Lett. **100** (2008) 242001, `arXiv:0802.2470 [hep-ph]`.

[359] J. L. Feng, I. Galon, F. Kling, and S. Trojanowski, *ForwArd Search ExpeRiment at the LHC*, Phys. Rev. D **97** (2018) 035001, `arXiv:1708.09389 [hep-ph]`.

[360] FASER Collaboration, *FASER's physics reach for long-lived particles*, Phys. Rev. D **99** (2019) 095011, `arXiv:1811.12522 [hep-ph]`.

[361] J. A. Evans, *Detecting Hidden Particles with MATHUSLA*, Phys. Rev. D **97** (2018) 055046, `arXiv:1708.08503 [hep-ph]`.

[362] D. Curtin et al., *Long-Lived Particles at the Energy Frontier: The MATHUSLA Physics Case*, `arXiv:1806.07396 [hep-ph]`.

[363] MATHUSLA Collaboration, *A Letter of Intent for MATHUSLA: a dedicated displaced vertex detector above ATLAS or CMS.*, `arXiv:1811.00927 [physics.ins-det]`.

[364] D. Dercks, N. Desai, J. S. Kim, K. Rolbiecki, J. Tattersall, and T. Weber, *CheckMATE 2: From the model to the limit*, Comput. Phys. Commun. **221** (2017) 383–418, `arXiv:1611.09856 [hep-ph]`.

[365] ATLAS Collaboration, *The ATLAS Experiment at the CERN Large Hadron Collider*, JINST **3** (2008) S08003.

[366] CMS Collaboration, *The CMS Experiment at the CERN LHC*, JINST **3** (2008) S08004.

[367] A. Hoecker, P. Speckmayer, J. Stelzer, J. Therhaag, E. von Toerne, and H. Voss, *TMVA: Toolkit for Multivariate Data Analysis*, PoS **ACAT** (2007) 040, `arXiv:0703039`.

[368] CMS Collaboration, *Particle-flow reconstruction and global event description with the CMS detector*, JINST **12** (2017) P10003, `arXiv:1706.04965 [physics.ins-det]`.

[369] ATLAS Collaboration, *Jet reconstruction and performance using particle flow with the ATLAS Detector*, Eur. Phys. J. C **77** (2017) 466, `arXiv:1703.10485 [hep-ex]`.

[370] ATLAS Collaboration, *Tagging and suppression of pileup jets*, ATLAS-CONF-2014-018, 2014.

[371] M. Cacciari and G. P. Salam, *Pileup subtraction using jet areas*, Phys. Lett. B **659** (2008) 119–126, `arXiv:0707.1378 [hep-ph]`.

[372] D. Bertolini, P. Harris, M. Low, and N. Tran, *Pileup Per Particle Identification*, JHEP **10** (2014) 059, `arXiv:1407.6013 [hep-ph]`.

[373] ATLAS Collaboration, *Jet energy scale measurements and their systematic uncertainties in proton-proton collisions at $\sqrt{s} = 13$ TeV with the ATLAS detector*, Phys. Rev. D **96** (2017) 072002, `arXiv:1703.09665 [hep-ex]`.

[374] CMS Collaboration, *Jet energy scale and resolution in the CMS experiment in pp collisions at 8 TeV*, JINST **12** (2017) P02014, `arXiv:1607.03663 [hep-ex]`.

[375] D. Krohn, J. Thaler, and L.-T. Wang, *Jet Trimming*, JHEP **02** (2010) 084, `arXiv:0912.1342 [hep-ph]`.

[376] S. D. Ellis, C. K. Vermilion, and J. R. Walsh, *Recombination Algorithms and Jet Substructure: Pruning as a Tool for Heavy Particle Searches*, Phys. Rev. D **81** (2010) 094023, `arXiv:0912.0033 [hep-ph]`.

[377] M. Dasgupta, A. Fregoso, S. Marzani, and G. P. Salam, *Towards an understanding of jet substructure*, JHEP **09** (2013) 029, `arXiv:1307.0007 [hep-ph]`.

[378] A. J. Larkoski, S. Marzani, G. Soyez, and J. Thaler, *Soft Drop*, JHEP **05** (2014) 146, `arXiv:1402.2657 [hep-ph]`.

[379] L. Asquith et al., *Jet Substructure at the Large Hadron Collider : Experimental Review*, `arXiv:1803.06991 [hep-ex]`.

[380] SLD Collaboration, *Precise measurement of the b quark fragmentation function in Z0 boson decays*, Phys. Rev. Lett. **84** (2000) 4300–4304, `arXiv:9912058 [hep-ex]`.

[381] ATLAS Collaboration, *Performance of b-jet Identification in the ATLAS Experiment*, JINST **11** (2016) P04008, `arXiv:1512.01094 [hep-ex]`.

[382] CMS Collaboration, *Identification of heavy-flavour jets with the CMS detector in pp collisions at 13 TeV*, JINST **13** (2018) P05011, `arXiv:1712.07158 [physics.ins-det]`.

[383] ATLAS Collaboration, *Optimisation and performance studies of the ATLAS b-tagging algorithms for the 2017-18 LHC run*, ATL-PHYS-PUB-2017-013, Geneva, 2017.

[384] D. Guest, J. Collado, P. Baldi, S.-C. Hsu, G. Urban, and D. Whiteson, *Jet Flavor Classification in High-Energy Physics with Deep Neural Networks*, Phys. Rev. D **94** (2016) 112002, `arXiv:1607.08633 [hep-ex]`.

[385] CMS Collaboration, *Performance of b tagging algorithms in proton-proton collisions at 13 TeV with Phase 1 CMS detector*, CMS-DP-2018-033, 2018.

[386] ATLAS Collaboration, *Measurements of b-jet tagging efficiency with the ATLAS detector using* $t\bar{t}$ *events at* $\sqrt{s} = 13$ *TeV*, JHEP **2018** (2018) 89.

[387] ATLAS Collaboration, *ATLAS Flavor-Tagging Calibration Results with 80.5 fb$^-$1*, Atlas-plot-ftag-2019-003, 2019.

[388] ATLAS Collaboration, *Measurement of b-tagging Efficiency of c-jets in* $t\bar{t}$ *Events Using a Likelihood Approach with the ATLAS Detector*, ATLAS-CONF-2018-001, Geneva, 2018.

[389] ATLAS Collaboration, *Calibration of light-flavour jet b-tagging rates on ATLAS proton-proton collision data at* $\sqrt{s} = 13$ *TeV*, ATLAS-CONF-2018-006, 2018.

[390] ATLAS Collaboration, *Boosted Higgs* $(\rightarrow b\bar{b})$ *Boson Identification with the ATLAS Detector at* $\sqrt{s} = 13$ *TeV*, ATLAS-CONF-2016-039, 2016.

[391] ATLAS Collaboration, *Flavor Tagging with Track Jets in Boosted Topologies with the ATLAS Detector*, ATL-PHYS-PUB-2014-013, 2014.

[392] ATLAS Collaboration, *Variable Radius, Exclusive-k_T, and Center-of-Mass Subjet Reconstruction for Higgs($\rightarrow b\bar{b}$) Tagging in ATLAS*, ATL-PHYS-PUB-2017-010, 2017.

[393] CMS Collaboration, *Performance of Deep Tagging Algorithms for Boosted Double Quark Jet Topology in Proton-Proton Collisions at 13 TeV with the Phase-0 CMS Detector*, CMS-DP-2018-046, 2018.

[394] CMS Collaboration, *Identification of double-b quark jets in boosted event topologies*, CMS-PAS-BTV-15-002, 2016.

[395] CMS Collaboration, *Inclusive search for a highly boosted Higgs boson decaying to a bottom quark-antiquark pair*, Phys. Rev. Lett. **120** (2018) 071802, `arXiv:1709.05543 [hep-ex]`.

[396] ATLAS Collaboration, *Search for boosted resonances decaying to two b-quarks and produced in association with a jet at $\sqrt{s}$ = 13 TeV with the ATLAS detector*, ATLAS-CONF-2018-052, 2018.

[397] ATLAS Collaboration, *Monte Carlo Calibration and Combination of In-situ Measurements of Jet Energy Scale, Jet Energy Resolution and Jet Mass in ATLAS*, ATLAS-CONF-2015-037, 2015.

[398] CMS Collaboration, *Observation of Higgs boson decay to bottom quarks*, Phys. Rev. Lett. **121** (2018) 121801, arXiv:1808.08242 [hep-ex].

[399] ATLAS Collaboration, *Observation of $H \to b\bar{b}$ decays and VH production with the ATLAS detector*, Phys. Lett. B **786** (2018) 59–86, arXiv:1808.08238 [hep-ex].

[400] CDF, D0 Collaboration, *Improved b-jet Energy Correction for $H \to b\bar{b}$ Searches at CDF*, arXiv:1107.3026 [hep-ex].

[401] CMS Collaboration, *Evidence for the Higgs boson decay to a bottom quark-antiquark pair*, Phys. Lett. B **780** (2018) 501–532, arXiv:1709.07497 [hep-ex].

[402] CMS Collaboration, *Search for resonant pair production of Higgs bosons decaying to bottom quark-antiquark pairs in proton-proton collisions at 13 TeV*, JHEP **08** (2018) 152, arXiv:1806.03548 [hep-ex].

[403] CMS Collaboration, *Search for the standard model Higgs boson produced in association with a W or a Z boson and decaying to bottom quarks*, Phys. Rev. D **89** (2014) 012003.

[404] P. J. Huber, *Robust Estimation of a Location Parameter*, Ann. Math. Statist. **35** (03, 1964) 73–101.

[405] ATLAS Collaboration, *Search for the $HH \to b\bar{b}b\bar{b}$ process via vector boson fusion production using proton-proton collisions at $\sqrt{s}$ = 13 TeV with the ATLAS detector*, ATLAS-CONF-2019-030, 2019.

[406] E. Schopf, N. Wermes, and I. Brock, *Search for the Higgs Boson Decay to Bottom and Charm Quarks*, CERN-THESIS-2018-145, 2018.

[407] CMS Collaboration, *Performance of reconstruction and identification of τ leptons decaying to hadrons and ν_τ in pp collisions at $\sqrt{s}$ = 13 TeV*, JINST **13** (2018) P10005, arXiv:1809.02816 [hep-ex].

[408] ATLAS Collaboration, *Reconstruction, Energy Calibration, and Identification of Hadronically Decaying Tau Leptons in the ATLAS Experiment for Run-2 of the LHC*, ATL-PHYS-PUB-2015-045.

[409] ATLAS Collaboration, *Measurement of the tau lepton reconstruction and identification performance in the ATLAS experiment using pp collisions at $\sqrt{s}$ = 13 TeV*, ATLAS-CONF-2017-029, 2017.

[410] A. Graves, *Supervised Sequence Labelling with Recurrent Neural Networks.* Studies in Computational Intelligence. Springer, Berlin, 2012. https://cds.cern.ch/record/1503877.

[411] https://atlas.web.cern.ch/Atlas/GROUPS/PHYSICS/PLOTS/TAU-2018-001.

[412] D. Kirchmeier, *Reconstruction and Identification of Boosted Tau Pair Topologies at ATLAS*,
       CERN-THESIS-2015-220, 2015.

[413] CMS Collaboration, *Tau identification in boosted topologies*, CMS-DP-2016-038, 2016.

[414] W. Lampl, S. Laplace, D. Lelas, P. Loch, H. Ma, S. Menke, S. Rajagopalan, D. Rousseau,
       S. Snyder, and G. Unal, *Calorimeter Clustering Algorithms: Description and Performance*,
       Atl-larg-pub-2008-002. atl-com-larg-2008-003, 2008.

[415] ATLAS Collaboration, *Electron and photon energy calibration with the ATLAS detector using
       LHC Run 1 data*, Eur. Phys. J. C **74** (2014) 3071, arXiv:1407.5063 [hep-ex].

[416] CMS Collaboration, *Performance of Electron Reconstruction and Selection with the CMS
       Detector in Proton-Proton Collisions at $\sqrt{s}$ = 8 TeV*, JINST **10** (2015) P06005,
       arXiv:1502.02701 [physics.ins-det].

[417] CMS Collaboration, *Performance of Photon Reconstruction and Identification with the CMS
       Detector in Proton-Proton Collisions at $\sqrt{s}$ = 8 TeV*, JINST **10** (2015) P08010,
       arXiv:1502.02702 [physics.ins-det].

[418] ATLAS Collaboration, *Measurement of the photon identification efficiencies with the ATLAS
       detector using LHC Run 2 data collected in 2015 and 2016*, Eur. Phys. J. C **79** (2019) 205,
       arXiv:1810.05087 [hep-ex].

[419] ATLAS Collaboration, *Electron and photon energy calibration with the ATLAS detector using
       2015-2016 LHC proton-proton collision data*, JINST **14** (2019) P03017, arXiv:1812.03848
       [hep-ex].

[420] CMS Collaboration, *Electron and photon performance in CMS with the full 2016 data
       sample*, CMS-DP-2017-004.

[421] ATLAS Collaboration, *Performance of the ATLAS Trigger System in 2015*, Eur. Phys. J. C **77**
       (2017) 317, arXiv:1611.09661 [hep-ex].

[422] CMS Collaboration, *The CMS trigger system*, JINST **12** (2017) P01020, arXiv:1609.02366
       [physics.ins-det].

[423] ATLAS Collaboration, *Technical Design Report for the Phase-II Upgrade of the ATLAS TDAQ
       System*, CERN-LHCC-2017-020. ATLAS-TDR-029, 2017.

[424] R. Gupta and J. Alison, *b-tagging efficiency for b-jet triggers*, ATL-COM-DAQ-2017-062, 2017.

[425] A. Zabi et al., *Triggering on electrons, jets and tau leptons with the CMS upgraded calorimeter
       trigger for the LHC RUN II*, JINST **11** (2016) no. 02, C02008.

[426] *PICMG 3.0 AdvancedTCA Base Specification (Shortform)*,
       https://www.picmg.org/?s=micro+TCA.

[427] N. Dev et al., *The CMS Level-1 electron and photon trigger: for Run II of LHC*, JINST **12** (2017)
       no. 02, C02014.

[428] ALEPH, DELPHI, L3, OPAL, LEP Electroweak Working Group Collaboration, *A Combination
       of preliminary electroweak measurements and constraints on the standard model*,
       arXiv:0511027 [hep-ex].

[429] BaBar Collaboration, *Measurement of the inclusive charmless semileptonic branching ratio of B mesons and determination of |V_{ub}|*, Phys. Rev. Lett. **92** (2004) 071802, arXiv:0307062 [hep-ex].

[430] BaBar Collaboration, *Measurements of moments of the hadronic mass distribution in semileptonic B decays*, Phys. Rev. D **69** (2004) 111103, arXiv:0403031 [hep-ex].

[431] BaBar Collaboration, *Determination of the branching fraction for $B \rightarrow X_c \ell \nu$ decays and of |V_{cb}| from hadronic mass and lepton energy moments*, Phys. Rev. Lett. **93** (2004) 011803, arXiv:0404017 [hep-ex].

[432] ATLAS, CMS Collaboration, *Combined Measurement of the Higgs Boson Mass in pp Collisions at $\sqrt{s} = 7$ and 8 TeV with the ATLAS and CMS Experiments*, Phys. Rev. Lett. **114** (2015) 191803, arXiv:1503.07589 [hep-ex].

[433] J. D'Hondt, S. Lowette, O. L. Buchmuller, S. Cucciarelli, F. P. Schilling, M. Spiropulu, S. Paktinat Mehdiabadi, D. Benedetti, and L. Pape, *Fitting of event topologies with external kinematic constraints in CMS*, CERN-CMS-NOTE-2006-023, 2006.

[434] CMS Collaboration, *Search for Higgs boson pair production in events with two bottom quarks and two tau leptons in proton-proton collisions at $\sqrt{s}$ =13TeV*, Phys. Lett. B **778** (2018) 101–127, arXiv:1707.02909 [hep-ex].

[435] CMS Collaboration, *Search for two Higgs bosons in final states containing two photons and two bottom quarks in proton-proton collisions at 8 TeV*, Phys. Rev. D **94** (2016) 052012, arXiv:1603.06896 [hep-ex].

[436] C. Vernieri, L. Rolandi, and A. Rizzi, *Search for resonances decaying to $H(b\bar{b})$ pairs with the CMS experiment at the LHC*, CERN-THESIS-2014-161, 2014.

[437] CMS Collaboration, *Searches for a heavy scalar boson H decaying to a pair of 125 GeV Higgs bosons hh or for a heavy pseudoscalar boson A decaying to Zh, in the final states with $h \rightarrow \tau\tau$*, Phys. Lett. B **755** (2016) 217–244, arXiv:1510.01181 [hep-ex].

[438] CMS Collaboration, *Search for Higgs boson pair production in the $\gamma\gamma b\bar{b}$ final state in pp collisions at $\sqrt{s} = 13$ TeV*, Physics Letters B **788** (2019) 7 − 36, arXiv:1806.00408 [hep-ex].

[439] N. Kumar and S. P. Martin, *LHC search for di-Higgs decays of stoponium and other scalars in events with two photons and two bottom jets*, Phys. Rev. D **90** (2014) 055007, arXiv:1404.0996 [hep-ph].

[440] CMS Collaboration, *Search for a massive resonance decaying to a pair of Higgs bosons in the four b quark final state in proton-proton collisions at $\sqrt{s} = 13$ TeV*, Phys. Lett. B **781** (2018) 244–269, arXiv:1710.04960 [hep-ex].

[441] CMS Collaboration, *Search for production of Higgs boson pairs in the four b quark final state using large-area jets in proton-proton collisions at $\sqrt{s} = 13$ TeV*, JHEP **01** (2019) 040, arXiv:1808.01473 [hep-ex].

[442] ATLAS Collaboration, *Measurements of Higgs boson properties in the diphoton decay channel with 36 fb^{-1} of pp collision data at $\sqrt{s} = 13$ TeV with the ATLAS detector*, Phys. Rev. D **98** (2018) 052005, arXiv:1802.04146 [hep-ex].

[443] CMS Collaboration, *Measurements of Higgs boson properties in the diphoton decay channel in proton-proton collisions at $\sqrt{s}$ = 13 TeV*, JHEP **11** (2018) 185, `arXiv:1804.02716` `[hep-ex]`.

[444] A. Papaefstathiou, L. L. Yang, and J. Zurita, *Higgs boson pair production at the LHC in the $b\bar{b}W^+W^-$ channel*, Phys. Rev. D **87** (2013) 011301, `arXiv:1209.1489` `[hep-ph]`.

[445] M. J. Dolan, C. Englert, N. Greiner, and M. Spannowsky, *Further on up the road: hhjj production at the LHC*, Phys. Rev. Lett. **112** (2014) 101802, `arXiv:1310.1084` `[hep-ph]`.

[446] C. Englert, F. Krauss, M. Spannowsky, and J. Thompson, *Di-Higgs phenomenology in $t\bar{t}hh$: The forgotten channel*, Phys. Lett. B **743** (2015) 93–97, `arXiv:1409.8074` `[hep-ph]`.

[447] M. J. Dolan, C. Englert, N. Greiner, K. Nordstrom, and M. Spannowsky, *hhjj production at the LHC*, Eur. Phys. J. C **75** (2015) 387, `arXiv:1506.08008` `[hep-ph]`.

[448] J. K. Behr, D. Bortoletto, J. A. Frost, N. P. Hartland, C. Issever, and J. Rojo, *Boosting Higgs pair production in the $b\bar{b}b\bar{b}$ final state with multivariate techniques*, Eur. Phys. J. C **76** (2016) 386, `arXiv:1512.08928` `[hep-ph]`.

[449] F. Kling, T. Plehn, and P. Schichtel, *Maximizing the significance in Higgs boson pair analyses*, Phys. Rev. D **95** (2017) 035026, `arXiv:1607.07441` `[hep-ph]`.

[450] S. Banerjee, B. Batell, and M. Spannowsky, *Invisible decays in Higgs boson pair production*, Phys. Rev. D **95** (2017) 035009, `arXiv:1608.08601` `[hep-ph]`.

[451] F. Bishara, R. Contino, and J. Rojo, *Higgs pair production in vector-boson fusion at the LHC and beyond*, Eur. Phys. J. C **77** (2017) 481, `arXiv:1611.03860` `[hep-ph]`.

[452] A. Adhikary, S. Banerjee, R. K. Barman, B. Bhattacherjee, and S. Niyogi, *Revisiting the non-resonant Higgs pair production at the HL-LHC*, JHEP **07** (2018) 116, `arXiv:1712.05346` `[hep-ph]`.

[453] J. H. Kim, K. Kong, K. T. Matchev, and M. Park, *Measuring the Triple Higgs Self-Interaction at the Large Hadron Collider*, Phys. Rev. Lett. **122** (2019) 091801, `arXiv:1807.11498` `[hep-ph]`.

[454] CMS Collaboration, *Search for nonresonant Higgs boson pair production in the $b\bar{b}b\bar{b}$ final state at $\sqrt{s}$ = 13 TeV*, JHEP **04** (2019) 112, `arXiv:1810.11854` `[hep-ex]`.

[455] ATLAS Collaboration, *Search for Higgs boson pair production in the $b\bar{b}WW^*$ decay mode at $\sqrt{s}$ = 13 TeV with the ATLAS detector*, JHEP **04** (2019) 092, `arXiv:1811.04671` `[hep-ex]`.

[456] CMS Collaboration, *Search for resonant and nonresonant Higgs boson pair production in the $b\bar{b}\ell\nu\ell\nu$ final state in proton-proton collisions at $\sqrt{s}$ = 13 TeV*, JHEP **01** (2018) 054, `arXiv:1708.04188` `[hep-ex]`.

[457] ATLAS Collaboration, *Search for Higgs boson pair production in the $WW^{(*)}WW^{(*)}$ decay channel using ATLAS data recorded at $\sqrt{s}$ = 13 TeV*, JHEP **05** (2019) 124, `arXiv:1811.11028` `[hep-ex]`.

[458] ATLAS Collaboration, *Search for pair production of Higgs bosons in the $b\bar{b}b\bar{b}$ final state using proton–proton collisions at $\sqrt{s}$ = 13 TeV with the ATLAS detector*, Phys. Rev. D **94** (2016) 052002, `arXiv:1606.04782` `[hep-ex]`.

[459] ATLAS Collaboration, *Optimisation of the ATLAS b-tagging performance for the 2016 LHC Run*, ATL-PHYS-PUB-2016-012, 2016.

[460] T. Chen and C. Guestrin, *XGBoost: A Scalable Tree Boosting System,* in *Proceedings of the 22Nd ACM SIGKDD International Conference on Knowledge Discovery and Data Mining*, KDD '16. 2016.

[461] CMS Collaboration, *Search for resonant pair production of Higgs bosons decaying to two bottom quark–antiquark pairs in proton–proton collisions at 8 TeV*, Phys. Lett. B **749** (2015) 560–582, arXiv:1503.04114 [hep-ex].

[462] P. Bryant and M. Shochet, *Search for Pair Production of Higgs Bosons in the Four Bottom Quark Final State Using Proton-Proton Collisions at $\sqrt{s}$ = 13 TeV with the ATLAS Detector*, CERN-THESIS-2018-208, 2018.

[463] J. Bellm et al., *Herwig 7.1 Release Note*, arXiv:1705.06919 [hep-ph].

[464] ATLAS Collaboration, *Measurement of Higgs boson properties in the diphoton decay channel using* 80 fb^{-1} *of pp collision data at $\sqrt{s}$ = 13 TeV with the ATLAS detector*, ATLAS-CONF-2018-028, 2018.

[465] CMS Collaboration, *Measurement of inclusive and differential Higgs boson production cross sections in the diphoton decay channel in proton-proton collisions at $\sqrt{s}$ = 13 TeV*, JHEP **01** (2019) 183, arXiv:1807.03825 [hep-ex].

[466] S. Bolognesi, Y. Gao, A. V. Gritsan, K. Melnikov, M. Schulze, N. V. Tran, and A. Whitbeck, *On the spin and parity of a single-produced resonance at the LHC*, Phys. Rev. D **86** (2012) 095031, arXiv:1208.4018 [hep-ph].

[467] M. V. Chizhov, V. A. Bednyakov, and J. A. Budagov, *On Resonance Search in Dijet Events at the LHC*, arXiv:1106.4161 [hep-ph].

[468] J. C. Collins and D. E. Soper, *Angular distribution of dileptons in high-energy hadron collisions*, Phys. Rev. D **16** (1977) 2219–2225.

[469] M. Frate, K. Cranmer, S. Kalia, A. Vandenberg-Rodes, and D. Whiteson, *Modeling Smooth Backgrounds and Generic Localized Signals with Gaussian Processes*, arXiv:1709.05681 [physics.data-an].

[470] P. Dauncey, M. Kenzie, N. Wardle, and G. Davies, *Handling uncertainties in background shapes: the discrete profiling method*, JINST **10** (2015) no. 04, P04015–P04015.

[471] K. Kondo, *Dynamical likelihood method for reconstruction of events with missing momentum. 1: method and toy models*, J. Phys. Soc. Jap. **57** (1988) 4126–4140.

[472] K. Kondo, *Dynamical likelihood method for reconstruction of events with missing momentum. 2: mass spectra for* 2 → 2 *processes*, J. Phys. Soc. Jap. **60** (1991) 836–844.

[473] A. Elagin, P. Murat, A. Pranko, and A. Safonov, *A new mass reconstruction technique for resonances decaying to* $\tau\tau$, Nucl. Instrum. Meth. A **654** (2011) 481, arXiv:1012.4686 [hep-ex].

[474] L. Bianchini, J. Conway, E. K. Friis, and C. Veelken, *Reconstruction of the Higgs mass in* $H \to \tau\tau$ *events by dynamical likelihood techniques*, J. Phys. Conf. Ser. **513** (2014) 022035.

[475] L. Bianchini, B. Calpas, J. Conway, A. Fowlie, L. Marzola, C. Veelken, and L. Perrini, *Reconstruction of the Higgs mass in events with Higgs bosons decaying into a pair of τ leptons using matrix element techniques*, Nucl. Instrum. Meth. A **862** (2017) 54, `arXiv:1603.05910 [hep-ex]`.

[476] M. Czakon and A. Mitov, *Top++: A Program for the Calculation of the Top-Pair Cross-Section at Hadron Colliders*, Comput. Phys. Commun. **185** (2014) 2930, `arXiv:1112.5675 [hep-ph]`.

[477] M. Czakon, M. L. Mangano, A. Mitov, and J. Rojo, *Constraints on the gluon PDF from top quark pair production at hadron colliders*, JHEP **07** (2013) 167, `arXiv:1303.7215 [hep-ph]`.

[478] J. M. Campbell, R. K. Ellis, P. Nason, and E. Re, *Top-Pair Production and Decay at NLO Matched with Parton Showers*, JHEP **04** (2015) 114, `arXiv:1412.1828 [hep-ph]`.

[479] A. Giraldi, G. Bagliesi, and K. Androsov, *Optimisation of a multivariate analysis technique for the $t\bar{t}$ background rejection in the search for Higgs boson pair production in $b\bar{b}\tau^{+}\tau^{-}$ decay channel with the CMS experiment at the LHC*, CERN-THESIS-2018-070, 2018.

[480] H. E. Haber and G. L. Kane, *The Search for Supersymmetry: Probing Physics Beyond the Standard Model*, Phys. Rept. **117** (1985) 75–263.

[481] F. Costanza, *Search for di-Higgs production at 13 TeV and prospects for HL-LHC.*, Presentation at European Physical Society - HEP, Ghent, Belgium, July 10-17, 2019, `https://indico.cern.ch/event/577856/contributions/3420200/`, 2019.

[482] J. H. Kim, M. Kim, K. Kong, K. T. Matchev, and M. Park, *Portraying Double Higgs at the Large Hadron Collider*, `arXiv:1904.08549 [hep-ph]`.

[483] M. L. Graesser and J. Shelton, *Hunting Mixed Top Squark Decays*, Phys. Rev. Lett. **111** (2013) 121802, `arXiv:1212.4495 [hep-ph]`.

[484] C. G. Lester and D. J. Summers, *Measuring masses of semiinvisibly decaying particles pair produced at hadron colliders*, Phys. Lett. B **463** (1999) 99–103, `arXiv:9906349 [hep-ph]`.

[485] M. Burns, K. Kong, K. T. Matchev, and M. Park, *Using Subsystem MT2 for Complete Mass Determinations in Decay Chains with Missing Energy at Hadron Colliders*, JHEP **03** (2009) 143, `arXiv:0810.5576 [hep-ph]`.

[486] A. J. Barr, T. J. Khoo, P. Konar, K. Kong, C. G. Lester, K. T. Matchev, and M. Park, *Guide to transverse projections and mass-constraining variables*, Phys. Rev. D **84** (2011) 095031, `arXiv:1105.2977 [hep-ph]`.

[487] P. Konar, K. Kong, and K. T. Matchev, $\sqrt{\hat{s}}_{min}$ *: A Global inclusive variable for determining the mass scale of new physics in events with missing energy at hadron colliders*, JHEP **03** (2009) 085, `arXiv:0812.1042 [hep-ph]`.

[488] P. Konar, K. Kong, K. T. Matchev, and M. Park, *RECO level $\sqrt{s}_{min}$ and subsystem $\sqrt{s}_{min}$: Improved global inclusive variables for measuring the new physics mass scale in $\not{E}_{T}$ events at hadron colliders*, JHEP **06** (2011) 041, `arXiv:1006.0653 [hep-ph]`.

[489] W. S. Cho, D. Kim, K. T. Matchev, and M. Park, *Probing Resonance Decays to Two Visible and Multiple Invisible Particles*, Phys. Rev. Lett. **112** (2014) 211801, `arXiv:1206.1546 [hep-ph]`.

[490] ATLAS Collaboration, *Searches for Higgs boson pair production in the hh → bbττ, γγWW**, *γγbb, bbbb channels with the ATLAS detector*, Phys. Rev. D **92** (2015) 092004, arXiv:1509.04670 [hep-ex].

[491] S. Nandan, *"HH→ 4τ final state"*, https://indico.cern.ch/event/731450/contributions/3093263/attachments/1712268/2760821/HHTo4tau.pdf, 2018. Oral Presentation at the Double Higgs boson production Workshop at FNAL.

[492] U. Baur, T. Plehn, and D. L. Rainwater, *Measuring the Higgs boson self coupling at the LHC and finite top mass matrix elements*, Phys. Rev. Lett. **89** (2002) 151801, arXiv:0206024 [hep-ph].

[493] U. Baur, T. Plehn, and D. L. Rainwater, *Determining the Higgs Boson Selfcoupling at Hadron Colliders*, Phys. Rev. D **67** (2003) 033003, arXiv:0211224 [hep-ph].

[494] Q. Li, Z. Li, Q.-S. Yan, and X. Zhao, *Probe Higgs boson pair production via the 3ℓ 2j+Ɇ mode*, Phys. Rev. D **92** (2015) 014015, arXiv:1503.07611 [hep-ph].

[495] J. Ren, R.-Q. Xiao, M. Zhou, Y. Fang, H.-J. He, and W. Yao, *LHC Search of New Higgs Boson via Resonant Di-Higgs Production with Decays into 4W*, JHEP **06** (2018) 090, arXiv:1706.05980 [hep-ph].

[496] K. Ehatäht, L. Marzola, and C. Veelken, *Reconstruction of the mass of Higgs boson pairs in events with Higgs boson pairs decaying into four τ leptons*, arXiv:1809.06140 [hep-ex].

[497] A. L. Read, *Presentation of search results: the CLs technique*, Journal of Physics G: Nuclear and Particle Physics **28** (2002) 2693–2704.

[498] E. Maguire, L. Heinrich, and G. Watt, *HEPData: a repository for high energy physics data*, J. Phys. Conf. Ser. **898** (2017) 102006, arXiv:1704.05473 [hep-ex].

[499] ATLAS Collaboration, *Search for squarks and gluinos in final states with jets and missing transverse momentum using 36 fb^{-1} of $\sqrt{s}$ = 13 TeV pp collision data with the ATLAS detector*, Phys. Rev. D **97** (2018) 112001, arXiv:1712.02332 [hep-ex].

[500] CMS Collaboration, *Search for supersymmetry in multijet events with missing transverse momentum in proton-proton collisions at 13 TeV*, Phys. Rev. D **96** (2017) 032003, arXiv:1704.07781 [hep-ex].

[501] GAMBIT Collaboration, *Global fits of GUT-scale SUSY models with GAMBIT*, Eur. Phys. J. C **77** (2017) 824, arXiv:1705.07935 [hep-ph].

[502] GAMBIT Collaboration, *Combined collider constraints on neutralinos and charginos*, Eur. Phys. J. C **79** (2019) 395, arXiv:1809.02097 [hep-ph].

[503] ATLAS Collaboration, *Search for new phenomena in the dijet mass distribution using $p − p$ collision data at $\sqrt{s}$ = 8 TeV with the ATLAS detector*, Phys. Rev. D **91** (2015) 052007, arXiv:1407.1376 [hep-ex].

[504] ATLAS Collaboration, *Search for new phenomena in dijet events using 37 fb^{-1} of pp collision data collected at $\sqrt{s}$ =13 TeV with the ATLAS detector*, Phys. Rev. D **96** (2017) 052004, arXiv:1703.09127 [hep-ex].

[505] ATLAS Collaboration, *Reinterpretation of searches for supersymmetry in models with variable R-parity-violating coupling strength and long-lived R-hadrons*, ATLAS-CONF-2018-003, 2018.

[506] CMS Collaboration, *Simplified likelihood for the re-interpretation of public CMS results*, CMS NOTE-2017/001, 2017.

[507] K. Cranmer, S. Kreiss, D. Lopez-Val, and T. Plehn, *Decoupling Theoretical Uncertainties from Measurements of the Higgs Boson*, Phys. Rev. D **91** (2015) 054032, `arXiv:1401.0080 [hep-ph]`.

[508] W. Verkerke and D. P. Kirkby, *The RooFit toolkit for data modeling*, eConf **C0303241** (2003) MOLT007, `arXiv:0306116 [physics]`.

[509] A pure-python implementation of Histfactory workspaces, `https://github.com/diana-hep/pyhf`.

[510] ROOT Collaboration, *HistFactory: A tool for creating statistical models for use with RooFit and RooStats*, CERN-OPEN-2012-016, 2012.

[511] *JSON*, `https://json.org/`.

[512] K. Cranmer and I. Yavin, *RECAST: Extending the Impact of Existing Analyses*, JHEP **04** (2011) 038, `arXiv:1010.2506 [hep-ex]`.

[513] ATLAS Collaboration, *Search for supersymmetry in final states with missing transverse momentum and multiple b-jets in proton-proton collisions at $\sqrt{s} = 13$ TeV with the ATLAS detector*, JHEP **06** (2018) 107, `arXiv:1711.01901 [hep-ex]`.

[514] DELPHES 3 Collaboration, *DELPHES 3, A modular framework for fast simulation of a generic collider experiment*, JHEP **02** (2014) 057, `arXiv:1307.6346 [hep-ex]`.

[515] ATLAS Collaboration, *Search for top-squark pair production in final states with one lepton, jets, and missing transverse momentum using 36 fb^{-1} of $\sqrt{s} = 13$ TeV pp collision data with the ATLAS detector*, JHEP **06** (2018) 108, `arXiv:1711.11520 [hep-ex]`.

[516] F. Chollet et al., *Keras*, `https://github.com/fchollet/keras`, 2015.

[517] *YAML*, `https://yaml.org/`.

[518] W. D. Goldberger and M. B. Wise, *Modulus stabilization with bulk fields*, Phys. Rev. Lett. **83** (1999) 4922–4925, `arXiv:9907447 [hep-ph]`.

[519] A. Carvalho, *Gravity particles from warped extra dimensions, predictions for LHC*, 2014.

[520] CMS Collaboration, *Search for resonances decaying to a pair of Higgs bosons in the $b\bar{b}q\bar{q}'\ell\nu$ final state in proton-proton collisions at $\sqrt{s} = 13$ TeV*, Submitted to: JHEP (2019) , `arXiv:1904.04193 [hep-ex]`.

[521] ATLAS and L. H. C. G. CMS Collaborations, *Procedure for the LHC Higgs boson search combination in Summer 2011*, CMS-NOTE-2011-005. ATL-PHYS-PUB-2011-11, 2011.

[522] ATLAS Collaboration, *Evidence for the associated production of the Higgs boson and a top quark pair with the ATLAS detector*, Phys. Rev. **D97** (2018) no. 7, 072003, `arXiv:1712.08891 [hep-ex]`.

[523] ATLAS Collaboration, *Search for the standard model Higgs boson produced in association with top quarks and decaying into a b$\bar{b}$ pair in pp collisions at $\sqrt{s} = 13$ TeV with the ATLAS detector*, Phys. Rev. D **97** (2018) 072016, arXiv:1712.08895 [hep-ex].

[524] ATLAS Collaboration, *Observation of Higgs boson production in association with a top quark pair at the LHC with the ATLAS detector*, Phys. Lett. B **784** (2018) 173–191, arXiv:1806.00425 [hep-ex].

[525] ATLAS Collaboration, *Measurement of the Higgs boson coupling properties in the $H \to ZZ^* \to 4\ell$ decay channel at $\sqrt{s} = 13$ TeV with the ATLAS detector*, JHEP **03** (2018) 095, arXiv:1712.02304 [hep-ex].

[526] ATLAS Collaboration, *Measurements of the Higgs boson production, fiducial and differential cross sections in the 4ℓ decay channel at $\sqrt{s} = 13$ TeV with the ATLAS detector*, ATLAS-CONF-2018-018, 2018.

[527] ATLAS Collaboration, *Measurements of VH, $H \to b\bar{b}$ production as a function of the vector boson transverse momentum in 13 TeV pp collisions with the ATLAS detector*, ATLAS-CONF-2018-053, 2018.

[528] ATLAS Collaboration, *Measurements of gluon-gluon fusion and vector-boson fusion Higgs boson production cross-sections in the $H \to WW^* \to e\nu\mu\nu$ decay channel in pp collisions at $\sqrt{s} = 13$ TeV with the ATLAS detector*, Phys. Lett. B **789** (2019) 508–529, arXiv:1808.09054 [hep-ex].

[529] ATLAS Collaboration, *Cross-section measurements of the Higgs boson decaying into a pair of τ-leptons in proton-proton collisions at $\sqrt{s} = 13$ TeV with the ATLAS detector*, Phys. Rev. D **99** (2019) 072001, arXiv:1811.08856 [hep-ex].